

Catalytic, Low Temperature Oxidation of Methane into Methanol over Copper-Exchanged Zeolites

by

Karthik Narsimhan
M.S., Massachusetts Institute of Technology (2014)
B.S., California Institute of Technology (2011)

Submitted to the Department of Chemical Engineering
In Partial Fulfillment of the Requirements for the Degree of

Doctor of Philosophy

at the

MASSACHUSETTS INSTITUTE OF TECHNOLOGY

February 2017

© 2017 Massachusetts Institute of Technology. All rights reserved.

Signature redacted

Signature of Author:

Department of Chemical Engineering

November 28, 2016

Signature redacted

Certified by:

Yuriy Román-Leshkov
Associate Professor of Chemical Engineering
Thesis Supervisor

Signature redacted

Accepted by:

Daniel Blankschtein
Herman P. Meissner (1929) Professor of Chemical Engineering
Chairman, Committee for Graduate Students



Catalytic, Low Temperature Oxidation of Methane into Methanol over Copper-Exchanged Zeolites

by

Karthik Narsimhan

Submitted to the Department of Chemical Engineering
On November 28, 2016 in Partial Fulfillment of the
Requirements for the Degree of Doctor of Philosophy in Chemical Engineering

Abstract

As production of shale gas has increased greatly in the United States, the amount of stranded shale gas that is flared as carbon dioxide has become significant enough to be considered an environmental hazard and a wasted resource. The conversion of methane, the primary component of natural gas, into methanol, an easily stored liquid, is of practical interest. However, shale wells are generally inaccessible to reforming facilities, and construction of on-site, conventional methanol synthesis plants is cost prohibitive. Capital costs could be reduced by the direct conversion of methane into methanol at low temperature. Existing strategies for the partial oxidation of methane require harsh solvents, need exotic oxidizing agents, or deactivate easily. Copper-exchanged zeolites have emerged as candidates for methanol production due to high methanol selectivity (> 99%), utilization of oxygen, and low reaction temperature (423-473 K). Despite these advantages, three significant shortcomings exist: 1) the location of surface intermediates on the zeolite is not well understood; 2) methane oxidation is stoichiometric, not catalytic; 3) there are few active sites and methanol yield is low.

This work addresses all three shortcomings. First, a new reaction pathway is identified for methane oxidation in copper-exchanged mordenite zeolites using tandem methane oxidation and Koch carbonylation reactions. Methoxy species migrate away from the copper active sites and adsorb onto Bronsted acid sites, signifying spillover on the zeolite surface. Second, a process is developed as the first instance of the catalytic oxidation of methane into methanol at low temperature, in the vapor phase, and using oxygen as the oxidant. A variety of commercially available copper-exchanged zeolites are shown to exhibit stable methanol production with high methanol selectivity. Third, catalytic methanol production rates and methane conversion are further improved 100- fold through the synthetic control of copper speciation in chabazite zeolites. Isolated monocopper species, directed through the one-pot synthesis of copper-exchanged chabazite zeolites, correlates with methane oxidation activity and is likely the precursor to the catalytic site. Together, these synthetic methods provide guidelines for catalyst design and further improvements in catalytic activity.

Thesis Supervisor: Yuriy Román-Leshkov
Title: Associate Professor of Chemical Engineering

Acknowledgements

This thesis would not have been possible without the advice, help, and encouragement of many people.

My thesis advisor, Yuriy Román-Leskhov, has always been my biggest supporter. His vision for my thesis was predicated on a strange idea that seemed as if it would never work. Naturally, I faced difficulties along the way, but his passion, enthusiasm, and guidance motivated me to work harder and eventually to succeed. His crazy ideas illustrated how creative and exciting research can be, especially when an idea happens to work, and that I should pursue any of my own half-baked ideas in the laboratory. He also taught me how to effectively communicate both oral and written science to be captivating and persuasive. Overall, I am grateful that he took a risk and gave me the opportunity to work for him because I learned invaluable skills to be a successful researcher in my future career.

I would also like to thank my thesis committee and other faculty members. Profs. Green and Tisdale had many useful and thoughtful suggestions and advice during my graduate studies and thesis committee meetings. Prof. Green had insightful questions that helped me tailor my work to have more practical applications. Prof. Tisdale was supportive of me, especially when my research was not working early in my Ph.D. I have a special thank you to Profs. Fisher and Lupis for their guidance and mentorship during my semester at Practice School.

Several collaborators made critical contributions to my research. I thank Prof. Vladimir Michaelis, Dr. Guinevere Mathies, and Prof. Robert G. Griffin for assistance with NMR and EPR spectroscopic measurements in my first publication. I would also like to thank Dr. Randall Meyer and Dr. Pedro Serna of the methane oxidation team from ExxonMobil's Corporate Strategic Research. They have been extremely engaged in helping with X-ray absorption spectroscopy measurements, modelling XAFS data, and in suggesting future directions for the project. I had a great time getting to know both of you. Lastly, Dr. Jeremy Kropf and Dr. John Katsoudas were tremendously accommodating and instructive while Kim and I were at Argonne National Laboratory.

I am indebted to several Román soldiers for their help in my research. Prof. Kenta Iyoki and Kimberly Dinh synthesized all of the CHA catalysts for the work on methane oxidation. Kenta has always been a zeolite whisperer, and I am sure he will develop some innovative syntheses in his academic career. Kim has been a fast learner and continues to do high quality work. I am confident her work will result in an even better thesis than mine. I would also like to thank Dr. William Gunther for his help with some EPR measurements in my first publication.

Outside of my immediate research, the Román group has been a constant source of entertainment and support. I have known Helen since our Caltech days, and she has always helped me pass classes or provide advice on practical matters. Sean was my late-night officemate whose Cherry MX Blues keyboard kept me awake. When not typing, his antics kept me laughing while somehow widening my scientific knowledge. Eric has become a good friend and drinking buddy with whom I can discuss anything. Jen has kept the lab safe despite my experiments and has helped me with infrared spectroscopy experiments. Manish was a great sounding board about life and soccer. Karthick was my misspelled namesake and foil who added plenty of cheerfulness. I remain and will

forever be the first Karthik in the lab. Yuran was another cheerful soul who kept my spirits high late at night. Daniel and I broke our GC several times, so I am grateful he gave me the opportunity to learn about GCs through repairing them. Aaron was quiet, but was a blast to hang out with the few times he went out with the group. Taka continued as the Japanese ambassador and brought tasty sake during lab events. Maria asked the difficult questions that compelled me to reflect upon my personal philosophies, ultimately making me a better person whether I wanted it or not. Anthony was a mentor and was quick with an entertaining story whenever I was bored. Marco and Stijn were amusing during our nights out. David and Air taught me how to build, operate, and troubleshoot reactors, an invaluable skill for my Ph.D.

The few times I was not in the laboratory doing research, my friends at MIT distracted me from the stresses of life. Sean, Mark, and Xiao insisted we go to Muddy' s at 4 every Friday and then FIFA later. Rosanna, Eric, and Thomas hosted many parties, such as the traditional Super Bowl, Christmas, and St. Patty' s Day parties. Steven always made our group' s nights in Boston memorable for both good and bad reasons. David and William were passionate sports fans with whom I discussed the latest games. The nights out in Boston with all of you are some of the most, or possibly the least, memorable times during my Ph.D. I would also like to thank my Practice School cohort of Sean Faltermeier, Nate, Sakul, Alex, Helen, Chris, Jicong, and Anasuya who traveled with me to Basel and Minneapolis. Our trips of sledding in the Alps, an interesting night in Zurich, Fasnacht 2013, Kienbesenzug in Liestal, and freezing in Minneapolis will forever be in my memories.

My older friends, Christina, Chief, Alan, Greg, Reuben, Jeff, Katie, Monika, Ohm, Dan, Johnson, Govind, Mohit, and Anant, were my safety blanket. I could always count on you guys to take me back to the old days, or to take me across the country, to forget everything about MIT. My life was research, but all of my friends have filled in the cracks to make my life whole.

Lastly, I have to acknowledge my family. My parents have always supported me in my interests. They instilled in me a great work ethic and that I should always do my best. My brother, Vivek, has been an inspiration to me even from my birth. I strive to be like him as often as possible. I am positive he will achieve excellence in his life. I also thank my grandmother, affectionately known as Paati, Amrit uncle, and Lidija auntie for their continued love and support.

I dedicate this thesis to my family.

Table of Contents

Chapter 1 : Introduction	11
Chapter 2 : Methane to Acetic Acid over Cu-Exchanged Zeolites: Mechanistic Insights from a Site-Specific Carbonylation Reaction	31
Chapter 3 : Catalytic Oxidation of Methane into Methanol over Copper-Exchanged Zeolites with Oxygen at Low Temperature	65
Chapter 4 : One-Pot Synthesis of Copper-Exchanged SSZ-13 Zeolites for the Oxidation of Methane into Methanol	105
Chapter 5 : Conclusions and Outlook.....	129
Chapter 6 : References.....	135

Chapter 1 : Introduction

1.1 Transportation of Shale Gas

Natural gas, consisting mainly of methane, is used as a fuel and chemical precursor. It has become increasingly important in recent years because it is low emission,¹ abundant, and cheap. Natural gas production in the United States has increased 38% since 2005. Shale gas rose from negligible contributions to 47% of natural gas production by 2014.² Coupled with domestic natural gas prices that are projected to remain low and stable through 2018 (< 3 USD per thousand cubic feet),³ long term demand that is projected to rise by 60%,⁴ and more than 20 quadrillion cubic feet in global reserves,⁵ there is substantial motivation to increase the long term usage of natural gas primarily due to advances in extraction techniques to access nonconventional shale gas wells.

The main challenge in utilizing shale gas, the fastest growing source of natural gas, is that shale rock formations are located in remote areas. The major shale wells in the United States are the Bakken, Marcellus, and Eagle Ford formations in North Dakota, Appalachian Mountains, and central Texas far from conventional refineries or storage facilities. Efficient storage of natural gas requires high pressure or low temperature, rendering on-site storage prohibitively expensive.⁶ This necessitates immediate transportation to established markets as cryogenically cooled liquid or as compressed gas, but the costs for cooling or compression facilities are large relative to the amount of gas shipped from small shale wells.⁷ If no economical method is available for natural gas transportation from stranded shale wells, the gas is flared into the atmosphere as carbon dioxide (CO₂). The World Bank estimates 134 billion cubic meters of natural gas was flared annually instead of utilized, resulting in significant greenhouse emissions and lost opportunities for economic use.⁸ To maximize the effective usage of natural gas, a smaller-scale, flexible, and cheaper method must be developed to transport stranded natural gas to refineries.

Chemical transformation of natural gas into liquid fuels, otherwise known as gas-to-liquid (GTL) technology, is one such storage method. GTL technology is a broad set of chemical reactions for converting methane, the primary component of natural gas,⁹ into liquid fuels as either methanol or larger hydrocarbons. Liquid fuels have higher bulk density than methane and are much easier to store and transport. Liquid fuels (methanol at 0.88 USD/gal¹⁰ and propane at 0.48 USD/gal¹¹) are valued higher than methane (0.48 USD/10⁶ gal).³ Lastly, the demand for methanol, gasoline, and diesel is predicted to

increase by 20%,¹² 40%, and 53%¹³ in the near future. The financial incentive to improve the storage of stranded natural gas has increased the urgency for innovation in GTL technologies.

There are two main methods of converting methane into liquid fuels: 1) indirectly through synthesis gas (syngas) or 2) directly into methanol or hydrocarbons. Details of these methods will be discussed in the following sections.

1.2 Indirect Gas-to-Liquids: Industrial Processes

The first step in GTL is the conversion of methane into syngas, a mixture of carbon monoxide (CO) and hydrogen (H₂). Methane is converted into syngas through steam reforming (equation 1.1). Steam reforming is highly endothermic and requires high reaction temperatures (1073-1273 K) to ensure high equilibrium conversion over a nickel catalyst.¹⁴⁻¹⁶



The next step is production of methanol or long chained hydrocarbons from syngas by hydrogenation of carbon monoxide. Methanol is produced on an industrial scale over a copper/zinc oxide/aluminum oxide (Cu/ZnO/Al₂O₃) catalyst from 523-553 K and 6-8 MPa.¹⁷ The actual reaction mechanism is outlined in equations 1.2-1.4. The overall reaction is the hydrogenation of CO into methanol (eqn. 1.4), but CO is actually oxidized into CO₂ through surface oxygen on the Cu/ZnO/Al₂O₃ catalyst or the water gas shift reaction (eqn. 1.2) and subsequently hydrogenated (eqn. 1.3).¹⁸⁻¹⁹



Long chain hydrocarbons are synthesized from Fischer-Tropsch synthesis through the hydrogenation/polymerization of CO (eqn. 1.5) with a cobalt or iron based catalyst. Cobalt catalysts operate from 473-513 K and 2-2.5 MPa to produce mainly diesel and long chain hydrocarbons (> C₅).²⁰⁻²¹ Iron based catalysts operate at higher temperatures of 603-623 K²² and 2.5 MPa, thereby producing C₃-C₅ alkanes and olefins in the vapor phase.²³



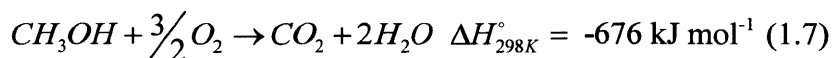
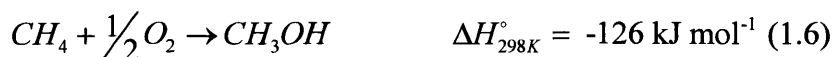
Out of all the possible liquid fuels that can be produced from GTL, the conversion of methane into methanol is the most advantageous process for the storage of stranded

natural gas. While gasoline and diesel are conventional transportation fuels, methanol can be converted into a variety of important commodity chemicals and fuels such as olefins,²⁴⁻²⁶ hydrocarbons and gasoline,²⁷⁻³⁰ and others.³¹⁻³⁵ Methanol can also be consumed as a fuel either by direct combustion in conventional engines or in fuel cells.³⁶⁻³⁷ Lastly, methanol synthesis is a simpler process with higher selectivity (> 99%) than Fischer-Tropsch synthesis which may require subsequent hydrocracking of long alkanes to produce middle distillates (diesel, gasoline).³⁸ Therefore, discussion will be limited to methanol as the liquid product from stranded natural gas.

While methanol produced from GTL is economical at industrial scales, the need for syngas causes this to be uneconomical at stranded gas wells. Steam reforming accounts for up to 60% of the investment cost of a methanol synthesis plant³⁹ due to its high operating temperature and cleanup operations. Additional unit operations in methanol synthesis cause the technical complexity,⁴⁰ capital cost,⁴¹ and investment risk of conventional GTL plants to be prohibitive at stranded sites.²⁰ To utilize GTL technology for storing stranded natural gas, steps must be taken to reduce technical complexity and capital costs of GTL through technical innovation. Reducing the size of GTL plants would reduce the capital costs of construction and reduce investment risk. Technoeconomic analysis shows that small, mobile GTL facilities at shale wells are highly profitable⁴² even under market uncertainty.⁴³ Accordingly, smaller and cheaper conventional GTL plants have been developed in an effort to monetize stranded gas.⁴⁴⁻⁴⁵ However, direct conversion of methane into methanol would minimize technical complexity, capital expenditure, and investment risk of GTL plants at stranded wells.

1.3 Direct Conversion of Methane into Methanol

While the partial oxidation of methane into methanol is thermodynamically accessible (eqn. 1.6), activating methane poses several challenges due to its physical properties. Methane possesses tetrahedral symmetry and no dipole nor magnetic moment to facilitate chemical attack.³⁹ Its C-H bond is the strongest of all alkanes (425 kJ mol⁻¹), requiring high temperatures or strong oxidizing agents for activation. However, methane can easily become over oxidized into CO₂ due to facile activation of the second, third, and fourth C-H bonds. For instance, methanol has weaker C-H bonds (389 kJ mol⁻¹) and is more easily oxidized into CO₂ under harsh reaction conditions (eqn. 1.7). To maximize the selectivity for methanol, catalysts must be developed to stabilize intermediates after the first C-H bond oxidation. They must also be reactive under mild oxidizing agents and low reaction temperatures.⁴⁶



Heterogeneous and homogeneous catalytic systems have been designed to directly convert methane into methanol but with limited potential in achieving economic conversion at scale. Heterogeneous catalysts V_2O_5 and MoO_3 operate at intermediate temperatures (623-773 K) and atmospheric pressure to achieve up to 16% yield of C_1 oxygenates but suffers from low methanol selectivity. A more successful homogeneous catalyst, the Pt based Periana catalyst, achieves high methanol yield and selectivity but requires fuming sulfuric acid as the solvent and is impractical environmentally. The most successful homogeneous catalysts are methane monooxygenase enzymes which can selectively convert methane into methanol at room temperature in the aqueous phase but denatures at moderate temperatures and is difficult to purify for scale-up. Lastly, copper-exchanged zeolites have emerged as an intriguing biomimetic heterogeneous analogs for low temperature and selective methane oxidation into methanol. However, these zeolites cannot catalytically convert methane into methanol. Details of each system will be provided in the next sections.

1.4 Supported V_2O_5 and MoO_3 Catalysts for Moderate-Temperature Methane Oxidation into Methanol and Formaldehyde

The first heterogeneous catalyst developed to convert methane directly into methanol were V_2O_5 and MoO_3 supported on SiO_2 . These metal oxides are redox active and insert oxygen into methyl radicals after the first H-abstraction from methane.⁴⁷ Isolated, partially reduced oxide species are the active centers for reaction.⁴⁸⁻⁴⁹ C_1 oxygenate yield (formaldehyde and methanol) is maximized at high temperature (773-923 K) and fuel rich conditions ($CH_4/O_2 = 1.8$, molar), achieving a maximum yield of 16%. However, NO is needed as a radical initiator⁵⁰ to form reactive hydroxide radicals for H-abstraction from methane.⁵¹ The requirement for NO_x in the reaction system precludes V_2O_5 and MoO_3 from being industrially relevant.

1.5 Homogeneous and Supported Periana Catalysts for Low Temperature Methane Oxidation into Methanol and Methylbisulfate

The most active synthetic catalyst for the partial oxidation of methane is the Periana catalyst. The homogeneous Periana catalyst (Figure 1-1, left) dissolved in fuming sulfuric acid reacts with methane below 423 K to produce methanol and methylbisulfate with conversion above 70% and selectivity above 80%.⁵² SO_4^{2-} ions act as the oxidizing agent while the bisulfate group prevents over-oxidation of methylbisulfate into CO_2 (eqn.

1.8). Methylbisulfate is then hydrolyzed into methanol with water (eqn. 1.9). However, the requirement for corrosion-resistant equipment, the high cost of sulfuric acid, and the difficulty in separating methanol from sulfuric acid severely limit the utility of this process.

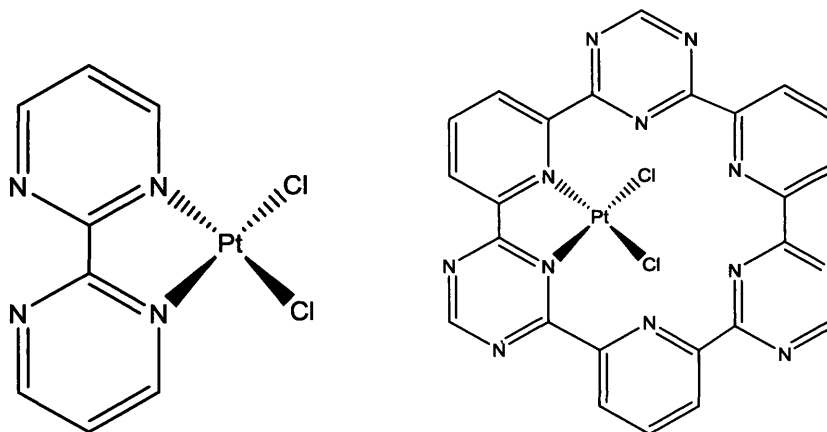
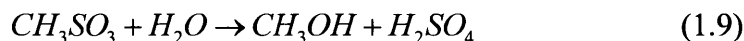
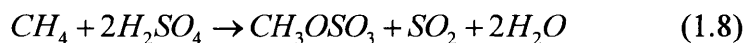


Figure 1-1. Periana (left) and supported Periana (right) catalysts



A heterogeneous version of the Periana catalyst has been synthesized (Figure 1-1, right) and shows high activity for methane partial oxidation. Pt metal is coordinated to a triazine-based framework and exhibits similar activity to the homogeneous Periana catalyst while being recyclable. However, this catalyst still requires strongly corrosive conditions.⁵³

1.6 Biological Conversion of Methane into Methanol

The gold standard for direct partial oxidation of methane into methanol at low temperature is the methane monooxygenase (MMO) enzyme. Two types of MMO enzymes, cytoplasmic MMO (soluble, sMMO) and membrane-bound MMO (particulate, pMMO), activate methane in aqueous medium using molecular oxygen at ambient temperature and neutral pH. The active site in sMMO is a bis(μ -oxo)diiron core.⁵⁴ Copper centers are present in pMMO, but the structure of the active site is hotly debated. Copper clusters are thought to insert oxygen into methane, but several researchers posit copper dimers⁵⁵ are active while recent publications also hypothesize that copper trimers⁵⁶⁻⁵⁷ are the active site. Despite the active site being unknown, pMMO is highly active (turnover frequency, TOF > 1 s⁻¹)⁵⁸ with methanol selectivity > 99%.⁵⁹ Unfortunately, the cost of MMO purification and sensitivity of the enzyme to temperature and pH hinder

use of MMO at industrial scales.⁶⁰ An inorganic, biomimetic catalyst analogous to MMO could alleviate these difficulties.

1.7 Biomimetic Inorganic Catalysts for Converting Methane into Methanol

The first heterogeneous analog to MMOs for methane oxidation were iron-exchanged zeolites. Fe-ZSM-5 converts methane into methanol at room temperature using nitrous oxide (N_2O) as the oxidant.⁶¹ After high temperature calcination (1173 K), N_2O is cleaved to form α -oxygen on a single Fe site. α -oxygen abstracts hydrogen from methane to form a strongly bound methoxy species that is hydrolyzed to yield $70 \mu\text{mol g}_{\text{cat}}^{-1}$ methanol.⁶² Unfortunately, N_2O is not a cheap, plentiful oxidizing agent, prohibiting use of this process at large scales. Fe-ZSM-5 can also be activated by hydrogen peroxide in aqueous solution at high turnover frequency.⁶³⁻⁶⁵ Product extraction for Fe-ZSM-5 with copper promoters are quite high, achieving up to $7000 \mu\text{mol g}_{\text{cat}}^{-1}$ of methanol at 85% selectivity.⁶³ However, the hydrogen peroxide oxidant is not efficiently used to oxidize methane. Elevated temperatures around 323 K causes hydrogen peroxide to degrade into water. Along with spectator iron species within Fe-ZSM-5, hydrogen peroxide is consumed at 6 times the rate of methanol production.⁶⁴ The high price of hydrogen peroxide relative to methanol as well as its unselective consumption makes this process uneconomical at large scales. Therefore, despite the promising activity over Fe-ZSM-5, another heterogeneous catalyst must be developed for the direct oxidation of methane.

Copper-exchanged zeolites have emerged as promising biomimetic catalysts for selective, partial oxidation of methane into methanol at low temperature. Cu-ZSM-5, a copper-exchanged zeolite, is activated by oxygen above 723 K and oxidizes methane into a surface bound methoxy species which is hydrolyzed into methanol.⁶⁶ The advantages of copper-exchanged zeolites relative to the other catalytic systems described above are that copper-exchanged zeolites utilize only oxygen as the oxidizing agent, activate C-H bonds under mild reaction conditions ($< 473 \text{ K}$), require relatively mild conditions ($> 623 \text{ K}$) for activation, are heterogeneous and thermally stable. The next section will provide a brief background of zeolite structure, preparation of metal-exchanged zeolites, and the reactivity and mechanism of methane oxidation over copper-exchanged zeolites.

1.8 Zeolite Structure

Zeolites are nanoporous, crystalline materials consisting of TO_4 tetrahedra arranged in a three-dimensional network where T is Si or Al. Up to 20 secondary building units can be formed by arranging these tetrahedra into different configurations (Figure 1-2). Larger, more complex structures can be formed by tessellating these secondary building

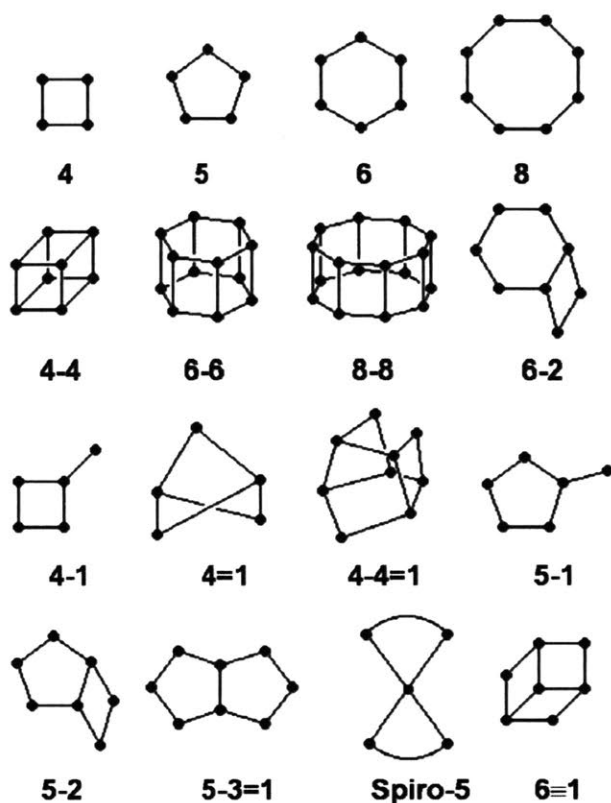


Figure 1-2. Common secondary building units of zeolite structures. Dots represent T atoms (Si or Al). O atoms are midpoints of segments.

units to form as many as 200 unique zeolite topologies of varying pore sizes and connectivity.

Zeolite topology is heavily dictated by the size and configuration of its pore channels and/or cages. The size of channels and channel intersections depends on the number of T atoms around the circumference of the pore. Zeolite pores generally range from 6-14 T atoms. Depending on how the secondary building units are arranged, the channels can be one, two, or three dimensional in space. Common industrially relevant zeolites are listed in Table 1-1. Additional details of the ZSM-5, MOR, and SSZ-13 topologies, the most relevant to this thesis, will be outlined below.

Table 1-1. Industrially important zeolite topologies

Topology	Framework	Cage Shape	Cage Size (Å) ⁶⁷	Channel Size (Å) ⁶⁸	Channel Geometry	Channel System
ZSM-5	MFI	–	–	5.3 × 5.6 5.1 × 5.5	10-MR 10-MR	2-D
Beta	BEA	–	–	6.6 × 6.7 5.6 × 5.6	12-MR 12-MR	3-D
Mordenite	MOR	–	–	6.5 × 7, 2.6 × 5.7	12-MR 8-MR	1-D
Ferrierite	FER	–	–	4.2 × 5.4 3.5 × 4.8	10-MR 8-MR	2-D
Y	FAU	Spherical	9.6 × 9.6	7.4 × 7.4	12-MR	3-D
SSZ-13	CHA	Ellipsoidal	9.4 × 9.4 × 12.7	3.8 × 3.8	8-MR	3-D

ZSM-5 consists of two 10-membered ring (10-MR) channels. The straight channel (5.3x5.6 Å) and sinusoidal channel (5.1x5.6 Å) are orthogonal and intersect to form large cavities. ZSM-5 is an industrial catalyst for shape selective cracking and isomerization reactions.⁶⁹⁻⁷²

MOR has two parallel, straight channels and side pockets. The large 12-MR channel is 6.5x7 Å and the small 8-MR channel is 2.6x5.7 Å. Connecting these parallel channels is an orthogonal 8-MR side pocket with an entrance of 3.9x5.7 Å. The confined environment in the 8-MR side pockets as well as its sinusoidal path stabilizes reactions with charged intermediates such as carbonylation.⁷³⁻⁷⁶ MOR is also used for alkane cracking and alkylation.⁷⁷⁻⁷⁸

CHA is a symmetric framework made of cages. The ellipsoidal cages consist of six 8-MR, two 6-MR, and twelve 4-MR. The entrance to these cages through the 8-MR are 3.8x3.8 Å. CHA type zeolites (SSZ-13, SAPO-34) are active for methanol-to-olefins. Copper-exchanged SSZ-13 is almost commercialized for the selective catalytic reduction of NO_x for diesel engine exhaust.⁷⁹⁻⁸⁰

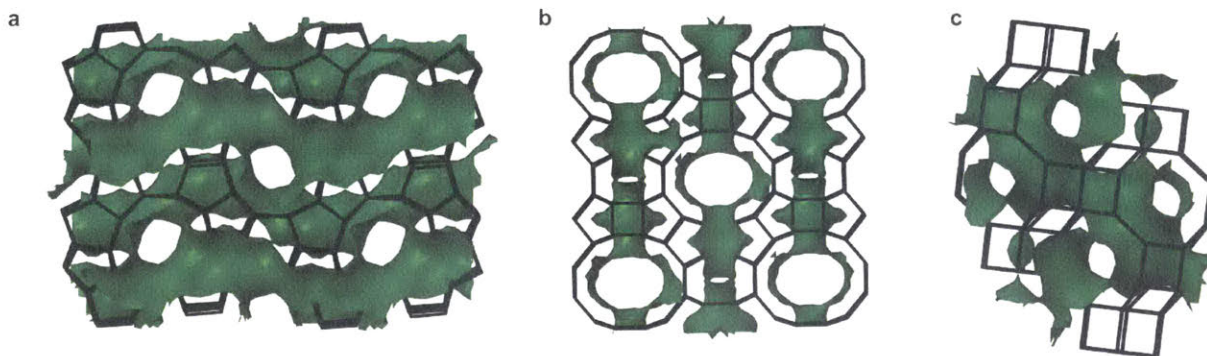


Figure 1-3. Framework structures of (a) ZSM-5 viewed along [010], (b) MOR viewed along [001], and (c) CHA (SSZ-13). Zeolite framework is in black (Si atoms only). Channel surfaces in green. Adapted from the International Zeolite Association Structure Database.⁶⁸

1.9 Location and Distribution of Framework Al Sites

The location, distribution, and concentration of framework Al sites in a zeolite has significant implications on the reactivity and selectivity of the zeolite.⁸¹ This is due to two effects: Lewis acidity in the vicinity of the framework Al site and confinement of the zeolite channel.

Al incorporated tetrahedrally into the zeolite framework introduces a net negative charge on the zeolite (AlO_4^-), necessitating reactive counter-cations to bond with adjacent framework oxygen atoms. When the counter-cation is a proton, the zeolite is in its acid form. Other cations, such as sodium or copper, can be used to neutralize the charge through ion exchange in aqueous environments. Divalent cations, such as Cu^{2+} , can only be stabilized in the vicinity of framework Al pairs (Figure 1-4). Depending on the nature of the counter cation, the zeolite can participate in a wide variety of reactions, such as alkane cracking with acidity⁶⁹⁻⁷⁰ or methane oxidation^{66, 82} and selective catalytic reduction⁸³⁻⁸⁴ with copper. Because the active counter cation is complexed near the framework Al, having a higher concentration of framework Al allows higher ion-exchange capacity of the zeolite and the formation of more active sites. Additionally, higher framework Al content will increase the number of Al pairs to stabilize higher valent cations, thereby affecting the types of cations in the zeolite.

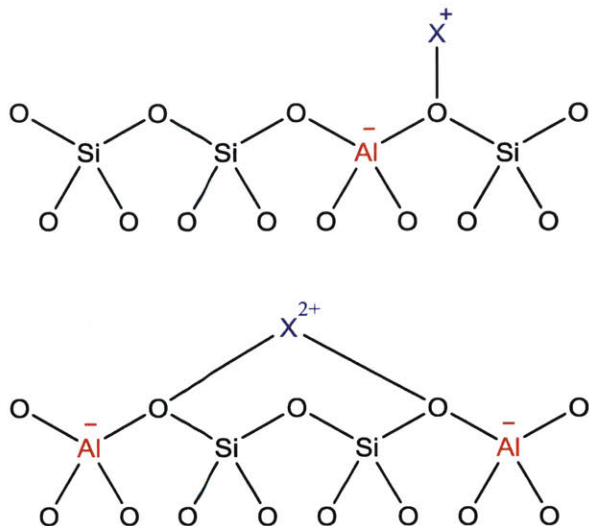


Figure 1-4. Framework Al and counter cations along a zeolite framework. A single valent cation X^+ is complexed near an Al site (above), while two nearby Al sites are needed to stabilize divalent cations (below).

The location and distribution of framework Al sites in the zeolite framework affects the accessibility of reactants to metal cations as well as the geometry of the cation-framework complex. Zeolite channels are shape selective based on the size of the pore. In zeolites with varying pore sizes, such as 12-MR and 8-MR in MOR or 10-MR and 8-MR in FER, large molecules are not able to diffuse through the small pores. For example, n-hexane is accessible to the 12-MR in MOR but not the 8-MR side pockets.⁸⁵ While small pores exclude large reactants, confinement effects in small pores stabilize charged intermediates thereby enabling unique reactivity. One of the best examples of zeolite structure affecting chemical reactivity is the carbonylation of dimethyl ether (DME) into acetic acid.

The carbonylation reaction is the insertion of carbon monoxide (CO) into organic substrates. The widest use of this reaction is the production of acetic acid from methanol on indium catalysts in the Cavita process.⁸⁶ Carbonylation has been used on heterogeneous catalysts, namely MOR and FER, for the carbonylation of alcohols and ethers to carboxylic acids and esters.⁸⁷⁻⁸⁸ In the carbonylation of DME (Figure 1-5), the reactant is adsorbed to Bronsted acid sites as a methoxy species. The surface methoxy species is then attacked by CO, forming a surface bound acylium cation. Reaction of water with the acylium cation restores the Bronsted acid site and yields gas phase acetic acid. The attack of CO on the methoxy groups occurs specifically on the acid sites in the 8-MR side pockets of MOR and FER.⁸⁹ CO attack is stabilized at the O33 position within the 8-MR side pocket due to the acid site and methoxy species being oriented along the

channel axis (Figure 1-6),⁷⁶ while acid sites (and methoxy species) are oriented orthogonal to the channel axis elsewhere. This prevents CO from attacking the methoxy species from above due to the confinement of side pocket. Additional charge stabilization of the transition state from lattice oxygen is much stronger in the 8-MR as compared to 10 and 12-MR of other zeolites.⁸⁹ Sodium exchange in MOR preferentially replaces Bronsted acid sites in the 8-MR side pockets, correlating to decreasing rates of dimethyl ether carbonylation.

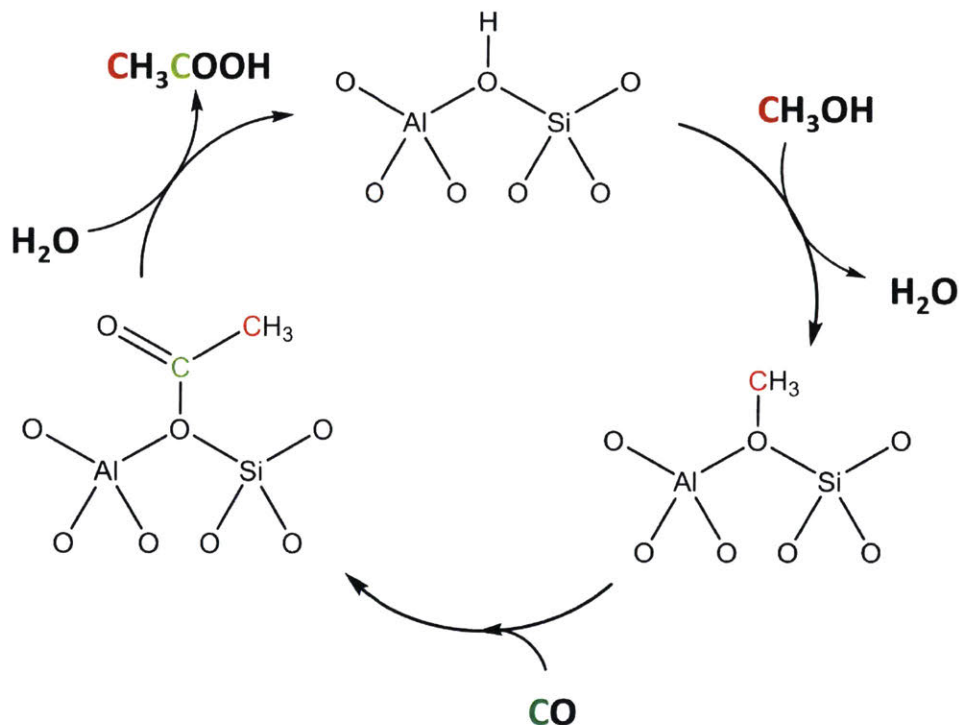


Figure 1-5. Reaction scheme of dimethyl ether carbonylation over H-MOR

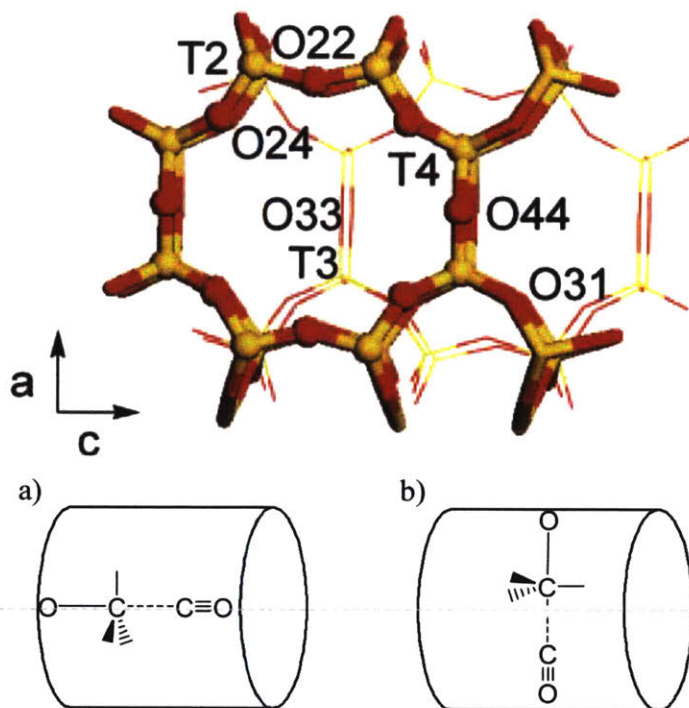


Figure 1-6. (Top) Structure of MOR viewed down the side pocket. (Bottom) Schematic representation of the relative orientation of the methoxy bond and the channel axis at the (a) O33 position, (b) other positions in the 8MR channel. Reprinted with permission from [76]. Copyright 2008 American Chemical Society.

Because the location and distribution of framework Al sites strongly impacts chemical reactivity of a zeolite, probing and controlling Al location and the distance between Al pairs is important to understand and improve the reactivity of the zeolite. The distribution of framework Al sites obeys Loewenstein's Rule where $\text{Al-O}-(\text{Si-O})_n\text{-Al}$ and $n \geq 1$, meaning no two Al sites can be next to each other.⁹⁰ High Si/Al zeolites have lower Al content, and by extension, larger distances between framework Al pairs and are less likely to stabilize divalent cations. Several methods have been developed to quantify the pairs of nearby framework Al sites. Cobalt exchanges into the zeolite as Co^{2+} . Co^{2+} remains in the +2 oxidation state after dehydration and coordinated to two proximal framework Al sites. Three types of framework Al configurations were classified.⁹¹⁻⁹³ The first type is a single Al atom in ring within the zeolite framework where Co^{2+} cannot be coordinated. The second type is a pair of nearby Al atoms where $1 \leq n \leq 2$ in $\text{Al-O}-(\text{Si-O})_n\text{-Al}$. The Al pair is contained in a given ring of the framework, and the close proximity favors coordination of Co^{2+} . The third type is a pair of distant Al atoms where $n > 2$ but are "visible" and close enough to stabilize Co^{2+} . Using UV-visible spectroscopy on cobalt exchanged zeolites, the location of these framework Al pairs can be deduced in the secondary building units of select zeolites like ZSM-5, MOR, FER, and BEA.⁹⁴ Dedec

and coworkers found that the location and arrangement of Al sites has a strong effect on the coordination and local charge of cations exchanged into the zeolite,⁹⁵ suggesting the importance of controlling Al distribution to understand the reactivity of zeolites.

1.10 Preparation of Copper-Exchanged Zeolites

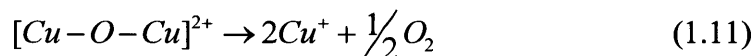
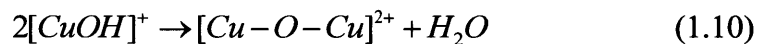
The presence of framework Al sites imparts local negative charge to the zeolite framework that is balanced with either protons or transition metal ions (TMI). While a wide variety of TMIs can be exchanged into zeolites, discussion will be limited to copper because copper is of interest for the direct oxidation of methane into methanol. Copper-exchanged zeolites are prepared either with aqueous or solid state ion-exchange. In aqueous ion-exchange, the parent zeolite in the Na or H form (Na^+ or H^+ as the counterion) is mixed in an aqueous solution of a copper salt. As an example, H-ZSM-5 would be mixed with Cu (II) acetate at room temperature for 24 h. During ion-exchange, Cu is in solution as $\text{Cu}(\text{H}_2\text{O})_6^{2+}$ and is able to diffuse into the zeolite pores and localize near two framework Al sites.⁹⁶ The pH of solution is kept below 6 to prevent the precipitation of $\text{Cu}(\text{OH})_2$ and the eventual formation of CuO_x in the zeolite.⁹⁷ The loading of Cu in the zeolite can be varied with the concentration of Cu salt in solution. The zeolite is then filtered, dried at 393 K overnight, and lastly the organics are removed by calcination of the zeolite at 823 K. Solid state ion-exchange involves the thermal treatment of a mixture of the zeolite and copper salt in flowing gas or vacuum to facilitate the diffusion of the ions into the zeolite.⁹⁸⁻⁹⁹ After both aqueous or solid-state ion-exchange, Cu^{2+} ions localize near proximal framework Al pairs after dehydration.

1.11 Copper Speciation and Migration After Thermal Pretreatment

Copper speciation in Cu-exchanged zeolites is dynamic and a function of copper loading, temperature, and framework Al distribution. Cu-exchanged zeolites prepared through aqueous ion-exchange initially have all Cu species present as $\text{Cu}(\text{H}_2\text{O})_6^{2+}$ complexed to proximal framework Al pairs. As copper loading increases to its theoretical limit ($\text{Cu}/\text{Al} = 0.5$), $\text{Cu}(\text{OH})(\text{H}_2\text{O})_5^+$ complexed to single Al sites can also form. As the zeolite is heated above 523 K,¹⁰⁰ the Cu complexes dehydrate to yield either bare Cu^{2+} or $[\text{CuOH}]^+$ species complexed to paired or single Al sites. The loss of water reduces the size of the first coordination sphere causing Cu ions to migrate to constrained locations, thereby maximizing the interaction of Cu with framework Al.¹⁰¹⁻¹⁰²

Further thermal treatments can change the oxidation state of Cu and also form oxide particles. Heating in inert atmospheres above 773 K causes some Cu to autoreduce into Cu^+ and lose any oxygen ligands.¹⁰³⁻¹⁰⁵ Cu^+ ions then migrate from paired Al sites to

single Al sites, possibly forming a Bronsted acid site from the free Al site. Under oxidizing atmospheres, Cu maintains its +2 oxidation state and can form oxides. At high Cu loadings ($\text{Cu}/\text{Al} > 0.3$), bulk CuO particles can form that are not associated with any framework Al sites.¹⁰⁶⁻¹⁰⁷ Partially charged, nanocluster Cu oxide particles can also form from the dehydration of nearby $[\text{CuOH}]^+$ (eqn. 1.10). Other copper-peroxo clusters have been observed in synthetic model catalysts and are hypothesized to be possible to form in zeolites.¹⁰⁸ Therefore, a large variety of Cu and Cu-oxo species are present in Cu-exchanged zeolites after dehydration or calcination. Isolated Cu^{2+} ions are predominantly present at low Cu loading ($\text{Cu}/\text{Al} < 0.20$) and low Al content as confirmed by electron paramagnetic resonance measurements.^{100, 109} Above Cu/Al of 0.20, the most thermodynamically stable paired Al sites are fully occupied by Cu^{2+} species, forcing additional Cu to bond as $[\text{CuOH}]^+$ to single Al sites and form Cu^+ , $[\text{Cu-O-Cu}]^{2+}$, and other $[\text{Cu}_x\text{O}_y]^{2+}$ sites after calcination. At $\text{Cu}/\text{Al} > 0.50$, additional Cu is no longer complexed to Al sites and bulk CuO is present in the zeolite. The variety of Cu complexes present in Cu-exchanged zeolites introduces difficulty in identifying Cu active sites and understanding the reaction mechanism of methane oxidation.



Controlling Cu speciation within Cu-exchanged zeolites would reduce the types of Cu complexes and more easily illuminate the true active species for methane oxidation. Because Cu speciation is influenced by the siting of framework Al sites, synthetic methods have been developed to yield a single type of framework Al site and subsequently a single Cu species. Zeolites are synthesized hydrothermally in basic solutions of aluminum halides, alkyl silicates, and alkali hydroxides. Organic structure directing agents (SDAs), usually amines, serve as nucleation points for assembly of the Al and Si tetrahedra and shaping agents for the channel or cage structure. The positive charge on the SDA also partially directs the location of Al tetrahedra (acid or Cu sites) due to the local charge balance. For example, tetramethylammonium cations under basic conditions have a positive charge and direct the formation of cages in the sodalite zeolite (Figure 1-7) as well as a framework Al site. Low Al content zeolites are synthesized using organic SDA agents, such as BEA and ZSM-5.¹¹⁰ Additional nucleation points for Al sites can form with the addition of alkali cations during hydrothermal synthesis. Na^+ ions are thought to organize zeolite structural subunits into amorphous solids which then dissolve and

transport Si and Al units in solution to other nucleation points. Using only alkali metals as nucleation agents crystallizes high Al content zeolites.¹¹¹

One synthetic method to control the types of framework Al sites was tuning the ratio of organic SDA and Na⁺ concentrations during synthesis. Common zeolite synthesis recipes include both Na⁺ and organic SDAs in the synthesis gel, resulting in a heterogeneous distribution of Al sites and types of Al pairs. Because Na⁺ is much smaller than SDAs, Na⁺ can fit between the SDA and crystallizing framework and form additional framework Al near Al directed from the SDA. This results in uncontrolled and stochastically distributed framework Al pairs throughout the zeolite framework (Figure 1-8)¹¹² and ultimately heterogeneous Cu speciation. Gradually eliminating Na⁺ content from the synthesis of SSZ-13 caused framework Al to become isolated with only one Al per cage due to geometric constraints of the SDA in the CHA cage.¹¹² Subsequent Cu exchange showed only [CuOH]⁺ complexed to isolated Al sites, indicating a homogeneous distribution of Cu due to the control of Al sites.

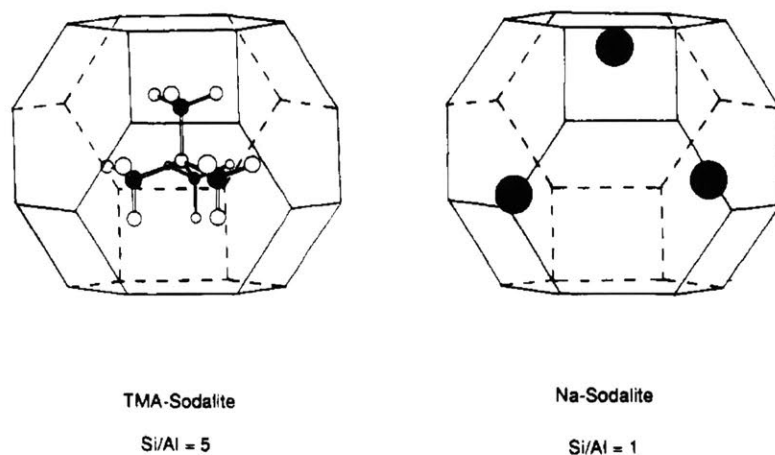


Figure 1-7. The organic structure directing agent tetramethylammonium cation occupying the cage of the sodalite zeolite. Counter cations occupy sites close to the ammonium cation in the SDA. Reprinted with permission from [110]. Copyright 1992 American Chemical Society.

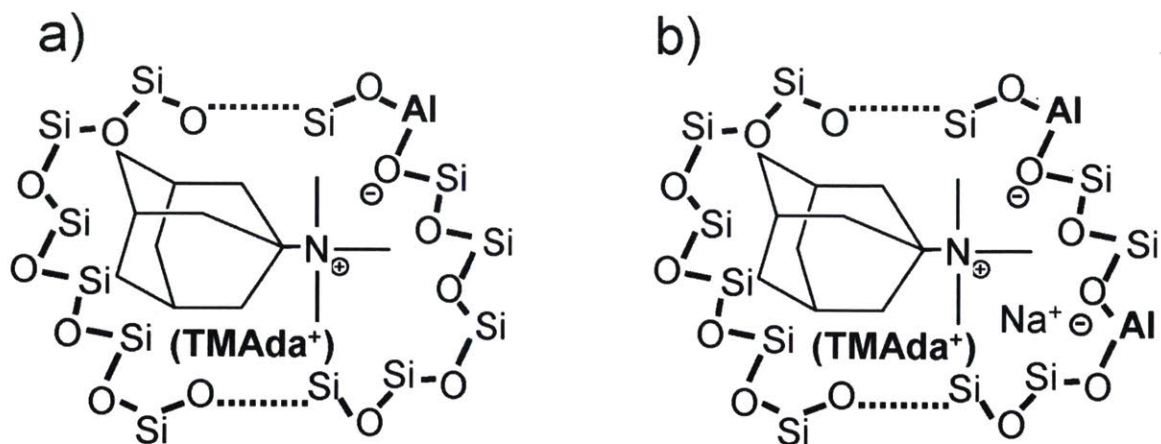


Figure 1-8. Organization of Si and Al atoms in the SSZ-13 (CHA) crystallization medium to form (a) isolated Al sites with trimethyladamantylammonium cations and (b) paired Al in the presence of trimethyladamantylammonium and sodium cations. Reprinted with permission from [112]. Copyright 2016 American Chemical Society.

A second synthetic method to control the Cu speciation involves complexing the Cu²⁺ ions with SDAs to control the location of Cu²⁺ during crystallization of the zeolite. Tetraethylenepentamine (TEPA) was added as an SDA in the synthesis of SSZ-13 in order to chelate to Cu²⁺. The Cu-TEPA complex is close in size to the trimethyladamantylammonium cation conventionally used in the synthesis of SSZ-13 where only one Cu-TEPA complex fits per SSZ-13 cage.¹¹³ Theoretically, the charged end of TEPA directs a framework Al site, causing the Cu²⁺ to complex to an isolated Al in the CHA cage of SSZ-13. TEPA-synthesized SSZ-13 has shown promising activity for the SCR of NO_x using ammonia as the reducing agent.¹¹⁴⁻¹¹⁷

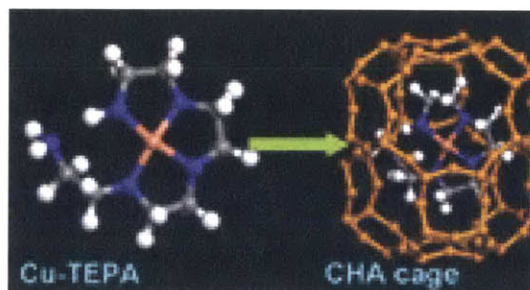


Figure 1-9. Cu-tetraethylenepentamine (Cu-TEPA) complex in solution and directing the formation of SSZ-13 (CHA) cages during synthesis. Reprinted with permission from [113]. Copyright 2011 Royal Society of Chemistry.

1.12 Copper-Exchanged Zeolites for the Direct Partial Oxidation of Methane into Methanol

Copper-exchanged zeolites (Cu-zeolite code, e.g. Cu-ZSM-5) have emerged as promising biomimetic catalysts for selective, partial oxidation of methane into methanol at low temperature. The first Cu-zeolite with observable methane oxidation activity was Cu-exchanged ZSM-5 from the Na parent form (Cu-Na-ZSM-5). After activation of Cu-Na-ZSM-5 with oxygen above 723 K⁸² and cooling below 473 K under oxygen atmosphere, Cu-Na-ZSM-5 oxidizes methane into a tightly bound surface methoxy species. Exposing the zeolite to liquid or gaseous water extracts the surface bound group as methanol. About 8 $\mu\text{mol g}_{\text{cat}}^{-1}$ methanol is extracted with > 99% selectivity.⁶⁶

The active site and mechanism for methane oxidation over Cu-Na-ZSM-5 is shown in Figure 1-10. After high temperature calcination of Cu-Na-ZSM-5 in oxygen above 723 K, a strong band at 22,700 cm^{-1} in the visible region appears. The intensity of this band appeared only after $\text{Cu}/\text{Al} = 0.20$.^{66, 104} This same band disappears after Cu-Na-ZSM-5 reacts with methane.⁶⁶ Resonance Raman spectroscopic and density functional theory (DFT) measurements pinpointed the $[\text{Cu-O-Cu}]^{2+}$ as the active site in the 10-MRs.¹¹⁸ This was consistent with methanol yield only appearing for $\text{Cu}/\text{Al} > 0.20$ but leveling off for $\text{Cu}/\text{Al} > 0.45$ ⁶⁶ when Cu pairs cease and bulk CuO_x forms. The $[\text{Cu-O-Cu}]^{2+}$ active site is hypothesized to perform hydrogen abstraction from methane between 373 to 473 K, resulting in a methyl radical.¹¹⁸ The methyl radical then localizes onto the zeolite surface although at an unknown location. Presumably, the methyl radical localizes onto another $[\text{Cu-O-Cu}]^{2+}$ site as a methoxy species or onto the same Cu active site as molecularly bound methanol. Water then extracts this surface bound species as methanol and hydrolyzes the $[\text{Cu-O-Cu}]^{2+}$ site as a hydroxyl group. Regeneration of the $[\text{Cu-O-Cu}]^{2+}$ site requires recalcination under oxygen above 723 K.

A similar UV-visible signature and active site was found to form in Cu-Na-MOR. Calcination under oxygen caused a 22,200 cm^{-1} band to form under similar Cu loadings to the $[\text{Cu-O-Cu}]^{2+}$ site as in Cu-Na-ZSM-5. This band also disappeared after reaction with methane.^{82, 119-121} A recent study by Sels and coworkers elucidated two $[\text{Cu-O-Cu}]^{2+}$ structures in the 8-MR side pockets and the main 12-MR channel.¹²² Methanol yield is higher with Cu-Na-MOR than with Cu-Na-ZSM-5, indicating that the active site and its reactivity are influenced by the environment of the zeolite.

Another type of copper active site was observed to form in Cu-H-MOR. Lercher and coworkers found through reactivity and XAFS studies that a $[\text{Cu}_3\text{O}_3]^{2+}$ species forms

at the entrance of the 8-MR side pocket facing the 12-MR channel of MOR¹²³ but only in the presence of Bronsted acidity. Na⁺ competes for the same exchange sites as Cu²⁺ at the entrance of the 8MR side pockets, thereby reducing the likelihood of having three neighboring Cu²⁺ ions to form the [Cu₃O₃]²⁺ site and forming the [Cu-O-Cu]²⁺ site instead.¹²⁴ DFT studies hypothesized a similar reaction mechanism for the trimetric active site as compared to the [Cu-O-Cu]²⁺ site (Figure 1-10). The first step is H-abstraction to form a protonated trimetric species and a methyl radical. However, the methyl radical is thought to rebound onto the same active site to form molecularly bound methanol. Extraction with water then deactivates the active site and elutes methanol.¹²³ The methanol yield in Cu-H-MOR was 160 μmol g_{cat}⁻¹, significantly higher than that of Cu-Na-ZSM-5 or Cu-Na-MOR, indicating the most active catalyst to date.

Other zeolite frameworks exchanged with copper are active for the direct oxidation of methane into methanol but contain unknown active sites. Cu-BEA, Cu-FER and Cu-Y all exhibit low partial oxidation activity (0-5 μmol g_{cat}⁻¹) but have no spectroscopic signatures for their active sites.⁸² Cu-SSZ-13 and other caged zeolites Cu-AFX and Cu-AEI are more active with methanol yields > 30 μmol g_{cat}⁻¹.¹²⁵ A recent DFT study by Kulkarni *et. al.* suggests that an isolated [Cu-OH]⁺ site in the CHA cages is the active site.¹²⁶

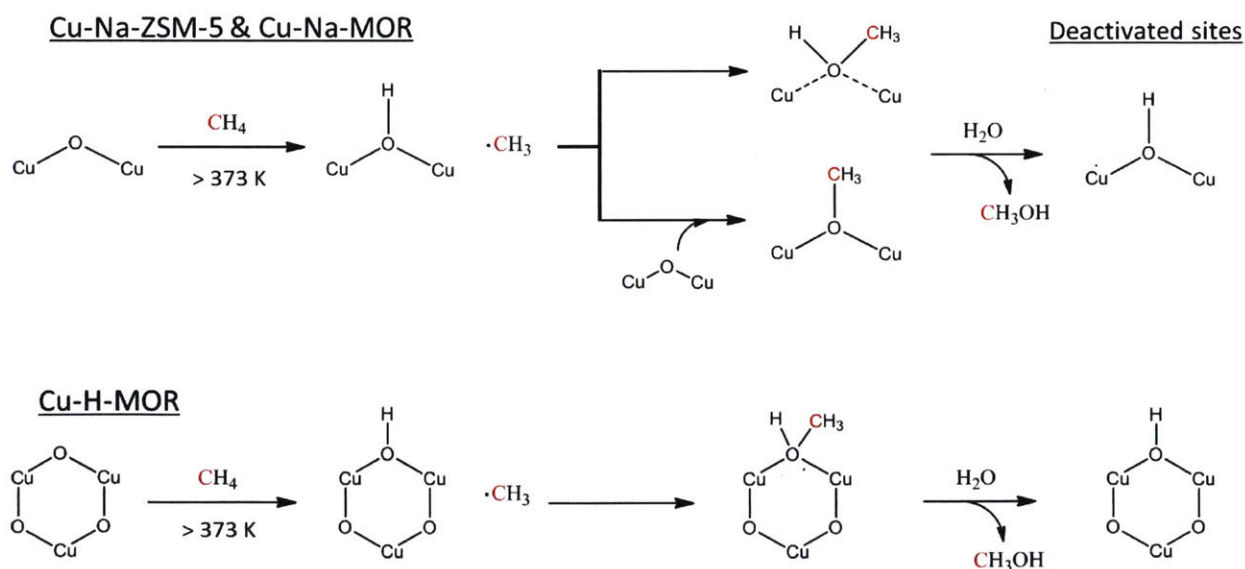


Figure 1-10. Hypothesized mechanism of methane oxidation over Cu-Na-ZSM-5, Cu-Na-MOR and Cu-H-MOR. The first step is the H-abstraction of methane over the active site. The second step is the localization of methyl radicals on the zeolite surface. The last step is the extraction of methanol and the deactivation of the active site. Scheme based on information from refs [66], [118], [122], and [123]

1.13 Scope of the Thesis

The objective of this thesis is to address the shortcomings of the Cu-zeolite systems for the low temperature, direct oxidation of methane into methanol.

The second chapter presents experiments conducted to verify the reaction intermediates and identify parallel reaction pathways of methane oxidation over Cu-MOR from both the sodium and acid parent forms. Methane oxidation and carbonylation were coupled to describe the location of surface intermediates after the initial H-abstraction step. Acetic acid and methanol products were produced directly from methane. Isotopic and spectroscopic measurements confirmed that methoxy species migrated from the copper active sites to carbonylation-active Bronsted acid sites after methane oxidation but no migration was observed from Na parent zeolites.

The third chapter discusses the development of the first direct, catalytic, continuous, and gas phase oxidation of methane into methanol with molecular oxygen at low temperature. Kinetic studies showed sustained catalytic activity and high methanol selectivity over a variety of Cu-exchanged zeolites, most notably ZSM-5, MOR, and SSZ-13. Transient and steady-state isotopically labelled experiments confirmed catalytic turnover. The catalytic rates and apparent activation energies were affected by the zeolite topology with SSZ-13 being the most active.

The fourth chapter investigates the improvement in catalytic methane oxidation activity through the control of Cu speciation in one-pot synthesized Cu-SSZ-13. Cu-SSZ-13 synthesized with TEPA exhibited higher methane oxidation activity and site-time yield from 493-623 K than ion-exchanged Cu-SSZ-13. Sintering of Cu into oxide particles was identified as the deactivation mechanism at higher Cu/Al, resulting in carbon dioxide production. Thermal stability, methanol production and methanol selectivity increased at high Si/Al and low Cu/Al due to decreased sintering of copper into oxide particles. Finally, infrared spectroscopy indicated that TEPA directed the formation of isolated Cu⁺ and Cu²⁺ species and monocopper Cu²⁺ species correlated with catalytic activity. Isolated Cu²⁺ species are likely the precursors of the catalytic methane oxidation active site in Cu-SSZ-13.

Chapter 2 : Methane to Acetic Acid over Cu-Exchanged Zeolites: Mechanistic Insights from a Site-Specific Carbonylation Reaction

2.1 Introduction

The selective conversion of methane to liquid oxygenated compounds, such as methanol or dimethyl ether, is an attractive strategy for obtaining value-added chemicals from abundant natural gas resources. Reforming natural gas followed by Fischer-Tropsch synthesis is currently effective only at large scales. In order to reach methane reserves at remote locations or spread over large fields and to reduce unwanted emissions from flaring, alternative conversion pathways must be implemented at smaller scales.^{38, 127} Low temperature oxidative routes for the activation of C-H bonds are thermodynamically and kinetically accessible. In nature, as in artificial systems, the key to selective methane oxidation is the ability to generate reactive oxygen species at metal active sites capable of attacking the strong C-H bonds of methane while avoiding overoxidation into carbon dioxide.

In enzymatic systems capable of converting methane into methanol, such as methane monooxygenases, iron¹²⁸⁻¹³¹ and copper^{58, 132} can generate electrophilic metal-oxygen species adept at attacking the strong C-H bonds of methane. Accordingly, numerous methane oxidation schemes have focused on the formation and reactivity of iron and copper-oxygen species in inorganic matrices. Most promising thus far are the iron-¹³³⁻¹³⁴ and copper-^{66, 82, 108, 135} exchanged ZSM-5 zeolites, where $\text{Fe}^{\text{IV}}=\text{O}$ ^{63, 136-138} and $\text{Cu}^{\text{II}}-\text{O}-\text{Cu}^{\text{II}}$ species^{118, 139-140} are believed to be key intermediates for the selective oxidation of methane to methanol. Both reactive centers oxidize methane into a surface bound methoxy group that is extracted as methanol by reacting with water. The pioneering work by Sels, Schoonheydt, and Solomon showed that methane oxidation in Cu-ZSM-5 occurs via hydrogen abstraction by a bent mono-(μ -oxo)dicupric core to form both a methyl radical and a $\text{Cu}^{\text{I}}-\text{OH}-\text{Cu}^{\text{II}}$ intermediate, which then combine through a rebound mechanism to form a bound methoxy species on a copper center.¹¹⁸ Oxidation activity is observed only for materials with Cu/Al molar ratios > 0.2 , which is the minimal metal content requirement to form the mono-(μ -oxo)dicupric cores. To date, it is not clear if

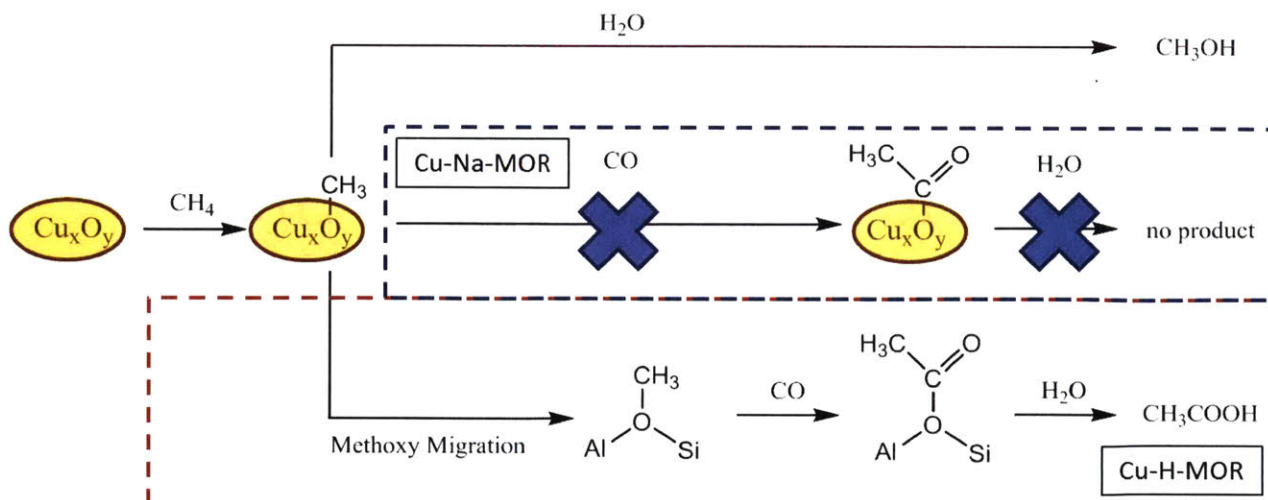


Figure 2-1. Methane oxidation and carbonylation over Cu-MOR exchanged from acid or sodium precursors. Reprinted with permission from [74]. Copyright 2015 American Chemical Society.

the methyl radicals rebound onto the same reactive center to form a metal-methoxy species,¹¹⁸ if they travel to another metal center,¹²⁰ or if the methoxy species readsorbs elsewhere on the zeolite framework.

In this work, the conversion of methane to acetic acid is demonstrated in copper-exchanged mordenite (Cu-MOR) using a tandem oxidation/carbonylation reaction sequence. Notably, the carbonylation reaction serves as a site-specific probe capable of identifying the location of methoxy groups within the zeolite, thereby providing important mechanistic insight for methane oxidation. Bhan et al. demonstrated that the carbonylation of methoxy species generated from the interaction of methanol or dimethyl ether with an acid site occurs preferentially in the eight-membered rings (8MR) side pockets of MOR and ferrierite.^{73, 75-76, 89, 141} Román-Leshkov et al. confirmed the same trend in carbonylation reactivity by synthetically placing framework aluminum sites within the 8MR pockets of ferrierite.¹⁴² Corma and co-workers showed computationally that the carbonylation rates are further enhanced by spectator copper (I) ions that facilitate CO attack on surface methoxy species in the 8MR pockets.¹⁴³ After the oxidation/carbonylation sequence, we show that Cu-MOR generates drastically higher amounts of acetic acid when compared to Cu-ZSM-5 under identical conditions (vide infra). We hypothesize that the oxidation-active copper species are responsible of converting methane into methoxy species, while the acid sites located in the 8MR pockets convert methoxy species into acyl groups in the presence of CO (see Figure 2-1). Given that methoxy species bound onto copper sites are unlikely to react with CO, we posit that the production of acetic acid requires the migration of methoxy groups to a carbonylation

active Brønsted acid site. To support this hypothesis, we present reactivity investigations using preferential titration and ^{13}C - and ^{18}O -labelled molecules coupled with spectroscopic and nuclear magnetic resonance (NMR) characterization studies. Our results show that, although some Cu sites in Cu-MOR are carbonylation active, acetic acid is mainly obtained by migration of methoxy groups into the 8MR pocket of H-MOR. Specifically, preferential titration experiments indicated that the amount of acetic acid produced was proportional to the number of Brønsted acid sites in the 8MR pockets. NMR and mass spectroscopy (MS) experiments using ^{13}C - and ^{18}O -labelled molecules confirmed that the intermediate species for carbonylation was a methoxy species localized on a Brønsted acid site. In addition, ultraviolet-visible (UV-vis) spectroscopic studies on Cu-MOR showed that the bent mono-(μ -oxo)dicupric species typically associated with the oxidation-active sites of Cu-Na-ZSM-5^{66, 82, 118, 135, 144} and Cu-Na-MOR^{120, 145} was not active for carbonylation. For samples prepared from the acid form of the zeolite and with Cu/Al < 0.2, the characterization data suggest the presence of an alternative oxidation site in Cu-H-MOR that is responsible for methane oxidation and subsequent methoxy migration.

2.2 Results and Discussion

Reactivity Studies

Tandem methane oxidation-carbonylation reaction sequences were investigated on Cu-MOR as a function of copper and acid content. Methane oxidation over Cu-MOR (Cu/Al = 0.36, Na/Al = 0.37) was first tested by activating the zeolite at 823 K under O_2 flow, cooling to 473 K under Ar, and flowing methane for 0.5 h. Water extraction yielded 12.3 $\mu\text{mol/gcat}$ of methanol, which is in agreement with previous extraction yields reported by Sels et al.⁶⁶ (11 μmol methanol/gcat from Cu-Na-MOR with Cu/Al = 0.43) and Alayon et al.¹²⁰ (13 $\mu\text{mol/g cat}$ methanol from Cu-Na-MOR at Cu/Al = 0.38).

Methane oxidation was coupled with carbonylation by flowing CO at 1000 kPa and 473 K immediately after oxidizing methane over the activated zeolite under strictly anhydrous conditions. In Cu-MOR, carbonylation of surface methoxy species¹⁴⁶⁻¹⁴⁷ may occur in three different locations: in acid sites located in the 8MR pockets, in acid sites in the 12MR main channel, and in copper-exchanged sites in both pore systems.^{32, 146-152} Bhan and co-workers demonstrated that methoxy species formed in the 8MR pockets of H-MOR are the most carbonylation active,⁸⁹ while those in the main channel undergo carbonylation

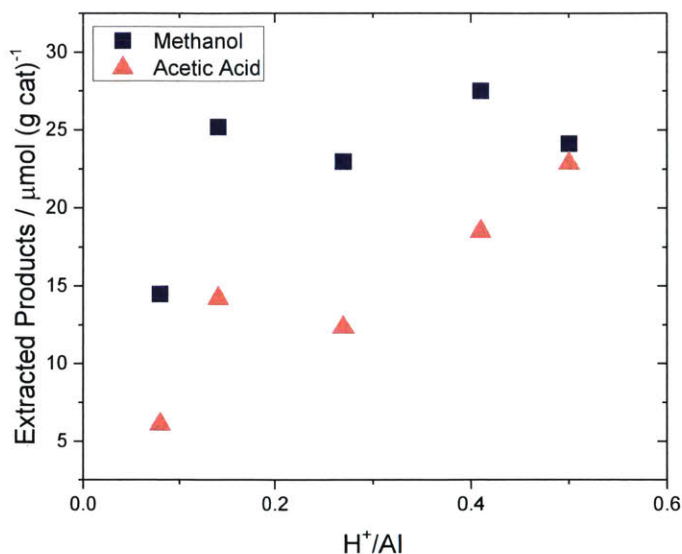


Figure 2-2. Methane oxidation and subsequent carbonylation on Cu-H-MOR at Cu/Al = 0.20 – 0.25. Methane oxidation conditions: Activation at 823 K under O₂, Reaction T = 473 K, Reaction time = 0.5 h. Carbonylation conditions: T = 473 K, Carbonylation Time = 0.5 h, P_{CO} = 1000 kPa. [H⁺] was calculated from a propylamine desorption method as described in previous studies (Supporting Information, Table S1).¹⁵³⁻¹⁵⁵ [Al³⁺] was calculated from elemental analysis using inductively coupled plasma atomic emission spectroscopy (ICP-AES). Reprinted with permission from [74]. Copyright 2015 American Chemical Society.

at much lower rates and preferentially decompose into hydrocarbons above 473 K.¹⁴¹ Importantly, carbonylation activity within Cu-MOR and H-MOR can be modulated by partially exchanging acid sites with sodium, which has been shown to preferentially titrate the Brønsted acid sites in the 8MR pockets over those in the 12MR.⁸⁹ Following this approach, we investigated the carbonylation of oxidized methane products as a function of Brønsted acid site content at a constant Cu/Al ratio of 0.20 – 0.25 (Figure 2-2). Deuterium oxide extraction showed that the parent Cu-MOR (Cu/Al = 0.20 and H/Al = 0.5) generated 22.9 and 24.1 μmol/gcat of acetic acid and methanol, respectively (Figure 2-2). As the acid sites in the 8MR pockets were progressively titrated from an H/Al of 0.4 to 0.27, acetic acid production decreased from 18.5 to 12.3 μmol/gcat. These extraction levels persisted until almost all of the Brønsted acid sites were titrated, at which point the acetic acid production decreased to 6.0 μmol/gcat. These data translate to an acetic acid production from copper sites, acid sites in the 12MR, and acid sites in the 8MR of 6.0, 6.5, and 10.5 μmol/gcat, respectively. A total exchange of acid sites was not achieved because, as observed by the groups of Bell,¹⁰³ Hall,⁸³ and Gorte,¹⁵⁵ Brønsted acid sites are always produced when copper is exchanged into Na-exchanged zeolites.

Based on the observed dependence of carbonylation activity on Brønsted acid site content within Cu-MOR with Cu/Al < 0.2, the acetic acid yield would be expected to approach 6.0 in the absence of any Brønsted acidity. Note that as the copper content in Cu-Na-MOR was increased above Cu/Al of 0.33, the carbonylation activity was completely quenched.

To directly measure the amount of organic carbon present in the zeolite after reaction, Cu-MOR samples were dissolved in hydrofluoric acid and the solution was analyzed with quantitative ^1H NMR. The total organic content from the zeolites changed significantly as a function of Brønsted acid content. The total number of products on Cu-H-MOR and Cu-Na-MOR was 60.9 and 22.0 $\mu\text{molcarbon/gcat}$, respectively (Supplemental Table S2-7). The ratio of water-extracted methanol and acetic acid to the total carbon content obtained via HF dissolution was 0.55 and 0.70 for Cu-H-MOR and Cu-Na-MOR, respectively. Although the amount of water-extracted organics from this Cu-H-MOR sample was slightly lower than that calculated for a replicate experiment with the same zeolite (Table S2-7, Figure 2-6), the variability in extraction was within the deviation previously found in Cu-ZSM-5.^{66, 82} Overall, extraction efficiencies and total carbon contents are in line with those previously calculated for Fe-H-ZSM-5⁶² and Cu-Na-ZSM-5 (Cu/Al = 0.58).⁸² The extraction efficiency could be increased by utilizing other solvent combinations, such as 10%(v) water/acetonitrile, but the overall change in extracted products would be small.⁶² More importantly, we note that the ratio of acetic acid to methanol calculated from the water-extracted products and from the HF dissolution method is nearly identical for Cu-Na-MOR and slightly higher for Cu-H-MOR (1.40 vs 1.08). Since extraction in water appears to marginally favor acetic acid, the relative amount of acetic acid is overestimated in the water-extracted values and the differences in product distribution observed for Cu-H-MOR and Cu-Na-MOR are thereby caused by the lack of carbonylation activity in the sodium sample and not because of selective extraction of methanol over acetic acid. Taken together, these data suggest that the number of active Cu sites is larger in Cu-H-MOR than in Cu-Na-MOR at similar Cu/Al ratios, assuming a 1:1 stoichiometry between active sites and products generated. The data are also in agreement with previous reports by Bhan and co-workers showing that for stop-flow carbonylation reactions of dimethyl ether on partially sodium exchanged H-MOR, lower levels of both acetic acid and total organic carbon are obtained when the Na/Al ratio is increased (Supporting Figure S2-18).^{89, 147}

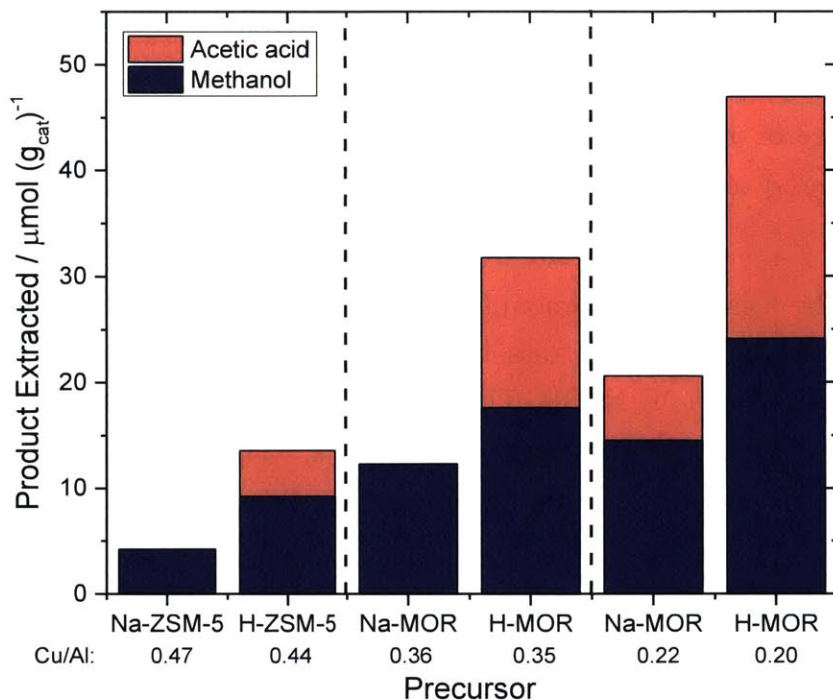


Figure 2-3. Methane oxidation and subsequent carbonylation on Cu-ZSM-5 and Cu-MOR exchanged from sodium and acid precursors. Zeolite precursors and Cu/Al contents are listed for each zeolite. Methane oxidation conditions: Activation at 823 K under O₂, Reaction T = 473 K, Reaction time = 0.5 h. Carbonylation conditions: T = 473 K, Carbonylation Time = 0.5 h, P_{CO} = 1000 kPa. Reprinted with permission from [74]. Copyright 2015 American Chemical Society.

For comparison, control methane oxidation/carbonylation reaction sequences were performed over Cu-ZSM-5. Although carbonylation products were detected, the amount of acetic acid in Cu-ZSM-5 was drastically lower when compared to that obtained with Cu-H-MOR. Specifically, methane oxidation/carbonylation on Cu-H-ZSM-5 generated only 4 μmol/g_{cat} of acetic acid out of 12 μmol/g_{cat} of total oxygenates. Proportionally, the methanol to acetic acid ratio produced by Cu-H-ZSM-5 was similar to that from a Cu-MOR zeolite without Brønsted acid sites in the 8 MR pockets (i.e., ca. 50% Na exchange or H/Al = 0.14), showing that acid sites in the 8MR pockets are necessary to obtain high acetic acid yields. We note that Cu-Na-ZSM-5 failed to produce acetic acid (Figure 2-3). Bhan and co-workers had shown that the rate of dimethyl ether carbonylation in H-ZSM-5 was negligible compared to the rate in H-MOR due to the lack of 8MR side pockets to stabilize the acetyl intermediate.⁸⁹ In batch reactions of dimethyl ether carbonylation over H-ZSM-5, acetic acid was produced but in very small amounts (0.02 mol acetic acid/mol Al, Supporting Figure S2-19). Based on these results, we surmise on the one hand, that the oxidation-active mono-(μ-oxo)dicupric site typically formed in Cu-Na-ZSM5 under these conditions is carbonylation inactive; and on the other,

that the methoxy species in Cu-H-ZSM-5 generated after the oxidation step have either migrated to Brønsted acid sites or a different copper site is formed in the presence of Brønsted acid sites that is active for both oxidation and carbonylation.

Table 2-1. Methanol extraction from zeolites calcined under $^{18}\text{O}_2$ and subsequent methane oxidation

Zeolite Precursor	Cu/Al	% $\text{CH}_3^{18}\text{OH}$ Extracted
H-ZSM-5	0.44	4.6
H-MOR	0.17	0.6
Na-MOR	0.22	34.0
Na-MOR	0.36	34.2

Reaction conditions: Activation at 723K under 30 mL/min $^{18}\text{O}_2$, Reaction T = 473 K, Reaction time = 0.5 h.

To verify the origin of methoxy species undergoing carbonylation, Cu-MOR and Cu-ZSM-5 were activated under $^{18}\text{O}_2$ before reacting with methane (see Table 2-1). Previously, Sels et al. had shown that $^{18}\text{O}_2$ activation of Cu-Na-ZSM-5 followed by methane oxidation generated methanol with 75% ^{18}O enrichment, thus demonstrating that the oxygen from the mono-(μ -oxo)dicupric site became part of the methoxy group of methanol.⁶⁶ Analysis of water-extracted methanol from Cu-H-ZSM-5 showed that enriched $\text{CH}_3^{18}\text{OH}$ constituted only 4.6%. Similarly, the percentages of $\text{CH}_3^{18}\text{OH}$ extracted from Cu-H-MOR and Cu-Na-MOR were 0.6 and 34%, respectively. In both cases, these values show a large decrease in ^{18}O content when acid sites are present in the zeolite. To exclude the possibility of isotopic scrambling by interaction of Me^{18}OH with acid sites during extraction, an aqueous $\text{CH}_3^{18}\text{OH}$ solution was mixed with Cu-H-MOR (Cu/Al = 0.17) at room temperature for several hours. The resulting solution contained 92.2% $\text{CH}_3^{18}\text{OH}$ (Table S2-4), indicating that no significant ^{18}O isotopic scrambling occurred when mixing labeled methanol in the presence of acid sites at conditions analogous to those of the water-extraction process. These results are in agreement with previous experimental and theoretical investigations showing the lack of interaction of methanol with acid sites in zeolites at room temperature.¹⁵⁶⁻¹⁶⁰ These data suggest that the oxygen in the oxidation-active copper site is not incorporated into the extracted methanol product when Brønsted acid sites are present.

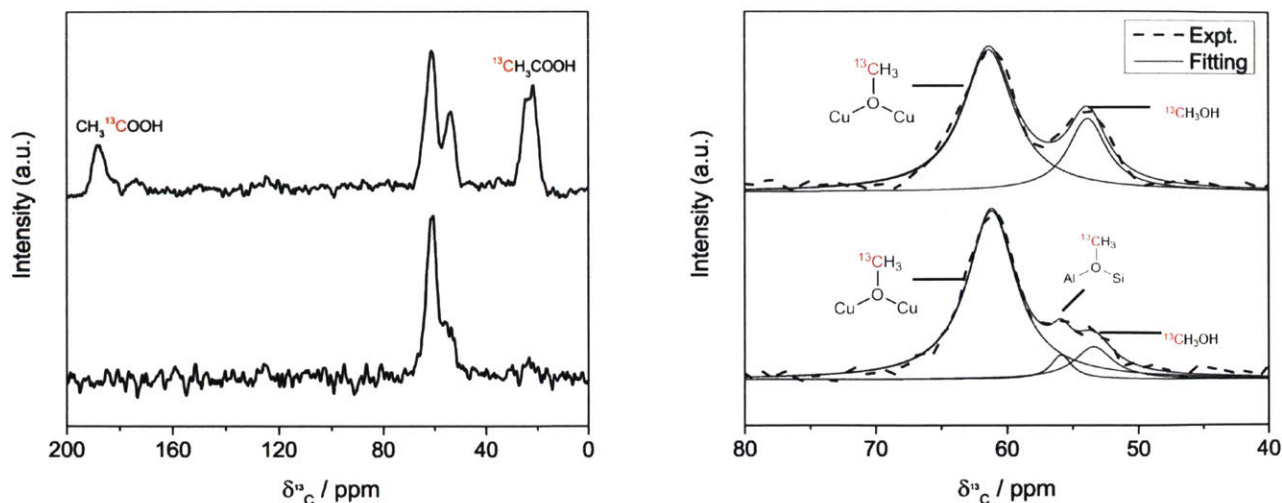


Figure 2-4. $^{13}\text{C}[^1\text{H}]$ cross-polarization (CP) MAS NMR spectra of Cu-MOR (H-MOR precursor, Cu/Al = 0.20) after $^{13}\text{CH}_4$ oxidation (bottom spectrum) and after $^{13}\text{CH}_4$ oxidation and ^{13}CO carbonylation (top spectrum). (Left) Full $^{13}\text{C}[^1\text{H}]$ CP MAS NMR spectra of Cu-H-MOR (Cu/Al = 0.20) after reaction with $^{13}\text{CH}_4$ (bottom) and $^{13}\text{CH}_4 + ^{13}\text{CO}$ (top). (Right) Enlarged spectral region containing methoxy resonances, with assignments. Simulated Lorentzian peaks (solid) are shown below the experimental spectra (dashed). Reprinted with permission from [74]. Copyright 2015 American Chemical Society.

The migration of the methoxy species from the copper sites to acid sites after methane oxidation was investigated with ^{13}C magic-angle spinning nuclear magnetic resonance (MAS NMR). As shown in Figure 2-4, three resonances are observed after reacting $^{13}\text{CH}_4$ on activated Cu-H-MOR (Cu/Al = 0.20, H/Al = 0.50), which are assigned to physisorbed methanol (53.4 ppm), methoxy species on Brønsted acid sites (55.9 ppm),¹⁴³ and methoxy species on a copper site (61.2 ppm, see Table S2-6, Figure S2-14 for justification). After carbonylation with ^{13}CO , the resonance at 55.9 ppm decayed with the concomitant appearance of resonances at 21.5 and 188.5 ppm, which are associated with the methyl and carbonyl functional groups of acetic acid. A similar trend was observed for Cu-H-MOR with a higher copper content (Figure S2-11). In contrast, Cu-Na-MOR (Cu/Al = 0.36, Na/Al = 0.33) only featured resonances at 53.4 ppm and 61.2 ppm after the methane oxidation step and did not feature resonances associated with acetic acid after the carbonylation step (Figure S2-12). These data offer strong evidence that the reaction intermediate undergoing carbonylation in Cu-H-MOR is a methoxy species on a Brønsted acid site.

Characterization Studies

The speciation of copper centers in Cu-MOR with varying Cu/Al and H/Al ratios was investigated with ultraviolet-visible (UV-vis) spectroscopy (Figure 2-5) for samples that were treated first under argon (Ar) at 823 K, then under oxygen (O₂) at 823 K, and finally under methane at 473 K. Heat treating Cu-H-MOR (Cu/Al = 0.2 and Na/Al = 0.03) under Ar generated a broad peak centered at 13,300 cm⁻¹ and a small shoulder at 16,700 cm⁻¹ (Figure 2-5A). These bands have been previously characterized as the d-d transitions of square pyramidal and square planar Cu²⁺ species coordinated to the zeolite framework.^{119, 161} After the O₂ treatment, the intensity of the 13,300 cm⁻¹ and 16,700 cm⁻¹ bands decreased to reveal a band at 12,500 cm⁻¹ and a broad shoulder at 9,600 cm⁻¹. For both Cu-Na-MOR samples, analogous visible-near infrared (NIR) bands were observed upon Ar and O₂ heat treatments. The d-d transitions at 13,600 cm⁻¹ and 16,750 cm⁻¹ featured reduced visible-NIR intensities after calcination. In contrast to Cu-H-MOR, the Cu-Na-MOR sample at Cu/Al = 0.36 featured a strong band at 22,200 cm⁻¹ (Figure 2-5C), while both Cu-Na-MOR samples did not possess the band at 12,500 cm⁻¹ (Figure 2-5B-C). Additionally, a very small shoulder at 9,600 cm⁻¹ was observed in Cu-Na-MOR (Cu/Al = 0.22) compared to the large shoulder in Cu-H-MOR.

A different redox behavior was observed after reacting methane over Cu-H-MOR or Cu-Na-MOR. For Cu-H-MOR, the d-d transitions at 9,600 cm⁻¹ and 12,500 cm⁻¹ decayed while the transitions at 13,300 cm⁻¹ and 16,700 cm⁻¹ were regenerated (Figure 2-5A). Taken together, these spectra show how the sites represented by the bands at 12,500 cm⁻¹ and 9,600 cm⁻¹ in Cu-H-MOR were created after high temperature activation under O₂ and were consumed after reaction with methane. Unlike Cu-H-MOR, the 22,200 cm⁻¹ band in Cu-Na-MOR (Cu/Al = 0.36) decayed after reaction with methane (Figure 2-5C). Additionally, the 12,500 cm⁻¹ band did not appear after calcination of either Cu-Na-MOR zeolite, but it did appear in Cu-H-MOR. Reaction with methane caused a very small decay in the shoulder at 9,600 cm⁻¹ in Cu-Na-MOR (Cu/Al = 0.22, Figure 2-5B), along with the restoration of the 13,600 and 16,750 cm⁻¹ bands in both Cu-Na-MOR samples (Figure 2-5B-C). Thus, the appearance of the methane oxidation active 9,600 cm⁻¹ band was unique to Cu-MOR samples with at least trace amounts of Brønsted acidity and carbonylation activity.

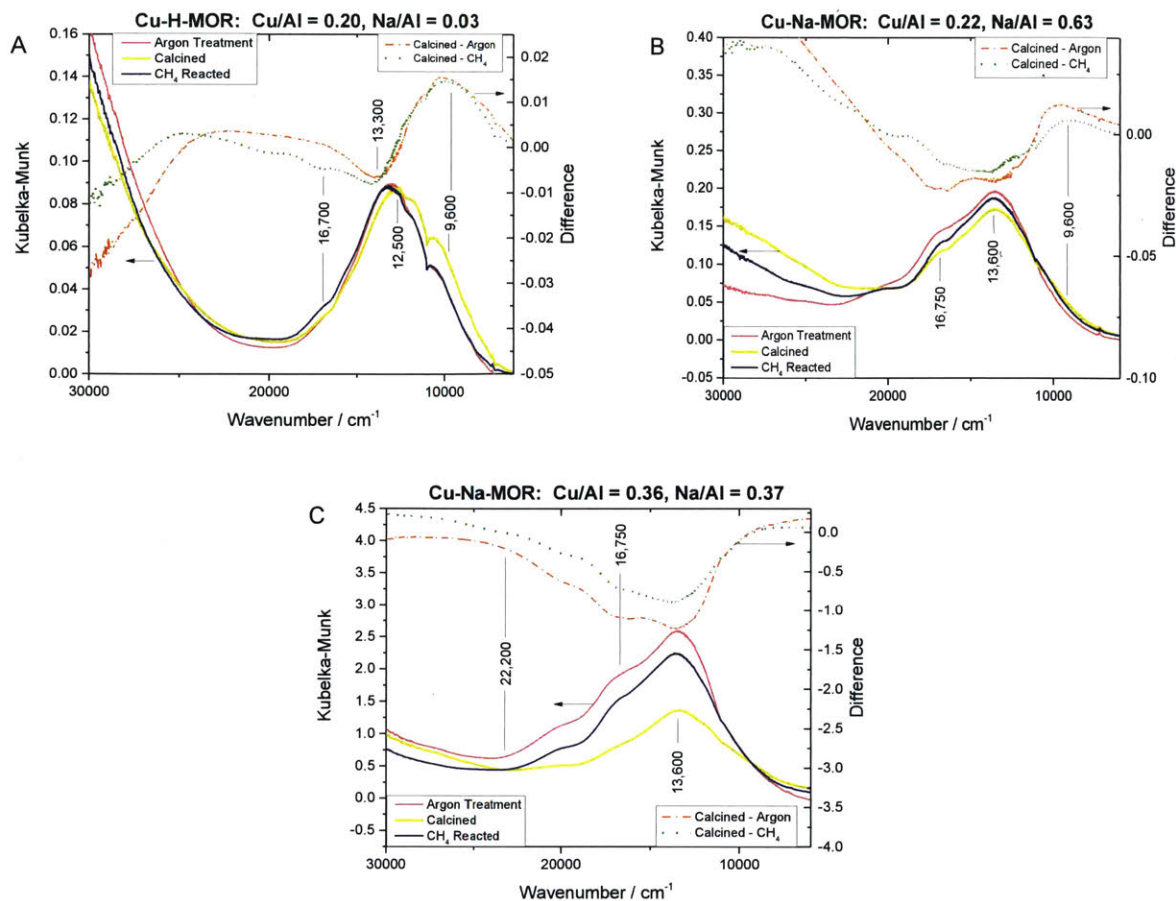


Figure 2-5. Diffuse Reflectance UV-visible spectra of (A) Cu-H-MOR (Cu/Al = 0.20, Na/Al = 0.03), (B) Cu-Na-MOR (Cu/Al = 0.22, Na/Al = 0.63), and (C) Cu-Na-MOR (Cu/Al = 0.36, Na/Al = 0.37). Zeolites were dried under argon at 823 K for 3 h (pink), calcined under oxygen at 823 K for 5 h (dashed gold), and reacted under CH₄ at 473 K for 2 h (navy). Difference spectra (calcined – argon, dash-dot orange; calcined – CH₄, dotted green) are shown. Reprinted with permission from [74]. Copyright 2015 American Chemical Society.

The exact nature of the methane oxidation active 9,600 cm^{-1} band in Cu-H-MOR is still unknown. Sels and coworkers have observed a similar shoulder at 9,200 cm^{-1} in Cu-Na-MOR decay upon reaction of calcined Cu-Na-MOR with methane,⁶⁶ however its appearance was inconsistent in Cu-MOR of different Si/Al and Cu/Al ratios.⁸² For this band to be a d-d transition of the square pyramidal or planar Cu^{2+} species absorbing at 13,300 cm^{-1} or 16,700 cm^{-1} , two observations must be true. First, the 9,600 cm^{-1} band should decay after thermal treatment in Ar for any Cu-MOR sample regardless of Brønsted acidity since all Cu-MOR samples contain both square pyramidal and planar species. Second, the intensity of the d-d transitions should correlate to the 9,600 cm^{-1} band. However, as shown in Figure 2-5, the 9,600 cm^{-1} band appeared prominently only in Cu-H-MOR and was either absent in carbonylation inactive Cu-Na-MOR (Cu/Al = 0.36, Figure 2-5C, Figure 2-3) or was a small shoulder in Cu-Na-MOR with trace Brønsted acidity (Figure 2-5A, Figure 2-2). Thus, the 9,600 cm^{-1} band appeared to form exclusively within Cu-MOR samples that were active for carbonylation after methane oxidation. Additionally, the 13,600 cm^{-1} and 16,700 cm^{-1} bands gained intensity after thermal treatment in Ar, but the 9,600 cm^{-1} band lost intensity (Figure 2-5A). Yet, the inverse trend was observed upon calcination of Cu-H-MOR, showing that the 9,600 cm^{-1} band could not represent the same Cu^{2+} species as the other d-d transitions. Thus, we can exclude the possibility of the 9,600 cm^{-1} band being an electronic transition of the 13,300 cm^{-1} and 16,700 cm^{-1} d-d transitions and is likely associated with a unique Cu center. While the 9,600 cm^{-1} band was present in carbonylation active Cu-Na-MOR (Cu/Al = 0.22 and H/Al = 63), the surface methoxy groups formed were still highly localized onto copper sites (Table 2-1). We note that the percentage of $\text{CH}_3^{18}\text{OH}$ extracted from Cu-Na-MOR samples with carbonylation inactive Cu/Al = 0.36 and carbonylation active Cu/Al = 0.22 ratios was identical. Additionally, $^{13}\text{C}[^1\text{H}]$ CP MAS NMR spectra showed no methoxy species on Brønsted acid sites in Cu-Na-MOR (Cu/Al = 0.36). These data suggest that the copper species represented by the 9,600 cm^{-1} band in Cu-H-MOR and Cu-Na-MOR (Cu/Al = 0.22) is both oxidation and carbonylation active and it is much more readily formed in the presence of Brønsted acidity.

The copper concentration range at which the 9,600 cm^{-1} band forms differs drastically from that required to form the mono-(μ -oxo)dicupric species. As previously reported for Cu-Na-ZSM-5 and Cu-Na-MOR, the transition at 22,700 cm^{-1} and 30,000 cm^{-1} associated with the mono-(μ -oxo)dicupric site is only observed for samples with Cu/Al > 0.20.^{66, 82, 118-120, 135, 144, 162} In Cu-Na-MOR, the mono-(μ -oxo)dicupric species

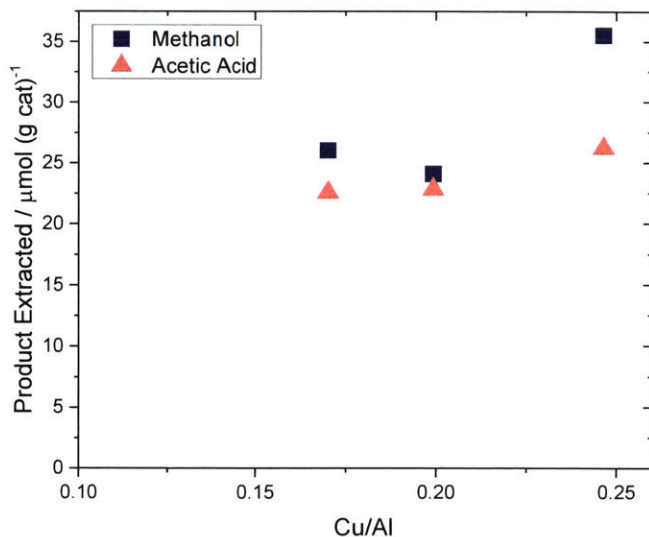


Figure 2-6. Methane Oxidation and Carbonylation on Cu-H-MOR with varying copper content. Methane oxidation conditions: Activation at 823 K under O₂, Reaction T = 473 K, Reaction time = 0.5 h. Carbonylation conditions: T = 473 K, Carbonylation Time = 0.5 h, P_{CO} = 1000 kPa. Reprinted with permission from [74]. Copyright 2015 American Chemical Society.

formed when the square planar Cu²⁺ species was exchanged into the zeolite.^{82, 119-120} Isolated square pyramidal Cu²⁺ species present at low copper contents was inactive for methane oxidation, proved difficult to reduce, and was shown not to form the mono-(μ-oxo)dicupric site.¹¹⁹ In Cu-H-MOR samples with low Cu/Al ratios (ranging from 0.17 to 0.10), the 9,600 cm⁻¹ band also decays after reaction with methane (Figure S2-16, A and B). At Cu/Al = 0.10, traces of the d-d transition at 16,700 cm⁻¹ were present, so it is possible that square planar or pyramidal Cu²⁺ could be the precursors to the methane oxidation active site. Interestingly, the yields of acetic acid and methanol from Cu-H-MOR at Cu/Al = 0.17 were 22.6 and 26.0 μmol/gcat (Figure 2-6), respectively, which are values virtually identical to those observed for Cu-H-MOR with a Cu/Al = 0.20. For samples with Cu/Al ratios of 0.25, the methanol extracted from the zeolite increased to 35.5 μmol/gcat. At this Cu/Al ratio, the mono-(μ-oxo)dicupric site should form within Cu-MOR, implying that the mono-(μ-oxo)dicupric site is solely responsible for the formation of the additional methanol and is not associated with the formation of acetic acid. This observation is consistent with the lack of carbonylation activity within Cu-Na-ZSM-5 (Figure 2-3).

The reactivity and characterization data suggest the presence of two coexisting pathways: methane oxidation/carbonylation at a copper center and methane oxidation followed by migration of methoxy species to a carbonylation-active Brønsted acid site.

The exact mechanism responsible for the migration of methoxy species from the copper site is unknown and requires further investigation. Previous methane oxidation studies over Cu-Na-ZSM-5 and Cu-Na-MOR reported that methanol was not evolved after flowing methane over the activated zeolite.⁶⁶ Along with DFT studies,¹¹⁸ the product after methane oxidation was a methoxy species bound to the mono-(μ -oxo)dicupric site. This was consistent with mechanisms of stoichiometric methane or benzene oxidation over Fe-ZSM-5 resulting in $(\text{Fe}^{\text{III}}\text{-OCH}_3)_\alpha$ ^{62, 163} or $(\text{Fe}^{\text{III}}\text{-OPh})_\alpha$ groups.¹⁶⁴⁻¹⁶⁵ Recently, Panov and coworkers¹⁶⁶ proposed a quasicatalytic reaction mechanism over Fe-H-ZSM-5 involving the surface diffusion of molecular methanol from the $\text{Fe}^{\text{III}}\text{-O}_\alpha$ active sites to the Brønsted acidsites. Desorption of methanol into the gas phase was not favorable under temperatures of 523 K; however, surface diffusion had a lower activation energy that allowed methanol to migrate within the zeolite at temperatures as low as 333 K. Unfortunately, no explanation was provided as to how molecular methanol was generated from surface methoxy species under water-free reaction conditions. To gain insight into the nature of the sites involved in the potential production of methanol from methoxy species, we performed X-band continuous-wave electron paramagnetic resonance (EPR) spectroscopy on Cu-H-MOR and two Cu-Na-MOR samples that were dried under Ar or calcined. The full-length spectra are shown in Figure S2-20. As the values of g_{zz} and A_{zz} are the most informative for identification of Cu^{2+} sites we show the low-field region of the spectra in detail in Figure 2-7. The spectra of the two Cu-Na-MOR samples ($\text{Cu}/\text{Al} = 0.36$, $\text{Na}/\text{Al} = 0.37$ vs $\text{Cu}/\text{Al} = 0.22$, $\text{Na}/\text{Al} = 0.63$), dried under Ar, are similar. Both spectra show features due to at least two species: one species with $g_{zz} = 2.33$ and $A_{zz} = 163 \times 10^{-4} \text{ cm}^{-1}$ (referred to as site 2 hereafter, see Table 2-2) and a second species to which we tentatively assign $g_{zz} = 2.27$ and $A_{zz} = 183 \times 10^{-4} \text{ cm}^{-1}$ following Vandelder et. al.¹¹⁹ and Delabie et. al.¹⁶¹ (called site 3 hereafter). In the spectrum of $\text{Cu}/\text{Al} = 0.22$ (blue) the features of site 2 are more prominent than in the spectrum of $\text{Cu}/\text{Al} = 0.36$ (black) and in addition this spectrum shows an unidentified signal at 272.6 mT marked with a *. The spectrum of Cu-H-MOR ($\text{Cu}/\text{Al} = 0.20$, $\text{Na}/\text{Al} = 0.03$), dried under Ar, clearly shows the features of site 2, and also a small fraction of species 3 appears to be present. In addition the spectrum shows a third species (called site 1) with $g_{zz} = 2.37$ and $A_{zz} = 149 \times 10^{-4} \text{ cm}^{-1}$. Upon calcination, the total signal of Cu^{2+} species reduces for all three zeolites. This was consistent with the reduction of the $13,300 \text{ cm}^{-1}$ and $16,700 \text{ cm}^{-1}$ signals for square pyramidal and planar Cu^{2+} species in Cu-H-MOR (Figure 2-5A) and the $13,600 \text{ cm}^{-1}$ and $16,750 \text{ cm}^{-1}$ signals in Cu-Na-MOR (Figure 2-5B-C). This signal loss in Figure 2-7 was attributed to the formation of EPR silent copper species, which occurs in significant

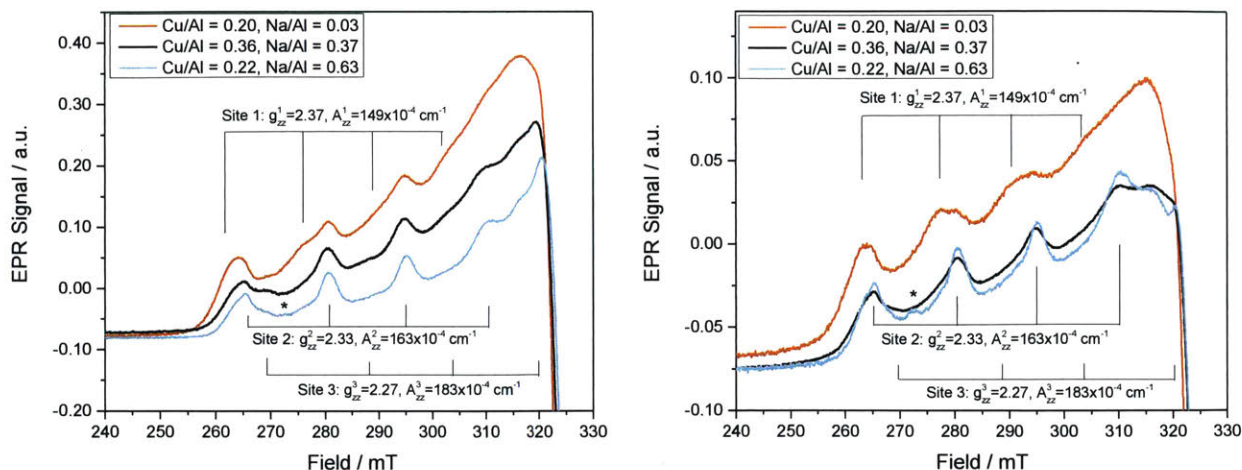


Figure 2-7. EPR Spectra (9.40 GHz) of (orange) Cu-H-MOR (Cu/Al = 0.20, Na/Al = 0.03), (black) Cu-Na-MOR (Cu/Al = 0.36, Na/Al = 0.37), and (cyan) Cu-Na-MOR (Cu/Al = 0.22, Na/Al = 0.63). (Left) Cu-MOR thermally treated under Ar for 3 h at 823 K and (Right) Cu-MOR calcined under O₂ for 5 h at 823 K and purged under Ar before acquisition. Reprinted with permission from [74]. Copyright 2015 American Chemical Society.

Table 2-2. EPR Parameters for Cu²⁺ Species in Cu-MOR Treated Under Argon and Oxygen

Cu ²⁺ Site	g_{zz}	A_{zz} (x 10 ⁻⁴ cm ⁻¹)	$g_{xx} = g_{yy}$	A_{xx} (x 10 ⁻⁴ cm ⁻¹)	d-d Trans. (cm ⁻¹)	Geometry
1	2.37	149	--	--	12,500	
2	2.33	163	2.06	18.2	13,600	Sq. pyramidal
3	2.27	183	2.09	42.8	16,750	Sq. planar

quantities above Cu/Al of 0.20.^{108, 162} Multiple EPR silent species could be responsible for methane oxidation activity in Cu-H-MOR (Cu/Al = 0.20) and Cu-Na-MOR (Cu/Al = 0.22), so the lack of the 22,200 cm⁻¹ band for the Cu-O-Cu site in their UV-vis spectra (Figure 2-5A-B) may suggest alternate copper active sites at low Cu/Al. After calcination, the relative contribution of species 1 to the spectrum of Cu-H-MOR increases. Species 2 is still clearly present, but the presence of species 3 cannot be established with certainty. A similar effect is seen in the spectra of the two calcined Cu-Na-MOR samples: the presence of species 2 is obvious, whereas the fraction of species 3 has become very small. Other authors have observed species in Cu-MOR with parameters similar to species 2 and 3. They are generally associated with a square pyramidal and a square planar Cu²⁺ site, respectively.^{95, 119, 139, 161, 167} A site with a high g -value of 2.37-2.40 has mainly been observed in Cu-MOR¹⁶⁸ and other zeolites that were not thermally treated, in which case they were always associated with hydrated Cu²⁺.¹⁶⁹⁻¹⁷¹ For instance, electron spin echo envelope modulation (ESEEM) spectroscopy attributed a $g_{zz} = 2.38$ signal to a Cu²⁺ species coordinated to three water molecules when the sample was evacuated at 323 K.¹⁷² Moreover, the 12,500 cm⁻¹ band we observe in calcined Cu-H-MOR (Figure 2-5A) has been

observed in untreated Cu-MOR and was associated with hydrated Cu^{2+} .¹¹⁹ It is tempting to speculate on how a hydrated Cu species could be involved in the reaction pathway. The presence of water molecules in close proximity to the copper species would allow for surface methoxy species to become hydrolyzed into molecular methanol, ultimately enabling a reaction pathway involving surface methanol diffusion, methoxy formation and subsequent carbonylation over the Brønsted acid sites. While our data confirm the presence of site 1, which has also been observed in Cu-MOR that was heated up to 783 K¹⁰² and Cu-H-MOR evacuated at 673 K,¹⁷² it is unclear if site 1 corresponds to a hydrated species. The experiments were performed under strict anhydrous conditions and it seems unlikely that that dehydration was incomplete for our samples. Indeed, near infrared (NIR) spectra on heat-treated Cu-MOR do not show simultaneous bands around 5200 cm^{-1} and ca. 7000 cm^{-1} corresponding to water molecules in the sample (Figure S2-17). Evidently, more detailed investigations are needed to understand the nature of the environment surrounding site 1.

2.3 Conclusions

Methane can be converted into acetic acid over copper exchanged mordenite zeolites. Reactivity and spectroscopic measurements on Cu-MOR with varying concentrations of Brønsted acid sites revealed notable differences in the types of Cu^{2+} species and product distributions from the tandem oxidation/carbonylation sequences. In Cu-Na-MOR without Brønsted acid sites, EPR and d-d transitions characteristic of square pyramidal and planar species were present, along with the characteristic 22,200 cm^{-1} band for the methane oxidation active site previously identified for Cu-ZSM-5. Accordingly, these materials showed methane oxidation activity but were carbonylation inactive above $\text{Cu}/\text{Al} = 0.30$. In contrast, Cu-MOR samples containing Brønsted acid sites were drastically more carbonylation active, even at Cu/Al ratios ≤ 0.2 . In these samples, spectroscopic data shows the presence of a new Cu^{II} site. After reaction with methane, a unique band at 9,600 cm^{-1} decayed, suggesting the presence of a different methane oxidation active site. The coupled methane oxidation and carbonylation reactions showed that when trace amounts of Brønsted acid sites were present, carbonylation activity was enhanced. A plausible pathway for the observed product distribution after oxidation/carbonylation sequences involves generating methanol from the immediate hydrolysis of the methyl group over the new Cu^{2+} site in Cu-H-MOR followed by re-adsorption over a carbonylation-active acid site in the zeolite framework. Methane oxidation over Cu-H-MOR has important consequences, since it generates methoxy species

that are located on the Brønsted acid sites of the zeolite that can serve as intermediates in many other types of reactions to create industrially relevant products.¹⁷³ The detailed characterization of the copper active sites is the focus of our current investigations.

2.4 Experimental Methods

Ion Exchange

Commercial zeolites NH₄-MOR (CBV21A, Si/Al = 10) and NH₄-ZSM-5 (CBV2314, Si/Al = 12.5) were purchased from Zeolyst International.

Sodium Exchange: Partially exchanged zeolites were prepared by mixing 1 g of zeolite in 36 mL of 0.05 M, 0.1M, 0.4 M, 0.820 M, or 1.64 M solutions of NaCH₃COO (> 99%, Sigma-Aldrich, *ReagentPlus*, CAS 127-09-3) at 353 K for 12 h. Zeolites were subsequently filtered while hot and rinsed with 120 mL of deionized H₂O. Zeolites were then dried for 4 h at 383 K in a drying oven. To prepare zeolites in the full sodium form, the above procedure was performed three times at an exchange concentration of 2.44M NaCH₃COO.

Copper Exchange of H-MOR for Na/Al < 0.55 (Cu/Al = 0.20 – 0.25): To ensure lower amounts of copper in the zeolite, partially exchanged zeolites into the copper form were prepared by mixing 1 g of H-MOR in 60 mL of 0.01M Cu(NO₃)₂•(H₂O)₃ (98%, Sigma-Aldrich, CAS 10031-43-3) at 298 K for 12 h. The suspension was then filtered at room temperature and rinsed with 300 mL of deionized H₂O. This procedure was followed for H-MOR with Na/Al < 0.55.

Copper Exchange of Partially Na exchanged MOR for Na/Al > 0.55 (Cu/Al = 0.20 – 0.25): As Na/Al increased above 0.55, higher levels of copper were exchanged into MOR from copper nitrate. To ensure that Cu/Al remained between 0.20-0.25, 1 g of Na-MOR with Na/Al > 0.55 was mixed in 60 mL of 0.005M Cu(NO₃)₂•(H₂O)₃ (99%, Sigma-Aldrich) at 298 K for 12 h. The filtering procedure was the same as noted above.

Copper Exchange of H-MOR (Variable Cu/Al): Exchange of copper into NH₄-MOR at various levels was prepared by suspending the zeolite into a 0.0025, 0.005, and 0.01 M solutions of Cu(NO₃)₂•(H₂O)₃ at room temperature for 12 h. The same filtering procedures were followed as above.

Copper Exchange of Na-MOR (Variable Cu/Al): Exchange of copper into Na-MOR at various Cu/Al was done as described above. Solutions of 0.0025, 0.00375, 0.005, and 0.01 M Cu(NO₃)₂•(H₂O)₃ solutions were mixed with Na-MOR at room temperature for 12 h. The zeolite was then filtered as described above.

After exchanges, all zeolite samples were calcined under 100 mL/min of dry air (Airgas) while being heated 1 K/min to 823 K and held for 5 h. Calcination converted the NH₄⁺ counter cations into H⁺, resulting in the Brønsted acid form of Cu-MOR. Copper, sodium,

and aluminum contents were determined using inductively coupled plasma atomic emission spectroscopy (ACTIVA-S, Horiba Scientific).

Methane Oxidation and Carbonylation Reactions

Methane oxidation and carbonylation reactions were conducted in a continuous, tubular flow reactor (stainless steel tube, O.D. 12.5 mm, wall thickness = 0.889 mm). The reactor tube was mounted inside of a single-zone furnace (850W / 115V, Applied Test Systems Series 3210). A thermocouple (Omega, model TJ36-CASS-18U) was aligned along the tube center such that its tip reached the middle of the height of the tube. Zeolite particles (1.5 g, sieved into 500 – 1000 μ m particles) were packed between quartz wool frits resting on the thermocouple. The thermocouple was connected to a Digi-Sense model 68900-10 temperature controller. The reactor was equipped with gas tanks for argon, oxygen, methane, and carbon monoxide (all ultra high purity from Airgas). All gas lines were run through molecular sieve 5A (S-trap, Sigma-Aldrich) and calcium hydride traps (95%, Sigma-Aldrich, CAS 7789-78-8) to remove trace amounts of water in the gas streams. Prior to reaction, the zeolite was calcined in 50 mL/min flowing oxygen for 5 h at 823 K and cooled under flowing oxygen to reaction temperature (473 K). Upon reaching reaction temperature, the bed was purged under 50 mL/min of Ar for 1 hr. The gas flow was then changed to the reaction mixture of 10 mL/min methane and 15 mL/min Ar for a 30 min reaction. After methane oxidation, the gas flow was changed to 200 mL/min of CO and the reactor was pressurized to 1000 kPa gauge pressure for 30 min. Afterwards, the reactor was immediately depressurized, purged under Ar and cooled to room temperature.

Methanol and acetic acid extraction was performed by removing the zeolite bed from the tube, weighing, and sealing into a glass vial. The zeolite was then suspended in deuterium oxide (2.5 mL D₂O/g zeolite) and stirred at 550 rpm for 2 h. The suspension was then transferred to conical vials and centrifuged for 10 min at 6,000 rpm. The supernatant was removed and its contents were analyzed using ¹H-NMR (Varian Mercury 300). For quantification of methanol and acetic acid, 1,4-dioxane (\geq 99%, Aldrich, CAS 123-91-1) was the internal standard (28.5 μ L dioxane / mL supernatant).

¹⁸O₂-Labeled Experiments

In the tubular reactor described above, 0.75 g of sieved zeolite (500 – 1000 μ m diameter) was packed into a stainless steel tube (O.D. 6.35 mm, wall thickness 0.889 mm) suspended on a quartz wool frit. The zeolite was calcined in flowing oxygen (50 mL/min) at 723 K for 4 h. The gas flow was switched to argon for 1 hr to destroy any formed

copper-oxo species. Then the flow was switched to 30 mL/min of $^{18}\text{O}_2$ (97 atom %, Sigma-Aldrich) for 4 min. The argon and $^{18}\text{O}_2$ calcination cycle was repeated two more times. The zeolite bed was cooled under $^{18}\text{O}_2$ to 473 K. The bed was purged under argon and then switched to methane (10 mL/min) for 30 min. After the reaction, the bed was cooled to room temperature. The zeolite was removed from the tube, suspended in 1.25 mL dH_2O , stirred for 2 h, and centrifuged for 10 min at 6,000 rpm. The supernatant was then injected into a GC-MS (Agilent Technologies, model 7890A) equipped with a Paraplot Q column (Agilent Technologies, 50 m x 0.32 mm ID, 10.0 μm). The oven was isothermal at 413 K for 7 min.

To determine if ^{18}O exchange occurs between ^{18}O -methanol and Bronsted acid sites at room temperature, 0.30 g of Cu-H-MOR (Cu/Al = 0.17) was suspended in a solution of 1.00 mL of 20 mM $\text{CH}_3^{18}\text{OH}$ in water and stirred at room temperature for 2 h. The mixture was centrifuged at 6000 rpm for 10 min, and the supernatant was extracted and injected into a GC-MS.

^{13}C -Methane Oxidation and Carbonylation

Methane oxidation and carbonylation reactions with ^{13}C labelled reagents were conducted in a similar setup as for the analogous reactions with ^{12}C reagents except the stainless steel tubular reactor had an O.D. of 6.35 mm and wall thickness of 0.889 mm. 0.400 g of zeolite sample (pelleted and sieved to 250 – 500 μm) were packed between quartz wool frits resting on a thermocouple (Omega, model TJ36-CASS-116U) aligned along the middle of the tube. The zeolite was calcined under oxygen for 5 h at 823 K and then purged under argon for 1 hour upon cooling to 473 K. Methane oxidation was performed by pressurizing the reactor to 103 kPa gauge under static $^{13}\text{CH}_4$ (99 atom %, Aldrich, CAS 6532-48-5) for 30 min. If carbonylation was to take place, the tubular reactor was purged twice with 103 kPa gauge of ^{13}CO (99 atom %, Aldrich, CAS 1641-69-6). The third refill was kept static in the reactor for 6 h. After reactions with the ^{13}C reagents, the reactor was purged with argon and cooled to room temperature.

^{13}C -MAS-NMR Experiments

For all experiments with ^{13}C reagents, the zeolite samples were cooled to room temperature under argon. The ends of the reactor were sealed from atmosphere, and the zeolite bed was transferred to a glovebox under argon atmosphere. The zeolite bed was then packed into 4 mm (o.d., 80 μl fill volume) ZrO_2 MAS rotors (Revolution NMR, Fort Collins, Co) equipped with a vespel drive tip (sealed using Epoxy) and a top cap containing two rubber o-rings.

Solid-state NMR experiments were performed using a home-built 500 MHz spectrometer (courtesy of Dr. D. Ruben, Francis Bitter Magnet Laboratory – MIT) equipped with a Magnex high field NMR magnet (11.7 T). ^{13}C magic-angle spinning (MAS) NMR experiments were collected using a 4 mm triple-resonance ($^1\text{H}/^{13}\text{C}/^{15}\text{N}$) Chemagnetics (Fort Collins, CO) probe equipped with a Kel-F stator housing. The spinning frequency was between 8 and 10 kHz and regulated with a Bruker MAS controller. Sample temperatures were maintained at 295 K and cooled to account for frictional heating using a stream of cooling gas. ^{13}C single pulse (Bloch) experiments were acquired using a $\pi/2$ of 2.5 μs ($^{13}\text{C} \gamma B_1/2\pi = 100$ kHz), and between 16 k and 64 k co-added transients. $^{13}\text{C}[^1\text{H}]$ cross polarization experiments were collected with a contact time of 2 ms and, between 2 k and 16 k co-added transients. The ^{13}C Hartmann-Hahn condition was optimized using a ramp on ^{13}C and 50 kHz $\gamma B_1/2\pi$ on ^1H . Recycle delays were between 1.5 and 30 seconds, depending on the Cu content. All data were acquired using high-power TPPM ^1H decoupling optimized for a $^1\text{H} \gamma B_1/2\pi = 100$ kHz. ^{13}C data were referenced using adamantane (40.49 ppm) as a secondary standard with respect to DSS, 4,4-dimethyl-4-silapentane-1-sulfonic acid (0 ppm). Variable temperature ^1H and ^{13}C experiments at -40, 0 and +40 $^\circ\text{C}$ were acquired using a home-built 700 MHz NMR Spectrometer equipped with a 3.2 mm triple-resonance ($^1\text{H}/^{13}\text{C}/^{15}\text{N}$) Chemagnetics probe. Samples were treated identically, although placed in 3.2 mm o.d. ZrO_2 rotors. ^{13}C acquisition parameters were similar as stated above although data was acquired at 18 kHz with a 1.5 ms contact time. ^1H MAS NMR data were acquired using a Bloch and Hahn-Echo experiment, 128 co-added transients and a recycle delay of 3 seconds.

UV-vis-NIR Spectroscopy

UV-vis spectra were taken with a Cary 5000 UV-Vis-NIR spectrometer (Agilent Technologies) equipped with a Praying Mantis diffuse-reflectance accessory (Harrick Instruments). Background spectra were sodium or acid form of the parent zeolite that were calcined (823 K, 5 h under oxygen) and the spectral range was from 4,800 cm^{-1} to 50,000 cm^{-1} . Samples were finely ground in a mortar and pestle and loaded into a Harrick high temperature reaction chamber equipped with quartz windows. The sample was calcined under flowing oxygen (50 mL/min) at 823 K for 5 h, cooled under oxygen, and then purged under Ar. The sample was subsequently heated to 823 K under argon for 3 h. After spectra were taken for both heat treatments, the parent copper zeolite was recalcined under oxygen at 823 K for 5 h, cooled to room temperature, and then exposed to methane flow (50 mL/min) at 473 K for 30 min. Before a spectrum was taken, the sample was cooled to room temperature and purged in argon for 1 hr.

Electron Paramagnetic Resonance (EPR) Spectroscopy

10-11 mg of sieved zeolite samples (500 – 1000 μm) were placed in Thin Wall Precision Quartz EPR tubes (4 mm OD, 250 mm length, Wilmad-Labglass, 707-SQ-250MM). For pre-treatment, the tube was lowered into a single-zoned furnace (GTF 11/50/150B, Carbolite). A thermocouple (Omega, model TJ36-CASS-116U) was placed inside the furnace alongside the EPR tube and connected to a temperature controller (YO-89000-00, 110V, Digi-Sense). Gas flow into the EPR tube was diffusion mediated by continuously flowing gas past the EPR tube through a rapid purge valve (Chemglass). The gas molecules are then able to diffuse into the EPR tube to the zeolite sample. The carrier gas was either oxygen or argon at 200 mL/min. The sample was heated 1 K/min to 823 K, soaked for 5 h, and cooled to room temperature. After reaching room temperature, the sample was purged under flowing argon (275 mL/min) for 2 h. While under argon, the sample was transferred into an argon atmosphere glovebox (UNILab, MBraun) where the EPR tube was sealed with epoxy resin.

X-band (9.5 GHz) EPR experiments were performed using a Bruker ElexSys E580 spectrometer using a rectangular ER 4122 SHQE-W1 cavity operating in TE₁₀₂ mode. Sample temperature control was achieved using an ESR 900 flow cryostat with liquid nitrogen and an ITC 503S temperature controller (Oxford Instruments). Powdered samples were maintained at 90 K during acquisition. Spectra were acquired with a microwave frequency of 9.40 GHz, a modulation amplitude of 0.2 mT and a microwave power of 0.63 mW

Propylamine Adsorption for Quantification of Bronsted Acid Sites

Propylamine adsorption and subsequent temperature programmed reaction/desorption were performed to quantify the Brønsted acid sites in select Cu-MOR zeolites. After adsorbing propylamine onto Brønsted acid sites and heating the zeolite, the proplamine decomposes into ammonia and propylamine in a one-to-one ratio per Bronsted acid site.¹⁵³⁻¹⁵⁴ Propylamine adsorption reactions were conducted in a quartz U-tube reactor (O.D.6.35 mm, Altamira AI-2210). The U-tube was mounted above a single-zone furnace (GTF 11/50/150B, Carbolite). A thermocouple (Omega, model TJ36-CASS-116U) was aligned along the tube center such that its tip just touched the top of the catalyst bed. Zeolite particles (10 - 50 mg) were packed between quartz wool frits just below the thermocouple. The reactor was equipped with gas tanks for 1% argon balance helium and dry air (Airgas). All gas lines were run through a molecular sieve 4A trap (Agilent Technologies) to keep the catalyst bed dry. Prior to reaction, the zeolite was

calcined in 90 mL/min flowing air for 5 h at 823 K and cooled to room temperature (298 K). The zeolite was purged under 100 mL/min of 1% Ar/He for 30 min. The gas flow was then passed through a saturator containing n-propylamine (98%, Aldrich, CAS 107-10-8) kept at 298 K for 1 h. The gas flow was switched to bypass the saturator and purge the zeolite bed of any excess propylamine for 30 min. The sample was then heated at 5 K/min to 523 K, held isothermal for 1 hr, and finally ramped at 5 K/min to 873 K. The concentration of propylamine ($m/z = 59$), propylene ($m/z = 41$), ammonia ($m/z = 17$), and argon ($m/z = 20$) were tracked on-line using a quadrupole mass spectrometer (Hiden HPR-20). The concentration of propylene was calibrated within the mass spectrometer immediately after the experiment by pulsing 5 mL samples of 1000 ppm propylene/1% Ar/He using a 6-way gas sampling valve (Vici E60, Valco Instruments). Calculation of $[H^+]$ was performed by setting $[H^+]$ equal to the number of propylamine molecules desorbing from the zeolite. Total $[Al^{3+}]$ was calculated by ICP-AES. It was assumed that all Al in the zeolite was tetrahedrally coordinated in the framework.

Table S2-3. Propylamine desorption over Cu-MOR samples in Figure 1

Na/Al	Cu/Al	$\mu\text{mol/g}_{\text{cat}}$ propylene	H^+/Al
0.03	0.20	278.5	0.50
0.11	0.23	214.3	0.41
0.16	0.22	193.5	0.27
0.36	0.24	149.2	0.14
0.64	0.22	101.9	0.08

Dissolution of Zeolites in Hydrofluoric Acid

To analyze the organic content on the zeolite surface after methane oxidation and carbonylation reactions, as described above, the 0.8g of zeolite was dissolved in 3.0 mL of 48 wt% hydrofluoric acid and stirred for 2 h. A 1 mL aliquot of the solution was diluted in 1 mL of deuterium oxide. 0.5 mL of the mixture was transferred to a Teflon liner (5 mm OD, 203.2 mm length, Wilmad Labglass) that was inserted into a standard quartz NMR tube for 1H -NMR analysis. 10 μL of 1,4-dioxane was used as an internal standard. A control experiment showed that both methanol and acetic acid were not destroyed in the hydrofluoric acid solution.

2.5 Supporting Figures and Tables

Extraction and Characterization of Methanol and Acetic Acid

Methane oxidation and carbonylation products were extracted from zeolites by suspension in deuterium oxide, stirring for 2 h, and centrifugation at 6,000 rpm for 10 min. To quantify the amount extracted, a 25 μ L internal standard of 1,4-dioxane (99%, Sigma-Aldrich, CAS 123-91-1) was injected into the NMR tube.

Referencing the peak for water to be 4.790 ppm¹⁷⁴, the peaks for methanol and acetic acid were found to be 3.30 and 1.97 ppm respectively (Figure S2-8B and C). The peaks from the product extraction from Cu-MOR (Cu/Al = 0.20) closely matched these peaks (3.32 and 2.03 ppm) (Figure S2-8A). The small shift in the NMR peaks for both compounds was likely due to trace leaching of cupric ions into solution.

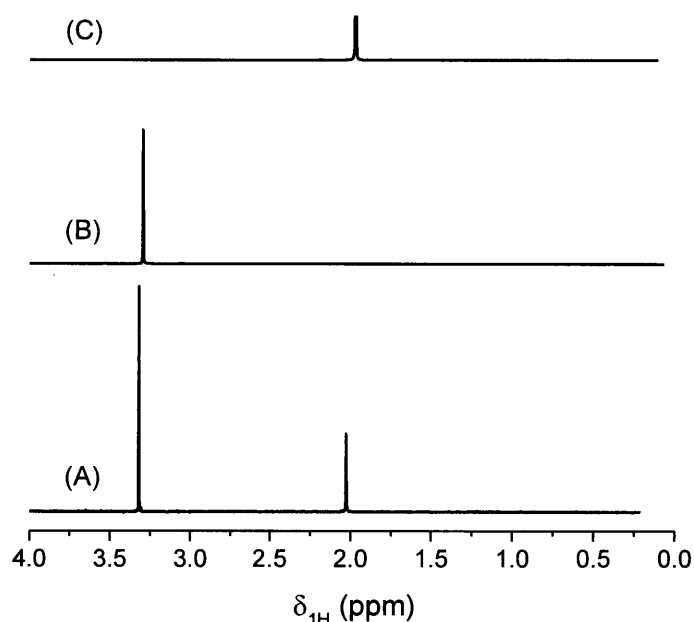


Figure S2-8. ¹H NMR spectra of the product extract from A) Cu-MOR (Cu/Al = 0.20), B) methanol in deuterium oxide, and C) acetic acid in deuterium oxide. Reprinted with permission from [74]. Copyright 2015 American Chemical Society.

¹⁸O₂-Calcination and Methane Oxidation over Cu-MOR

To quantify the percentage of methanol in solution consisting of CH₃¹⁸OH, a calibration curve was made using various mixtures of CH₃¹⁶OH and CH₃¹⁸OH. Volumetric mixtures of 0%, 10%, 25%, 50%, and 100% CH₃¹⁸OH were prepared and injected into a GC-MS. These compositions were then plotted against the ratio of the mass fragments at 33 and 31. A correlation with excellent linearity was recovered (Figure S2-9).

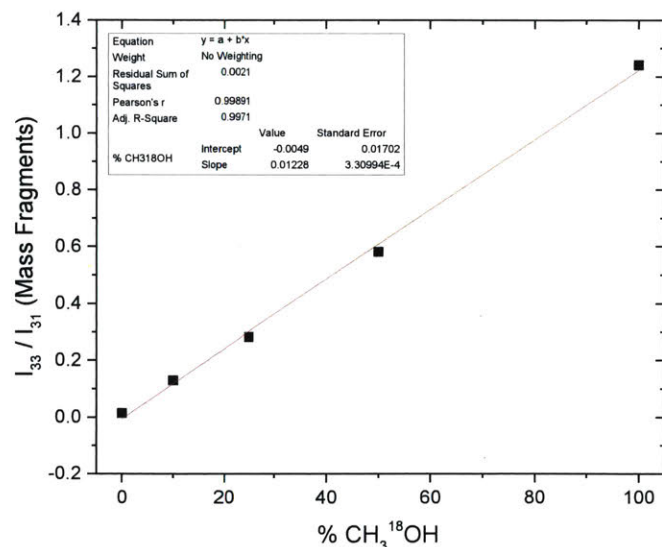


Figure S2-9. Calibration Curve of the composition of CH₃¹⁸OH in solution as separated by GC-MS. Reprinted with permission from [74]. Copyright 2015 American Chemical Society.

One possible source of CH₃¹⁶OH during extraction could have been the adsorption of CH₃¹⁸OH onto a Bronsted acid site to form a methoxy species that would rehydrate into CH₃¹⁶OH. To determine the extent of ¹⁸O exchange between CH₃¹⁸OH and Bronsted acid sites in Cu-H-MOR (Cu/Al = 0.17), the zeolite was suspended and mixed (600 rpm) in a 20 mM solution of CH₃¹⁸OH in water for 2 h. The resulting suspension was centrifuged at 6000 rpm for 10 min, and the supernatant was extracted and injected into a GC-MS. Compared to the amount of CH₃¹⁸OH in the as-prepared 20 mM CH₃¹⁸OH solution, the percent of extracted CH₃¹⁸OH dropped by only 7.8% after mixture with Cu-H-MOR. Thus, the extent of ¹⁸O scrambling at room temperature was significantly less compared to the 99.4% and 64% scrambling observed in Cu-H-MOR and Cu-Na-MOR, respectively, after reactions. Thus, loss in CH₃¹⁸OH extraction must have occurred from migration of the CH₃¹⁸OH from a copper site to a Brønsted acid site immediately after methane oxidation and before extraction.

Table S2-4. CH₃¹⁸OH Extraction from Cu-H-MOR Suspended in CH₃¹⁸OH/Water Solution

Treatment	% CH ₃ ¹⁸ OH
CH ₃ ¹⁶ OH	0.0
20 mM CH ₃ ¹⁸ OH (as prepared)	100
20 mM CH ₃ ¹⁸ OH (mixed with Cu-H-MOR)	92.2
CH ₄ Oxidation (Cu-H-MOR, Cu/Al = 0.17)	0.6
CH ₄ Oxidation (Cu-Na-MOR, Cu/Al = 0.22)	34

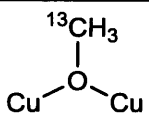
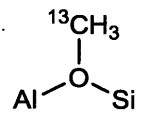
The percentage of $\text{CH}_3^{18}\text{OH}$ extracted from Cu-Na-MOR was significantly lower than that observed by Sels and coworkers on Cu-Na-ZSM-5.⁶⁶ On Cu-Na-ZSM-5, $\text{CH}_3^{18}\text{OH}$ extraction was around 75% from the zeolite, while $\text{CH}_3^{18}\text{OH}$ extraction from Cu-Na-MOR was at 36% in this study. This was likely attributed to incomplete destruction of the $\text{Cu}^{\text{II}}\text{-O-Cu}^{\text{II}}$ active sites⁶⁶ and isotopic exchange with ^{16}O over other copper oxides¹⁷⁵ during calcination under $^{18}\text{O}_2$. Varying the number of calcination cycles with $^{18}\text{O}_2$ produced higher $\text{CH}_3^{18}\text{OH}$ extracted from Cu-Na-MOR (Table S2-5). As the number of calcination cycles under $^{18}\text{O}_2$ increased, the percentage of $\text{CH}_3^{18}\text{OH}$ extracted after methane oxidation doubled. Thus, in the limit of several calcination cycles, the majority of methanol extracted from Cu-Na-MOR would likely be $\text{CH}_3^{18}\text{OH}$.

Table S2-5. $\text{CH}_3^{18}\text{OH}$ Extraction from Cu-Na-MOR zeolites calcined multiple times under $^{18}\text{O}_2$

Cu/Al	# $^{18}\text{O}_2$ Calcination Cycles	% $\text{CH}_3^{18}\text{OH}$
0.22	2	17.9
0.22	3	36.0
0.36	1	12.5
0.36	3	36.2

Surface Characterization of Products Using ^{13}C -MAS-NMR

Table S2-6. ^{13}C Chemical Shifts of Methoxy Species on Cu-MOR

Species	^{13}C Chemical Shift (ppm)	Species #
	61	1
	56-57	2
$^{13}\text{CH}_3\text{OH}$	53	3

$^{13}\text{C}[^1\text{H}]$ CP MAS NMR experiments confirmed the products of the methane oxidation and carbonylation reactions on surface of Cu-MOR. In Cu-H-MOR (Cu/Al = 0.20), three peaks at 53.4, 55.9, and 61.2 ppm formed in the methoxy region upon $^{13}\text{CH}_4$ oxidation (Figure S2-10). The peak at 53.4 ppm was attributed to chemisorbed methanol. The peak at 55.9 ppm were methoxy species formed on Bronsted acid sites.¹⁴³ Several possibilities existed for the nature of the methoxy species at 61.2 ppm. Various adsorbed dimethyl ether species have resonances from 60 – 65 ppm,¹⁴³ but the formation of dimethyl ether from highly dispersed oxidation active sites was highly unlikely. Thus, the peak at

61.2 ppm likely corresponded to a methoxy species on a copper site. Since Cu^{2+} species are paramagnetic, a resonance of a methoxy species on a Cu^{2+} site could undergo severe broadening and an induced chemical shift to higher or lower frequency – hence making it difficult to observe. However, the binding of the methoxy species after methane oxidation over the mono-(μ -oxo)dicupric site is a methoxy species bridging the $\text{Cu}^{\text{II}}\text{-O-Cu}^{\text{II}}$ site. Since the mono-(μ -oxo)dicupric site is magnetically coupled (spin ad-mixed) and EPR silent, a methoxy species on that site should be observable using MAS NMR. Moderately fast MAS NMR experiments were performed at variable temperature to further probe any paramagnetic shift effects – no additional resonances appeared at lower or higher frequency nor were the resonance observed sensitive to temperature.¹⁷⁶⁻¹⁷⁷ Furthermore, control adsorption of $^{13}\text{CH}_3\text{OH}$ onto Cu-H-MOR did not reveal the 61.2 ppm signal but other signals at 60.0 and 64.6 ppm (Figure S2-14), suggesting that the nature of this resonance is not molecular dimethyl ether or methanol on Cu^{2+} ions. Thus, the 61.2 ppm signal was tentatively attributed to the bridging methoxy species on the mono-(μ -oxo)dicupric active site. After carbonylation, peaks at 188.5, 24.7, and 21.5 ppm appeared. The peaks at 188.5 and 21.5 were from the formation of acetic acid on the Cu-MOR surface.¹⁷⁸ Since there was no other resonance other than at 188.5, the carbonyl carbon of acetic acid was not bound to the zeolite framework or a copper site.¹⁷⁸⁻¹⁷⁹ Thus, the peak at 24.7 ppm is most likely the methyl group of acetic acid interacting with Bronsted acid sites through hydrogen bonding. After carbonylation under ^{13}CO for 6 h, the peak at 55.9 ppm for methoxy species on Bronsted acid¹⁴³ sites disappeared. Additionally, the ratio of the areas of the 61.2 and 53.4 peaks reduced from 6.67 to 2.55. This reduction in the area of the 61.2 signal could have arisen through the reaction of a carbonylation active copper site or the decomposition of methoxy species over 6 h at 473 K. Regardless, methoxy species formed on Bronsted acid sites and were involved in the carbonylation reaction.

Even at lower Bronsted acid site count and higher copper content, the same peak around 56 ppm decreased after carbonylation. Over Cu-H-MOR ($\text{Cu}/\text{Al} = 0.47$), the same peaks at 61.3, 55.5, and 53.4 ppm were observed after reaction with $^{13}\text{CH}_4$ (Figure S2-11). After exposure to ^{13}CO for 6 h, two new resonances at 21.5, 24.7, and 188.5 ppm appeared, corresponding to acetic acid. Within the methyl region, the peak at 55.5 ppm decreased relative to the 53.4 and 61.3 ppm peaks, as in Cu-H-MOR ($\text{Cu}/\text{Al} = 0.20$), showing that the Bronsted acid sites were directly involved in carbonylation.

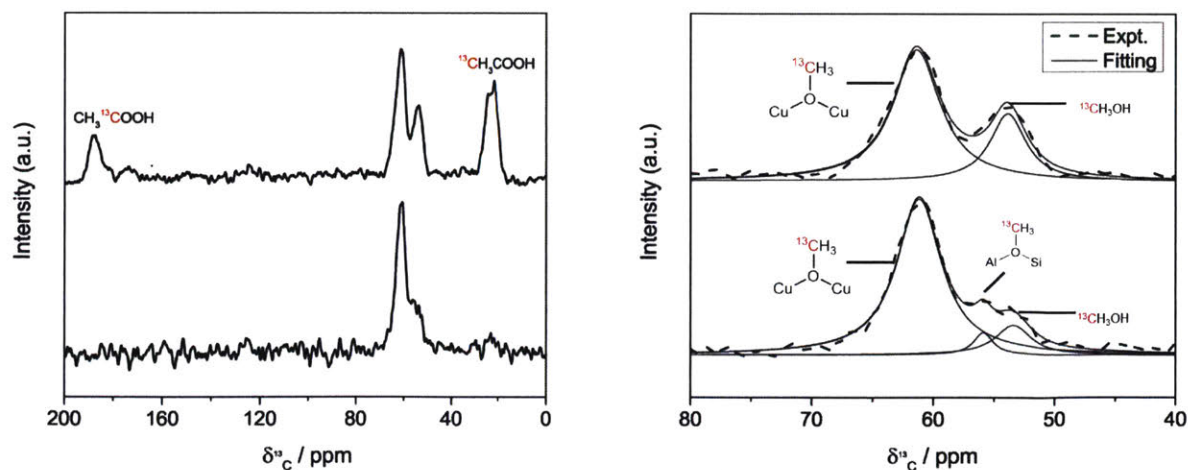


Figure S2-10. $^{13}\text{C}[^1\text{H}]$ CP MAS NMR spectra of Cu-MOR (H-MOR precursor, Cu/Al = 0.20) after $^{13}\text{CH}_4$ oxidation (bottom spectrum) and after $^{13}\text{CH}_4$ oxidation and ^{13}CO carbonylation (top spectrum). (Left) Full ^{13}C MAS NMR spectra of Cu-H-MOR (Cu/Al = 0.20) after reaction with $^{13}\text{CH}_4$ (bottom) and $^{13}\text{CH}_4 + ^{13}\text{CO}$ (top). (Right) Enlarged spectral region containing methoxy resonances. Simulated (solid) Lorentzian peaks are shown below the experimental (dashed) spectra. Reprinted with permission from [74]. Copyright 2015 American Chemical Society.

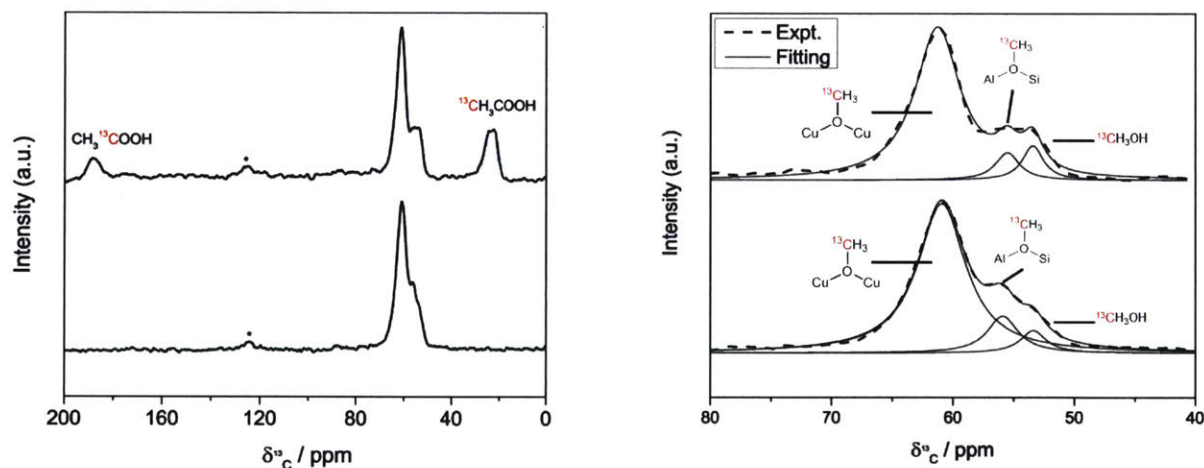


Figure S2-11. $^{13}\text{C}[^1\text{H}]$ CP MAS NMR spectra of Cu-MOR (H-MOR precursor, Cu/Al = 0.47) exchanged at pH = 6.47 after $^{13}\text{CH}_4$ oxidation (bottom spectrum) and after $^{13}\text{CH}_4$ oxidation and ^{13}CO carbonylation (top spectrum). (Left) Full ^{13}C MAS NMR spectra of Cu-H-MOR (Cu/Al = 0.47) after reaction with $^{13}\text{CH}_4$ (bottom) and $^{13}\text{CH}_4 + ^{13}\text{CO}$ (top). (Right) Enlarged spectral region containing methoxy resonances. Simulated (solid) Lorentzian peaks are shown below the experimental (dashed) spectra. Reprinted with permission from [74]. Copyright 2015 American Chemical Society.

However, when the carbonylation activity was quenched in Cu-Na-MOR, no methoxy species were observed to form on Bronsted acid sites. Only two resonances formed upon Cu-Na-MOR after $^{13}\text{CH}_4$ oxidation: at 60.9 and 53.6 ppm (Figure S2-12). After carbonylation with ^{13}CO , the 60.9 ppm peak reduced in height relative to the 53.6 ppm peak and formed resonances at 22.5 ppm. This peak most likely resulted from surface

coke forming from the decomposition of methyl groups over the six hour carbonylation. The peak at 86.7 ppm is methanediol. These assignments were supported by the ^{13}C -NMR spectrum of the products extracted from the Cu-Na-MOR surface (Figure S2-13). The observed resonances in the liquid extraction were at 82.3 and 49.5 ppm. The 14.2 ppm resonance in the liquid extraction appeared to be an artifact. Regardless, no acetic acid was observed to form on Cu-Na-MOR, showing that Bronsted acidity and surface methoxy species are intermediates for the carbonylation reaction.

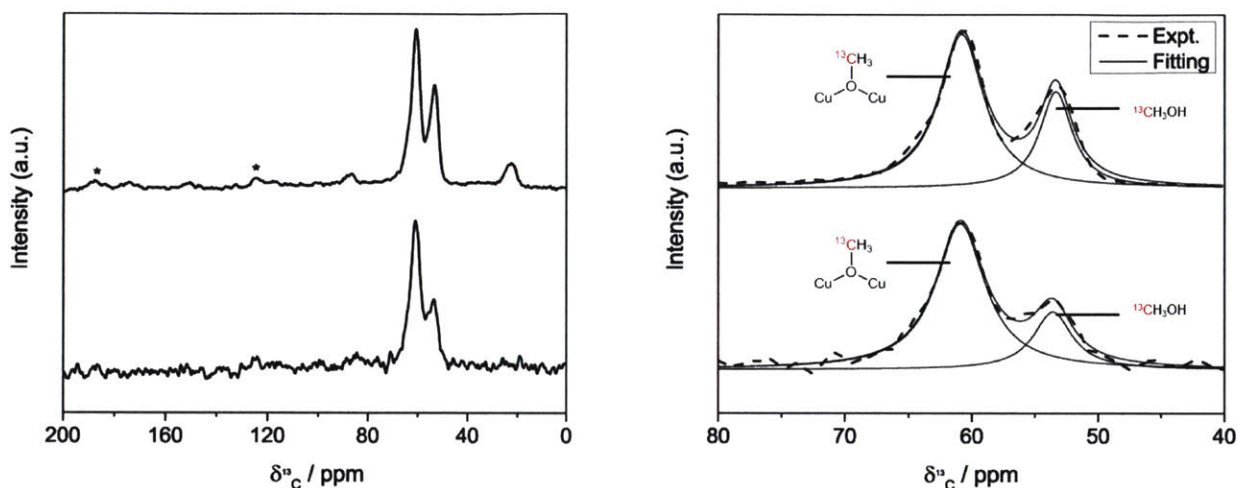


Figure S2-12. $^{13}\text{C}[^1\text{H}]$ CP MAS NMR spectra of Cu-MOR (Na-MOR precursor, Cu/Al = 0.36) after $^{13}\text{CH}_4$ oxidation (bottom spectrum) and after $^{13}\text{CH}_4$ oxidation and ^{13}CO carbonylation (top spectrum). (Left) Full ^{13}C MAS NMR spectra of Cu-Na-MOR (Cu/Al = 0.36) after reaction with $^{13}\text{CH}_4$ (bottom) and $^{13}\text{CH}_4 + ^{13}\text{CO}$ (top). (Right) Enlarged spectral region containing methoxy resonances. Simulated (solid) Lorentzian peaks are shown below the experimental (dashed) spectrum. Reprinted with permission from [74]. Copyright 2015 American Chemical Society.

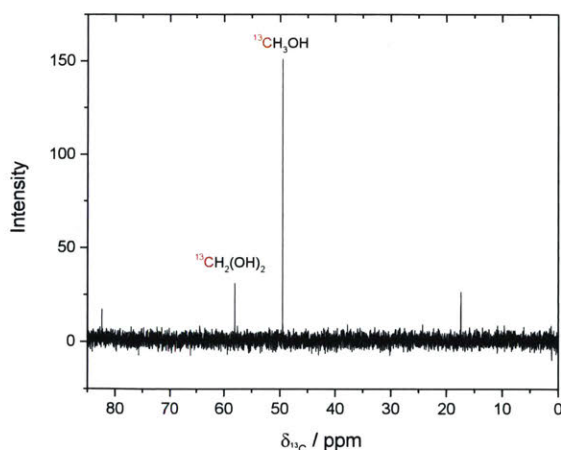


Figure S2-13. ^1H -NMR of liquid extraction in D_2O of Cu-Na-MOR (Cu/Al = 0.36, Na/Al = 0.37) after reaction with $^{13}\text{CH}_4 + ^{13}\text{CO}$ for 6 h. Reprinted with permission from [74]. Copyright 2015 American Chemical Society.

Control Adsorption of ^{13}C -Methanol and Acetic Acid on Cu-MOR

Methanol was adsorbed onto Cu-H-MOR (Cu/Al = 0.20) and produced four peaks (Figure S2-14) in the methoxy region. The two peaks at the lowest field corresponded to methanol (53 ppm) and surface methoxy species on a Bronsted acid site (56 ppm). The assignment for the surface methoxy species was in agreement with a past assignment¹⁴³ of methoxy species (57 ppm) on H-MOR (CBV20A, Si/Al = 10, Zeolyst) from the same vendor as the H-MOR used in this study. The two peaks at 60.0 and 64.6 ppm most likely corresponded to either dimethyl ether or methanol adsorbed onto copper ions. However, the exact nature of these peaks was unknown.

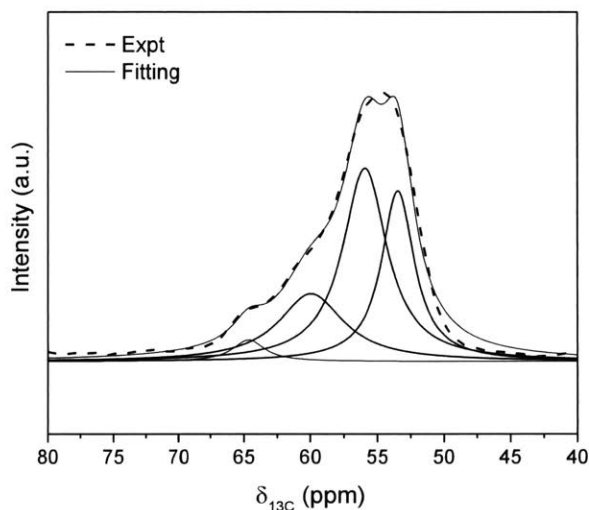


Figure S2-14. $^{13}\text{C}[^1\text{H}]$ CP MAS NMR spectra ^{13}C -Methanol adsorbed onto Cu-H-MOR (Cu/Al = 0.20). Simulated (solid) Lorentzian peaks are shown below the experimental (dashed) spectrum. Reprinted with permission from [74]. Copyright 2015 American Chemical Society.

The methyl group of acetic acid was examined by adsorbing ^{13}C -acetic acid (^{13}C on methyl group only) onto Cu-H-MOR (Cu/Al = 0.20). Three peaks were found at 24.7, 22.0, and 19.7 ppm. The 22.0 ppm and 19.7 shifts corresponded to the methyl group of acetic acid physisorbed onto the zeolite. The higher field peak at 24.7 ppm was the methyl group of acetic acid when the carbonyl oxygen was either interacting with a copper site or a proximal Bronsted acid site through hydrogen bonding.

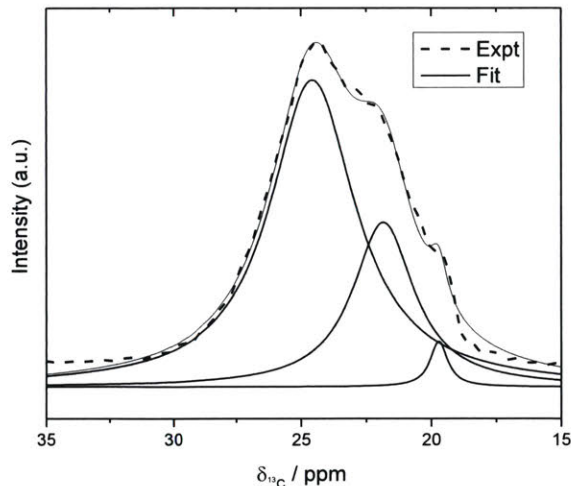


Figure S2-15. $^{13}\text{C}[^1\text{H}]$ CP MAS NMR spectrum of ^{13}C -Acetic Acid (Methyl group) adsorbed onto Cu-H-MOR (Cu/Al = 0.20). Simulated (solid) Lorentzian peaks are shown below the experimental (dashed) spectrum. Reprinted with permission from [74]. Copyright 2015 American Chemical Society.

UV-vis-NIR Spectroscopy

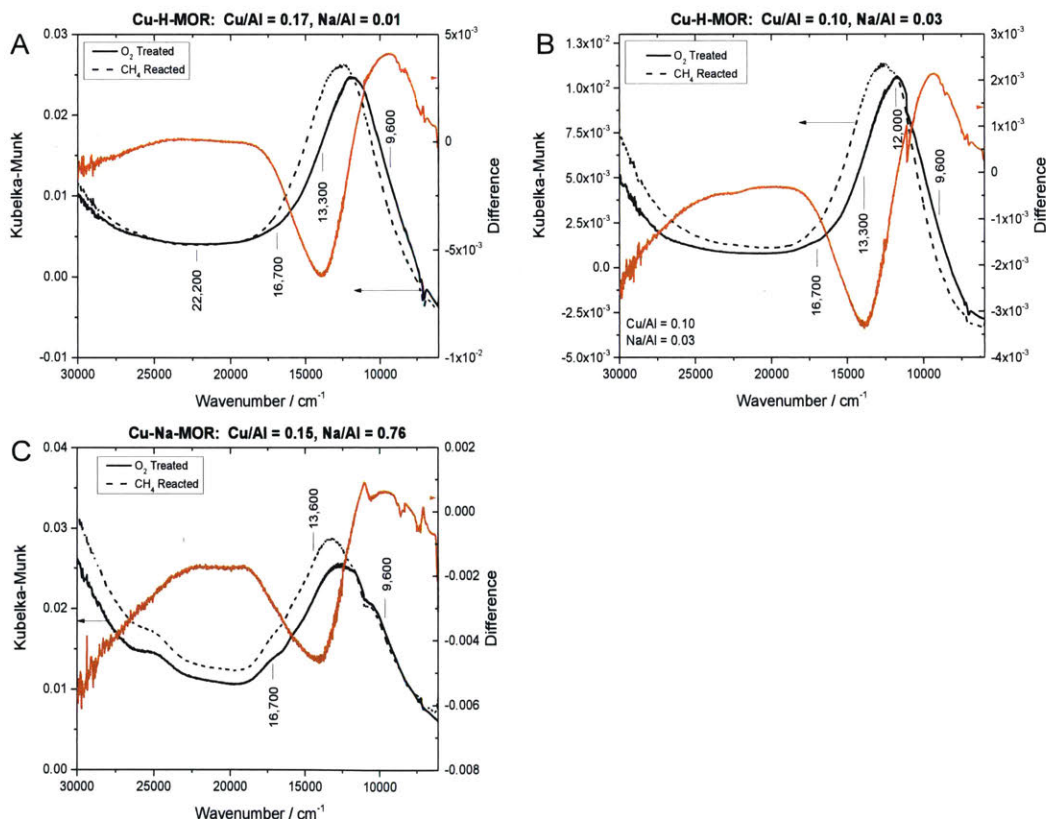


Figure S2-16. Diffuse Reflectance UV-visible spectra of (A) Cu-H-MOR (Cu/Al = 0.17), (B) Cu-H-MOR (Cu/Al = 0.10), and (C) Cu-Na-MOR (Cu/Al = 0.15). Each zeolite was calcined under oxygen (solid) at 823 K for 5 h and reacted under methane (dashed) at 473 K for 2 h. Difference spectrum (calcined - CH_4 reacted) is in orange. Reprinted with permission from [74]. Copyright 2015 American Chemical Society.

Figure S2-16 shows the visible region of Cu-MOR samples at low copper content ($\text{Cu}/\text{Al} < 0.20$) after calcination and then reaction after methane. In the Cu-H-MOR samples (A and B), the intensity of the $13,300\text{ cm}^{-1}$ band decreased after reaction with methane as well as a shoulder at $9,600\text{ cm}^{-1}$. Only a trace of the band at $22,200\text{ cm}^{-1}$ was visible in sample A. In contrast to Cu-H-MOR, the sodium exchanged Cu-MOR had only a very small shoulder at $9,600\text{ cm}^{-1}$ (C).

Figure S2-17 shows the visible and near-infrared regions of Cu-MOR zeolites at various copper content and Bronsted acidity after calcination under oxygen. No bands characteristic of water were observed at $5,200\text{ cm}^{-1}$ and $7,000\text{ cm}^{-1}$, thereby ruling out the possibility of water as the agent for the migration of methoxy species away from the copper centers.

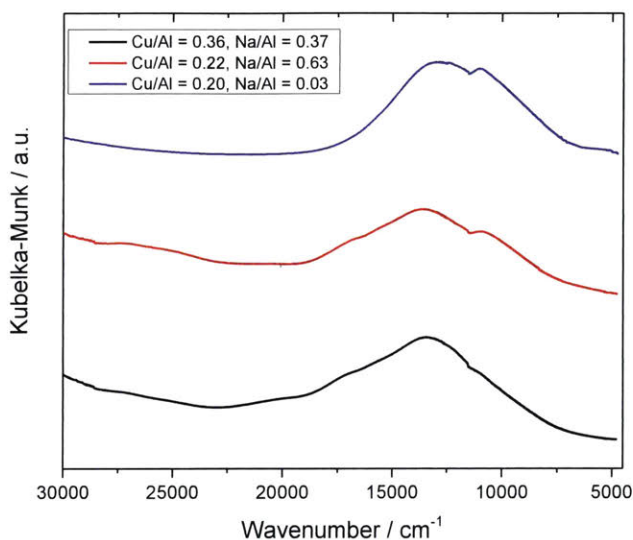


Figure S2-17. Vis-NIR Spectra of Cu-MOR zeolites calcined under oxygen (823 K) for 5 h. Reprinted with permission from [74]. Copyright 2015 American Chemical Society.

Dissolution of Cu-MOR in Hydrofluoric Acid (HF)

After methane oxidation and carbonylation reactions over Cu-MOR, the total organic content on the zeolite surface was quantified by dissolving the zeolite in hydrofluoric acid. The product distribution from Cu-H-MOR ($\text{Cu}/\text{Al} = 0.17$) and Cu-Na-MOR ($\text{Cu}/\text{Al} = 0.22$, $\text{Na}/\text{Al} = 0.55$) shows that more acetic acid is produced when Bronsted acid sites are present. Additionally, the acetic acid-to-methanol ratio is at least as high as when products are extracted with water compared to the true surface composition.

Table S2-7. Product Extractions from Cu-MOR from Dissolution in HF vs. Extraction in D₂O

Parent Zeolite	Cu/Al	Na/Al	HF Dissolution ($\mu\text{mol/g}_{\text{cat}}$)		D ₂ O Extraction ($\mu\text{mol/g}_{\text{cat}}$)		Extraction Efficiency (%)
			Methanol	Acetic Acid	Methanol	Acetic Acid	
H-MOR	0.17	0.02	29.2	31.7	14.2	19.8	55
H-MOR ^a	0.17	0.02			26.0	22.6	80
Na-MOR	0.22	0.55	14.6	7.4	10.5	5.0	70

a: This experiment corresponds to Cu-H-MOR (Cu/Al = 0.17) in Figure 2-6. Extraction efficiency was calculated based on total organic content of the HF dissolution experiment

Dimethyl Ether Carbonylation on H-MOR and H-ZSM-5

Kinetic studies of dimethyl ether carbonylation on H-MOR by Iglesia and coworkers^{89, 146-147} were conducted in packed-bed reactors under steady-state flow conditions. Since the reactions in this work were conducted in a stop-flow, batchwise manner, control reactions of dimethyl ether carbonylation on H-MOR were conducted to confirm the same dependence of the extent of carbonylation on the Bronsted acid content within the 8-membered rings^{75-76, 89}.

Dimethyl ether carbonylation reactions were performed in the same packed bed reactor described in the experimental setup for methane oxidation reactions. H-MOR or H-ZSM-5 (1.5 g, 500 – 1000 μm particles) were packed between quartz wool frits. Prior to reaction, the zeolite was calcined in 50 mL/min flowing oxygen (UHP, Airgas) for 5 h at 823 K and cooled under flowing oxygen to reaction temperature (473 K). The gas flow was changed to 50 mL/min of Ar for 1 hr to purge the system. Afterwards, the reaction mixture of 10 mL/min of dimethyl ether and 15 mL/min Ar for a 30 min reaction was brought over the zeolite bed. Upon saturating the surface with methoxy groups, carbonylation was performed with 200 mL/min of carbon monoxide (CO) at 10 bar gauge pressure for 30 min. Afterwards, the reactor was immediately depressurized, purged under Ar and cooled to room temperature. Once at room temperature, the zeolite bed was removed from the tube, weighed, and put into a sealed glass vial. The extraction procedure followed was identical to that described above for methane oxidation.

Carbonylation of dimethyl ether performed in stop flow mode still exhibited the same dependence of acetic acid production on Bronsted acidity. As the sodium content increased in H-MOR, the extracted acetic acid and methyl acetate decreased. Previous infrared spectroscopic studies on the same type of H-MOR zeolite (CBV21A, Zeolyst) calculated the H/Al of Bronsted acid sites in the 8-membered rings to be 0.55⁸⁹. For Na/Al above 0.55, the extracted acetic acid and methyl acetate was essentially zero. Thus, the stop flow experiments reinforced that Bronsted acidity in the 8-membered rings was

needed for carbonylation to occur, which was analogous to the continuous flow experiments.

The methanol extracted remained roughly constant despite the sodium content of H-MOR (Figure S2-18). At low Na/Al, the methanol extracted was predominantly from the Bronsted acid sites in the 12-membered rings where carbonylation was not favorable. For $\text{Na/Al} < 0.55$, the number of Bronsted acid sites in the 12-membered rings should remain constant from the sites in the 8MR pockets being preferentially quenched by sodium, so the methanol extracted should be roughly constant. However, for Na/Al of 0.8, the number of Bronsted acid sites must have been reduced such that the methanol extracted will decrease. The increased methanol extracted at high sodium content could have reflected the adsorption of dimethyl ether on sodium cations and its subsequent hydrolysis during extraction.

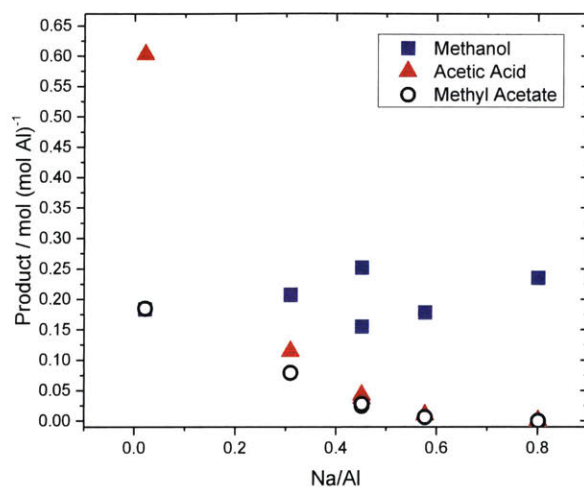


Figure S2-18. Carbonylation of Dimethyl Ether over H-MOR. Reaction conditions described in this section. Reprinted with permission from [74]. Copyright 2015 American Chemical Society.

Comparing the carbonylation activity of H-ZSM-5 with that of H-MOR, the amount of acetic acid extracted from H-ZSM-5 was 30-fold lower per aluminum site (Figure S2-19). This illustrated the importance of the Bronsted acid sites in 8-membered rings for carbonylation activity.

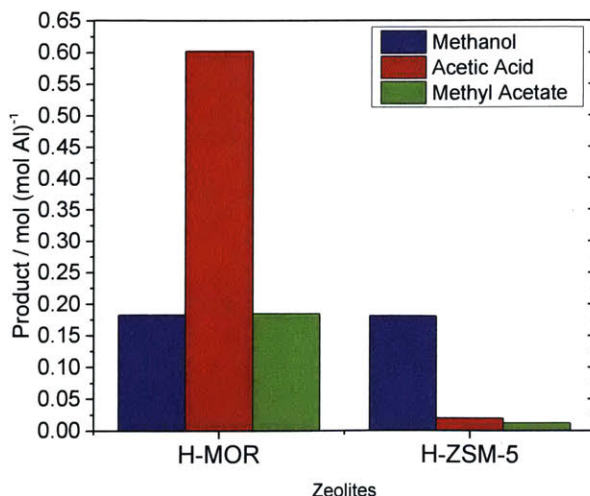


Figure S2-19. Carbonylation of dimethyl ether over H-MOR (Si/Al = 10) and H-ZSM-5 (Si/Al = 11.5). Reaction conditions described in this section. Reprinted with permission from [74]. Copyright 2015 American Chemical Society.

X-band EPR Spectra of Cu-MOR Samples

The full X-band EPR spectra of the Cu-MOR samples is shown in Figure S2-20. In the perpendicular region, the hyperfine splitting patterns of each Cu²⁺ species were not well resolved due to overlapping features. Only in Cu-Na-MOR with Cu/Al = 0.22 was a specific g_{xx} resolved as 2.06. The hyperfine splitting was more well defined after calcination in Cu-Na-MOR with Cu/Al = 0.36, possibly from another Cu²⁺ species becoming EPR silent.

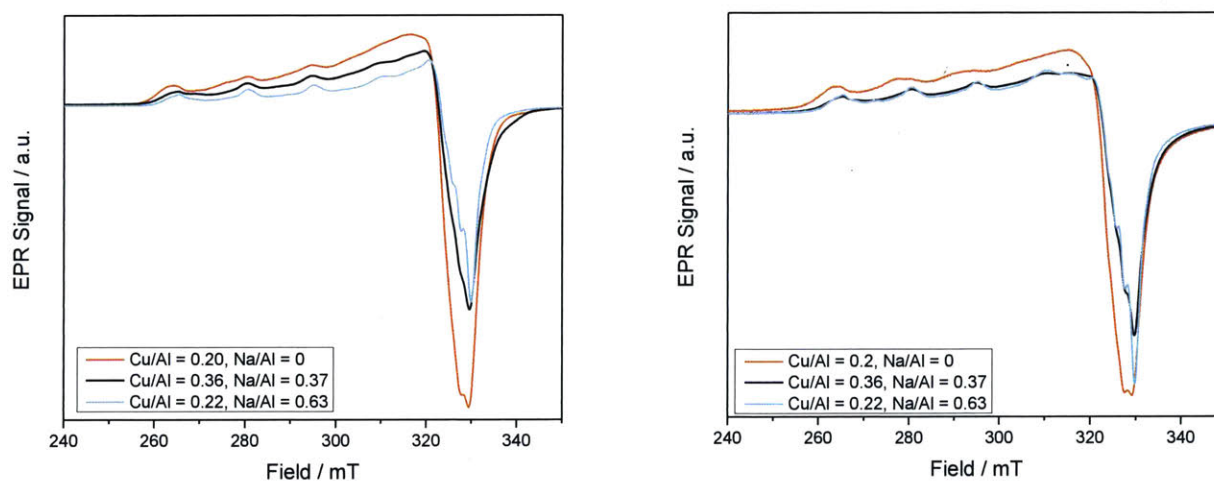


Figure S2-20. EPR Spectra (9.40 GHz) of (orange) Cu-H-MOR (Cu/Al = 0.20, Na/Al = 0.03), (black) Cu-Na-MOR (Cu/Al = 0.36, Na/Al = 0.37), and (cyan) Cu-Na-MOR (Cu/Al = 0.22, Na/Al = 0.63). (Left) Cu-MOR thermally treated under Ar for 3 h at 823 K and (Right) Cu-MOR calcined under O₂ for 5 h at 823 K and purged under Ar before acquisition. Reprinted with permission from [74]. Copyright 2015 American Chemical Society.

Chapter 3 : Catalytic Oxidation of Methane into Methanol over Copper-Exchanged Zeolites with Oxygen at Low Temperature

3.1 Introduction

To date, no man-made catalyst can convert methane (CH_4) and oxygen (O_2) directly into methanol (CH_3OH) at low temperature. For more than 100 years, the selective oxidation of this simple alkane has remained unsolved. This transformation, however, is essential to exploit our highly abundant natural gas reserves, particularly those located in distributed fields or stranded wells that cannot be accessed with large, capital-intensive reforming facilities. Although oxidative C-H bond activation of CH_4 is thermodynamically and kinetically accessible at low temperatures, the large bond dissociation energy (435 kJ mol^{-1}) of this molecule hinders C-H cleavage reactions via homolytic or heterolytic pathways. Consequently, few catalysts are capable of preventing over-oxidation to carbon dioxide (CO_2). Several alternative strategies for activating methane have been reported, including multi-step oxyfunctionalization with Periana catalysts,⁵²⁻⁵³ borylation,¹⁸⁰ and electrophilic carbene insertion,¹⁸¹⁻¹⁸² but all have fallen short of producing methanol directly and do not use oxygen as the oxidizing agent. In contrast, methane monooxygenase enzymes are capable of oxidizing CH_4 selectively into CH_3OH using O_2 at room temperature.^{58, 128, 132} While such biocatalysts are difficult to scale-up, the nature of their active sites provides inspiration for the development of synthetic oxidation catalysts. In this respect, iron-^{134, 156} and copper-^{66, 74, 118} exchanged zeolites have emerged as a promising class of materials capable of selectively oxidizing CH_4 into surface-bound methoxy species by hosting active sites akin to those found in CH_4 monooxygenases. Despite their potential, these materials have only been shown to oxidize CH_4 to CH_3OH stepwise and stoichiometrically with molecular oxygen (O_2)^{66, 82, 120} or catalytically with hydrogen peroxide,⁶³ making the process prohibitively expensive. Here, we report the first instance of catalytic gas phase oxidation of CH_4 into CH_3OH with O_2 under mild conditions. Copper-exchanged zeolite catalysts of various topologies maintain sustained activity and high CH_3OH selectivity at 483 K while transient kinetic experiments with isotopically labeled molecules confirm catalytic turnover. The discovery of catalytically

active sites for CH₃OH production in zeolites will be the foundation to develop new strategies for low temperature catalytic methane oxidation.

3.2 Results and Discussion

The stoichiometric oxidation of CH₄ to CH₃OH over copper-exchanged zeolites is believed to occur over mono-(μ -oxo) dicupric cores^{118, 122} or [Cu₃O₃]²⁺ trimeric sites¹²³⁻¹²⁴ generated by flowing anhydrous O₂ over the zeolite at temperatures above 723 K. These highly reactive electrophilic metal-oxygen species are adept at attacking the strong C-H bonds of CH₄, generating surface-bound methoxy groups at temperatures below 473 K.⁷⁴ Methoxy groups are typically extracted as CH₃OH by reacting with H₂O, which deactivates the copper sites and necessitates high temperature reactivation under anhydrous O₂ to perform the next oxidation cycle.^{118, 120} In the present study, stoichiometric and catalytic CH₃OH production regimes are observed during the gas phase oxidation of CH₄ over copper-exchanged zeolites with the MFI topology in the sodium (Cu-Na-ZSM-5) or proton (Cu-H-ZSM-5) forms at 483 K and atmospheric pressure (Figure 3-1). Similar to previous studies, the catalysts were activated under flowing O₂ at 823 K, cooled to reaction temperature, purged with helium (He) for 1 h, and contacted with a pure CH₄ stream for 0.5 h.^{66, 82, 118} However, unlike previous studies using only H₂O for extraction, we hydrolyzed surface-bound methoxy species by flowing a gas mixture comprised of 3.2 kPa of H₂O, 0.0025 kPa of O₂ and balance CH₄. Under these conditions, Cu-Na-ZSM-5 (Cu/Al = 0.37, Na/Al = 0.26) and Cu-H-ZSM-5 (Cu/Al = 0.31) evolved 37 μ mol g_{cat}⁻¹ and 82 μ mol g_{cat}⁻¹ of stoichiometric CH₃OH, respectively. These values are more than two times higher than those obtained with Cu-Na-ZSM-5 using only He, O₂ and H₂O as the extracting gas (9.6 μ mol g_{cat}⁻¹) or those reported by Lobo et. al. (16 μ mol g_{cat}⁻¹)¹²⁵ using 3.2 kPa H₂O in N₂ at 473 K and Schoonheydt et. al. (8 μ mol g_{cat}⁻¹)^{66, 82} using a 50% v/v acetonitrile aqueous solution for 1 h at 298 K to extract the oxidized products.

Remarkably, sustained CH₄ oxidation activity was observed when continuing to feed the CH₄, H₂O and O₂ gas mixture after all stoichiometric CH₃OH was extracted (Figure 1). Steady state CH₃OH production rates of 0.88 \pm 0.02 μ mol h⁻¹ g_{cat}⁻¹ and 1.81 \pm 0.01 μ mol h⁻¹ g_{cat}⁻¹ were measured for Cu-Na-ZSM-5 and Cu-H-ZSM-5, respectively. Over Cu-Na-ZSM-5, CH₃OH was the main product generated (as determined by ¹H nuclear magnetic resonance, Figure S3-4) with a selectivity of 70.6 \pm 0.4%, while CO₂ was the only byproduct generated at a rate of 0.38 \pm 0.02 μ mol h⁻¹ g_{cat}⁻¹ (Figure S3-5). CO₂ selectivity did not increase when higher conversions were simulated by introducing CH₃OH as a reagent at identical conditions (Supporting Information Section S2, Figure S3-6-7);

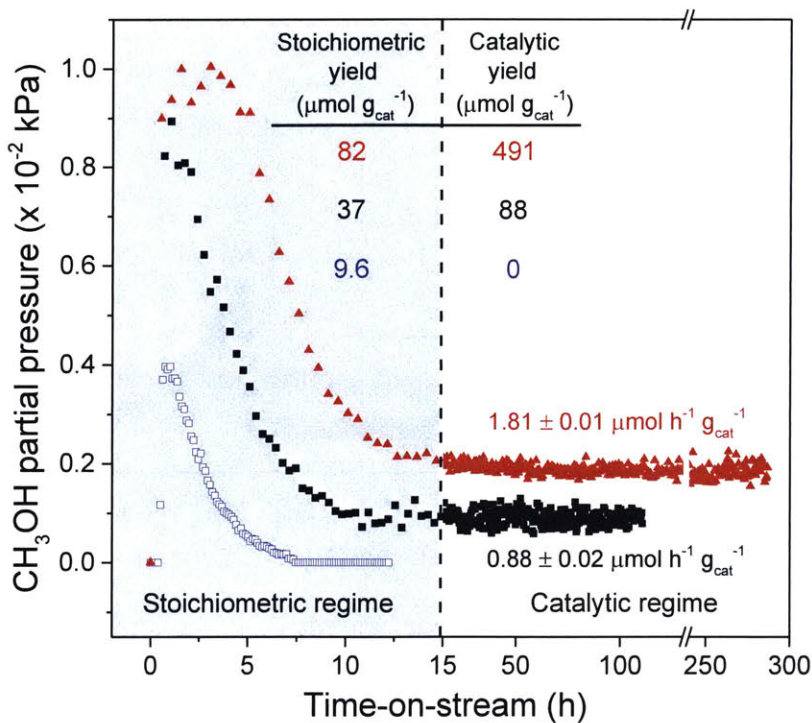


Figure 3-1. CH₄ oxidation over Cu-ZSM-5. Catalyst pretreatment: 5 h at 823 K under flowing O₂, cooled to 483 K under O₂ flow and then purged under He for 0.5 h. Initial dry CH₄ oxidation: 0.5 h under 2400 mL h⁻¹ g_{cat}⁻¹ of CH₄ at 483 K. CH₃OH partial pressure (kPa) with He/H₂O/O₂ over (□) Cu-Na-ZSM-5 (Cu/Al = 0.37, Na/Al = 0.26): T = 483 K, WHSV = 2400 mL h⁻¹ g_{cat}⁻¹, P_{He} = 98.1 kPa, P_{H₂O} = 3.2 kPa, P_{O₂} = 0.0025 kPa (25 ppm). CH₃OH partial pressure (kPa) with CH₄, H₂O, and O₂ over (■) Cu-Na-ZSM-5 and (▲) Cu-H-ZSM-5 (Cu/Al = 0.31): T = 483 K, WHSV = 2400 mL h⁻¹ g_{cat}⁻¹, P_{CH₄} = 98.1 kPa, P_{H₂O} = 3.2 kPa, P_{O₂} = 0.0025 kPa (25 ppm). Reprinted with permission from [183]. Copyright 2016 American Chemical Society.

although, most of CH₃OH was dehydrated into dimethyl ether in the presence of acid sites at these conditions (> 60% yield). Notably, the steady state CH₃OH production rates persisted without apparent deactivation, generating a total of 88 μmol g_{cat}⁻¹ over 108 h with Cu-Na-ZSM-5—a value roughly five times higher than that reported for the stoichiometric oxidation over Cu-Na-ZSM-5.¹²⁵ Similarly, Cu-H-ZSM-5 generated a total of 491 μmol g_{cat}⁻¹ over 288 h—a value ca. 1.4 times larger than the total copper content of the zeolite (Figure S3-8). The excess CH₃OH produced per copper atom in Cu-H-ZSM-5 coupled with the lack of sustained CH₃OH production in the absence of CH₄ in the extracting gas mixture over Cu-Na-ZSM-5 (Figure 3-1, open symbols) are strong evidence that CH₄ is oxidized catalytically over H₂O-tolerant copper sites.

Catalytic turnover was verified with transient experiments using isotopically labeled molecules coupled with on-line mass spectrometry (MS). ¹³C methoxy species were deposited on the zeolite by flowing ¹³CH₄ (16.8 kPa ¹³CH₄ [99 atom% ¹³C, Sigma-Aldrich])

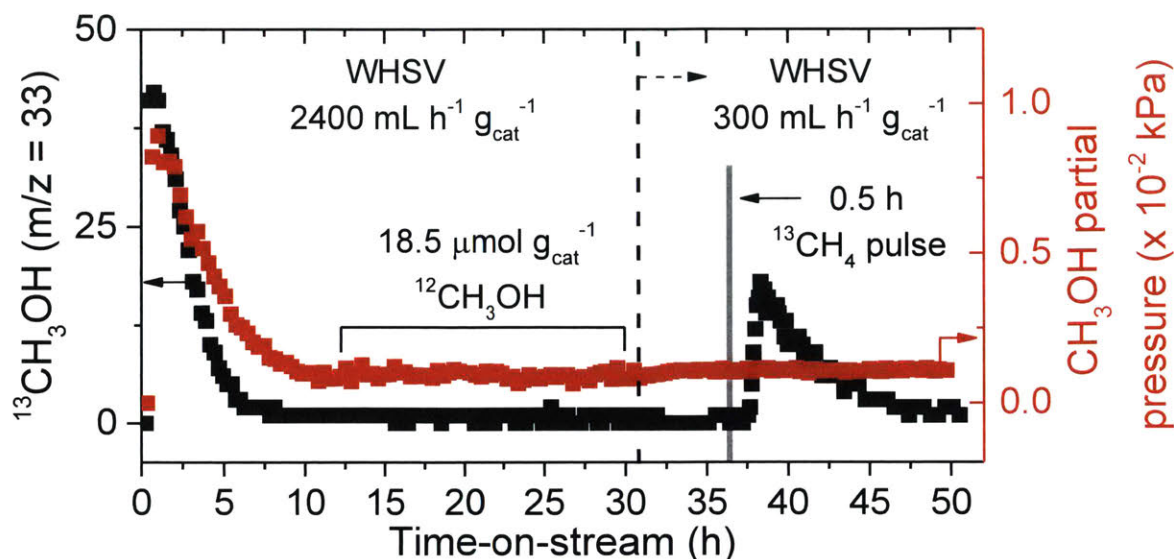


Figure 3-2. Transient, isotopically labeled kinetic experiments over Cu-Na-ZSM-5 (Cu/Al = 0.37, Na/Al = 0.26). Catalyst pretreatment: 5 h at 823 K under flowing O₂, cooled to 483 K under O₂ flow and purged under He for 0.5 h. Initial CH₄ oxidation: 0.5 h under 2400 mL h⁻¹ g_{cat}⁻¹ of 17% ¹³CH₄ / He at 483 K. Reaction conditions: T = 483 K, WHSV = 2400 mL h⁻¹ g_{cat}⁻¹, P_{12CH₄} = 98.1 kPa, P_{H₂O} = 3.2 kPa, P_{O₂} = 0.0025 kPa (25 ppm). After 31 h on-stream, WHSV was reduced to 300 mL h⁻¹ g_{cat}⁻¹ represented by the dashed line. Gray area denotes 0.5 h pulse of P_{13CH₄} = 98 kPa, P_{H₂O} = 3.2 kPa, P_{O₂} = 0.0025 kPa. Reprinted with permission from [183]. Copyright 2016 American Chemical Society.

with balance He) over an activated Cu-Na-ZSM-5 sample for 0.5 h at 483 K and then flowing a regular ¹²CH₄/H₂O/O₂ gas mixture to extract the methoxy species (detailed procedure found in Figure S3-9A). As shown in Figure 3-2, enriched ¹³CH₃OH (m/z = 33) was detected in the stoichiometric regime, but unlabeled ¹²CH₃OH was observed in the steady state regime, thus suggesting that new, unlabeled ¹²C methoxy species are formed after the initial ¹³C methoxy species are hydrolyzed. Next, the reaction was allowed to proceed at steady state at a measured rate of 0.88 μmol CH₃OH h⁻¹ g_{cat}⁻¹ for 21 h (equivalent to the production of 18.5 μmol g_{cat}⁻¹ of ¹²CH₃OH). At this point, the weight hourly space velocity (WHSV) was reduced from 2400 mL h⁻¹ g_{cat}⁻¹ to 300 mL h⁻¹ g_{cat}⁻¹ and the gas mixture was switched to ¹³CH₄/H₂O/O₂ for 0.5 h before resuming the flow of the regular, unlabeled gas mixture. This effective pulse of labeled ¹³CH₄ resulted in the production of labeled ¹³CH₃OH as evidenced by a detectable pulse of the m/z = 33 signal without significantly altering steady state production of CH₃OH (Figure 3-2). Similar ¹³C enrichment profiles were observed for CO₂ during both isotope switching experiments (Figure S3-10). Analogous behavior was observed for similar experiments carried out over Cu-H-ZSM-5 (Figure S3-11). Control experiments using ¹²CH₄ to populate the activated catalyst with unlabeled ¹²C methoxy species did not generate a significant amount of ¹³CH₃OH in the stoichiometric or steady state regimes (Figure S3-9B, S11B), thereby

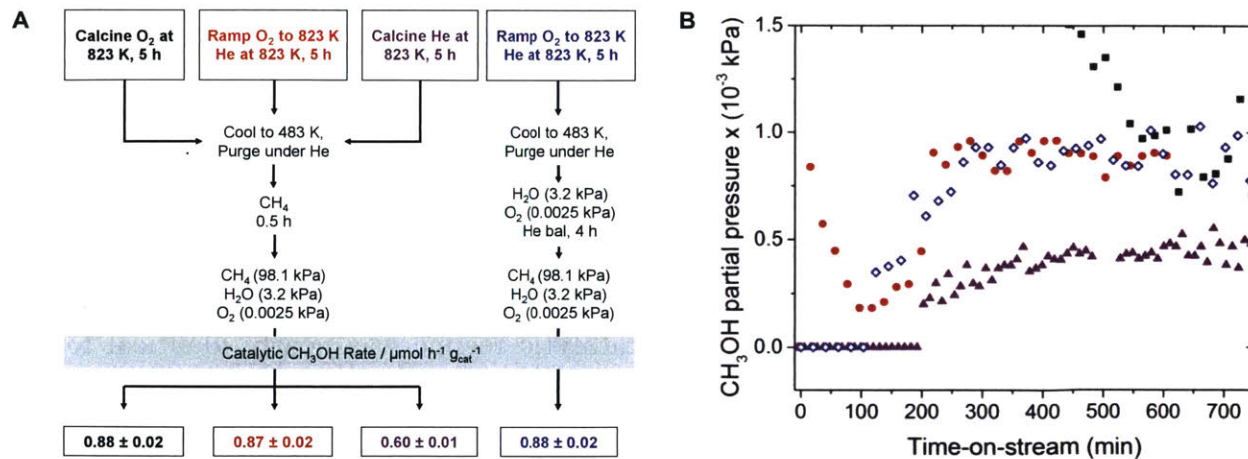


Figure 3-3. Thermal pretreatments and onset of steady state CH₄ oxidation over Cu-Na-ZSM-5 (Cu/Al = 0.37). (A) Thermal pretreatments, reaction conditions for all pretreatments, and catalytic CH₃OH production rates. The symbol ± denotes 95% confidence interval. (B) Evolution of catalytic CH₃OH production for each pretreatment outlined in (A); t=0 denotes when the CH₄/H₂O/O₂ gas flow was started. Reaction conditions: T = 483 K, WHSV = 2400 mL h⁻¹ g_{cat}⁻¹, P_{CH₄} = 98.1 kPa, P_{H₂O} = 3.2 kPa, P_{O₂} = 0.0025 kPa. Reprinted with permission from [183]. Copyright 2016 American Chemical Society.

ruling out artifacts or potential effects arising from natural abundance ¹³CH₄ in the unlabeled gas stream. Kinetic measurements on Cu-Na-ZSM-5 at 483 K show first, half, and zero order dependencies with respect to CH₄, H₂O and O₂, respectively (Supporting Information Section S7, Figure S3-12). Importantly, replacing CH₄ with CD₄ in the extracting gas during steady state operation at a WHSV of 240 mL h⁻¹ g_{cat}⁻¹ decreased the CH₃OH production rate from 0.090 to 0.055 $\mu\text{mol h}^{-1} \text{g}_{\text{cat}}^{-1}$ (Figure S3-13). This change corresponds to a kinetic isotope effect (KIE) of 1.6 ± 0.1 , thus indicating that C-H abstraction is a kinetically relevant step in the catalytic cycle. Taken together, the data from the transient ¹³CH₄ pulse experiments, the reaction rate order dependencies, and the kinetic isotope effect confirm catalytic turnover.

Gas pretreatments were varied to gain insight into the origin of catalytic and stoichiometric sites in Cu-Na-ZSM-5 (see Figure 3-3, S3.14-15). Specifically, Cu-Na-ZSM-5 samples were subjected to three pretreatments at 873 K prior to regular CH₄ oxidation and extraction at 483 K: i) calcination under O₂ and then under He (20 ppm O₂); ii) calcination under He (20 ppm O₂); or iii) calcination under He without O₂ (< 0.1 ppm, Figure S3-14). In all cases, stoichiometric CH₃OH production drastically diminished (98 - 100%) but catalytic CH₃OH production was only moderately affected (0 - 60%) (Figure 3-3). Treating activated Cu-Na-ZSM-5 with He above 723 K has been shown to eliminate the mono-(μ -oxo) dicupric cores for stoichiometric CH₄ oxidation.⁸² The absence of the mono-(μ -oxo) dicupric sites during steady state methane oxidation was confirmed with

UV-visible spectroscopic and online gas chromatographic measurements over Cu-Na-ZSM-5 (Cu/Al=0.37) (Supporting Information Section S9, Figures S3.16-S18). Interestingly, van Bokhoven et. al. observed a small fraction of H₂O-tolerant sites in copper-exchanged mordenite (Cu-MOR) that did not require high temperature reactivation for stoichiometric CH₄ oxidation experiments after exposure to H₂O.^{121, 184} However, in the present study, exposing Cu-Na-ZSM-5 to H₂O/O₂/He at 483 K prior to contacting it with CH₄ completely eliminated stoichiometric CH₃OH production but did not affect catalytic CH₃OH production. Note the onset of the catalytic regime was nearly identical for all samples (240 min on-stream) after exposure to CH₄/H₂O/O₂ irrespective of the pretreatment used. The similarity of catalytic rates and onset of CH₃OH production for all pretreated Cu-Na-ZSM-5 samples implies the catalytic sites are different from those responsible for stoichiometric CH₄ oxidation, and the catalytic sites are either generated or activated when copper species are exposed to CH₄, H₂O and O₂ at reaction conditions rather than during the high temperature pretreatment.

An induction period preceding the onset of catalytic CH₄ oxidation suggests that copper speciation changes under reaction conditions. The CH₃OH production profile for a regular CH₄ oxidation and extraction experiment using Cu-Na-ZSM-5 pretreated at 823 K first with O₂ and then with He (20 ppm O₂) shows that catalytic production began after 240 min on-stream despite H₂O breaking through the catalyst bed after 25 min (Figure S3-15). A comparable induction process was observed when Cu-Na-ZSM-5 was pretreated without O₂ and exposed to a CH₄/H₂O gas mixture at 483 K (Figure S3-14). In this case CH₃OH was detected only ca. 300 min after O₂ was introduced into the system. Hydrated copper species are known to weakly associate with the zeolite framework, becoming mobile and easily oxidized.¹⁰⁰ In copper-exchanged zeolites with the chabazite topology (Cu-SSZ-13), hydrated Cu²⁺ ions have been shown to migrate under flowing wet O₂/N₂ (and trace NO and NH₃) gas mixtures between 403–523 K during the selective catalytic reduction (SCR) of NO_x¹⁸⁵ to form transient dimeric active sites.¹⁰¹ The strong similarities between the reaction temperature and the gaseous atmosphere (H₂O/O₂) used during both the SCR of NO_x and the oxidation of CH₄ could imply that mobile, hydrated copper species also rearrange into active sites for catalytic CH₄ oxidation as they do for the SCR of NO_x.

Catalytic CH₄ oxidation was investigated as a function of the copper content and Brønsted acidity of the zeolite (see Table S3-2). A control experiment with H-ZSM-5 (Si/Al = 11.5) not subjected to copper exchange did not generate CH₃OH, thereby confirming that trace transition metal impurities in the zeolite are not responsible for catalytic behavior. Higher Cu/Al ratios in Cu-Na-ZSM-5 and Cu-H-ZSM-5 increased the

Table 3-1. Catalytic CH₄ oxidation rates for various zeolite topologies.

Material	Framework	Cage Shape	Cage Size (Å) ⁶⁷	Channel Size (Å) ⁶⁸	Si/Al _{tot} ^b	Cu/Al _{tot} ^c	Specific Activity ^d	STY (h ⁻¹ × 10 ⁻³) ^e
H-ZSM-5	MFI	–	–	5.3 × 5.6 5.1 × 5.5	13.2	0.31	1.79 ± 0.02	5.2 ± 0.05
H-Beta	BEA	–	–	6.6 × 6.7 5.6 × 5.6	13.3	0.30	0.80 ± 0.01	2.4 ± 0.04
MCM-41	MCM-41	–	–	30	16.1	0.74	0.36 ± 0.02	0.6 ± 0.03
H-ZSM-5	MFI	–	–	5.3 × 5.6 5.1 × 5.5	13.9	0.13	0.84 ± 0.02	6.0 ± 0.17
H-Mordenite	MOR	–	–	6.5 × 7, 2.6 × 5.7	11.1	0.14	0.84 ± 0.01	4.6 ± 0.08
H-Ferrierite	FER	–	–	4.2 × 5.4 3.5 × 4.8	10.6	0.12	0.44 ± 0.01	2.7 ± 0.04
Na-ZSM-5	MFI	–	–	5.3 × 5.6 5.1 × 5.5	13.6	0.37	0.88 ± 0.02	2.2 ± 0.04
Na-Y	FAU	Spherical	9.6 × 9.6	7.4 × 7.4	4.6	0.45	0.30 ± 0.01	0.3 ± 0.01
Na-SAPO-34	CHA	Ellipsoidal	9.4 × 9.4 × 12.7	3.8 × 3.8	0.6	0.02	0.84 ± 0.03	7.9 ± 0.29
Na-SSZ-13	CHA	Ellipsoidal	9.4 × 9.4 × 12.7	3.8 × 3.8	13.8	0.50	3.12 ± 0.01	6.1 ± 0.03
CuO _x -MFI ^f	MFI			5.3 × 5.6 5.1 × 5.5	∞	∞	0	0
CuO _x -BEA ^f	BEA			6.6 × 6.7 5.6 × 5.6	∞	∞	0	0
H-ZSM-5 ^f	MFI			5.3 × 5.6 5.1 × 5.5	12.9	0	0	0

Catalyst pretreatment: 5 h at 823 K under flowing O₂, cooled to 483 K under O₂ flow and then purged under He for 0.5 h. Initial CH₄ oxidation: 0.5 h under 2400 mL h⁻¹ g_{cat}⁻¹ CH₄ at 483 K. Reaction conditions: T = 483 K, WHSV = 2400 mL h⁻¹ g_{cat}⁻¹, P_{CH₄} = 98.1 kPa, P_{H₂O} = 3.2 kPa, P_{O₂} = 0.0025 kPa (25 ppm). ^a Si/Al_{nom} denotes the nominal silicon to aluminum ratio in the zeolite based on commercial figures or ratios of SiO₂ to Al₂O₃ in synthesis procedures. ^b Si/Al_{tot} denotes the ratio of silicon to aluminum atoms ratio within the zeolite calculated using data from inductively coupled plasma mass spectrometry (ICP-MS) measurements. ^c Cu/Al_{tot} denotes the ratio of copper to aluminum atoms within the zeolite calculated using ICP-MS. ^d Specific activity = μ mol_{CH₃OH} h⁻¹ g_{cat}⁻¹. ^e Site time yield (STY) defined as mol CH₃OH (mol Cu)⁻¹ h⁻¹. ^f T = 483 K, WHSV = 2400 mL h⁻¹ g_{cat}⁻¹, P_{CH₄} = 93.1 kPa, P_{H₂O} = 3.2 kPa, P_{O₂} = 0.051 kPa. The ± symbol denotes 95% confidence intervals.

steady state specific activity (defined as $\mu\text{mol}_{\text{MeOH}} \text{h}^{-1} \text{g}_{\text{cat}}^{-1}$), but decreased the site-time yield (STY, defined as $\text{mol}_{\text{CH}_3\text{OH}} \text{mol}_{\text{Cu}}^{-1} \text{h}^{-1}$), suggesting that the number of active sites does not increase proportionally with the total amount of copper. The presence of Brønsted acid sites increased specific activity and STY for all samples with similar Cu/Al ratios. Indeed, different apparent activation energies (E_a^{app}) were observed between the sodium and proton forms of Cu-ZSM-5 (Table S3-2). Density functional theory calculations over Cu-ZSM-5 have shown that Brønsted acid sites change the energetics of the formation of mono-(μ -oxo) dicupric cores with NO.¹⁸⁶ While mono-(μ -oxo) dicupric cores are likely not present under reaction conditions for catalytic CH₄ oxidation, Brønsted acid sites could impart similar changes in the energetics of formation of the catalytic sites.

The catalytic rates and E_a^{app} values of CH₄ oxidation are heavily influenced by zeolite topology (see Table 3-1, Table S3-2). Cu-MOR, featuring 12-membered ring (MR) pores intersected by sinusoidal 8-MR pores, exhibited either comparable or lower activity at 483 K than that of Cu-H-ZSM-5 (Table S3-2). However, a significantly higher E_a^{app} of 149 kJ/mol resulted in higher CH₃OH rates at temperatures above 483 K when compared to those of Cu-H-ZSM-5 (Figure S3-19). These results suggest the site speciation and reaction environment within MOR may play a role in stabilizing kinetically relevant transition states. Other topologies, including ferrierite (FER), beta (BEA), Y (FAU) and caged-based SSZ-13 and SAPO-34 (CHA) also oxidize CH₄ into CH₃OH but with different rates than those of ZSM-5. Zeolites with large pores at high Cu/Al (0.30 – 0.50) including BEA (12-MR, $6.6 \times 6.7 \text{ \AA}$ and $5.6 \times 5.6 \text{ \AA}$) and FAU ($7.4 \times 7.4 \text{ \AA}$ windows) showed 50% and 70% lower overall activity when compared to MFI. MCM-41, an amorphous aluminosilicate with large pores of 30 Å, had nearly an order of magnitude lower STY than ZSM-5, indicating that a crystalline, microporous structure with small pores is preferable for catalytic CH₄ oxidation. At low Cu/Al (0.12 – 0.14), Cu-H-ZSM-5 has the highest specific activity and STY (Table 3-1), while FER (intersecting 10-MR [$4.2 \times 5.4 \text{ \AA}$] and 8-MR [$3.5 \times 4.8 \text{ \AA}$]) was half as active as ZSM-5. While Cu-ZSM-5 had the highest specific activity and STY compared to the small-pore zeolites tested, the cage-based aluminosilicate SSZ-13 and the silicoaluminophosphate SAPO-34 with the CHA topology (8-MR windows of $3.8 \times 3.8 \text{ \AA}$, ellipsoidal cages of $9.4 \times 9.4 \times 12.7 \text{ \AA}$) featured higher STY of $6.1 \times 10^{-3} \text{ h}^{-1}$ and $7.9 \times 10^{-3} \text{ h}^{-1}$, respectively, than those in Cu-Na-ZSM-5 or Cu-H-ZSM-5 at similar Cu/Al ratios (Table 3-1). These studies indicate the catalytic sites or the kinetically relevant transition states are sensitive to the zeolite topology, with

materials featuring small pores or cage-based structures showing enhanced performance when compared to those with large pores.

Taking advantage of the large E_a^{app} for Cu-Na-SSZ-13 (Cu/Al = 0.50, 100 ± 2.1 kJ mol⁻¹), the reaction temperature was systematically increased to achieve higher catalytic rates. The CH₃OH production rate increased from 2.2×10^{-3} to 31.6×10^{-3} mol_{CH₃OH} (mol Cu)⁻¹ h⁻¹ when increasing the temperature from 463 to 533 K before a decrease in rates was observed (Figure S3-20). The large E_a^{app} coupled with the stable CH₃OH production over a wide range of temperature suggest that Cu-SSZ-13 zeolites could be further engineered to enhance further catalytic rates. In summary, copper-exchanged zeolites offer a broad and robust platform for the low temperature, catalytic oxidation of CH₄ into CH₃OH using O₂.

3.3 Conclusions

The nature of the catalytic active sites for CH₄ oxidation into CH₃OH over copper-exchanged zeolites is currently unknown. A recent report by von Bokhoven et. al. observed the formation of copper oxide clusters in Cu-MOR after the cyclic, isothermal, and stoichiometric oxidation of CH₄ into CH₃OH.¹⁸⁴ It was hypothesized that these oxide clusters were active for isothermal cyclic CH₄ oxidation. We did not observe steady state activity for large copper oxide nanoparticles supported on pure silica MFI between 483-543 K (average size 30 nm for CuO_x, Table 3-1, Figure S3.21-23) or on pure silica BEA (average size 60 nm for Cu₂O, 41 nm for CuO, Table 3-1, Figure S3.24-25). However, we cannot rule out that ultra-small copper oxide clusters copper species stabilized by aluminum in the zeolite framework or defect sites are responsible for catalytic activity. Diffuse reflectance UV-visible spectroscopic measurements show peaks forming at 20,800, 26,800, and 30,000 cm⁻¹ during steady state CH₃OH production (Figure S18C.1-2, D.1-2), possibly corresponding to copper oxide species¹⁰⁸ generated during reaction. Future work will focus on identifying and characterizing the catalytic site(s) as well as devising strategies to maximize catalytic activity.

3.4 Experimental Methods

Materials

Commercial zeolites. Zeolites MOR (mordenite, CBV21A, Si/Al = 10), ZSM-5 (MFI, CBV2314, Si/Al = 11.5), BEA (beta, CP814E, Si/Al = 12.5), FER (ferrierite, CP914C, Si/Al = 10), and Y (FAU, CBV100, Si/Al = 5.1) were purchased from Zeolyst International. MCM-41 (Aluminosilicate Al-MCM-41, Si/Al = 12) was purchased from ACS Materials. All zeolites were in the ammonium form except for Y and MCM-41, which were in the sodium form.

Zeolite Synthesis

Synthesis of SSZ-13 (CHA): sodium hydroxide (99.99%, Sigma-Aldrich) was dissolved in H₂O and mixed with N,N,N-trimethyl-1-adamantanamine hydroxide solution (Ada, 25 wt % in H₂O, Sachem) followed by the addition of aluminum hydroxide (80.3 wt % Al(OH)₃, SPI Pharma 0250) to obtain a colorless solution. After the addition of colloidal silicon dioxide (SiO₂) (Ludoxff LS-30), the colorless solution was stirred at room temperature for 2 h. The final composition of the mixture was 0.1 Na₂O: 0.033 Al₂O₃: 1.0 SiO₂: 44 H₂O: 0.1 (Ada)₂O. This mixture was transferred to a 23-mL Teflon-lined stainless steel autoclave (No. 4749, Parr Instruments) and was then subjected to hydrothermal treatment at 433 K for 4 days in an oven under autogenous pressure and rotation (60 rpm). After hydrothermal treatment, the product was separated from the mother liquor by centrifugation, washed several times with distilled H₂O, and dried at 393 K. SSZ-13 samples were calcined under dry air (Dry Size 300, Airgas) with the following temperature profile: heat 1 K min⁻¹ to 423 K and hold for 2 h at 423 K, then heat 1 K min⁻¹ to 623 K and hold for 2 h at 623 K, and lastly heat 1 K min⁻¹ to 853 K and hold for 10 h.

Synthesis of SAPO-34 (CHA): Aluminum oxide (Al₂O₃) (Catapalff B) and colloidal silicon dioxide (SiO₂) (Ludoxff AS-40) were added to a mixture of phosphoric acid (85 wt %, Sigma-Aldrich) and H₂O. Diethylamine (DEA, 99.5%, Sigma-Aldrich) was added to the mixture to obtain a gel with the composition of 0.8 P₂O₃: Al₂O₃: 0.6 SiO₂: 50 H₂O: 2 DEA. The mixture was stirred for 0.5 h and then subjected to hydrothermal treatment at 423 K for 7 days with 60 rpm rotation. After hydrothermal treatment, the product was separated from the mother liquor by centrifugation, washed several times with distilled H₂O, and dried at 393 K. SAPO-34 samples were calcined under dry air (Dry Size 300, Airgas) with the same temperature profile stated for SSZ-13 samples.

Synthesis of pure silica Beta: Si-BEA was synthesized based on a procedure reported by Cambor et.al.¹⁸⁷ Aqueous tetraethylammonium hydroxide (27.169 g, 35 wt% in H₂O,

Sigma-Aldrich) and tetraethyl orthosilicate (24.160 g, 99%, Sigma Aldrich) were added to a Teflon [polytetrafluoroethylene (PTFE)] dish and stirred at 250 rpm at room temperature for 90 min. Deionized H₂O (15 mL) was added and the solution was left uncovered on the stir plate for 12 h to reach a total mass of 33.046 g after evaporation of ethanol and some of the H₂O. Next, hydrofluoric acid (2.627 g, 48wt% in H₂O, > 99.99% trace metals basis, Sigma-Aldrich) was added drop wise and mixed using a PTFE spatula, resulting in a thick gel. Additional H₂O was added to aid homogenization and the sol-gel was allowed to evaporate to 33.848 g. The final molar composition was 1 SiO₂:0.56 TEAOH:0.56 HF:7.5 H₂O. The gel was transferred to a 45 mL PTFE-lined stainless steel autoclave and heated to 413 K for 7-20 days under static conditions. The product was separated from the mother liquor by filtration, washed with distilled H₂O, and dried at 373 K. The zeolite was calcined under dry air (Dry Size 300, Airgas) with the same temperature profile stated for SSZ-13 samples.

Synthesis of pure silica MFI: Si-MFI was synthesized based on a procedure reported by Persson et.al.¹⁸⁸ Aqueous tetrapropylammonium hydroxide (12.00 g, 1.0 M in H₂O, Sigma-Aldrich) and tetraethyl orthosilicate (5.00 g, 99%, Sigma Aldrich) were added to a Teflon [polytetrafluoroethylene (PTFE)] dish and stirred at 300 rpm at room temperature for 60 min. The molar composition was 1 SiO₂:0.5 TPAOH:22 H₂O. The gel was transferred to a 23 mL PTFE-lined stainless steel autoclave and heated to 453 K for 2 days under static conditions. The product was separated from the mother liquor by centrifugation, washed with distilled H₂O, and dried at 373 K. The zeolite was calcined under dry air (Dry Size 300, Airgas) with the same temperature profile stated for SSZ-13 samples.

Ion-Exchange

Sodium exchange. The following procedure was used to ion-exchange all zeolites: 1 g of zeolite was stirred in 36 mL of 2.44 M sodium acetate (> 99%, Sigma-Aldrich) at 353 K for 4 h. Zeolites were subsequently filtered while hot and rinsed with 120 mL of deionized H₂O. Zeolites were then dried for 4 h at 393 K in a drying oven. The above procedure was repeated three times.

Copper exchange. The following procedure was used to ion-exchange all zeolites: 1 g of zeolite was stirred in 60 mL of 0.001 - 0.05 M solutions of copper (II) acetate monohydrate (> 99%, Sigma-Aldrich) at room temperature overnight. The suspension was then filtered at room temperature and rinsed with 300 mL of deionized H₂O. The zeolite was dried overnight at 393 K in a drying oven and subsequently calcined under dry air (Dry Size 300, Airgas) at 823 K for 5 h with a heating ramp of 1 K min⁻¹.

Incipient Wetness Impregnation

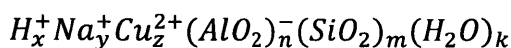
CuO_x-BEA. 0.23 g of a 0.23 M solution of copper (II) nitrate trihydrate (> 99%, Sigma-Aldrich) was added dropwise to 0.30 g of Si-BEA under vigorous stirring, yielding 1.1 wt% of CuO_x on the BEA zeolite. CuO_x-BEA was dried overnight at 383 K and then calcined at 853 K for 10 h under flowing dry air (Dry Size 300, Airgas) with a heating ramp of 1 K min⁻¹. The resultant zeolite had a gray color.

CuO_x-MFI. 0.239 g of a 0.241 M solution of copper (II) nitrate was added dropwise to 0.352 g of Si-MFI under vigorous stirring, yielding 1.1 wt% of CuO_x on the MFI zeolite. CuO_x-MFI was dried overnight and calcined in the same way as stated for CuO_x-BEA. The resultant zeolite had a gray color.

Characterization

Elemental analysis. Copper (Cu), sodium (Na), aluminum (Al), and iron (Fe) contents were determined using inductively coupled plasma mass spectrometry (ICP-MS) (Agilent 7900). 2.0 – 10.0 mg of zeolite were placed in a polyethylene microfuge tube (1.5 mL) and digested in 0.1 mL hydrofluoric acid (48 wt %, trace metals basis, Sigma-Aldrich) for 3 h. The hydrofluoric acid solution was diluted to a total mass of 10.0 g using 2 wt % aqueous nitric acid (HNO₃) (veritas purity, GFS Chemicals). 0.10 g of this solution was then added to two solutions: 1) 0.10 g of 1 part per million (ppm) erbium in 2 wt% HNO₃ solution; 2) 9.80 g of 2 wt% HNO₃. The final concentration of each element was 10 parts per billion (ppb) erbium and between 10 to 300 ppb for Cu, Na, Al, and Fe. A five point calibration curve was built using the following ICP standard solutions: 1,000 ppm Cu in 2 wt% HNO₃, 1,000 ppm Al in 2 wt% HNO₃, 1,000 ppm Na in 2 wt% HNO₃, and 1,000 ppm Fe in 2 wt% HNO₃. All standard solutions were purchased from Sigma-Aldrich (TraceCERT).

Calculations of molar ratios Si/Al_{tot} and Cu/Al_{tot}. The unit cell of a zeolite is given by:



where subscripts refer to the molar ratios of each component within the unit cell of a zeolite. Local charge balance was assumed to occur within the zeolite, requiring $x = n - 2z - y$.

From the unit cell given above, the mass balance of the unit cell is given by the following equation on a per gram zeolite basis:

$$1 = a \frac{g \text{ SiO}_2}{g \text{ zeolite}} + b \frac{g [\text{AlO}_2]^-}{g \text{ zeolite}} + c \frac{g \text{ Cu}^{2+}}{g \text{ zeolite}} + d \frac{g \text{ Na}^+}{g \text{ zeolite}} + e \frac{g \text{ H}^+}{g \text{ zeolite}} + f \frac{g \text{ H}_2\text{O}}{g \text{ zeolite}}$$

where each coefficient represents the weight percent of each species. The weight percent of Al, Cu, and Na were directly calculated using ICP-MS, allowing b , c , and d to be determined. Converting the weight percentages of Al, Cu, and Na to mole percentages per gram zeolite, e was then calculated using the local charge balance of cations on the zeolite framework. The weight percentage of H₂O (f) was assumed to be equal to the weight percentage of H₂O in the zeolite framework unit cell (2 – 7 wt %).⁶⁸ The mass balance was then solved for the weight percentage of SiO₂ (a).

$$\text{Si}/\text{Al}_{\text{tot}} \text{ was calculated by } \frac{\text{Si}}{\text{Al}_{\text{tot}}} = \frac{a m_{\text{AlO}_2}}{b m_{\text{SiO}_2}} \times \frac{1 \text{ mol Si}}{1 \text{ mol SiO}_2} \times \frac{1 \text{ mol AlO}_2}{1 \text{ mol Al}}$$

where m_i is the molar mass of element i .

$$\text{Cu}/\text{Al}_{\text{tot}} \text{ was calculated by } \frac{\text{Cu}}{\text{Al}_{\text{tot}}} = \frac{c m_{\text{AlO}_2}}{b m_{\text{Cu}}} \times \frac{1 \text{ mol AlO}_2}{1 \text{ mol Al}}$$

Powder x-ray diffraction. The crystal structures of zeolite catalysts were determined from powder x-ray diffraction patterns collected using a Bruker D8 diffractometer using Cu-K α radiation ($\lambda = 1.5418 \text{ \AA}$, 40 kV, 40 mA). Data were recorded in the range of 3-50 2 θ with an angular step size of 0.02° and a counting time of 0.068 s per step.

Surface area and pore volume quantification. Nitrogen adsorption and desorption isotherms were measured on a Quantachrome Autosorb iQ apparatus at liquid nitrogen temperature (77 K). Prior to the adsorption analysis, all samples were pelletized and degassed under vacuum for 12 h at 623 K. Micropore volume and total pore volume were determined from the amount of N₂ adsorbed at $P/P_0 = 0.01$ and $P/P_0 = 0.95$, respectively.

Transmission Electron Microscopy (TEM). Transmission electron microscopy was performed on a JEOL 2010F equipped with a field emission gun (FEG) operating at 200 kV. Magnifications of obtained images ranged from 50,000x to 100,000x.

Coupled in-situ UV-Vis-NIR Spectroscopy and Online Gas Chromatography. UV-Vis spectroscopy was performed on a Cary 5000 UV-Vis-NIR spectrometer (Agilent Technologies) equipped with a DiffusIR diffuse reflectance accessory (PIKE Technologies) and environmental chamber (HTV, PIKE Technologies) with a quartz window. Absolute reflectance was measured from 11,000 cm⁻¹ to 52,600 cm⁻¹ with a scan rate of 11,700 cm⁻¹ min⁻¹. All spectra were normalized with respect to background spectra of hydrated Na-ZSM-5. The gas outlet from the environmental temperature chamber was connected to a

gas chromatograph (Agilent Technologies, model 6890N) equipped with an S-bond column (Restek Rt-S-bond, 30 m, 0.25 mm ID, #19770) and flame ionization detector. The oven temperature was isothermal at 373 K for 10 min.

To conduct in-situ CH₄ oxidation reactions, the temperature was controlled using a PIKE PC Controlled Temperature Module. Cu-ZSM-5 (Cu/Al = 0.37) was ground into a fine powder before loading 10.0 mg into the sample cell. The flow of gases, including He (ultra high purity, Airgas), O₂ (ultra high purity, Airgas), 1% O₂/He (ultra high purity, Airgas), and CH₄ (research grade, Airgas) were controlled with independent mass flow controllers (Brooks Instruments LLC). H₂O (typically 3.2 kPa) was introduced into the gas stream using a saturator maintained at 298 K.

Catalytic CH₄ Oxidation Reactions

CH₄ oxidation reactions were conducted in a continuous, tubular flow reactor (stainless steel tube, O.D. 12.5 mm, wall thickness = 0.889 mm). The reactor tube was mounted inside of a single-zone furnace (850W / 115V, Applied Test Systems Series 3210). Temperature was controlled using a thermocouple (Omega, model TJ36-CASS-18U) mounted slightly downstream of the catalyst bed connected to a temperature controller (Digi-Sense model 68900-10). 2.0 g of zeolite particles (pelletized and sieved into 500–1000 μm particles) were packed between quartz wool plugs and rested on the thermocouple in the middle of the furnace heating zone. The flow of gases, including He (ultra high purity, Airgas), O₂ (ultra high purity, Airgas), 1% O₂ in N₂ (ultra high purity, Airgas), and CH₄ (research grade, Airgas) were controlled with independent mass flow controllers (Brooks Instruments LLC). H₂O (typically 3.2 kPa) was introduced into the gas stream using saturator maintained at 298 K. O₂ partial pressure entering the catalyst bed was monitored with an O₂ sensor (3000-G-115BTP, Omega Instruments) placed at the entrance of the furnace. Prior to reaction, the zeolite was usually calcined in situ under 50 mL min⁻¹ flowing O₂ for 5 h at 823 K and cooled under flowing O₂ to reaction temperature (473–498 K). Details for different pretreatment protocols are explicitly stated in the Figure captions. Upon reaching reaction temperature, the zeolite was purged under 50 mL min⁻¹ of He for 0.5 h. The gas flow was then changed to 80 mL min⁻¹ CH₄ for 0.5 h followed by 80 mL min⁻¹ of CH₄, H₂O, and O₂ (typically 98.1 kPa, 3.2 kPa, and 0.0025 kPa respectively). CH₃OH partial pressures evolved during catalytic CH₄ oxidation were quantified using a gas chromatograph (Agilent Technologies, model 6890N) equipped with an S-bond column (Restek Rt-S-bond, 30 m, 0.25 mm ID, #19770) and flame ionization detector. The oven temperature was isothermal at 373 K for 30 min.

Simulated high conversion CH₄ oxidation experiments were performed in the same reactor described above. Catalyst activation was the same as described above. Liquid reactants CH₃OH and H₂O were introduced into the gas stream via saturators maintained at 273 K and 298 K respectively. The reaction mixture of 0.70 kPa CH₃OH, 2.25 kPa H₂O, and variable O₂ partial pressure was attained by combining two gas streams at the inlet of the reactor: 1) 15 mL min⁻¹ He directed through CH₃OH contained in a saturator, and 2) 65 mL min⁻¹ total of 1% O₂ in He and/or He gas streams directed through H₂O contained in a saturator. CH₃OH, dimethyl ether, CO₂, and H₂O were monitored using a gas chromatograph (Agilent Technologies, model 6890N) equipped with thermal conductivity detector and a Carboxen 1006 PLOT column (Sigma-Aldrich, 30 m, 0.32 mm ID, #24241-U). The oven temperature profile was initially 313 K for 2 min, then ramped 10 K min⁻¹ to 393 K, and then isothermal for 15 min.

Product quantification. Calibration curves for CH₃OH were constructed using a known vapor pressure of CH₃OH taken into a CH₄ stream. CH₃OH vapor pressure was controlled by immersing the saturator containing CH₃OH into cooling baths at several temperatures (e.g. ice water at 273 K, dry ice in ethanol at 201 K, etc). Relative response factors were calculated using the gas chromatograph between known CH₄ and CH₃OH partial pressures. Calibration curves for CO₂ were constructed by flowing known mixtures of 1% CO₂/helium and helium to a gas chromatograph-mass spectrometer.

The following definitions were used to quantify experimental data:

The large partial pressure of CH₄ in the gas stream during catalytic CH₄ oxidation reactions prevented the accurate quantification of CH₄ consumption. As such, CH₄ conversion was assumed to be equal to the total molar flow rate of carbon of all observed products divided by the initial molar flow rate of CH₄:

$$X_{CH_4} = \frac{\sum_{i=1}^N C_i F_i}{F_{CH_4,0}}$$

where X_{CH_4} is the conversion of CH₄, F_i is the molar flow rate of product i , C_i is the number of carbon atoms in product i , $\sum C_i F_i$ is the total molar flow rate of carbon of all products, and $F_{CH_4,0}$ is the initial molar flow rate of CH₄.

As explained above, the amount of CH₄ consumed was not quantifiable. Thus, product selectivity for catalytic CH₄ oxidation was defined as:

$$S_i = \frac{C_i F_i}{\sum_{i=1}^N C_i F_i}$$

where S_i is the selectivity of product i , C_i is the number of carbon atoms in product i , F_i is the molar flow rate of product i , and $\Sigma C_i F_i$ is the total molar flow rate of carbon of all products.

For CH₃OH oxidation experiments, CH₃OH conversion was defined as:

$$X_{\text{CH}_3\text{OH}} = 1 - \frac{F_{\text{CH}_3\text{OH}}}{F_{\text{CH}_3\text{OH},0}}$$

where $X_{\text{CH}_3\text{OH}}$ is the conversion of CH₃OH, $F_{\text{CH}_3\text{OH}}$ is the molar flow rate of CH₃OH at steady state, and $F_{\text{CH}_3\text{OH},0}$ is the initial molar flow rate of CH₃OH.

Product selectivity was defined as:

$$S_i = \frac{C_i F_i}{F_{\text{CH}_3\text{OH},0} - F_{\text{CH}_3\text{OH}}}$$

where S_i is the product selectivity, C_i is the carbon number for product i , F_i is the molar flow rate of product i , and $F_{\text{CH}_3\text{OH},0} - F_{\text{CH}_3\text{OH}}$ is the molar flow rate of CH₃OH reacted at steady state.

Product yield was defined as:

$$Y_i = \frac{C_i F_i}{F_{\text{CH}_3\text{OH},0}}$$

where Y_i was the yield for product i , F_i is the steady state molar flow rate of product i , C_i is the number of carbon atoms in product i , and $F_{\text{CH}_3\text{OH},0}$ is the initial molar flow rate of CH₃OH.

Transient experiments with isotopically labelled molecules. The isotopically labeled experiments were performed in the reactor setup described in the introduction to the Catalytic CH₄ oxidation reactions subsection. ¹³C-methoxy species were deposited on the zeolite surface by exposing a freshly activated zeolite to 50 mL min⁻¹ of 17% ¹³CH₄/He (using ¹³CH₄ [99 atom % ¹³C, Sigma Aldrich]) for 0.5 h. ¹³C-methoxy species were extracted with a mixture of ¹²CH₄/H₂O/O₂ (98.1/3.2/0.0025 kPa). ¹³CH₄ pulses were introduced by flowing a 3.2 kPa H₂O, 0.0025 kPa O₂, and balance ¹³CH₄ gas mixture at a flow rate of 10 mL min⁻¹ for 0.5 h before resuming a flow of 3.2 kPa H₂O, 0.0025 kPa O₂, and ¹²CH₄ balance. CH₃OH and CO₂ isotopes were analyzed using a gas chromatograph (Agilent Technologies, model 7890N) equipped with a quadrupole mass spectrometer and an S-bond column (Restek Rt-S-bond, 30 m, 0.25 mm ID, #19770). The oven temperature

profile was isothermal at 373 K for 30 min. $^{13}\text{CO}_2$ was tracked with $m/z = 45$. $^{13}\text{CH}_3\text{OH}$ was monitored using $m/z = 33$ instead of 32 because of small O_2 leaks into the gas chromatograph-mass spectrometer. O_2 leaks elevated the $m/z = 32$ signal and prevented the detection of trace $^{13}\text{CH}_3\text{OH}$ signals relative to background O_2 . However, $m/z = 33$ did not interfere with O_2 .

3.5 Supporting Figures and Tables

Section S1: Product Identification for CH₄ Oxidation over Cu-Na-ZSM-5 (Cu/Al = 0.37)

Cu-Na-ZSM-5 was activated under oxygen (O₂) for 5 h at 823 K, cooled to reaction temperature at 483 K under flowing O₂, and then purged under helium (He) for 1 h. After reaction with methane (CH₄) for 0.5 h, an extraction gas of 3.2 kPa of water (H₂O), 0.0025 kPa O₂ and CH₄ balance was flowed over the Cu-Na-ZSM-5 bed. A steady state methanol (CH₃OH) rate of 0.88 μmol h⁻¹ g_{cat}⁻¹ was achieved after 10 h on-stream (Figure 3-1). A condenser was placed in-line downstream from the catalyst bed. Next, the gas stream containing CH₄/H₂O/O₂ and the oxidation products was passed through the condenser maintained at 201 K in a dry ice-ethanol bath. After 6 h on-stream, the frozen products were thawed in D₂O, removed from the in-line condenser, and injected into a quartz nuclear magnetic resonance (NMR) tube (528-PP-7, Wilmad LabGlass) for analysis. ¹H-NMR performed on the condensate in a 500 MHz spectrometer (Varian Inova-500) showed CH₃OH as the only product (Figure S3-4). Gas phase products of the reactor effluent were analyzed using a gas chromatograph equipped with a quadrupole mass spectrometer (Agilent 7890N). The only gas phase product from the reaction was carbon dioxide (CO₂). Assuming CO₂ and CH₃OH were the only reaction products, the steady state CH₄ conversion was 0.0014% and the CH₃OH selectivity was 70.6% (Figure S3-5).

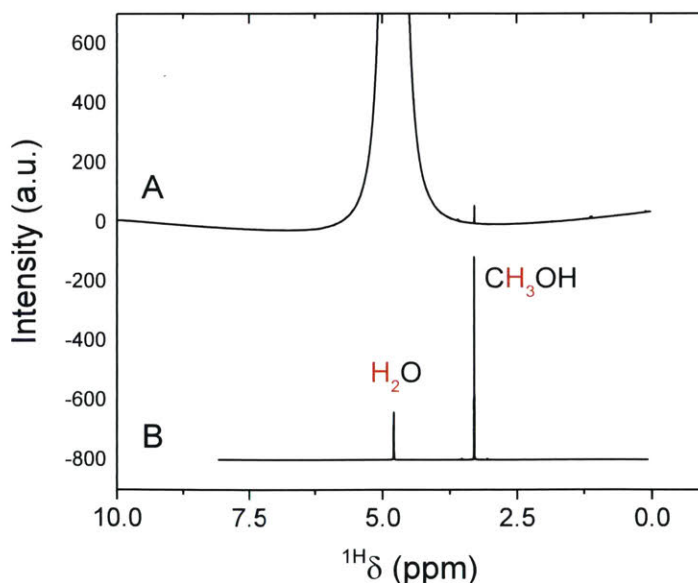


Figure S3-4. ¹H-NMR spectrum of liquid oxygenated products from CH₄ oxidation over Cu-Na-ZSM-5 (Cu/Al = 0.37) collected in a dry ice/ethanol cold trap.

(A) ¹H-NMR of liquid products from steady state CH₄ oxidation over Cu-Na-ZSM-5 (Cu/Al = 0.37, Na/Al = 0.26) condensed in a condenser immersed in a dry ice-ethanol bath after 6 h on-stream. (B) ¹H-NMR of a CH₃OH standard in D₂O. Reprinted with permission from [183].

Copyright 2016 American Chemical Society.

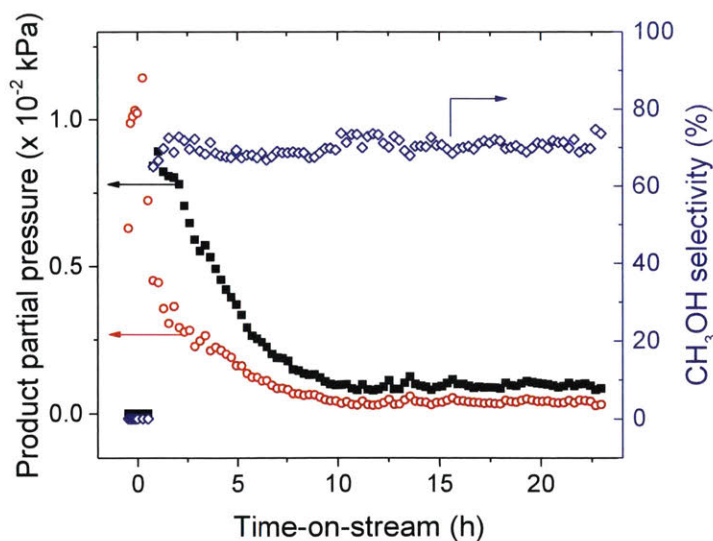


Figure S3-5. Selectivity and product partial pressures for CH₄ oxidation over Cu-Na-ZSM-5 (Cu/Al = 0.37, Na/Al = 0.26). Catalyst pretreatment: 5 h at 823 K under flowing O₂, cooled to 483 K under O₂ flow and then purged under He for 0.5 h. Initial CH₄ oxidation: 0.5 h under 2400 mL h⁻¹ g_{cat}⁻¹ of CH₄ at 483 K. Reaction conditions: T = 483 K, WHSV = 2400 mL h⁻¹ g_{cat}⁻¹, P_{CH₄} = 98.1 kPa, P_{H₂O} = 3.2 kPa, P_{O₂} = 0.0025 kPa (25 ppm). (▪) CH₃OH partial pressure (kPa). (○) CO₂ partial pressure (kPa). (◇) CH₃OH selectivity. Reprinted with permission from [183]. Copyright 2016 American Chemical Society.

Section S2: Simulation of High Conversion CH₄ Oxidation via CH₃OH Oxidation over Cu-Na-ZSM-5 (Cu/Al = 0.37)

The over-oxidation of CH₃OH into CO₂ at higher CH₄ conversion levels was simulated by introducing CH₃OH as a reactant. The direct oxidation of CH₄ into CH₃OH over copper-exchanged ZSM-5 under regular conditions generated a conversion of 0.0014 %. At these conditions, the low O₂ partial pressure (0.0025 kPa) was sufficient to convert CH₄ into CH₃OH (4.5 × 10⁻⁴ kPa O₂ is needed to produce CH₃OH at a rate of 0.88 μmol h⁻¹ g_{cat}⁻¹), but it was observed that the excess O₂ further oxidized CH₃OH into CO₂ at 483 K (30% selectivity to CO₂). Therefore, since higher conversion of CH₄ (e.g. 1%) will require more O₂ in the reaction mixture, the excess O₂ at this scale could also over-oxidize CH₃OH into CO₂ decreasing the overall selectivity of the process.

To evaluate CO₂ selectivity at higher CH₄ conversions, CH₃OH was used as a reactant to simulate the gas composition the Cu-Na-ZSM-5 (Cu/Al = 0.37) catalyst bed would encounter at 100% CH₄ conversion. After activating Cu-Na-ZSM-5 for 5 h at 823 K under O₂, the zeolite bed was cooled to 483 K and purged under He for 1 h. Then a reaction mixture of 0.70 kPa CH₃OH, variable O₂ partial pressure, 2.25 kPa H₂O and He was passed over the catalyst bed. Flowing this reaction mixture over Cu-Na-ZSM-5 and

measuring the extent of CO₂ production can be used as a surrogate to calculate the maximum CO₂ selectivity. A 0.70 kPa partial pressure of CH₃OH simulated a CH₄ partial pressure of 0.70 kPa being fully converted into CH₃OH. The O₂ partial pressure was varied to represent unreacted or excess O₂ from a typical CH₄ oxidation experiment. Helium (He) was used instead of CH₄ in the gas mixture to isolate CH₃OH oxidation and exclude the coadsorption of CH₄ on the zeolite surface. The gas mixture composed of 0.70 kPa CH₃OH, 2.25 kPa H₂O, and O₂ was flowed over the Cu-Na-ZSM-5 catalyst for 5 h at 483 K before the steady state gas composition was analyzed in order to allow for changes in copper speciation that occur in regular CH₄ oxidation experiments (Figure 3-3, Figure S3-14). As the O₂ partial pressure was increased from 0.21 kPa to 2.70 kPa, the CO₂ yield increased from 6.8% to 24% (Figure S3-6A). The rate order of O₂ in CH₃OH oxidation was ca. 0.50 (Figure S3-6B). As expected, lower amounts of O₂ relative to CH₃OH (lower O₂/CH₃OH partial pressure ratio) suppress the formation of CO₂. However, even having up to 4 times the partial pressure of O₂ as CH₃OH only generated a 24% yield and 25% selectivity of CO₂, which was a lower CO₂ selectivity than that observed during regular CH₄ oxidation experiments over Cu-Na-ZSM-5 at similar conditions (Figure S3-5, P_{O2}/P_{CH3OH} = 2.5). Therefore, these results suggest that CH₄ oxidation to higher conversions will not result in a substantial increase in CO₂ production or a decrease in CH₃OH selectivity at 483 K.

CO₂ selectivity could be further reduced by lowering the temperature of the simulated gas mixture over Cu-Na-ZSM-5. As the reaction temperature was lowered to 463 K, the CO₂ yield and selectivity decreased from 24% to 7.4% (Figure S3-7). These data show that CH₃OH selectivity could increase beyond 70% by lowering the reaction temperature (< 483 K) in a high conversion CH₄ oxidation process.

CH₃OH conversion was greater than 90% for the simulated, high conversion CH₄ oxidation experiments (Figure S3-6A) where the vast majority of CH₃OH was converted into dimethyl ether (DME) (> 60% yield). DME is produced from the acid-catalyzed dehydration of CH₃OH.¹⁸⁹ Brønsted acid sites in zeolites are well known to perform this reaction between 473 and 573 K.^{157, 190} However, zeolites can still produce DME even with trace Brønsted acidity,¹⁹¹ such as that present in sodium-exchanged ZSM-5.¹⁹² CH₃OH dehydration is thermodynamically favorable under the CH₃OH oxidation reaction conditions of 483 K, 0.70 kPa CH₃OH, and 2.25 kPa H₂O. The reaction $2 \text{CH}_3\text{OH} \leftrightarrow (\text{CH}_3)_2\text{O} + \text{H}_2\text{O}$ has a chemical equilibrium constant (K_{eq}) of 14.8 under these reaction conditions, and the equilibrium conversion of CH₃OH to DME would be 92%.

In the simulated, high conversion CH_4 oxidation experiments, the DME yield decreased from 80% to 62% as the O_2 partial pressure increased from 0.21 kPa to 2.7 kPa (Figure S3-6A), consistent with CH_3OH or DME being oxidized into CO_2 . At a lower temperature of 463 K, the DME yield increased from 62% to 74% (Figure S3-7).

DME was not observed in typical CH_4 oxidation experiments over Cu-Na-ZSM-5 due to the low equilibrium conversion of CH_3OH into DME. At steady state, taking the CH_3OH partial pressure to be 10^{-3} kPa and the H_2O partial pressure to be 3.2 kPa, the equilibrium conversion of CH_3OH into DME at 483 K would be 0.90%. The theoretical maximum amount of DME that could be produced was below the detection limit of the gas chromatograph used to quantify steady state rates.

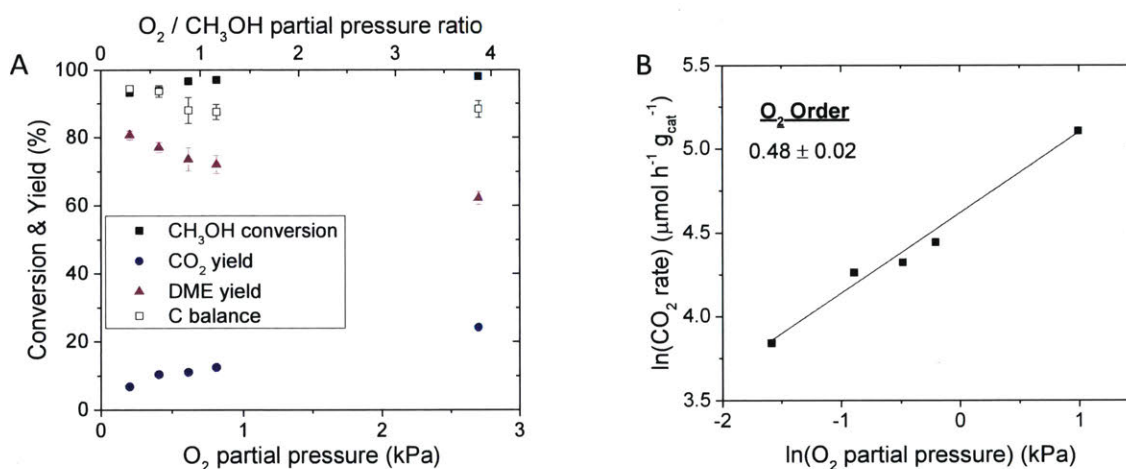


Figure S3-6. Simulation of high conversion CH_4 oxidation over Cu-Na-ZSM-5 versus O_2 partial pressure. (A) CH_3OH oxidation as a function of O_2 partial pressure and (B) order of O_2 for CH_3OH oxidation over Cu-Na-ZSM-5 (Cu/Al = 0.37, Na/Al = 0.26). (A) Pretreatment: 5 h at 823 K under O_2 , cooled under O_2 flow to 483 K and then purged 0.5 h under He. Reaction conditions: $T = 483$ K, $\text{WHSV} = 2400 \text{ mL h}^{-1} \text{g}_{\text{cat}}^{-1}$, $P_{\text{CH}_3\text{OH}} = 0.70$ kPa, $P_{\text{H}_2\text{O}} = 2.25$ kPa, He balance. (B) Same conditions as (A). Error bars and ffi denote 95% confidence intervals. Reprinted with permission from [183]. Copyright 2016 American Chemical Society.

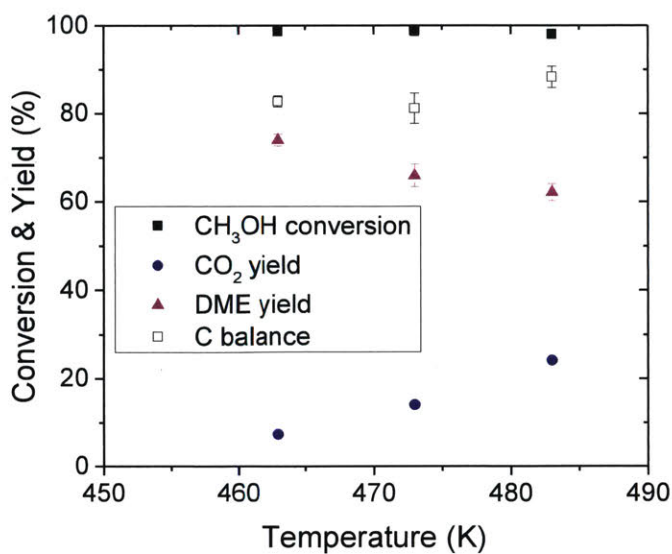


Figure S3-7. Simulation of high conversion CH₄ oxidation over Cu-Na-ZSM-5 versus reaction temperature. Pretreatment: 5 h at 823 K under O₂, cooled under O₂ flow to 483 K and purged 0.5 h under He. Reaction conditions: WHSV = 2400 mL h⁻¹ g_{cat}⁻¹, P_{CH₃OH} = 0.70 kPa, P_{H₂O} = 2.25 kPa, P_{O₂} = 2.70 kPa, He balance. Error bars denote 95% confidence intervals. Reprinted with permission from [183]. Copyright 2016 American Chemical Society.

Section S3: Steady-state CH₃OH Production over Cu-H-ZSM-5 (Cu/Al = 0.31)

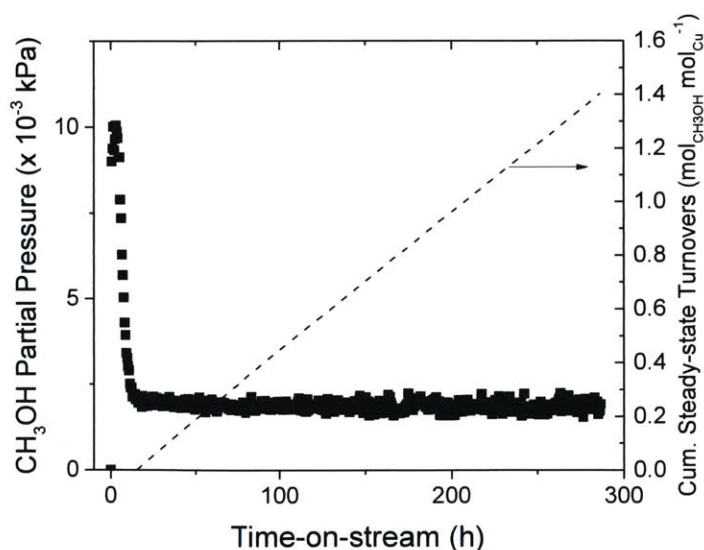


Figure S3-8. CH₄ oxidation over Cu-H-ZSM-5 (Cu/Al = 0.31). Catalyst pretreatment: 5 h at 823 K under flowing O₂, cooled to 483 K under O₂ flow and then purged under He for 0.5 h. Initial CH₄ oxidation: 0.5 h under 2400 mL h⁻¹ g_{cat}⁻¹ of CH₄ at 483 K. Reaction conditions: T = 483 K, WHSV = 2400 mL h⁻¹ g_{cat}⁻¹, P_{CH₄} = 98.1 kPa, P_{H₂O} = 3.2 kPa, P_{O₂} = 0.0025 kPa (25 ppm). Dashed line denotes cumulative turnovers collected at steady-state. Reprinted with permission from [183]. Copyright 2016 American Chemical Society.

Section S4: ^{13}C -Isotopically Labeled Control Experiments over Cu-Na-ZSM-5 (Cu/Al = 0.37)

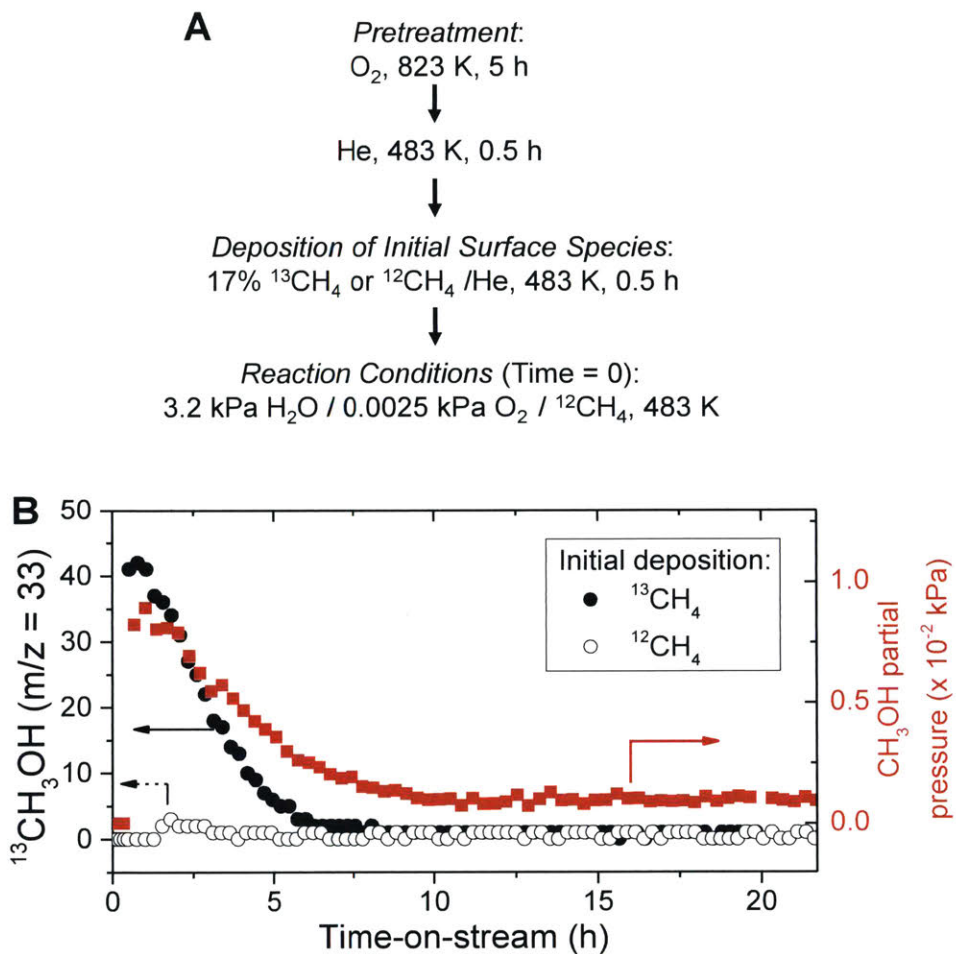


Figure S3-9. Isotopically labeled kinetic experiments over Cu-Na-ZSM-5 (Cu/Al = 0.37, Na/Al = 0.26). (A) Experimental pretreatment protocols used for the initial deposition of surface species on Cu-Na-ZSM-5 with $^{13}\text{CH}_4$ or $^{12}\text{CH}_4$. (B) Extraction of CH_3OH from the Cu-Na-ZSM-5 surface initially deposited by $^{13}\text{CH}_4$ (●) or $^{12}\text{CH}_4$ (○). Reaction conditions: $T = 483$ K, $\text{WHSV} = 2400$ $\text{mL h}^{-1} \text{g}_{\text{cat}}^{-1}$, $P_{^{12}\text{CH}_4} = 98.1$ kPa, $P_{\text{H}_2\text{O}} = 3.2$ kPa, $P_{\text{O}_2} = 0.0025$ kPa (25 ppm). Reprinted with permission from [183]. Copyright 2016 American Chemical Society.

Section S5: $^{13}\text{CO}_2$ Production during Transient, Isotopically Labeled Experiments over Cu-Na-ZSM-5 (Cu/Al = 0.37)

^{13}C methoxy species were deposited on the zeolite by flowing $^{13}\text{CH}_4$ (16.8 kPa $^{13}\text{CH}_4$ [99 atom% ^{13}C , Sigma-Aldrich] with balance He) over activated Cu-Na-ZSM-5 for 0.5 h at 483 K and then using a regular $^{12}\text{CH}_4/\text{H}_2\text{O}/\text{O}_2$ gas mixture to evolve oxidation products from the zeolite. As shown in Figure S3-10A, enriched $^{13}\text{CO}_2$ ($m/z = 45$) is quickly produced in the stoichiometric regime, but unlabeled $^{12}\text{CO}_2$ is observed in the steady state regime, thus suggesting unlabeled ^{12}C surface species are oxidized into $^{12}\text{CO}_2$ once the ^{13}C species are depleted. The reaction rate remained at steady state (rate = $0.88 \mu\text{mol}_{\text{CH}_3\text{OH}} \text{h}^{-1} \text{g}_{\text{cat}}^{-1}$) for 21 h at a weight hourly space velocity (WHSV) of $2400 \text{ mL h}^{-1} \text{g}_{\text{cat}}^{-1}$ (equivalent to the production of $18.5 \mu\text{mol g}_{\text{cat}}^{-1}$ of $^{12}\text{CH}_3\text{OH}$). Next, the gas mixture was switched to $^{13}\text{CH}_4/\text{H}_2\text{O}/\text{O}_2$ for 0.5 h at a WHSV = $300 \text{ mL h}^{-1} \text{g}_{\text{cat}}^{-1}$ before resuming the flow of the regular, unlabeled mixture. This $^{13}\text{CH}_4$ pulse resulted in the production of $^{13}\text{CO}_2$ during steady state CH_3OH production as evidenced by the pulse of $m/z = 45$ signal in Figure S3-10A. Control experiments using $^{12}\text{CH}_4$ to populate the activated catalyst with unlabeled ^{12}C methoxy species did not generate a significant amount of $^{13}\text{CO}_2$ in the stoichiometric or steady state regimes (Figure S3-10C).

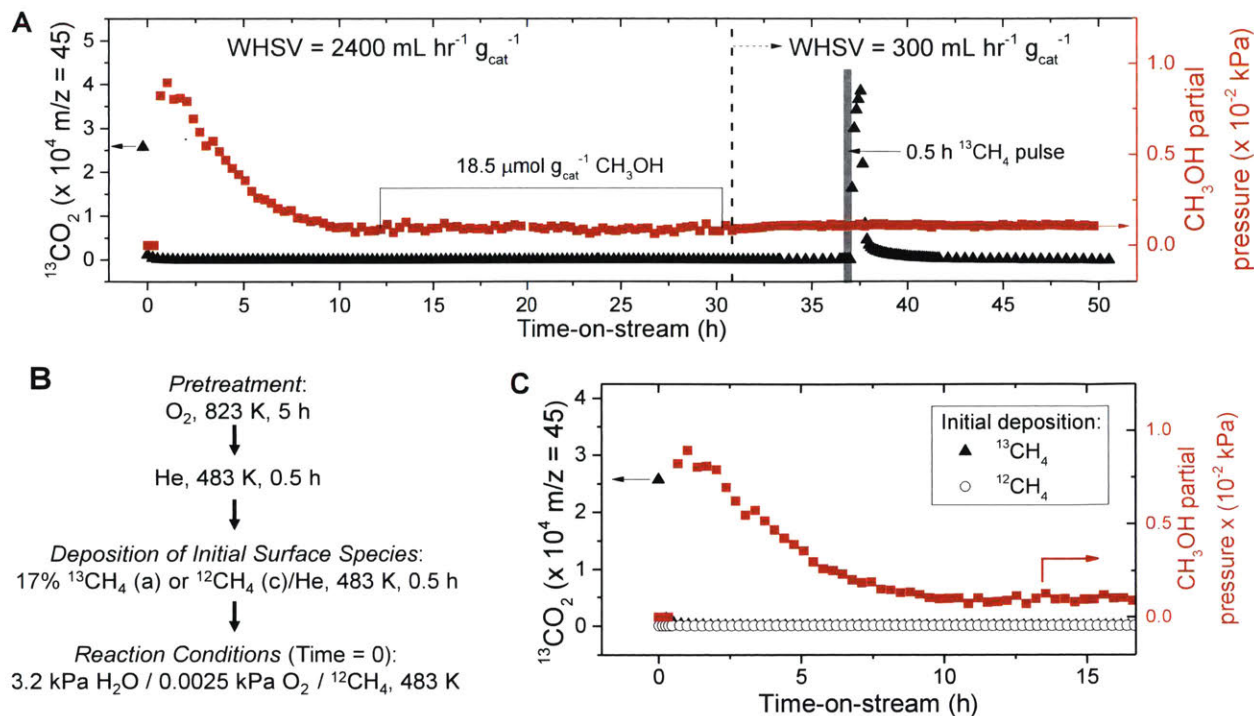


Figure S3-10. Transient, isotopically labeled kinetic experiments over Cu-Na-ZSM-5 (Cu/Al = 0.37, Na/Al = 0.26). (A) ¹³CO₂ production from initial deposition of ¹³CH₄ on Cu-Na-ZSM-5 surface and transient, pulsed ¹³CH₄. (B) Experimental pretreatments for panels (A) and (C). (C) Comparison of ¹³CO₂ production using ¹³CH₄ or ¹²CH₄ after activation of Cu-Na-ZSM-5. (A) Reaction conditions: T = 483 K, WHSV = 2400 mL h⁻¹ g_{cat}⁻¹, P_{12CH₄} = 98.1 kPa, P_{H₂O} = 3.2 kPa, P_{O₂} = 0.0025 kPa (25 ppm). After 31 h on-stream, WHSV was reduced to 300 mL h⁻¹ g_{cat}⁻¹. Gray area denotes 0.5 h pulse of P_{13CH₄} = 98 kPa, P_{H₂O} = 3.2 kPa, P_{O₂} = 0.0025 kPa. (▲) ¹³CO₂ evolution and (■) CH₃OH partial pressure (kPa). (C) Reaction conditions: T = 483 K, WHSV = 2400 mL h⁻¹ g_{cat}⁻¹, P_{12CH₄} = 98.1 kPa, P_{H₂O} = 3.2 kPa, P_{O₂} = 0.0025 kPa. Initial deposition of surface species used either 17% ¹³CH₄ (▲) or ¹²CH₄ (○) in He at 483 K. Reprinted with permission from [183]. Copyright 2016 American Chemical Society.

Section S6: Transient, Isotopically Labeled Kinetic Experiments over Cu-Na-ZSM-5 (Cu/Al = 0.37)

Catalytic turnover was also verified over Cu-H-ZSM-5 (Cu/Al = 0.31) using similar experimental procedures as outlined in Figure S3-9A. When an activated Cu-H-ZSM-5 was reacted with ¹³CH₄ before extraction (Figure S3-11A), a large pulse of ¹³CH₃OH was observed in the stoichiometric regime. However, as CH₃OH production approached steady state, ¹³CH₃OH production declined and resulted in the production of exclusively ¹²CH₃OH (Figure S3-11B). However, virtually no ¹³CH₃OH was extracted from the zeolite when ¹²CH₄ was used for the initial reaction. These experiments show that the source carbon for CH₃OH produced at steady state must come from gas phase ¹²CH₄, thereby indicating turnover on the Cu-H-ZSM-5 surface.

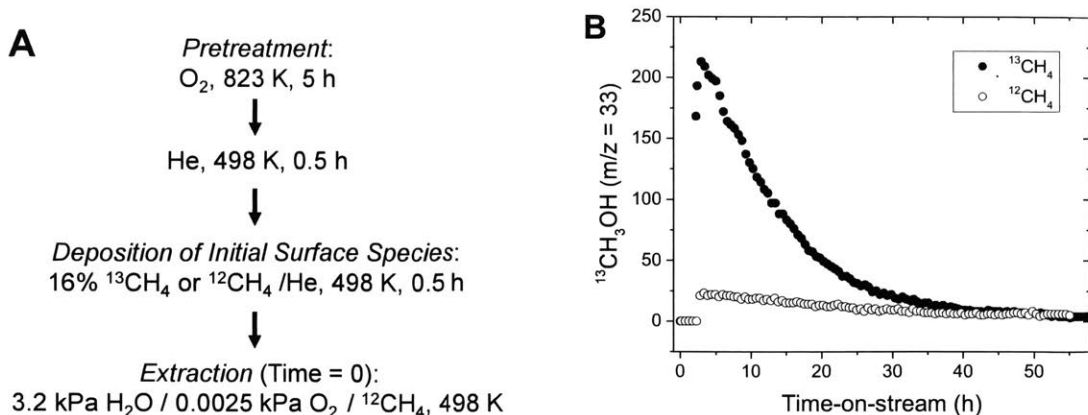


Figure S3-11. Isotopically labeled studies over Cu-H-ZSM-5 (Cu/Al = 0.31). (A) Experimental pretreatments for panel (B). (B) Extraction of ¹³CH₃OH from Cu-H-ZSM-5 surface initially deposited by ¹³CH₄ (●) or ¹²CH₄ (○). Reaction conditions: T = 498 K, WHSV = 300 mL h⁻¹ g_{cat}⁻¹, P_{12CH₄} = 98.1 kPa, P_{H₂O} = 3.2 kPa, P_{O₂} = 0.0025 kPa (25 ppm). Reprinted with permission from [183]. Copyright 2016 American Chemical Society.

Section S7: Kinetic Order Dependence of Reactants and Transient, Isotopic Pulsing of CD₄ over Cu-Na-ZSM-5 (Cu/Al = 0.37)

The partial pressure of O₂ was varied over Cu-Na-ZSM-5 (Cu/Al = 0.37, Na/Al = 0.26) to deduce the order of O₂ on catalytic CH₄ oxidation activity. After activating the zeolite under O₂ at 823 K for 5 h, Cu-Na-ZSM-5 was cooled to 483 K under O₂ flow, purged under He, and reacted under dry 75% CH₄/He at 483 K for 0.5 h. Afterwards, 3.2 kPa H₂O and O₂ were then introduced into the reactant stream. The O₂ partial pressure was controlled using a 1% O₂/N₂ gas stream co-fed with He while maintaining CH₄ and H₂O partial pressures at 72.5 kPa and 3.2 kPa respectively. As the partial pressure of O₂ decreased, the observed catalytic CH₃OH production rate remained fairly constant, showing the rate was zero order with respect to O₂ (Figure S3-12A).

The catalytic CH₃OH production rate demonstrated positive kinetic orders with respect to CH₄ and H₂O partial pressures. The rate dependence of CH₄ was investigated by varying CH₄ partial pressure from 49 to 98 kPa while maintaining H₂O and O₂ partial pressures constant at 3.2 kPa and 0.0025 kPa respectively. The catalytic rate of CH₃OH production exhibited a first order dependence on CH₄ partial pressure (Figure S3-12B), indicating the dilution of CH₄ in the reaction feed is undesired. Similarly, H₂O increased the production of CH₃OH from Cu-Na-ZSM-5. H₂O vapor pressure was controlled between 1.1 to 3.2 kPa using aqueous CaCl₂ solutions in a saturator maintained at 298 K. The CH₄ and O₂ partial pressures were kept constant at 98 and 0.0025 kPa respectively. CH₃OH production decreased as the H₂O partial pressure decreased (Figure S3-12C) by

order of 0.5. As expected, when no H₂O was delivered to the catalyst, no CH₃OH was detected, indicating that H₂O was necessary for CH₃OH extraction.

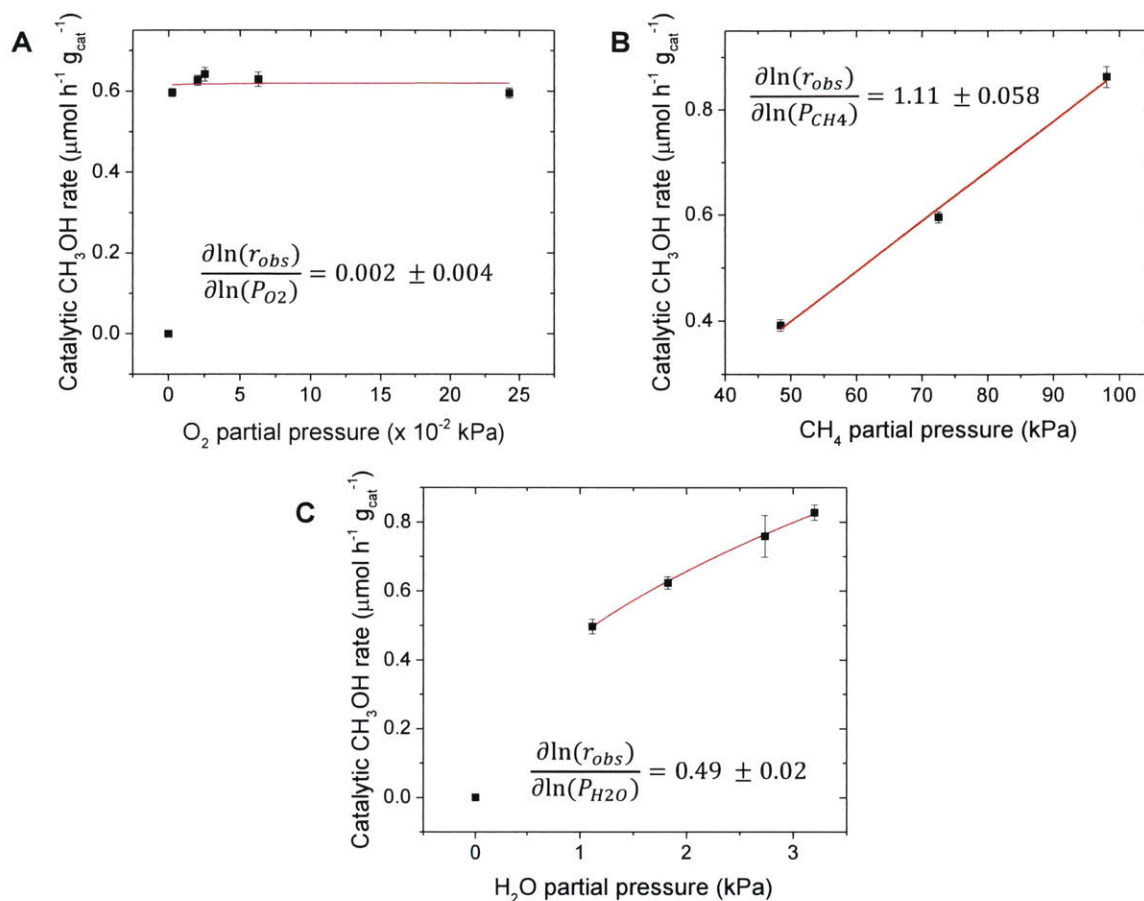


Figure S3-12. Kinetic order of reactants for catalytic CH₄ oxidation over Cu-Na-ZSM-5 (Cu/Al = 0.37). The effect of (A) O₂ partial pressure, (B) CH₄ partial pressure, and (C) H₂O partial pressure on CH₄ oxidation over Cu-Na-ZSM-5. Catalyst pretreatment: 5 h at 823 K under flowing O₂, cooled to 483 K under O₂ flow and then purged under He for 0.5 h. Initial CH₄ oxidation: 0.5 h under 2400 mL h⁻¹ g_{cat}⁻¹ CH₄. Reaction conditions: (A) T = 483 K, WHSV = 2400 mL h⁻¹ g_{cat}⁻¹, P_{CH₄} = 72.5 kPa, P_{H₂O} = 3.2 kPa, He balance. (B) T = 483 K, WHSV = 2400 mL h⁻¹ g_{cat}⁻¹, P_{H₂O} = 3.2 kPa, P_{O₂} = 0.0025 kPa (25 ppm), P_{He} balance. (C) T = 483 K, WHSV = 2400 mL h⁻¹ g_{cat}⁻¹, P_{CH₄} = 98.1 kPa, P_{O₂} = 0.0025 kPa (25 ppm), P_{H₂O} controlled via saturator filled with aqueous CaCl₂ solutions, P_{He} = balance. Error bars and \pm denote 95% confidence intervals. Reprinted with permission from [183]. Copyright 2016 American Chemical Society.

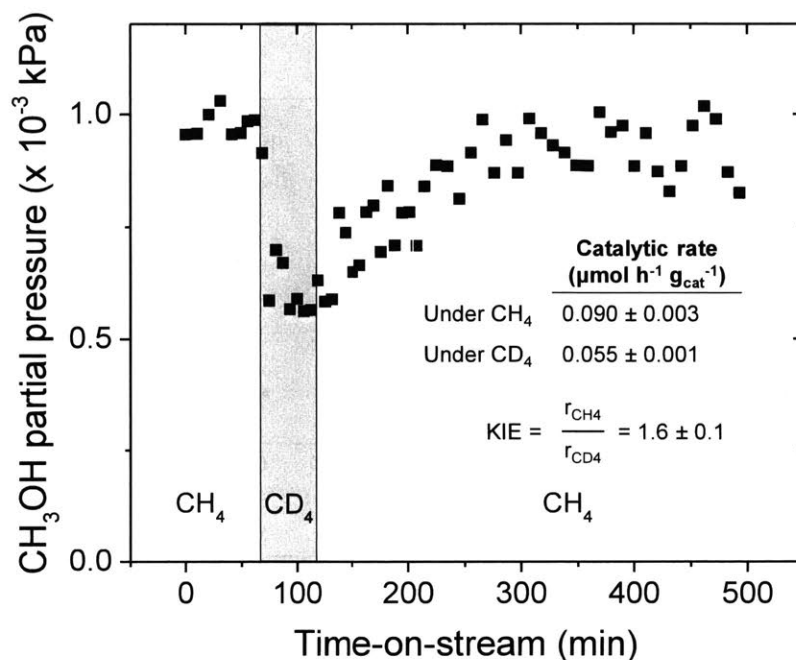


Figure S3-13. Transient, isotopically labeled CD_4 pulse over Cu-Na-ZSM-5 (Cu/Al = 0.37, Na/Al = 0.26). Catalyst pretreatment: 5 h at 823 K under flowing O_2 , cooled to 483 K under O_2 flow and then purged under He for 0.5 h. Initial CH_4 oxidation: 0.5 h under $240 \text{ mL h}^{-1} \text{g}_{\text{cat}}^{-1}$ CH_4 . Reaction conditions: $T = 483 \text{ K}$, $\text{WHSV} = 240 \text{ mL h}^{-1} \text{g}_{\text{cat}}^{-1}$, $P_{\text{CH}_4} = 98.1 \text{ kPa}$, $P_{\text{H}_2\text{O}} = 3.2 \text{ kPa}$, $P_{\text{O}_2} = 0.0025 \text{ kPa}$ (25 ppm). Gray area denotes 0.75 h pulse of CD_4 : $\text{WHSV} = 240 \text{ mL h}^{-1} \text{g}_{\text{cat}}^{-1}$, $P_{\text{CD}_4} = 98.1 \text{ kPa}$, $P_{\text{H}_2\text{O}} = 3.2 \text{ kPa}$, $P_{\text{O}_2} = 0.0025 \text{ kPa}$ (25 ppm). KIE = kinetic isotope effect. r_{CH_4} = catalytic CH_3OH production rate under CH_4 . r_{CD_4} = catalytic CH_3OH production rate under CD_4 . \pm denotes 95% confidence interval. Reprinted with permission from [183]. Copyright 2016 American Chemical Society.

Section S8: Thermal Pretreatments and the Onset of Catalytic Activity over Cu-Na-ZSM-5 (Cu/Al = 0.37)

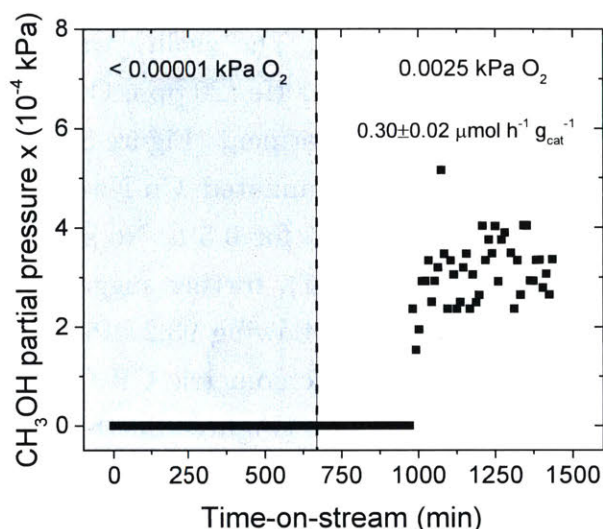


Figure S3-14. CH_4 oxidation over Cu-Na-ZSM-5 (Cu/Al = 0.37, Na/Al = 0.26) pretreated under O_2 -free conditions. Catalyst pretreatment: 5 h at 823 K under He ($< 0.00001 \text{ kPa O}_2$), cooled to 483 K under He flow. Initial CH_4 oxidation: 0.5 h under $2400 \text{ mL h}^{-1} \text{ g}_{\text{cat}}^{-1} \text{ CH}_4$. Reaction conditions: $T = 483 \text{ K}$, $\text{WHSV} = 2400 \text{ mL h}^{-1} \text{ g}_{\text{cat}}^{-1}$, $P_{\text{CH}_4} = 98.1 \text{ kPa}$, $P_{\text{H}_2\text{O}} = 3.2 \text{ kPa}$. Background colors: Gray: $P_{\text{O}_2} = < 0.00001 \text{ kPa}$ (0.1 ppm), White: $P_{\text{O}_2} = 0.0025 \text{ kPa}$ (25 ppm). O_2 levels reduced to $< 0.00001 \text{ kPa}$ using a CuO trap. \pm denotes 95% confidence interval. Reprinted with permission from [183]. Copyright 2016 American Chemical Society.

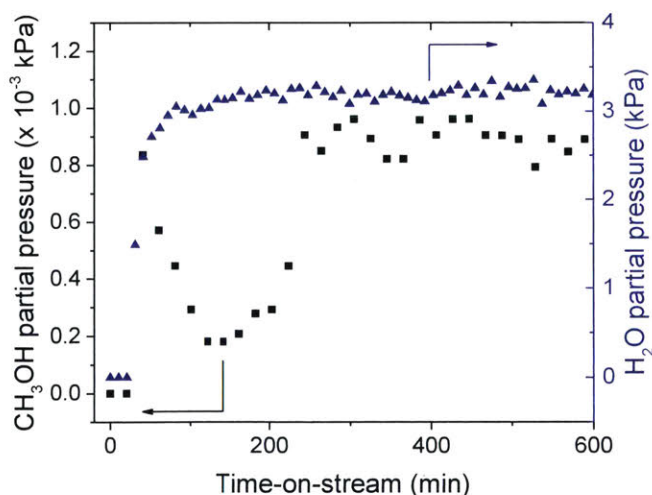


Figure S3-15. H_2O breakthrough over Cu-Na-ZSM-5 (Cu/Al = 0.37, Na/Al = 0.26) during CH_4 oxidation. (■) CH_3OH partial pressure (kPa). (▲) H_2O partial pressure (kPa). Pretreatment: ramped under O_2 , 5 h at 823 K under He (20 ppm O_2), cooled to 483 K under He. Initial CH_4 oxidation: 0.5 h under $2400 \text{ mL h}^{-1} \text{ g}_{\text{cat}}^{-1} \text{ CH}_4$. Reaction conditions: $T = 483 \text{ K}$, $\text{WHSV} = 2400 \text{ mL h}^{-1} \text{ g}_{\text{cat}}^{-1}$, $P_{\text{CH}_4} = 98.1 \text{ kPa}$, $P_{\text{H}_2\text{O}} = 3.2 \text{ kPa}$, $P_{\text{O}_2} = 0.0025 \text{ kPa}$ (25 ppm). Reprinted with permission from [183]. Copyright 2016 American Chemical Society.

Section S9: In-situ Diffuse Reflectance UV-visible Spectroscopy and Online Gas Chromatography Measurements over Cu-Na-ZSM-5 (Cu/Al = 0.37)

UV-visible spectroscopic and online gas chromatographic measurements were performed over Cu-Na-ZSM-5 (Cu/Al=0.37) to gain insight into copper speciation during pretreatments and steady-state operation. The zeolite was heated at 5 K/min under flowing O₂ to 823 K and then calcined under He (20 ppm O₂) at 823 K for 2 h. A shoulder at 22,700 cm⁻¹ decayed within 1 h of He treatment (Figure S3-16), indicating the majority of the mono-(μ-oxo) dicupric cores were eliminated. Cu-Na-ZSM-5 was then cooled to 483 K under He and then exposed to pure CH₄ for 0.5 h. No significant changes in the UV-visible spectra were observed (Figure S3-17), further suggesting the elimination of most of the mono-(μ-oxo) dicupric cores. After flowing 93.2 kPa CH₄, 0.051 kPa O₂, and 3.2 kPa H₂O at 483 K, a small amount of stoichiometric CH₃OH was extracted from zeolite before steady-state CH₃OH production (Figure S3-18A), consistent with kinetic experiments (Figure 3-3, red symbols). During stoichiometric CH₃OH production, there were no changes in the 22,700 cm⁻¹ region (Figure S3-18B.1-2). Lastly, no bands were present at 22,700 cm⁻¹ peak during steady-state CH₃OH production (Figure S3-18C.1-2, D.1-2), indicating the mono-(μ-oxo) dicupric cores are likely not present during catalytic operation.

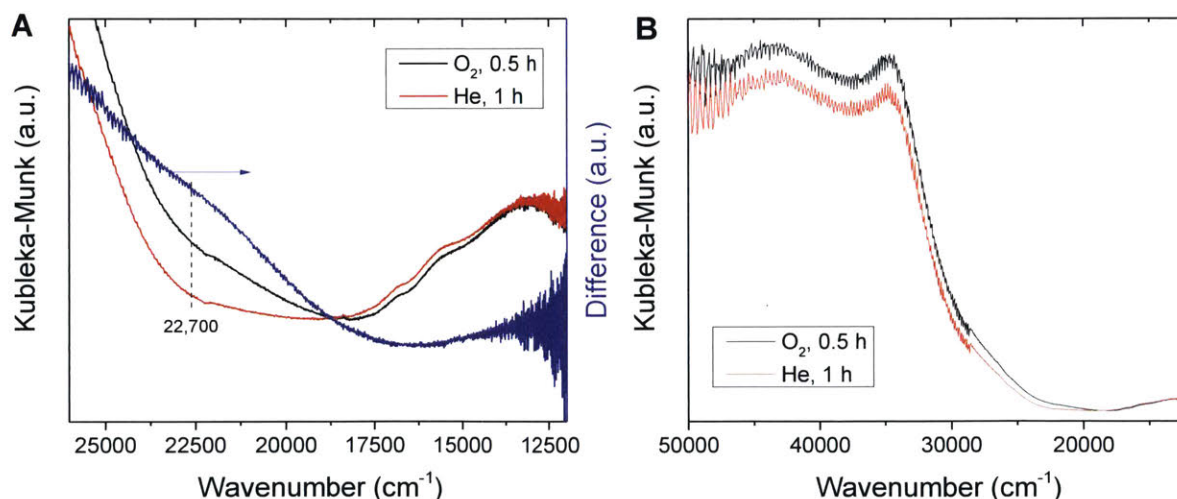


Figure S3-16. In-situ diffuse reflectance UV-visible spectra of Cu-Na-ZSM-5 (Cu/Al = 0.37) in the (A) visible region and (B) full region. Cu-Na-ZSM-5 was heated under flowing O₂ (5 K/min) to 823 K and held for 0.5 h (black) and then calcined under He (20 ppm O₂) for 2 h (red). Difference spectra (calcined in O₂—calcined in He) are shown (blue, right axis). The decay of the 22,700 cm⁻¹ band after He treatment is highlighted. Reprinted with permission from [183]. Copyright 2016 American Chemical Society.

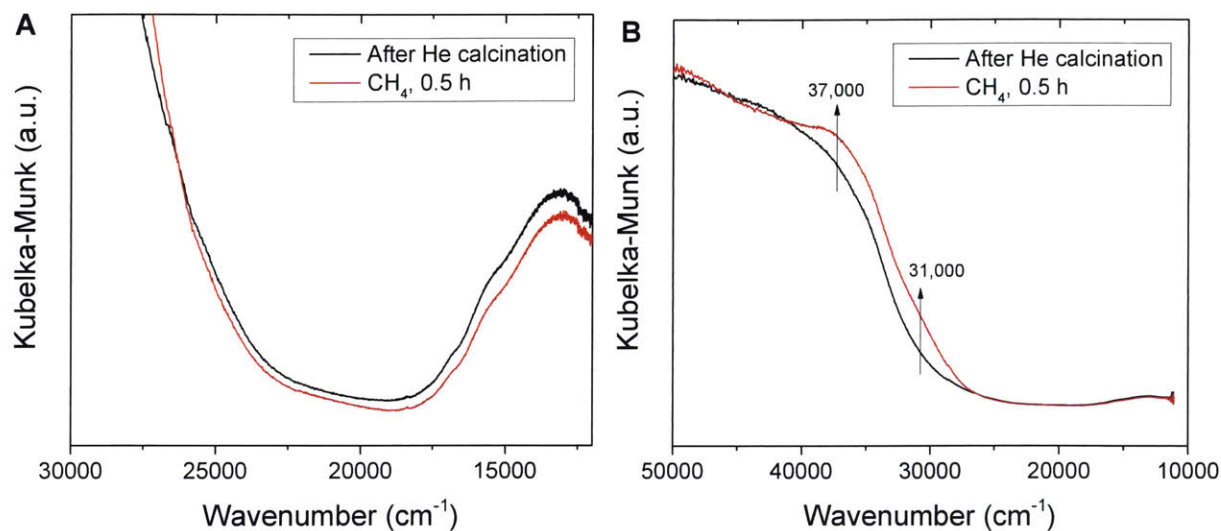


Figure S3-17. In-situ diffuse reflectance UV-visible spectra of Cu-Na-ZSM-5 (Cu/Al = 0.37) in the (A) visible region and (B) full spectra. Catalyst pretreatment: heated to 823 K under flowing O₂, calcined 2 h at 823 K under He (20 ppm O₂) and cooled to 483 K under He. The zeolite was then exposed to CH₄ for 0.5 h. No significant differences were observed in the visible region. Reprinted with permission from [183]. Copyright 2016 American Chemical Society.

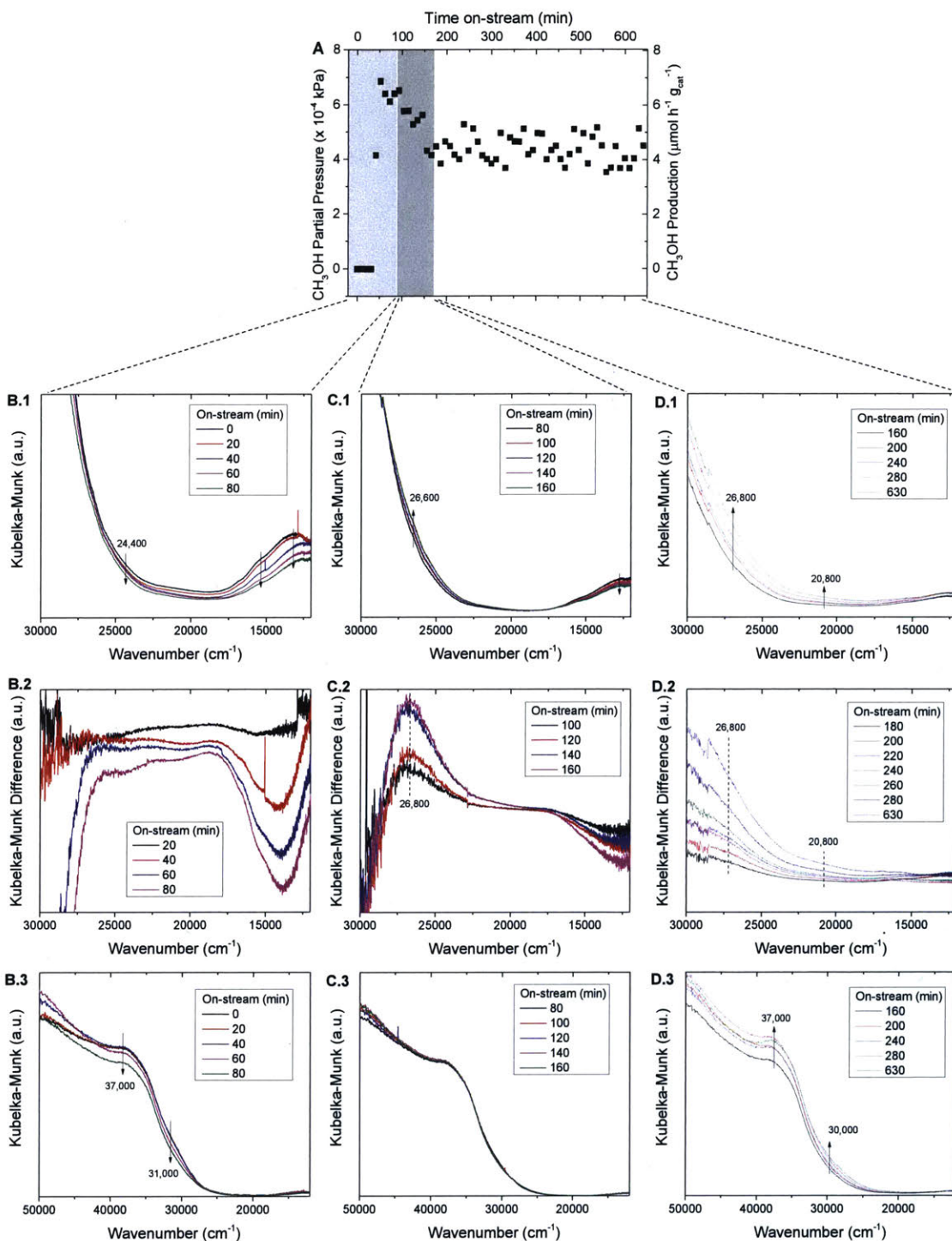


Figure S3-18. Combined in-situ diffuse reflectance UV-visible spectroscopy and online gas chromatography measurements for catalytic CH₄ oxidation over Cu-Na-ZSM-5 (Cu/Al = 0.37). Catalyst pretreatment: heating to 823 K under flowing O₂, 2 h at 823 K under He, cooled to 483 K under flowing He. Initial CH₄ oxidation: 0.5 h under 25000 mL h⁻¹ g_{cat}⁻¹ of CH₄ at 483 K. Reaction conditions: T = 483 K, WHSV = 25000 mL h⁻¹ g_{cat}⁻¹, P_{CH₄} = 93.2 kPa, P_{H₂O} = 3.2 kPa, P_{O₂} = 0.051 kPa. (A) CH₃OH production from Cu-Na-ZSM-5 measured by gas chromatography. (B.1-B.3) diffuse reflectance UV-vis spectra of the 0-80 min time on-stream interval corresponding to the onset of stoichiometric and the onset of steady-state CH₃OH production. The difference spectra in (B.2) subtracts the spectrum at 0 min from each spectrum in the 20-80 min time on-stream interval. (C.1-C.3) diffuse reflectance UV-vis spectra of the 80-160 min time on-stream interval corresponding to the end of stoichiometric and the onset of steady-state CH₃OH production. The difference spectra in (C.2) subtracts the spectrum at 80 min from each spectrum in the 100-160 min time on-stream interval. (D.1-D.3) diffuse reflectance UV-vis spectra of the 160-630 min time on-stream interval corresponding to steady-state CH₃OH production. The difference spectra in (D.2) subtracts the spectrum at 160 min from each spectrum in the 180-630 min time on-stream interval. Reprinted with permission from [183]. Copyright 2016 American Chemical Society.

Section S10: Catalytic CH₄ Oxidation over Cu-ZSM-5 and Cu-MOR Zeolites

Table S3-2. CH₄ oxidation over Cu-exchanged ZSM-5 and MOR zeolites

Material	Framework	Si/Al _a ^{nom}	Co-Cation	Si/Al _b ^{tot}	Cu/Al _c ^{tot}	Specific Activity _d	STY ^e (x 10 ⁻³ h ⁻¹)	E _a ^{app f} (kJ/mol)
ZSM-5	MFI	11.5	Na ⁺	13.1	0.17	0.51	2.7	47 ± 2
				13.6	0.37	0.88	2.2	54 ± 5
			H ⁺	13.9	0.13	0.84	6.0	88 ± 6
				14.1	0.38	1.51	3.8	80 ± 2
Mordenite	MOR	10	Na ⁺	11.4	0.14	0.30	1.8	92 ± 3
			H ⁺	11.1	0.14	0.84	4.6	149 ± 2

Catalyst pretreatment: 5 h at 823 K under flowing O₂, cooled to 483 K under O₂ flow and then purged under He for 0.5 h. Initial CH₄ oxidation: 0.5 h under 2400 mL h⁻¹ g_{cat}⁻¹ CH₄. Reaction conditions: T = 483 K, WHSV = 2400 mL h⁻¹ g_{cat}⁻¹, P_{CH₄} = 98.1 kPa, P_{H₂O} = 3.2 kPa, P_{O₂} = 0.0025 kPa (25 ppm). ± denotes 95% confidence intervals

^a nominal ratio of silicon to aluminum atoms in each zeolite based on commercial figures.

^b ratio of total silicon to aluminum atoms in each zeolite sample. Determined using inductively coupled plasma mass spectrometry (ICP-MS).

^c ratio of total copper to aluminum atoms in each zeolite sample. Determined using ICP-MS.

^d specific activity is defined as μmol_{CH₃OH} h⁻¹ g_{cat}⁻¹.

^e Site-time yield (STY) is defined as mol CH₃OH (mol Cu)⁻¹ h⁻¹.

^f E_a^{app} is defined as apparent activation energy (kJ/mol).

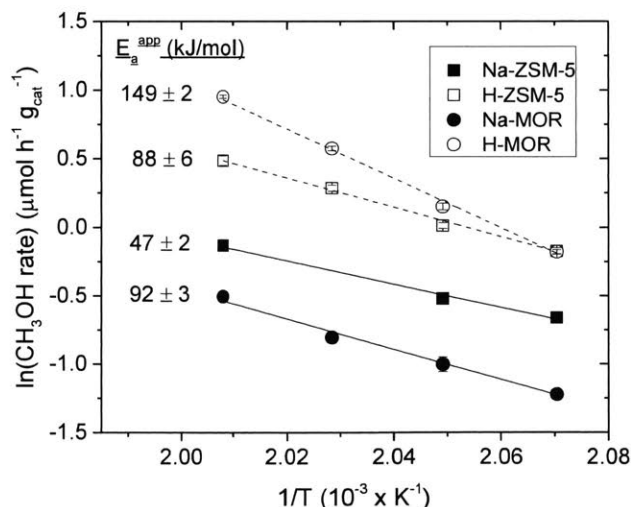


Figure S3-19. Arrhenius plot of catalytic CH₄ oxidation over Cu-ZSM-5 and Cu-MOR zeolites.

Open symbols: zeolites with Brønsted acid sites (ZSM-5 had Cu/Al = 0.13, MOR had Cu/Al = 0.14). Closed symbols: zeolites with sodium as counter ions (ZSM-5 had Cu/Al = 0.17, MOR had Cu/Al = 0.14). Catalyst pretreatment: 5 h at 823 K under flowing O₂, cooled to 483 K under O₂ flow and then purged under He for 0.5 h. Initial CH₄ oxidation: 0.5 h under 2400 mL h⁻¹ g_{cat}⁻¹ CH₄. Reaction conditions: T = 483 K, WHSV = 2400 mL h⁻¹ g_{cat}⁻¹, P_{CH₄} = 98.1 kPa, P_{H₂O} = 3.2 kPa, P_{O₂} = 0.0025 kPa (25 ppm). E_a^{app} = apparent activation energy in kJ/mol for each zeolite. ± denotes 95% confidence intervals. Reprinted with permission from [183].

Copyright 2016 American Chemical Society.

Section S11: CH₄ Oxidation vs. Temperature over Cu-Na-SSZ-13 (Cu/Al = 0.50)

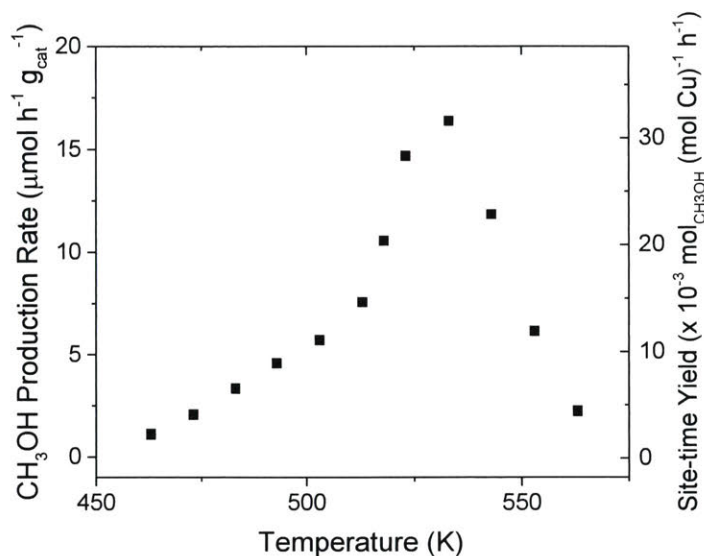


Figure S3-20. Catalytic CH₄ oxidation over Cu-Na-SSZ-13 (Cu/Al = 0.50) as a function of reaction temperature. Catalyst pretreatment: 5 h at 823 K under flowing O₂, cooled to 483 K under O₂ flow and then purged under He for 0.5 h. Initial CH₄ oxidation: 0.5 h under 2400 mL h⁻¹ g_{cat}⁻¹ CH₄. Reaction conditions: WHSV = 3600 mL h⁻¹ g_{cat}⁻¹, P_{CH₄} = 88.9 kPa, P_{H₂O} = 3.2 kPa, P_{O₂} = 0.088 kPa, He balance. Error bars denote 95% confidence intervals. Reprinted with permission from [183]. Copyright 2016 American Chemical Society.

Section S12 CH₄ Oxidation over CuO_x-Zeolites Prepared by Incipient Wetness Impregnation

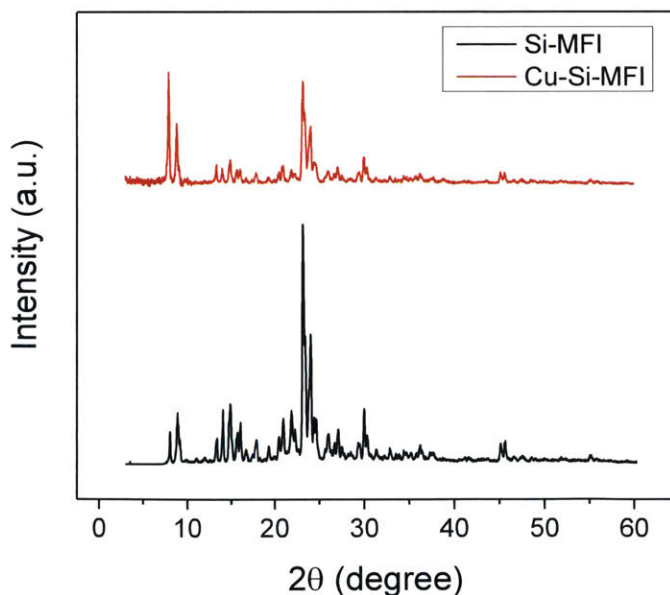


Figure S3-21. Powder x-ray diffraction pattern of CuO_x-Si-MFI (1.1 wt% Cu). No reflections for CuO nor Cu₂O could be detected in the diffraction pattern. Reprinted with permission from [183]. Copyright 2016 American Chemical Society.

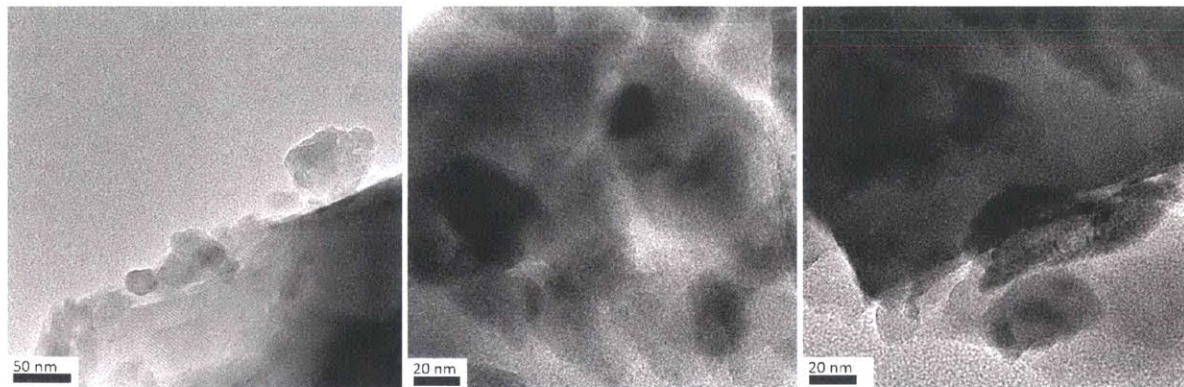


Figure S3-22. TEM Images of CuO_x-Si-MFI (1.1 wt% Cu). Large CuO_x particles are observed with average size 30 ± 20 nm. Reprinted with permission from [183]. Copyright 2016 American Chemical Society.

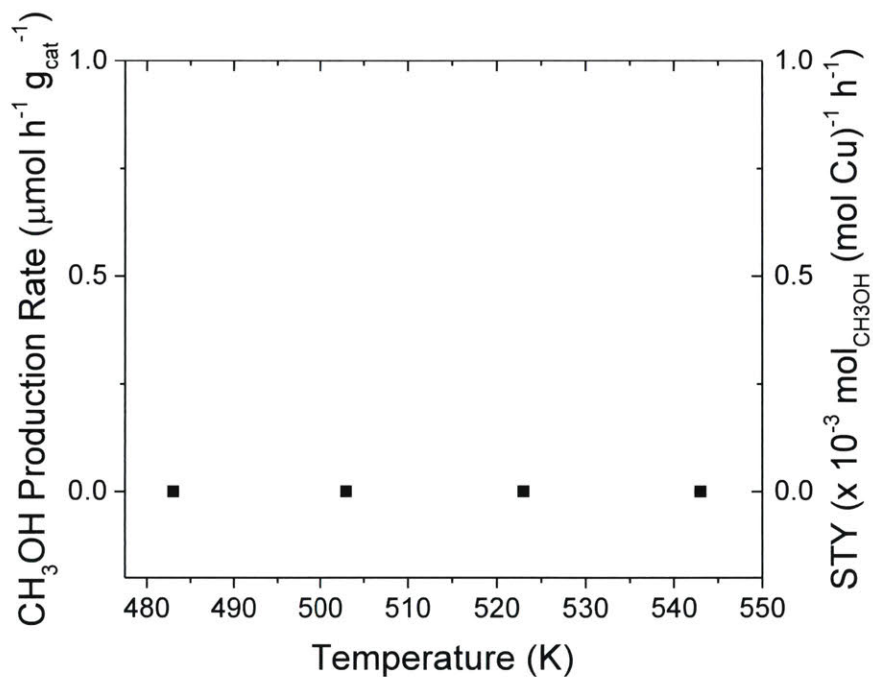


Figure S3-23. Catalytic CH₄ oxidation over CuO_x-MFI (1.1 wt% Cu) as a function of reaction temperature. Catalyst pretreatment: 5 h at 823 K under flowing O₂, cooled to 483 K under O₂ flow and then purged under He for 0.5 h. Initial CH₄ oxidation: 0.5 h under 2400 mL h⁻¹ g_{cat}⁻¹ CH₄. Reaction conditions: WHSV = 2400 mL h⁻¹ g_{cat}⁻¹, P_{CH₄} = 93.1 kPa, P_{H₂O} = 3.2 kPa, P_{O₂} = 0.051 kPa, He balance. Reprinted with permission from [183]. Copyright 2016 American Chemical Society.

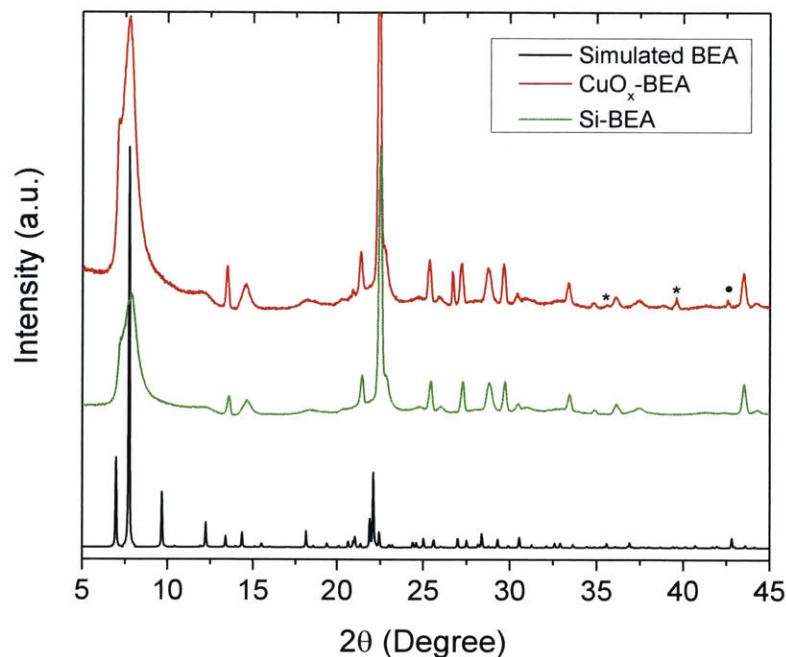


Figure S3-24. Powder x-ray diffraction patterns of $\text{CuO}_x\text{-BEA}$ (1.1 wt% Cu).

* denotes reflections of CuO and • denotes reflections of Cu_2O .¹⁹³ The average CuO particle size was estimated to be 41 nm for CuO ($2\theta = 39.6^\circ$) and 60 nm for Cu_2O ($2\theta = 42.6^\circ$) using the Sherrer equation. Reprinted with permission from [183]. Copyright 2016 American Chemical Society.

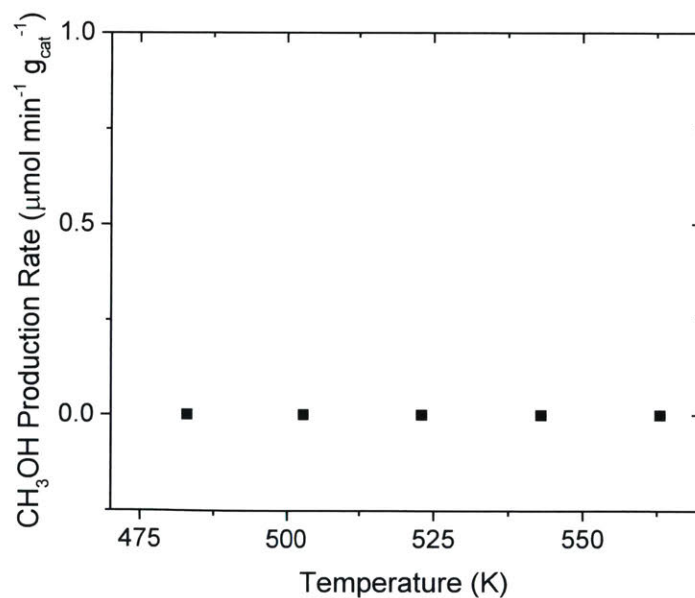


Figure S3-25. Catalytic CH_4 oxidation over $\text{CuO}_x\text{-BEA}$ (1.1 wt% Cu) as a function of reaction temperature. Catalyst pretreatment: 5 h at 823 K under flowing O_2 , cooled to 483 K under O_2 flow and then purged under He for 0.5 h. Initial CH_4 oxidation: 0.5 h under $2400 \text{ mL h}^{-1} \text{ g}_{\text{cat}}^{-1}$ CH_4 . Reaction conditions: $\text{WHSV} = 2420 \text{ mL h}^{-1} \text{ g}_{\text{cat}}^{-1}$, $P_{\text{CH}_4} = 93.1 \text{ kPa}$, $P_{\text{H}_2\text{O}} = 3.2 \text{ kPa}$, $P_{\text{O}_2} = 0.051 \text{ kPa}$, He balance. Reprinted with permission from [183]. Copyright 2016 American Chemical Society.

Section S12: Materials Characterization

Table S3-3. Elemental composition, pore volume and surface area analysis (BET) of Cu-exchanged zeolites

Material ^a	Framework	Si/Al ^b	Si/Al _{tot} ^c	Cu/Al ^d	Cu wt% ^e	Fe/Al ^f	V _{micro} (cm ³ g _{cat} ⁻¹) ^g
Na-ZSM-5	MFI	11.5	13.6	0.37	2.5	0.01	0.14
Na-ZSM-5	MFI	11.5	13.1	0.17	1.2	0.01	0.14
H-ZSM-5	MFI	11.5	13.2	0.31	2.2	0.01	0.14
H-ZSM-5	MFI	11.5	13.9	0.13	0.9	0.01	0.15
H-ZSM-5	MFI	11.5	12.9	0	0	0.00	0.16
<hr/>							
Na-MOR	MOR	10	11.4	0.14	1.1	0.01	0.17
H-MOR	MOR	10	11.1	0.14	1.1	0.01	0.19
H-MOR	MOR	10	10.4	0	0	0.00	0.20
<hr/>							
Na-SSZ-13	CHA	15	13.8	0.50	3.3	0.00	0.24

^a zeolite material with parent counter cation form before copper-exchange. Na denotes sodium form, H denotes proton form.

^b nominal ratio of total silicon to aluminum atoms in the zeolite based on commercial figures or ratios of SiO₂ to Al₂O₃ in synthesis procedures.

^c calculated ratio of total silicon to aluminum atoms in the zeolite. Quantified using inductively coupled plasma mass spectrometry (ICP-MS).

^d calculated ratio of total copper to aluminum atoms in copper-exchanged zeolite. Quantified using ICP-MS.

^e weight percent of copper in copper-exchanged zeolite.

^f calculated ratio of total iron to aluminum atoms in copper-exchanged zeolite. Quantified using ICP-MS. Fe/Al was quantified to provide an estimate of iron impurities in copper-exchanged zeolites.

^g micropore volume of copper-exchanged zeolites determined by BET analysis.

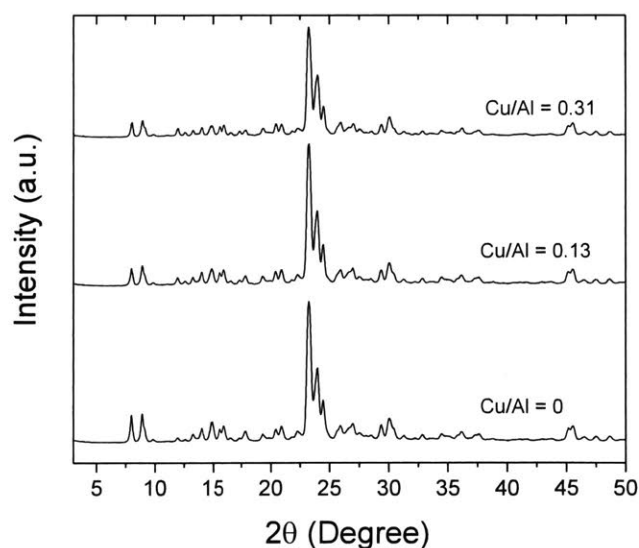


Figure S3-26. Powder x-ray diffraction patterns of Cu-exchanged H-ZSM-5 (Si/Al = 12.9 – 13.9) catalysts. After ion exchange, drying, and calcination, no reflections were observed corresponding to copper or copper oxide particles (< 3 nm). Reprinted with permission from [183]. Copyright 2016 American Chemical Society.

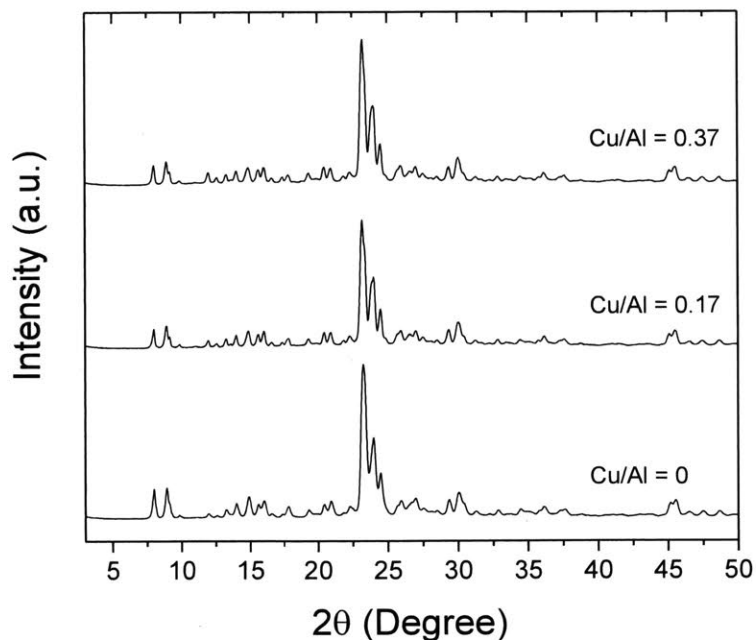


Figure S3-27. Powder x-ray diffraction patterns of Cu-exchanged Na-ZSM-5 (Si/Al = 12.9 – 13.6) catalysts. After ion exchange, drying, and calcination, no reflections were observed corresponding to copper or copper oxide particles (< 3 nm). Reprinted with permission from [183]. Copyright 2016 American Chemical Society.

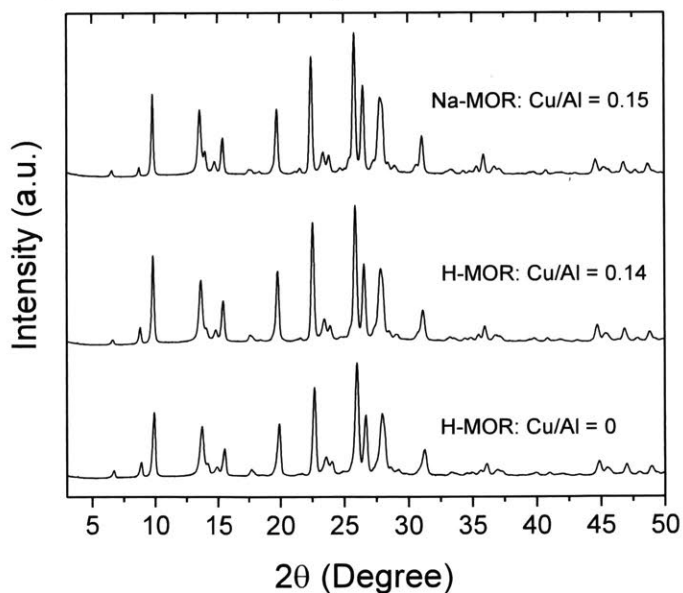


Figure S3-28. Powder x-ray diffraction patterns of Cu-exchanged MOR (Si/Al = 10.4 – 11.4) catalysts. After ion exchange, drying, and calcination, no reflections were observed corresponding to copper or copper oxide particles (< 3 nm). Reprinted with permission from [183]. Copyright 2016 American Chemical Society.

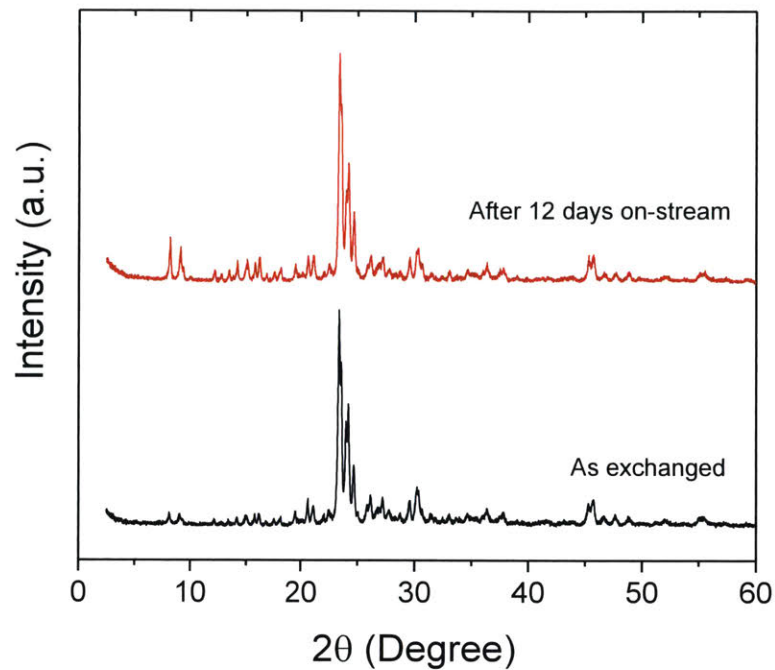


Figure S3-29. Powder x-ray diffraction of Cu-H-ZSM-5 (Cu/Al = 0.31) after exchange and after CH₄ oxidation for 12 days-on-stream. Reprinted with permission from [183]. Copyright 2016 American Chemical Society.

Chapter 4 : One-Pot Synthesis of Copper-Exchanged SSZ-13 Zeolites for the Oxidation of Methane into Methanol

4.1 Introduction

Copper-exchanged zeolites have achieved the holy grail of catalysis as a synthetic catalyst able to oxidize methane (CH_4) directly into methanol (CH_3OH) under mild conditions with molecular oxygen (O_2) and water (H_2O).¹⁸³ This chemistry has the potential to forgo large, expensive reforming facilities and enable construction of modular plants to convert stranded shale gas into transportable liquid fuels. However, current CH_4 conversion over Cu-exchanged zeolites (0.001%) is far too low to be economically viable and must approach that of methane monooxygenase enzymes to be feasible.^{58, 128, 132} Additionally, diverse Cu speciation at undefined locations precludes the detailed characterization of the catalytic active site. Control of Cu speciation is essential to identify the catalytic active site for further improvements in catalytic activity. Here, we report the one-pot synthesis of Cu-SSZ-13 (chabazite structure, CHA) using tetraethylenepentamine (TEPA) as a structure directing agent^{113-114, 116-117} under sodium-free conditions¹¹² to yield a highly active CH_4 oxidation catalyst. Isolated Cu^{2+} species correlate with CH_4 oxidation activity. TEPA-synthesized Cu-SSZ-13 (Cu-SSZ-13-T) exhibits higher catalytic activity and site-time yield ($\text{mol}_{\text{CH}_3\text{OH}} (\text{mol Cu})^{-1} \text{min}^{-1}$) than ion-exchanged Cu-SSZ-13 (Cu-SSZ-13-I) and > 100 times the activity of Cu-Na-ZSM-5.¹⁸³ These results imply isolated Cu^{2+} species are the precursors to the catalytic site and the control of Cu speciation is vital in catalyst development for the commercialization of direct CH_4 oxidation into CH_3OH .

4.2 Results and Discussion

Two synthetic techniques were used to control Cu speciation within Cu-SSZ-13: 1) using TEPA as a structure directing agent and 2) controlling framework Al pairing with Na^+ ions. Cu-SSZ-13-T has exhibited high activity and hydrothermal stability for NO_x selective catalytic reduction (SCR) of NH_3 ¹¹⁴⁻¹¹⁷ due to differences in its Cu speciation compared to ion-exchanged Cu-SSZ-13. Density functional theory predicts TEPA strongly chelates to Cu^{2+} ions under alkaline conditions¹¹³ to form a complex close to the

size of the CHA cage.¹⁹⁴ Cu^{2+} incorporates into SSZ-13 within the Cu-TEPA complex¹¹³⁻¹¹⁴ without any evidence of Cu oxide particles, implying one Cu^{2+} species is initially positioned within each CHA cage. This hypothesis is corroborated by the observation of well-dispersed Cu ions in Cu-SSZ-13-T compared to mixes of Cu ions and oxides in Cu-SSZ-13-I.¹¹⁵ The presence of isolated Cu^{2+} ions correlates to NH_3 SCR,¹⁹⁵⁻¹⁹⁷ possibly explaining how TEPA is beneficial for SCR. The types of Cu^{2+} ions in Cu-SSZ-13 can be further controlled by the presence of Na^+ during hydrothermal synthesis. Gounder and coworkers have demonstrated Na^+ directs the formation of Al pairs in the SSZ-13 framework and the exchange of one Cu per two Al sites¹¹² consistent with Cu^{2+} localized in the 6-membered ring (MR) of CHA.¹⁹⁸⁻²⁰¹ Elimination of Na^+ results in isolated Al sites and the exchange of $[\text{CuOH}]^+$ sites. Kulkarni *et. al.* recently calculated isolated $[\text{CuOH}]^+$ in the 8MR as the active site for the stoichiometric oxidation of CH_4 into CH_3OH in Cu-SSZ-13.¹²⁶ In this study, isolated Cu ions were exchanged into SSZ-13 by the Na^+ -free synthesis of Cu-SSZ-13-T for catalytic CH_4 oxidation in order to avoid the CuO_x species shown to be inactive for catalytic CH_4 oxidation.¹⁸³

Na^+ -free synthesized Cu-SSZ-13-T yields isolated Cu species. Synthesis of Cu-SSZ-13-T under Na^+ -free conditions produced the same crystalline structure as SSZ-13 synthesized using conventional techniques (Figure S4-6).²⁰² No reflections for CuO or Cu_2O were observed for $\text{Cu}/\text{Al} < 0.11$, indicating no large CuO_x particles were present for low Cu loadings. Evidence for isolated Cu species was corroborated with UV-visible spectroscopic measurements. UV-visible spectra collected for Cu-SSZ-13-T samples under ambient atmosphere showed only transitions at $12,500\text{ cm}^{-1}$ for the hydrated Cu^{2+} d-d transition²⁰³ and the $48,000\text{ cm}^{-1}$ O—Cu charge transfer band for isolated Cu^{2+} (Figure S4-7).²⁰⁴ At higher Cu loading, another band around $37,000\text{ cm}^{-1}$ appeared, attributed to another O—Cu charge transfer that has been observed in Cu-SSZ-13-I.¹⁹⁸ No bands were observed between $21,000\text{--}30,000\text{ cm}^{-1}$ characteristic of charge transfer bands of extraframework oxygen ligands to Cu species in dicupric-oxo species.^{66, 108, 205} UV-vis spectroscopic measurements along with powder x-ray diffraction patterns suggest no Cu_xO_y clusters are present in Cu-SSZ-13-T and Cu speciation is predominantly isolated.

Isolated Cu species in Cu-SSZ-13-T are predominantly coordinated to isolated framework Al sites as Cu^+ and Cu^{2+} species. Cu species in Cu-SSZ-13-T are a mixture of Cu^+ and Cu^{2+} species after activation in 1% O_2/He at 823 K for 5 h. XANES spectra showed $1s \rightarrow 4p$ transitions at 8983 eV of two or three coordinate $\text{Cu}^{+98, 205-206}$ and the $1s \rightarrow 4p_z + \text{ligand} \rightarrow \text{Cu}$ transition of Cu^{2+} at 8987 eV^{100, 207-211} (Figure S4-8). Interestingly, the $1s \rightarrow 3d$ transition of Cu^{2+} at 8977 eV was not visible in several Cu-SSZ-13-T samples after

activation. The types of Cu^+ species were investigated with CO adsorption coupled with infrared spectroscopy. After activating Cu-SSZ-13-T under 1% O_2/He at 673 K for 3 h and cooling to 298 K, the surface of Cu-SSZ-13-T was saturated with CO and then purged under flowing He for 1 h. Only one peak was observed at 2155 cm^{-1} that increased with Cu loading (Figure S4-9). Two Cu^+ sites have been observed using CO adsorption over ion-exchanged Cu-SSZ-13: 2155 cm^{-1} and 2135 cm^{-1} . Peden and coworkers hypothesized the 2135 cm^{-1} band corresponds to Cu^+ in the constrained 6-MR that was occupied first during ion-exchange while the 2155 cm^{-1} band corresponds to Cu^+ in the larger CHA cages.²¹²⁻²¹³ This observation was supported by Lamberti *et. al.* where they observed the formation of bulkier dicarbonyl-Cu species only with the 2155 cm^{-1} Cu^+ species.²⁰⁴ Density functional theory calculations closely simulated the experimentally observed infrared shift of both Cu^+ -CO species. Göltl *et. al.* predicted the 2135 cm^{-1} band is Cu^+ near two Al sites in the 6-MR of CHA with an extra proton balancing the total charge, while the 2155 cm^{-1} band is Cu^+ near a single Al site in the 6-MR.¹⁹⁹ The presence of only the 2155 cm^{-1} band in Cu-SSZ-13-T suggests Cu^+ species are mainly near isolated Al sites in the SSZ-13 framework.

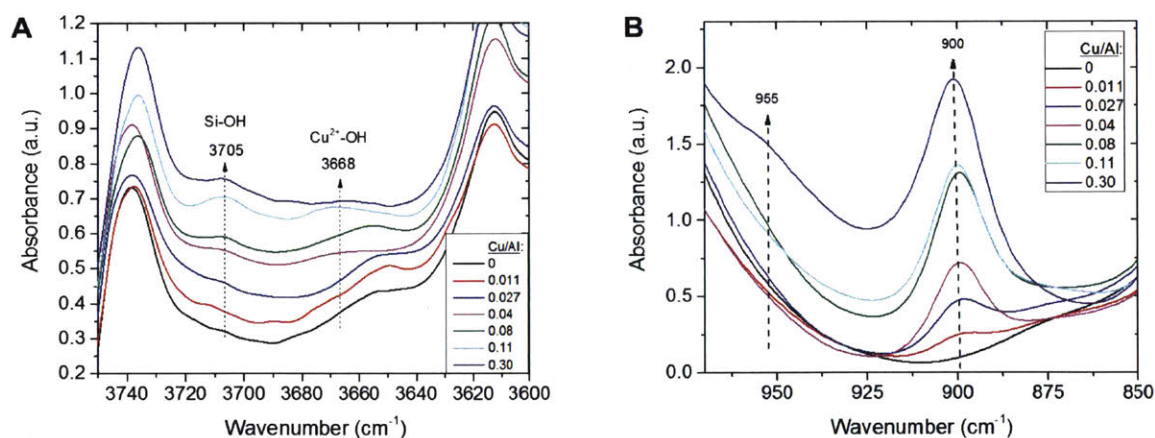


Figure 4-1. Infrared spectroscopy of Cu-SSZ-13-T (Si/Al = 13-15). Pretreatment: calcined under 1% O_2/He at 673 K for 3 h. Spectra were acquired at 298 K under flowing He. Samples were normalized with respect to Si-O stretching vibrations around 1900 cm^{-1} .

Co^{2+} ion-exchange into SSZ-13-T supports the notion of mostly isolated framework Al sites within Cu-SSZ-13-T. Gounder and co-workers have demonstrated bare Co^{2+} only exchanges into Cu-SSZ-13-I to nearby “visible” Al pairs within SSZ-13, enabling the fraction of paired framework Al sites to be quantified.¹¹² After exchange of Cu-SSZ-13-T (Si/Al = 13.3, Cu/Al = 0.28) with Co^{2+} , the final Co/Al ratio was 0.05. Bare Co^{2+} was confirmed by the presence of Co^{2+} d-d transitions around $20,000\text{ cm}^{-1}$ (Figure S4-10). This

indicated that 10 percent of all Al sites constitute pairs, a smaller fraction than the $\text{Co}/\text{Al} = 0.10$ saturation point found for SSZ-13 zeolites ($\text{Si}/\text{Al}=15$) synthesized in the presence of Na^+ .¹¹² These studies indicated under Na^+ -free Cu-SSZ-13-T synthesis conditions, the fraction of Al pairs is less than 10 percent and trace Na^+ ions likely direct the formation of small fractions of Al pairs. The low amount of framework Al pairs causes Cu^{2+} -OH species to form at $\text{Cu}/\text{Al} \geq 0.04$ in Cu-SSZ-13-T (Figure 4-1A). A band appears at 3668 cm^{-1} , roughly the region of the Cu-OH stretch observed in Cu-SSZ-13-I.^{204, 211, 214} The intensity of this stretch increased with Cu/Al, indicating more Cu-OH species form with higher Cu loading. Additionally, a clear band formed at 900 cm^{-1} that also increased with respect to Cu/Al (Figure 4-1B). This stretch is thought to correspond to Cu^{2+} species perturbing T-O-T framework vibrations,^{100, 212, 215-216} however the Cu^{2+} species represented by this band is contested. Peden and coworkers suggested the band at 895 cm^{-1} is bare Cu^{2+} in constrained environments coordinated to two framework Al sites in the 6-MR prisms.^{212, 215} This siting is supported by several X-ray diffraction studies of Cu-SSZ-13-I.^{200, 217-218} However, in all of these studies, Cu-SSZ-13-I was synthesized with Na^+ in the synthesis medium, which is known to produce a large proportion of Al pairs¹¹² that preferentially stabilize bare Cu^{2+} in the 6-MR at low Cu loading.^{126, 198-199} We have demonstrated about ten percent of framework Al sites are present in Cu-SSZ-13-T, which would rule out bare Cu^{2+} species for $\text{Cu}/\text{Al} > 0.05$ from the mismatch in the local charge balance. The 900 cm^{-1} peak could correspond to Cu^{2+} -OH species as the 3668 cm^{-1} peak appears for $\text{Cu}/\text{Al} > 0.04$ when Al pairs are saturated in Cu-SSZ-13-T (Figure 4-1A). Borfecchia et. al. have hypothesized the band at 905 cm^{-1} in Cu-SSZ-13-I ($\text{Cu}/\text{Al} = 0.44$) corresponds to Cu^{2+} -OH species near a single Al site.²¹¹ Similar Cu^{2+} -OH species²¹⁹ and other metal-hydroxide species²²⁰⁻²²¹ have been assigned in other systems around 900 cm^{-1} . For either interpretation of the 900 cm^{-1} band, Cu species in Cu-SSZ-13-T (Na^+ -free synthesis) are isolated Cu^+ and Cu^{2+} species.

Synthesis of Cu-SSZ-13-T under Na^+ -free conditions confers higher catalytic activity for CH_4 oxidation and site-time yield ($\text{mol}_{\text{CH}_3\text{OH}} (\text{mol Cu})^{-1} \text{ min}^{-1}$) than that of Cu-SSZ-13-I. Both Cu-SSZ-13-T ($\text{Si}/\text{Al} = 14.7$) and Cu-SSZ-13-I ($\text{Si}/\text{Al} = 13.9$) at $\text{Cu}/\text{Al} = 0.08$ were activated under flowing 1% O_2/He for 5 h at 823 K, cooled to 493 K, purged under He for 0.5 h, and contacted with the reaction mixture of 88.3 kPa CH_4 , 3.2 kPa H_2O , 0.098 kPa O_2 , and He balance. At 493 K, Cu-SSZ-13-T produced $0.10 \mu \text{mol}_{\text{CH}_3\text{OH}} \text{ min}^{-1} \text{ g}_{\text{cat}}^{-1}$ and $1.23 \times 10^{-3} \text{ mol}_{\text{CH}_3\text{OH}} (\text{mol Cu})^{-1} \text{ min}^{-1}$ while Cu-SSZ-13-I had $0.067 \mu \text{mol}_{\text{CH}_3\text{OH}} \text{ min}^{-1} \text{ g}_{\text{cat}}^{-1}$ and $7.79 \times 10^{-4} \text{ mol}_{\text{CH}_3\text{OH}} (\text{mol Cu})^{-1} \text{ min}^{-1}$. This difference in CH_3OH production and site-time yield persisted at temperatures up to 623 K (Figure 4-2). Interestingly, the

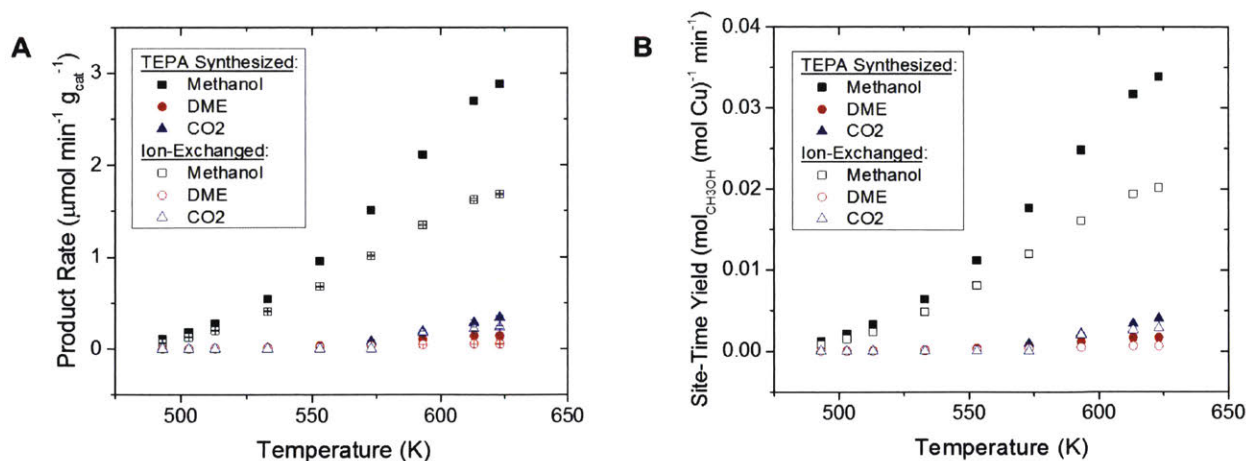


Figure 4-2. CH₄ oxidation over Cu-SSZ-13-T (Si/Al = 14.7, Cu/Al = 0.08) and Cu-SSZ-13-I (Si/Al = 13.9, Cu/Al = 0.08). Catalyst Pretreatment: 5 h under 1% O₂/He at 823 K, cooled to 493 K, and exposed to 6000 mL h⁻¹ g_{cat}⁻¹ of 88.3 kPa CH₄, 3.2 kPa H₂O, 0.098 kPa O₂, He balance for 4 h; Reaction Conditions: WHSV = 6000 mL h⁻¹ g_{cat}⁻¹, P_{CH₄} = 88.3 kPa, P_{H₂O} = 3.2 kPa, P_{O₂} = 0.098 kPa, P_{He} balance.

selectivity of both Cu-SSZ-13 catalysts was similar (Figure S4-11). Higher CH₃OH production and site-time yield for Cu-SSZ-13-T suggests TEPA directs the formation of catalytic sites while ion-exchange has more spectator Cu ions. Infrared spectroscopic measurements over both catalysts calcined under 1% O₂/He at 673 K for 3 h shows more isolated Cu²⁺-OH in Cu-SSZ-13-T than in Cu-SSZ-13-I (3660 cm⁻¹ band, Figure S4-12) as well as isolated Cu²⁺ species (897-900 cm⁻¹). UV-vis spectra also indicate a lower intensity band at 37,000 cm⁻¹ in Cu-SSZ-13-T, implying TEPA directs the production of the more active Cu²⁺ species at 48,000 cm⁻¹ (Figure S4-7B). Simultaneously, fewer Cu⁺ species were in Cu-SSZ-13-T than in Cu-SSZ-13-I, evidenced by the 955 cm⁻¹ band (Figure S4-12B) in Cu-SSZ-13.²¹⁵ A similar 966 cm⁻¹ in Cu-ZSM-5 has been attributed to Cu⁺.^{216, 222} This implied Cu⁺ are spectators for CH₄ oxidation while isolated Cu²⁺ are possibly precursors to the catalytic site.

Catalytic activity of Na⁺-free Cu-SSZ-13-T correlates strongly with the amount of isolated Cu²⁺ species initially present. Cu-SSZ-13-T zeolites (Si/Al = 13-15, variable Cu/Al) were calcined under 1% O₂/He at 823 K for 5 h, cooled to 493 K, and exposed to the reaction mixture of CH₄/O₂/H₂O. Steady-state CH₄ oxidation at 493 K showed an increase in CH₃OH production rate with Cu/Al (Figure 4-3A). However, the site-time yield remained constant at Cu/Al ≤ 0.08 and gradually decreased at higher loadings, indicating the introduction of spectator Cu species in SSZ-13 (Figure 4-3B) for Cu/Al > 0.08. The origin of CH₃OH production appeared to be correlated to the area of the 900

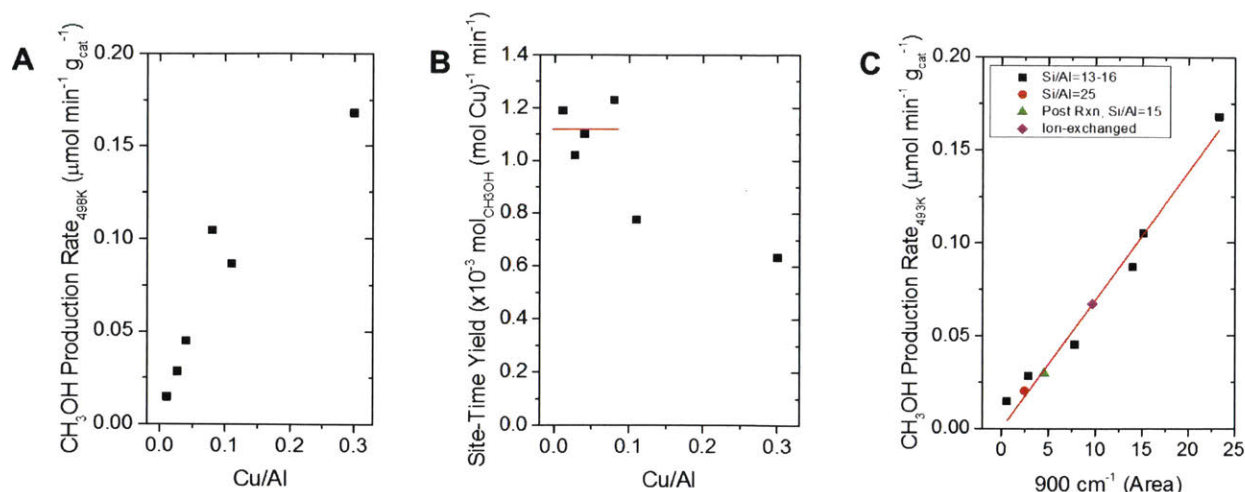


Figure 4-3. (A) CH₃OH production rate and (B) site-time yield over Cu-SSZ-13-T (Si/Al = 13-16) vs Cu/Al. Catalyst Pretreatment: 5 h under 1% O₂/He at 823 K, cooled to 493 K, and exposed to 6000 mL h⁻¹ g_{cat}⁻¹ of 88.3 kPa CH₄, 3.2 kPa H₂O, 0.098 kPa O₂, He balance for 4 h; Reaction Conditions: T = 493 K, WHSV = 6000 mL h⁻¹ g_{cat}⁻¹, P_{CH₄} = 88.3 kPa, P_{H₂O} = 3.2 kPa, P_{O₂} = 0.098 kPa, P_{He} balance. **(C) CH₃OH production rate of Cu-SSZ-13-T at 493 K vs. area of the 900 cm⁻¹ peak.** Catalyst pretreatment: 3 h under flowing 1% O₂/He at 673 K, then cooling to 298 K.

cm⁻¹ band for Cu²⁺ species (Figure 4-3C). Interestingly, integration of the 897 cm⁻¹ band in Cu-SSZ-13-I (Si/Al = 13.9, Cu/Al = 0.08) falls along the linear correlation, which would imply isolated Cu²⁺ species are the precursors to catalytic sites. However, the increase in CH₃OH production rate with respect to Cu/Al in Cu-SSZ-13-T (Figure 4-3A) and the predominance of Cu²⁺-OH species in Cu-SSZ-13-T with Cu/Al > 0.04 could imply Cu²⁺-OH as the precursor to the catalytic active site.

To gain insight into the catalytic site, CH₃OH production over Cu-SSZ-13-T (Na⁺-free) was studied as a function of Cu/Al and temperature. Between 493-553 K, the CH₃OH production rate increased with Cu loading (Figure 4-4A). However, CH₃OH production deviated from Arrhenius behavior above 553 K (Figure 4-4B). CH₃OH production levels off and even decreases at higher temperatures as Cu/Al increases, and the temperature of maximum CH₃OH production rate decreased with Cu/Al (Figure 4-4A). The loss in CH₃OH production coincided with CO₂ production (Figure 4-4A, B, D) and was more prevalent at higher Cu/Al. Simultaneously, the site-time yield was similar for Cu/Al < 0.08 below 553 K and then decreased with Cu/Al at higher temperatures (Figure 4-4C). A larger proportion of Cu species are utilized for CH₃OH production, are more selective to CH₃OH, and are active at higher temperatures at low Cu/Al, possibly suggesting an isolated Cu species is the catalytic site.

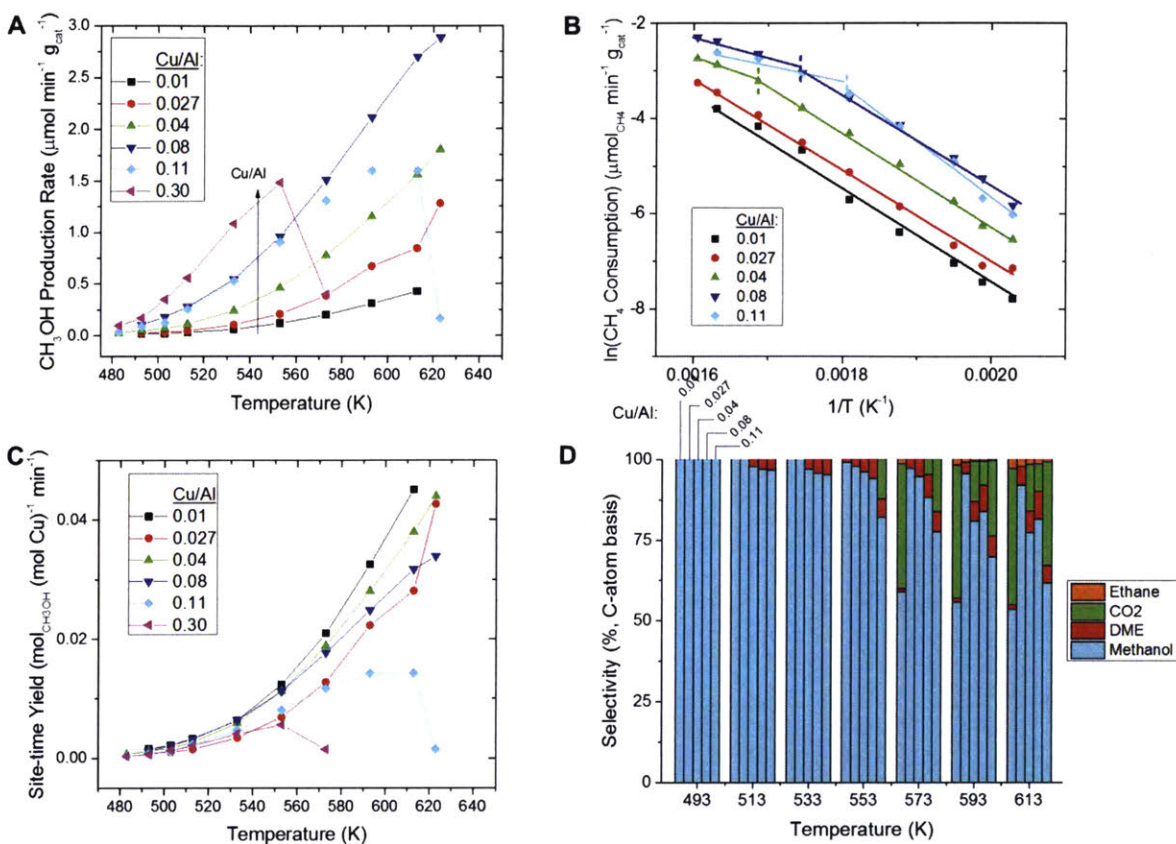


Figure 4-4. CH₄ oxidation over Cu-SSZ-13-T (Na⁺-free, Si/Al = 13-15) for various copper loading. **A)** CH₃OH production rate vs temperature. **B)** Arrhenius plot of CH₄ consumption. **C)** site-time yield vs temperature. **D)** selectivity vs temperature. Catalyst Pretreatment: 5 h under 1% O₂/He at 823 K, cooled to 493 K, and exposed to 6000 mL h⁻¹ g_{cat}⁻¹ of 88.3 kPa CH₄, 3.2 kPa H₂O, 0.098 kPa O₂, He balance for 4 h; Reaction Conditions: WHSV = 6000 mL h⁻¹ g_{cat}⁻¹, P_{CH₄} = 88.3 kPa, P_{H₂O} = 3.2 kPa, P_{O₂} = 0.098 kPa, P_{He} balance.

Further increasing the distance between Cu ions, accomplished by reducing the Al content (Si/Al) for a given surface coverage of Cu (Cu/Al), increased CH₃OH selectivity and the temperature of maximum CH₃OH production rate. After CH₄ oxidation over Cu-SSZ-13-T (Si/Al=14.9, Cu/Al=0.04) up to 643 K, the zeolite was calcined under 1% O₂/He at 823 K for 5 h, cooled to 493 K, and exposed to the CH₄/O₂/H₂O reaction mixture. The steady-state rate decreased from 0.06 to 0.03 μmol_{CH₃OH} min⁻¹ g_{cat}⁻¹ (Figure S4-13A). However, Cu-SSZ-13-T (Si/Al=25.1, Cu/Al=0.05) did not deactivate after CH₄ oxidation up to 673 K, subsequent calcination, and CH₄ oxidation at 493 K (Figure S4-13B). The reaction temperature was then increased to 623 K. Product rates were almost identical to fresh Cu-SSZ-13-T at all temperatures (Figure 4-5A). At 623 K, the steady-state CH₃OH production rate was exceptionally stable up to 130 h on-stream

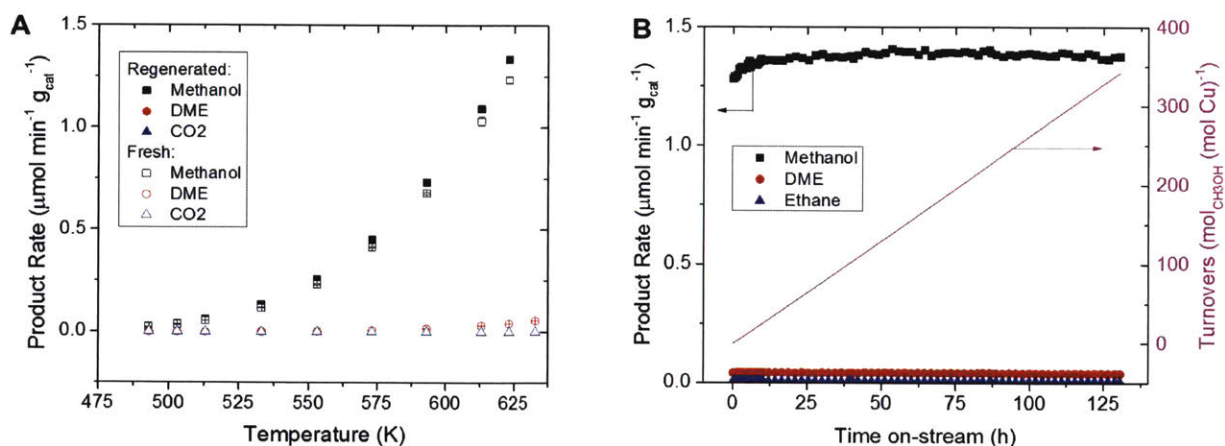


Figure 4-5. CH₄ oxidation before and after reaction over Cu-SSZ-13-T (Si/Al = 25.1, Cu/Al = 0.05). Fresh denotes catalyst before any CH₄ oxidation reactions. Regenerated denotes Cu-SSZ-13-T that underwent CH₄ oxidation up to 673 K and was then recalcined in-situ before another set of reactions. Catalyst Pretreatment: 5 h under 1% O₂/He at 823 K, cooled to 493 K, and exposed to 6000 mL h⁻¹ g_{cat}⁻¹ of 88.3 kPa CH₄, 3.2 kPa H₂O, 0.098 kPa O₂, He balance for 4 h; Reaction Conditions: WHSV = 6000 mL h⁻¹ g_{cat}⁻¹, P_{CH₄} = 88.3 kPa, P_{H₂O} = 3.2 kPa, P_{O₂} = 0.098 kPa, P_{He} balance.

(Figure 4-5B). The cause of deactivation of CH₃OH production appears to be agglomeration of Cu into CuO_x. Diffuse reflectance UV-vis spectroscopy shows the appearance of a broad band around 23,000 cm⁻¹ and the disappearance of the 37,000 cm⁻¹ band at high Cu/Al in Cu-SSZ-13-T (Si/Al = 13-16) after reaction up to 643 K. The 23,000 cm⁻¹ band is less prevalent in Cu-SSZ-13-T (Si/Al = 25.1, Cu/Al = 0.05) after reaction up to 673 K (Figure S4-14). The appearance of the 23,000 cm⁻¹ band, characteristic of CuO_x nanoparticles,²²³⁻²²⁴ at the expense of a O–Cu charge transfer band at 37,000 cm⁻¹ as well as the loss in the 900 cm⁻¹ band of isolated Cu²⁺ species (Figure S4-15B) supports the agglomeration of Cu²⁺ species into CuO_x. CuO_x particles may form in structural defects within the Cu-SSZ-13-T zeolites as indicated by the losses in 3705 and 3500 cm⁻¹ signals (Figure S4-15A) attributed to vicinal silanol groups and nests in the zeolite.²²⁵ Comparison of activity of Cu-SSZ-13-T at the same Cu weight percent but different Si/Al shows the same CH₃OH production rate and site-time yield (Figure S4-16), highlighting while distance between Cu species did not affect the CH₄ oxidation rate, CuO_x formation was more prevalent with more framework Al (Figure S4-14A, F). This could suggest the mechanism of deactivation is the migration of Cu ions along framework Al sites into silanol nests, ultimately forming CuO_x at high reaction temperatures (> 573 K). Cu species are partially hydrated and mobile under CH₄ oxidation reaction conditions,^{101, 214} possibly allowing the migration of Cu species along Al sites into neighboring SSZ-13 cages to sinter. Upon sintering, CuO is known to oxidize CH₃OH into

CO₂ with O₂.²²⁶ Quicker sintering into CuO_x at higher temperature could explain CO₂ production at the expense of CH₃OH production. Higher Si/Al would increase the distance between Al sites and the pathlength between Cu ions and thus reduce the sintering of isolated Cu active sites into CuO_x for CO₂ production.

Combining the design principles of maximizing Cu content while maintaining isolated Cu²⁺ species improves catalytic CH₄ oxidation activity, CH₄ conversion, and reduces CO₂ selectivity such that CH₄ oxidation can be coupled with other chemistry involving CH₃OH. Cu-SSZ-13-T (Si/Al = 14.7, Cu/Al = 0.08) reached its maximum CH₃OH production rate of 173 μmol_{CH₃OH} h⁻¹ g_{cat}⁻¹ at 623 K with 10% CO₂ selectivity and 0.1% CH₄ conversion. The corresponding rates over Cu-Na-ZSM-5 (Si/Al = 13.6, Cu/Al = 0.37) at 483 K were 0.88 μmol_{CH₃OH} h⁻¹ g_{cat}⁻¹, 29% CO₂ selectivity, and 0.001% CH₄ conversion.¹⁸³ CH₃OH production over Cu-Na-ZSM-5 could not be further increased above 523 K due to complete overoxidation of CH₃OH into CO₂. Thus, rational design of isolated Cu²⁺ species using Na⁺-free synthesis with TEPA has enabled a 100-fold improvement in CH₄ oxidation activity while improving CH₃OH selectivity compared to conventionally studied ion-exchanged Cu-zeolites.

4.3 Conclusions

This drastic improvement in CH₃OH production rates over Cu-SSZ-13-T has allowed CH₄ oxidation to be coupled with CH₃OH-to-olefins chemistry. Increasing the pressure of the CH₄/O₂/H₂O reaction mixture between 0.1 MPa to 1.1 MPa over Cu-SSZ-13-T (Si/Al = 24.7, Cu/Al = 0.09) at 643 K favored the formation ethane, ethylene, and CO₂ production (Figure S4-17). C₂ production was about 0.1 μmol min⁻¹ g_{cat}⁻¹ at 1.1 MPa. Ethane and ethylene selectivity were as high as 11% and 33% at 1.1 MPa with traces of C₃ products. Cu-SSZ-13-T zeolites could likely be engineered into highly stable CH₄-to-olefin catalysts through exploration of the synthetic and reaction parameters. In summary, rational design of isolated Cu²⁺ species in Cu-SSZ-13 using Na⁺-free synthesis with TEPA results in highly improved CH₄ partial oxidation catalysts. While impressive strides have been made in improving catalytic activity of CH₄ partial oxidation over Cu-exchanged zeolites, experimental evidence for the structure of catalytic site(s) is needed. Future work will focus on elucidating its structure and the reaction mechanism in order to further improve catalytic activity.

4.4 Experimental Methods

Zeolite Synthesis

Synthesis of Na-SSZ-13 (CHA): sodium hydroxide (99.99%, Sigma-Aldrich) was dissolved in H₂O and mixed with N,N,N-trimethyl-1-adamantanamine hydroxide solution (Ada, 25 wt % in H₂O, Sachem) followed by the addition of aluminum hydroxide (80.3 wt % Al(OH)₃, SPI Pharma 0250) to obtain a colorless solution. After the addition of colloidal silicon dioxide (SiO₂) (Ludoxff LS-30), the colorless solution was stirred at room temperature for 2 h. The final composition of the mixture was 0.1 Na₂O: 0.033 Al₂O₃: 1.0 SiO₂: 44 H₂O: 0.1 (Ada)₂O. This mixture was transferred to a 23-mL Teflon-lined stainless steel autoclave (No. 4749, Parr Instruments) and was then subjected to hydrothermal treatment at 433 K for 5 days in an oven under autogenous pressure and rotation (60 rpm). After hydrothermal treatment, the product was separated from the mother liquor by centrifugation, washed several times with distilled H₂O, and dried at 393 K. SSZ-13 samples were calcined under dry air (Dry Size 300, Airgas) with the following temperature profile: heat 1 K min⁻¹ to 423 K and hold for 2 h at 423 K, then heat 1 K min⁻¹ to 623 K and hold for 2 h at 623 K, and lastly heat 1 K min⁻¹ to 853 K and hold for 10 h.

Synthesis of Na free SSZ-13 (CHA): sodium free SSZ-13 was synthesized in the same manner as Na-SSZ-13 except sodium hydroxide was replaced with N,N,N-trimethyl-1-adamantanamine hydroxide. The final composition of the mixture was 0.033 Al₂O₃: 1.0 SiO₂: 44 H₂O: 0.2 (Ada)₂O.

Synthesis of Cu-SSZ-13-T (CHA): One-pot Cu-SSZ-13-T was synthesized in the same manner as Na free SSZ-13 except copper sulfate pentahydrate (99.999% trace metals basis, Sigma-Aldrich) was first dissolved in water followed by the addition of tetraethylenepentamine (TEPA, technical grade, Sigma-Aldrich) and stirred for an hour before the addition of N,N,N-trimethyl-1-adamantanamine hydroxide. The final composition of the mixture was x⁻¹ Al(OH)₃: 1.0 SiO₂: 44 H₂O: 0.4 AdaOH: y CuSO₄: 1.1y TEPA. x was either 15 or 30 and y ranged from (0.05-0.3)*x .

Ion Exchange

Ammonium exchange. The following procedure was used to ion-exchange Na-SSZ-13 zeolites: 1 g of zeolite was stirred in 60 mL of a 1.0 M solution of ammonium nitrate (≥ 99%, Sigma-Aldrich) at 353 K for 4 h. The suspension was then filtered at room temperature and rinsed with 300 mL of deionized H₂O. The zeolite was dried overnight at 393 K in a drying oven. This process was repeated three more times. After the final exchange, the zeolite was calcined under dry air (Dry Size 300, Airgas) at 823 K for 5 h

with a heating ramp of 1 K min⁻¹. Ammonium exchange was only performed once for Na free-SSZ-13.

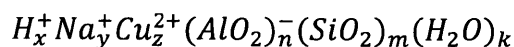
Copper exchange. The following procedure was used to ion-exchange all zeolites: 1 g of zeolite was stirred in 150 mL of 0.0003 - 0.004 M solutions of copper (II) acetate monohydrate (> 99%, Sigma-Aldrich) at room temperature overnight. The initial pH was adjusted to 5.7 with aqueous sodium hydroxide. The suspension was then filtered at room temperature and rinsed with 400 mL of deionized H₂O. The zeolite was dried overnight at 393 K in a drying oven and subsequently calcined under dry air (Dry Size 300, Airgas) at 823 K for 5 h with a heating ramp of 1 K min⁻¹.

Cobalt exchange. The following procedure was used to ion-exchange all zeolites: 1 g of zeolite was stirred in 150 mL of 1.0 M ammonium nitrate solution overnight at room temperature overnight. The suspension was then filtered at room temperature and rinsed with 400 mL of deionized H₂O. The zeolite was dried overnight at 393 K in a drying oven and subsequently calcined under dry air (Dry Size 300, Airgas) at 823 K for 5 h with a heating ramp of 1 K min⁻¹. This process was repeated with 0.25 M cobalt (II) nitrate hexahydrate (ACS reagent, ≥ 98%, Sigma-Aldrich) and then 0.50 M cobalt (II) nitrate to ensure saturation.

Characterization

Elemental analysis. Copper (Cu), sodium (Na), aluminum (Al), and iron (Fe) contents were determined using inductively coupled plasma mass spectrometry (ICP-MS) (Agilent 7900). 2.0 – 10.0 mg of zeolite were placed in a polyethylene microfuge tube (1.5 mL) and digested in 0.1 mL hydrofluoric acid (48 wt %, trace metals basis, Sigma-Aldrich) for 3 h. The hydrofluoric acid solution was diluted to a total mass of 10.0 g using 2 wt % aqueous nitric acid (HNO₃) (veritas purity, GFS Chemicals). 0.10 g of this solution was then added to two solutions: 1) 0.10 g of 1 part per million (ppm) erbium in 2 wt% HNO₃ solution; 2) 9.80 g of 2 wt% HNO₃. The final concentration of each element was 10 parts per billion (ppb) erbium and between 10 to 300 ppb for Cu, Na, Al, and Fe. A five point calibration curve was built using the following ICP standard solutions: 1,000 ppm Cu in 2 wt% HNO₃, 1,000 ppm Al in 2 wt% HNO₃, 1,000 ppm Na in 2 wt% HNO₃, and 1,000 ppm Fe in 2 wt% HNO₃. All standard solutions were purchased from Sigma-Aldrich (TraceCERT).

Calculations of molar ratios Si/Al_{tot} and Cu/Al_{tot}. The unit cell of a zeolite is given by:



where subscripts refer to the molar ratios of each component within the unit cell of a zeolite. Local charge balance was assumed to occur within the zeolite, requiring $x = n - 2z - y$.

From the unit cell given above, the mass balance of the unit cell is given by the following equation on a per gram zeolite basis:

$$1 = a \frac{g \text{ SiO}_2}{g \text{ zeolite}} + b \frac{g [\text{AlO}_2]^-}{g \text{ zeolite}} + c \frac{g \text{ Cu}^{2+}}{g \text{ zeolite}} + d \frac{g \text{ Na}^+}{g \text{ zeolite}} + e \frac{g \text{ H}^+}{g \text{ zeolite}} + f \frac{g \text{ H}_2\text{O}}{g \text{ zeolite}}$$

where each coefficient represents the weight percent of each species. The weight percent of Al, Cu, and Na were directly calculated using ICP-MS, allowing b , c , and d to be determined. Converting the weight percentages of Al, Cu, and Na to mole percentages per gram zeolite, e was then calculated using the local charge balance of cations on the zeolite framework. The weight percentage of H₂O (f) was assumed to be equal to the weight percentage of H₂O in the zeolite framework unit cell (2 – 7 wt %).⁶⁸ The mass balance was then solved for the weight percentage of SiO₂ (a).

$$\text{Si}/\text{Al}_{\text{tot}} \text{ was calculated by } \frac{\text{Si}}{\text{Al}_{\text{tot}}} = \frac{a m_{\text{AlO}_2}}{b m_{\text{SiO}_2}} \times \frac{1 \text{ mol Si}}{1 \text{ mol SiO}_2} \times \frac{1 \text{ mol AlO}_2}{1 \text{ mol Al}}$$

where m_i is the molar mass of element i .

$$\text{Cu}/\text{Al}_{\text{tot}} \text{ was calculated by } \frac{\text{Cu}}{\text{Al}_{\text{tot}}} = \frac{c m_{\text{AlO}_2}}{b m_{\text{Cu}}} \times \frac{1 \text{ mol AlO}_2}{1 \text{ mol Al}}$$

Powder x-ray diffraction. The crystal structures of zeolite catalysts were determined from powder x-ray diffraction patterns collected using a Bruker D8 diffractometer using Cu-K α radiation ($\lambda = 1.5418 \text{ \AA}$, 40 kV, 40 mA). Data were recorded in the range of 3-40 2θ with an angular step size of 0.02° and a rate of 4° min⁻¹.

UV-Vis-NIR Spectroscopy. UV-Vis-NIR spectroscopy was performed on a Cary 5000 UV-Vis-NIR spectrometer (Agilent Technologies) equipped with a DiffusIR diffuse reflectance accessory (PIKE Technologies). Absolute reflectance was measured at ambient conditions from 11,100 cm⁻¹ to 52,600 cm⁻¹ with a scan rate of 11,700 cm⁻¹ min⁻¹. All spectra were normalized with respect to background spectra of hydrated H-SSZ-13 (Si/Al = 15).

IR Spectroscopy. Infrared spectroscopic measurements were collected using a Vertex 80 spectrometer (Bruker Instruments) equipped with a liquid nitrogen cooled mercury-cadmium-telluride detector. Experiments were performed in a high temperature reaction cell for transmission acquisition (HTC-3, Harrick Scientific). 5.0 mg of a zeolite sample

was pressed into a 0.7 cm diameter wafer. Zeolite samples were calcined in flowing 1% O₂/He (ultra-high purity, Airgas) for 3 h at 673 K before cooling to 298 K for acquisition. All spectra were collected at 4 cm⁻¹ resolution, averaged over 256 scans, and baseline corrected. Spectra were normalized with respect to the T-O-T vibrations between 2082 and 1589 cm⁻¹. Integration of the peaks around 900 cm⁻¹ was carried out by drawing a linear baseline from around 877 to 923 cm⁻¹.

CO adsorption. CO adsorption was performed on zeolite samples prepared and pretreated as described in the IR Spectroscopy section. Once the zeolite sample cooled to 298 K under flowing 1% O₂/He, the gas was switched to flowing He. CO gas (ultra-high purity, Airgas) was introduced to the sample by pulsing fixed volumes (25 μL, 1000 μL, 5000 μL) using a 6-way gas-sampling valve (Vici E60, Valco Instruments). The partial pressure of CO introduced to the zeolite sample was controlled by using either a 1000 ppm CO/He (Airgas) or pure CO gas stream in the 6-way gas sampling valve. CO was pulsed over the zeolite sample until the surface was completely saturated. Spectra were collected after CO-saturated samples were purged under flowing He for 1 h.

X-ray absorption spectroscopy (XAS). XAS experiments were carried out on the bending magnet beamline of the Materials Research Collaborative Access Team (MRCAT, Sector 10) at the Advanced Photon Source (APS) at Argonne National Laboratory. A cryogenically cooled double-crystal Si(111) monochromator was used with an uncoated glass mirror to minimize the presence of harmonics. Spectra were recorded in transmission mode with the ionization chambers optimized for the maximum current with linear response using gas mixtures to give 10% absorption in the incident X-ray detector (6% He in N₂) and 70% absorption in the transmission X-ray detector (42% Ar in N₂). A Cu metal foil spectrum was simultaneously collected while measuring sample spectra to calibrate the Cu K-edge to 8979 eV. XANES and EXAFS spectra were collected while the catalyst was exposed to the various gas treatments. For each treatment, the data were averaged over three spectra.

XAS experiments. The catalysts were ground into a fine powder, loaded in the sample cell, and pressed in place with a sample press. Between 0.015 and 0.030 g of catalyst was loaded, optimized to give EXAFS spectra with a total absorption between one and two and an edge step around unity.

EXAFS spectra were collected before heating under ambient conditions. Catalysts were calcined in 1% O₂ in He at 823 K for 1 h with a ramp of 5 K min⁻¹ and 30 min holds at 423 K and 523 K. After cooling to 483 K, EXAFS spectra were collected and the

catalysts were then pretreated in a flow of 15 mL min⁻¹ He and 2.87 mL min⁻¹ 1% O₂ in He that was directed through an H₂O saturator maintained at 298 K (typically 3.2 kPa). Fast XANES (~6 min per scan) spectra were collected until no change in the spectra were observed, at which point EXAFS spectra were collected and the gas flow was then switched to 16 mL min⁻¹ CH₄, O₂ and H₂O (98.1 kPa CH₄, 0.0025 kPa O₂, 3.2 kPa H₂O). Fast XANES spectra were again collected until no change could be observed and followed by EXAFS spectra collection.

XAS data fitting. XAS data were processed and fitted using the Athena and Artemis software from the Demeter package. Spectra were normalized using third-order polynomials in both the pre- and post-edge regions and were calibrated using the first zero-crossing of the second derivative of the Cu metal foil spectrum. EXAFS data were fit from $k = 3$ to $\sim 11 \text{ \AA}^{-1}$.

Surface area and pore volume quantification. Nitrogen adsorption and desorption isotherms were measured on a Quantachrome Autosorb iQ apparatus at liquid nitrogen temperature (77 K). Prior to the adsorption analysis, all samples were pelletized and degassed under vacuum for 12 h at 623 K. Micropore volume and total pore volume were determined from the amount of N₂ adsorbed at $P/P_0 = 0.01$ and $P/P_0 = 0.95$, respectively.

Catalytic CH₄ Oxidation Reactions

CH₄ oxidation reactions were conducted in a continuous, tubular flow reactor (stainless steel tube, O.D. 6.25 mm, wall thickness = 0.889 mm). The reactor tube was mounted inside of a single-zone furnace (850W / 115V, Applied Test Systems Series 3210). Temperature was controlled using a thermocouple (Omega, model TJ36-CASS-116U) mounted slightly downstream of the catalyst bed connected to a temperature controller (Digi-Sense model 68900-10). 0.25 g of zeolite particles (pelletized and sieved into 250–420 μm particles) were packed between quartz wool plugs and rested on the thermocouple in the middle of the furnace heating zone. The flow of gases, including He (ultra high purity, Airgas), 1% O₂ in He (ultra high purity, Airgas), and CH₄ (research grade, Airgas) were controlled with independent mass flow controllers (Brooks Instruments LLC). H₂O (typically 3.2 kPa) was introduced into the gas stream using saturator maintained at 298 K. Prior to reaction, the zeolite was calcined in situ under 40 mL min⁻¹ flowing 1% O₂/He for 5 h at 823 K and cooled under the same gas flow to reaction temperature (483–493 K). Upon reaching reaction temperature, the zeolite was purged under 25 mL min⁻¹ of 0.098 kPa O₂, 3.2 kPa H₂O, He balance for 4 h. The gas flow was then changed to 25 mL min⁻¹ of 88.3 kPa CH₄, 3.2 kPa H₂O, 0.098 kPa O₂, He balance. CH₃OH, dimethyl ether

(DME), CO₂, and alkane partial pressures evolved during catalytic CH₄ oxidation were quantified using a gas chromatograph (Agilent Technologies, model 6890N). The gas chromatograph was equipped with an S-bond column (Restek Rt-S-bond, 30 m, 0.25 mm ID, #19770) connected a flame ionization detector and a Carboxen 1006 PLOT column (Sigma-Aldrich, 30 m, 0.32 mm ID, #24241-U) connected to a thermal conductivity detector operating simultaneously. The oven temperature was isothermal at 303 K for 7 min, ramped at 10 K min⁻¹ to 383 K, and held isothermal for 5 min.

Once steady-state CH₃OH production was achieved at 483-493 K, the reaction temperature was increased in order to study steady-state CH₄ oxidation as a function of temperature. The catalytic rates reported herein were stable within the first 6 h on-stream of observation for all catalysts. For temperatures < 593 K, we have verified the order in which temperatures are studied does not change the observed steady-state CH₃OH production rates, indicating no permanent change in the catalyst properties.

Product quantification. Calibration curves for CH₃OH were constructed using a known vapor pressure of CH₃OH taken into a CH₄ stream. CH₃OH vapor pressure was controlled by immersing the saturator containing CH₃OH into cooling baths at several temperatures (e.g. ice water at 273 K, dry ice in ethanol at 201 K, etc). Relative response factors were calculated using the gas chromatograph between known CH₄ and CH₃OH partial pressures. Calibration curves for CO₂ and DME were constructed by flowing known mixtures of 1% CO₂/He or 10% DME/He and He to a gas chromatograph.

The following definitions were used to quantify experimental data:

The large partial pressure of CH₄ in the gas stream during catalytic CH₄ oxidation reactions prevented the accurate quantification of CH₄ consumption. As such, CH₄ conversion was assumed to be equal to the total molar flow rate of carbon of all observed products divided by the initial molar flow rate of CH₄:

$$X_{CH_4} = \frac{\sum_{i=1}^N C_i F_i}{F_{CH_4,0}}$$

where X_{CH_4} is the conversion of CH₄, F_i is the molar flow rate of product i , C_i is the number of carbon atoms in product i , $\sum C_i F_i$ is the total molar flow rate of carbon of all products, and $F_{CH_4,0}$ is the initial molar flow rate of CH₄.

As explained above, the amount of CH₄ consumed was not quantifiable. Thus, product selectivity for catalytic CH₄ oxidation was defined as:

$$S_i = \frac{C_i F_i}{\sum_{i=1}^N C_i F_i}$$

where S_i is the selectivity of product i on a C-atom basis, C_i is the number of carbon atoms in product i , F_i is the molar flow rate of product i , and $\sum C_i F_i$ is the total molar flow rate of carbon of all products.

4.5 Supporting Figures and Tables

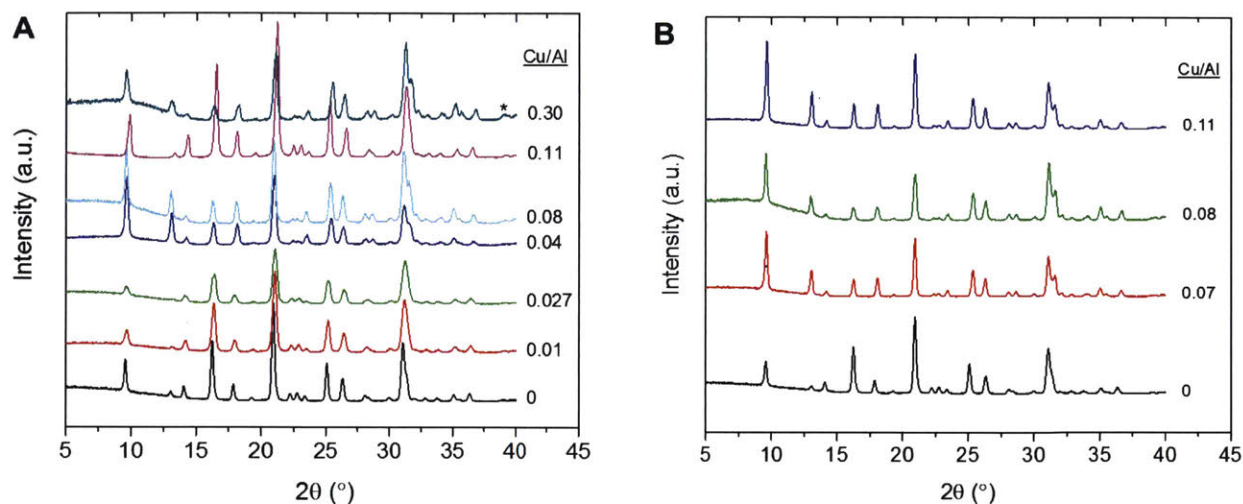


Figure S4-6. Powder x-ray diffraction patterns of (A) Cu-SSZ-13-T (Si/Al = 13-16) vs. Cu/Al and (B) Cu-SSZ-13-I (Si/Al = 13-16). All materials were freshly calcined under flowing dry air at 853 K for 10 h. * denotes the reflection for CuO ($2\theta = 39.6^\circ$).

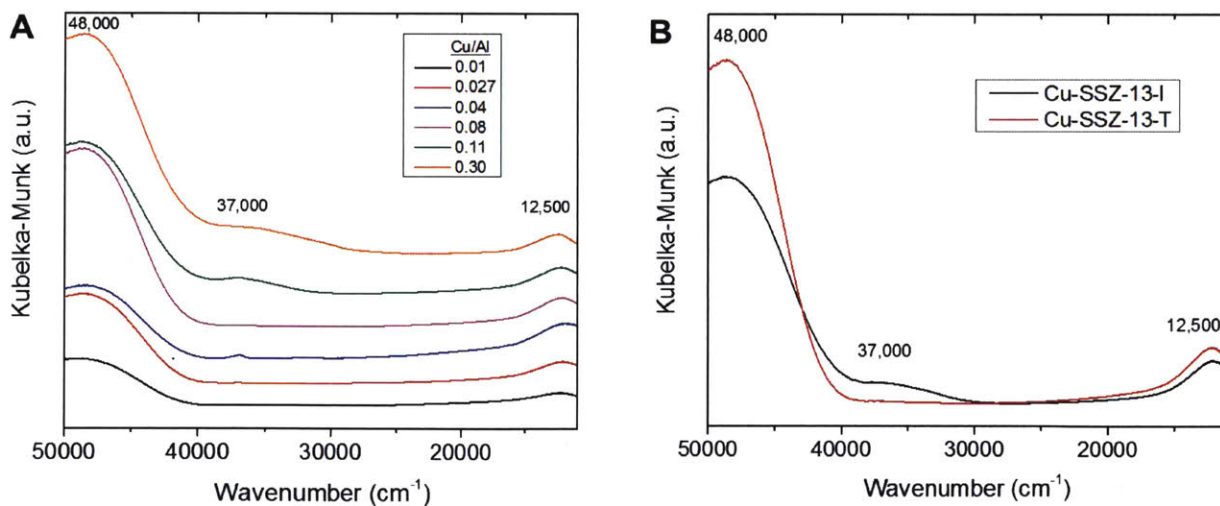


Figure S4-7. UV-visible spectroscopy of fresh Cu-SSZ-13 zeolites. (A) Cu-SSZ-13-T zeolites (Si/Al = 13-16) vs. Cu/Al and (B) Cu-SSZ-13-I (Si/Al = 13.9, Cu/Al = 0.08) compared to Cu-SSZ-13-T (Si/Al = 14.7, Cu/Al = 0.08). All spectra were collected under ambient atmosphere.

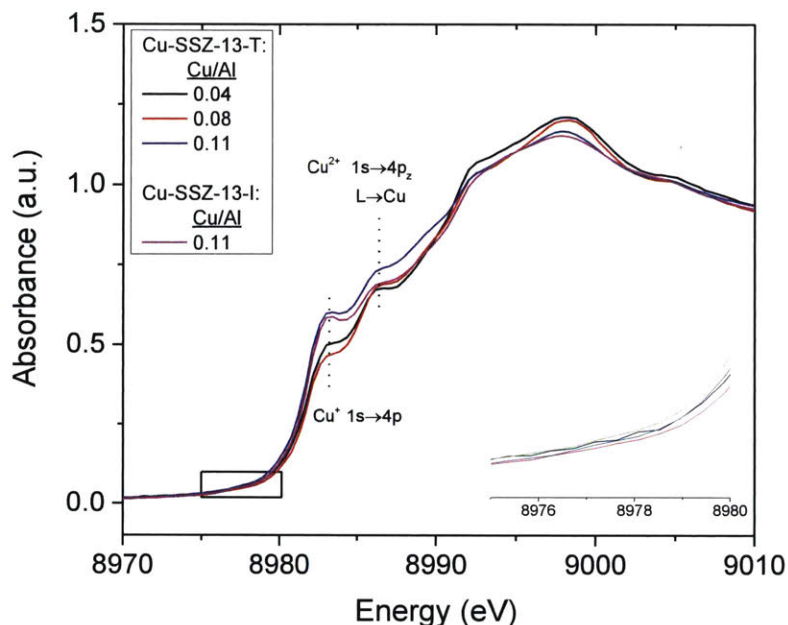


Figure S4-8. In-situ Cu K-edge XANES spectra of Cu-SSZ-13 zeolites. Cu-SSZ-13-T and Cu-SSZ-13-I zeolites (Si/Al = 13-16) were calcined under flowing 1% O_2 /He for 5 h at 823 K and cooled to 483 K before acquisition. Inset shows the magnification of the pre-edge region highlighted by the black box in the main panel.

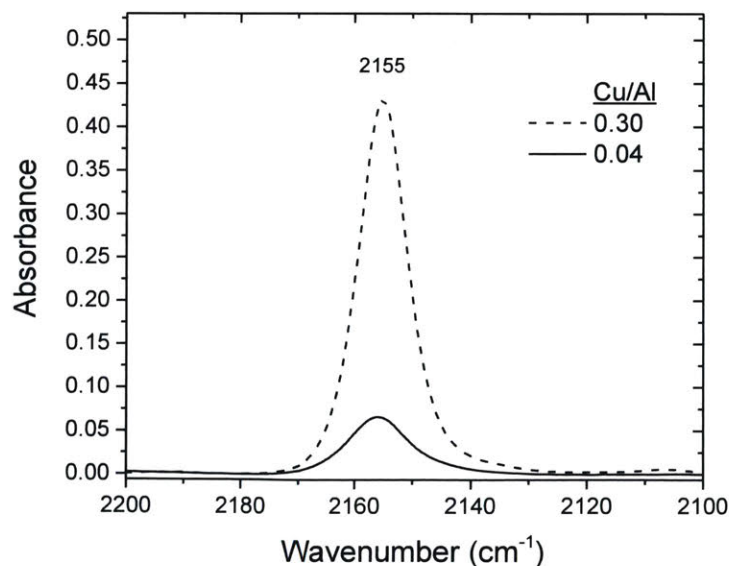


Figure S4-9. Infrared spectroscopy of CO-saturated Cu-SSZ-13-T (Si/Al = 14-16). Zeolite samples were activated under flowing 1% O_2 /He at 673 K for 3 h, cooled to 298 K, and then purged under flowing He before the introduction of CO. After saturation with CO, the sample was purged under flowing He for 1 h.

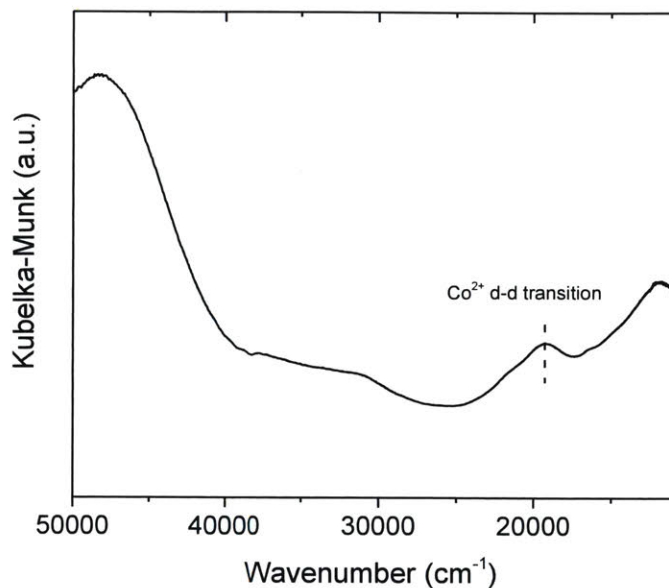


Figure S4-10. UV-visible spectroscopy of Cu-SSZ-13-T (Si/Al = 13.1, Cu/Al = 0.29) exchanged with Co. Final composition: Si/Al = 13.1, Co/Al = 0.05). All spectra were collected under ambient atmosphere.

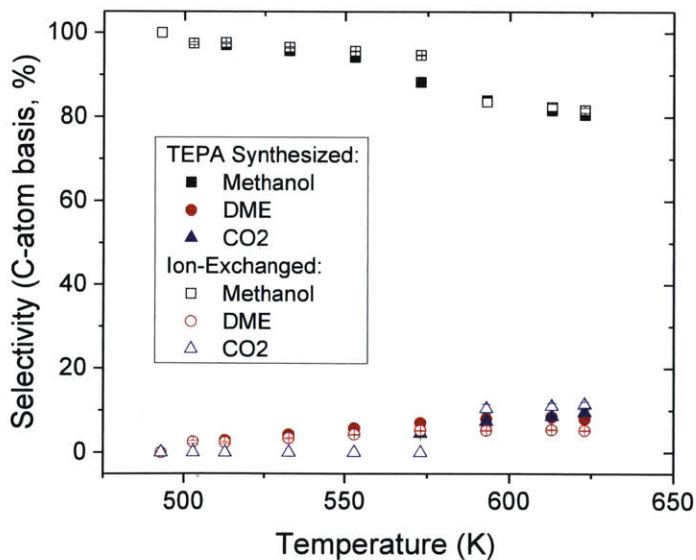


Figure S4-11. Product selectivity vs temperature over Cu-SSZ-13-T (Si/Al = 14.7, Cu/Al = 0.08) and Cu-SSZ-13-I (Si/Al = 13.9, Cu/Al = 0.08). Catalyst Pretreatment: 5 h under 1% O₂/He at 823 K, cooled to 493 K, and exposed to 6000 mL h⁻¹ g_{cat}⁻¹ of 88.3 kPa CH₄, 3.2 kPa H₂O, 0.098 kPa O₂, He balance for 4 h; Reaction Conditions: WHSV = 6000 mL h⁻¹ g_{cat}⁻¹, P_{CH₄} = 88.3 kPa, P_{H₂O} = 3.2 kPa, P_{O₂} = 0.098 kPa.

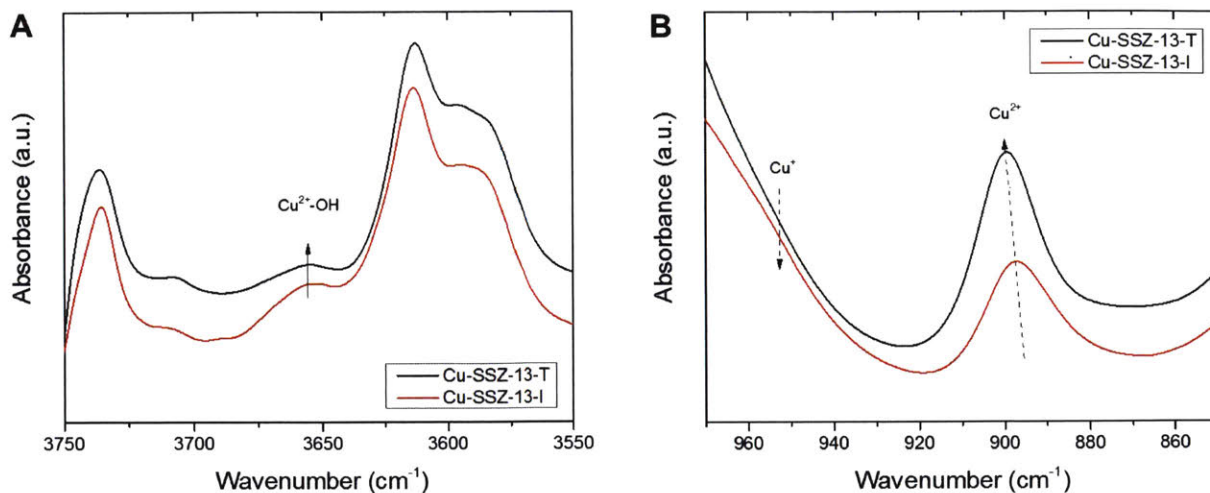


Figure S4-12. Infrared spectroscopy of Cu-SSZ-13-T (Si/Al = 14.7, Cu/Al = 0.08) and Cu-SSZ-13-I (Si/Al = 13.9, Cu/Al = 0.08). Zeolite samples were activated under flowing 1% O₂/He at 673 K for 3 h, cooled to 298 K, and then purged under flowing He before acquisition.

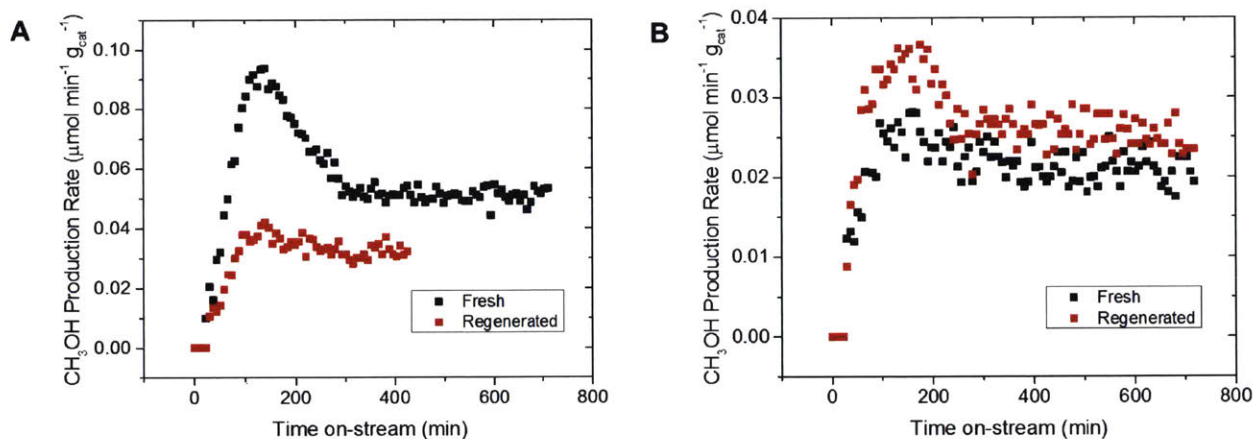


Figure S4-13. CH₄ oxidation before and after reaction over Cu-SSZ-13-T. Fresh denotes catalyst before any CH₄ oxidation reactions. Regenerated denotes Cu-SSZ-13-T that underwent CH₄ oxidation and was then recalcined in-situ before another set of reactions. A) Si/Al = 14.9, Cu/Al = 0.04. Underwent CH₄ oxidation up to 643 K before in-situ calcination. B) Si/Al = 25.1, Cu/Al = 0.05. Underwent CH₄ oxidation up to 673 K before in-situ calcination. Catalyst Pretreatment: 5 h under 1% O₂/He at 823 K, cooled to 493 K, and exposed to 6000 mL h⁻¹ g_{cat}⁻¹ of 88.3 kPa CH₄, 3.2 kPa H₂O, 0.098 kPa O₂, He balance for 4 h; Reaction Conditions: WHSV = 6000 mL h⁻¹ g_{cat}⁻¹, P_{CH₄} = 88.3 kPa, P_{H₂O} = 3.2 kPa, P_{O₂} = 0.098 kPa.

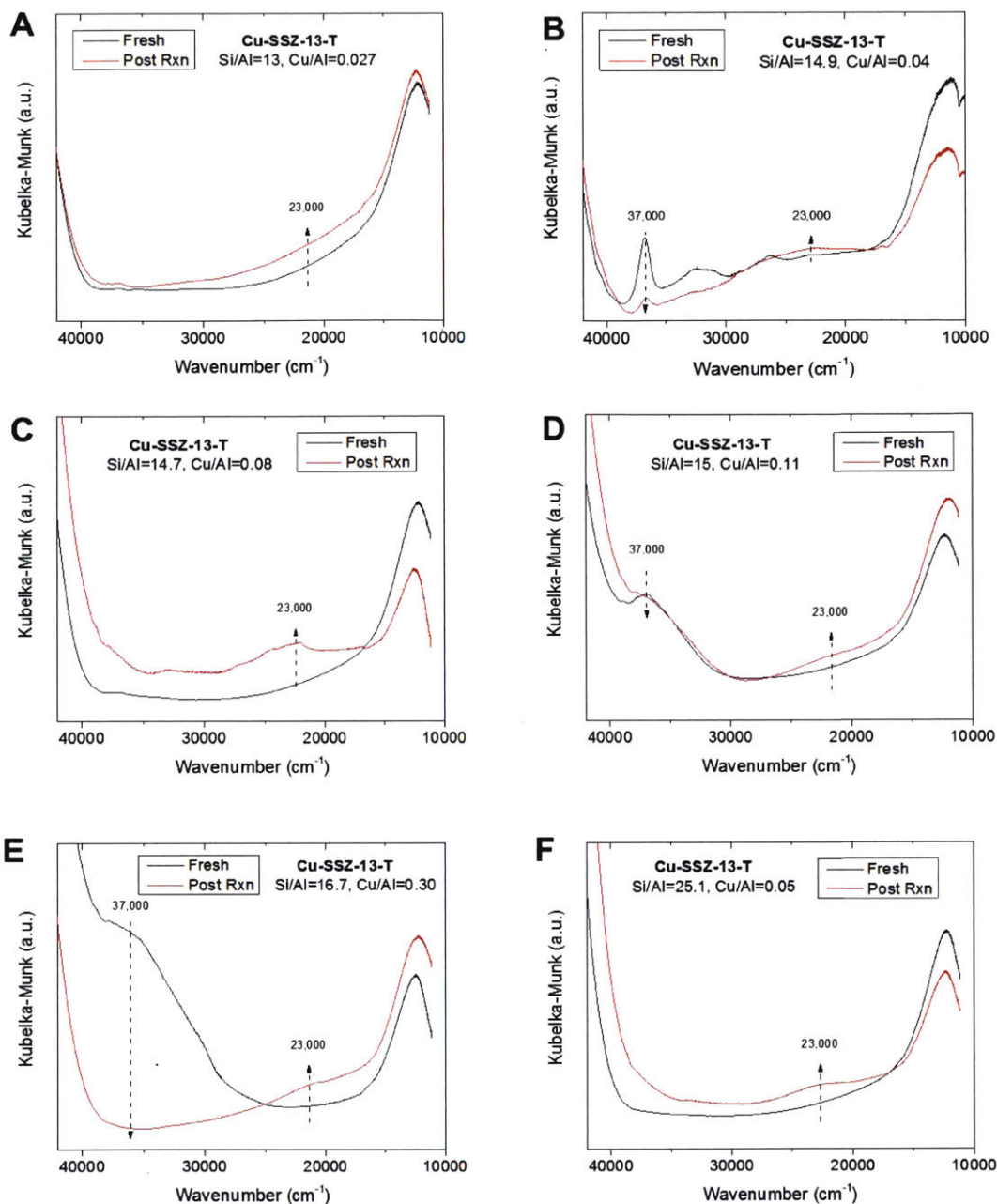


Figure S4-14. UV-visible spectroscopy of fresh and post reaction Cu-SSZ-13-T zeolites. Fresh denotes catalyst before any CH₄ oxidation reactions. Regenerated denotes Cu-SSZ-13-T that underwent CH₄ oxidation and was then recalcined in-situ before another set of reactions. (A)-(E) Underwent CH₄ oxidation up to 643 K before in-situ calcination. (F) Underwent CH₄ oxidation up to 673 K before in-situ calcination. Catalyst Pretreatment: 5 h under 1% O₂/He at 823 K, cooled to 493 K, and exposed to 6000 mL h⁻¹ g_{cat}⁻¹ of 88.3 kPa CH₄, 3.2 kPa H₂O, 0.098 kPa O₂, He balance for 4 h; Reaction Conditions: WHSV = 6000 mL h⁻¹ g_{cat}⁻¹, P_{CH₄} = 88.3 kPa, P_{H₂O} = 3.2 kPa, P_{O₂} = 0.098 kPa. All spectra were collected under ambient atmosphere.

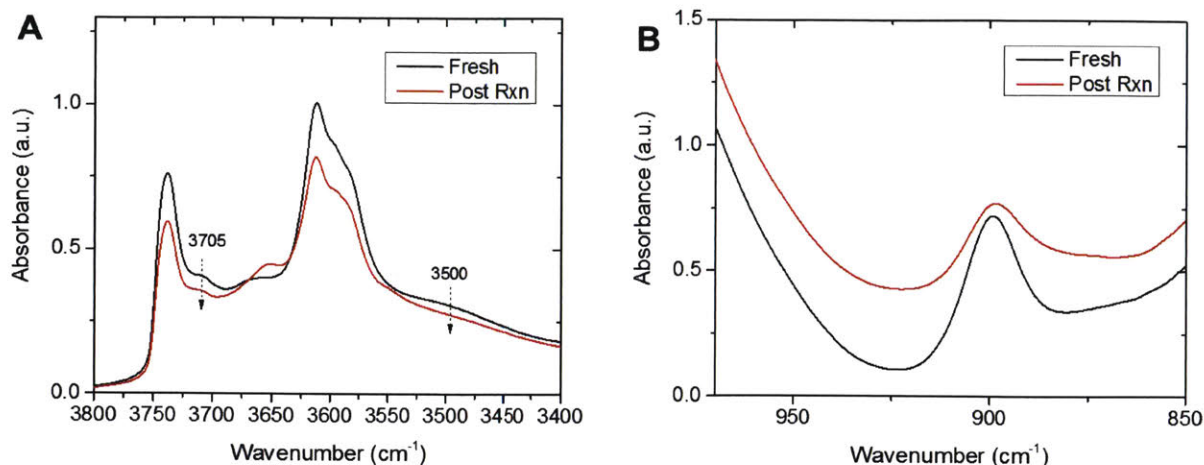


Figure S4-15. Infrared spectroscopy of fresh and post reaction Cu-SSZ-13-T (Si/Al = 14.9, Cu/Al = 0.04). Fresh denotes catalyst before any CH₄ oxidation reactions. Regenerated denotes Cu-SSZ-13-T that underwent CH₄ oxidation up to 643 K and was then recalcined in-situ before another reaction at 493 K. Catalyst Pretreatment: 5 h under 1% O₂/He at 823 K, cooled to 493 K, and exposed to 6000 mL h⁻¹ g_{cat}⁻¹ of 88.3 kPa CH₄, 3.2 kPa H₂O, 0.098 kPa O₂, He balance for 4 h; Reaction Conditions: WHSV = 6000 mL h⁻¹ g_{cat}⁻¹, P_{CH₄} = 88.3 kPa, P_{H₂O} = 3.2 kPa, P_{O₂} = 0.098 kPa. Zeolite samples were activated under flowing 1% O₂/He at 673 K for 3 h, cooled to 298 K, and then purged under flowing He before acquisition.

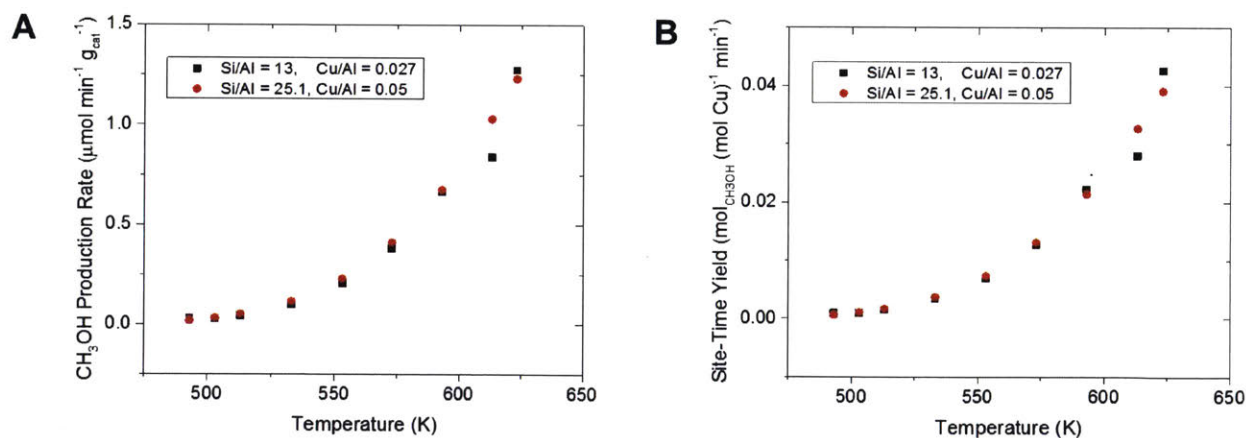


Figure S4-16. CH₄ oxidation over Cu-SSZ-13-T with 0.20 Cu wt% vs. temperature. Catalyst Pretreatment: 5 h under 1% O₂/He at 823 K, cooled to 493 K, and exposed to 6000 mL h⁻¹ g_{cat}⁻¹ of 88.3 kPa CH₄, 3.2 kPa H₂O, 0.098 kPa O₂, He balance for 4 h; Reaction Conditions: WHSV = 6000 mL h⁻¹ g_{cat}⁻¹, P_{CH₄} = 88.3 kPa, P_{H₂O} = 3.2 kPa, P_{O₂} = 0.098 kPa.

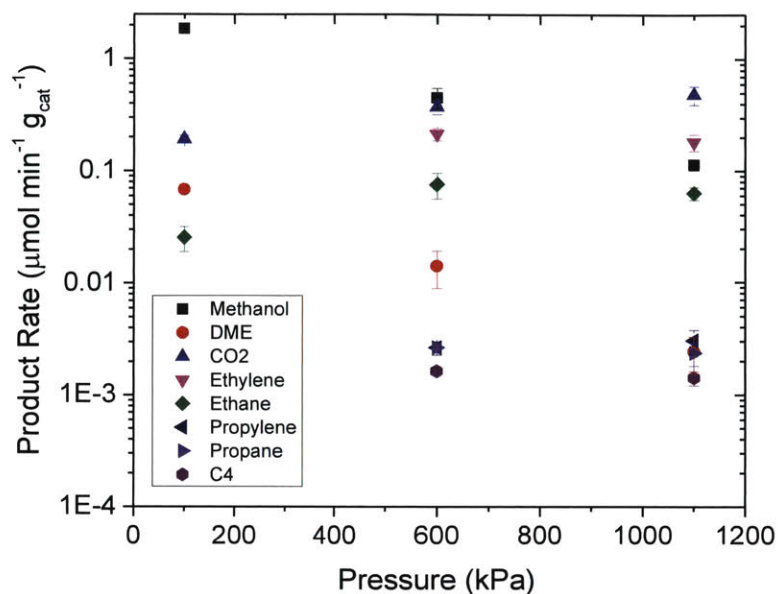


Figure S4-17. CH_4 oxidation coupled with CH_3OH -to-olefins over Cu-SSZ-13-T (Si/Al = 24.7, Cu/Al = 0.09). Catalyst Pretreatment: 5 h under 1% O_2/He at 823 K, cooled to 493 K, and exposed to $6000 \text{ mL h}^{-1} \text{g}_{\text{cat}}^{-1}$ of 88.3 kPa CH_4 , 3.2 kPa H_2O , 0.098 kPa O_2 , He balance for 4 h; Reaction Conditions: $T = 643 \text{ K}$, $\text{WHSV} = 6000 \text{ mL h}^{-1} \text{g}_{\text{cat}}^{-1}$, $P_{\text{CH}_4}:P_{\text{O}_2}:P_{\text{He}} = 901:1:99$; $P_{\text{H}_2\text{O}} = 3.2 \text{ kPa}$, Time = 7 h for each pressure.

Chapter 5 : Conclusions and Outlook

5.1 Contributions to Catalysis

The objective of the work presented in this thesis is to engineer a process to utilize copper-exchanged zeolites as highly active catalysts to directly oxidize methane into methanol 1) at low temperature, 2) in the vapor phase, and 3) using only molecular oxygen as the oxidizing agent. The primary strategy to aid in designing this process was to understand the reaction mechanisms and structure of the active sites in copper-exchanged zeolites. While this goal was not fully achieved, this work lays the foundation for designing copper-exchanged zeolite catalysts with greater activity for commercial development.

Three contributions have been made towards developing a highly active copper-exchanged zeolite catalyst for the direct oxidation of methane into methanol. First, experimental evidence has been obtained showing that after stoichiometric methane oxidation over copper-exchanged ZSM-5 and MOR, methoxy species are localized onto Bronsted acid sites instead of the copper active sites. Methoxy species on Bronsted acid sites are intermediates for a variety of reactions,¹⁷³ indicating that methane can be an even more versatile platform chemical in the future. More importantly, this parallel pathway provides evidence of surface spillover on copper-exchanged zeolite surfaces, possibly enabling the copper active sites to catalytically turn over. Second, a process for catalytic methane oxidation into methanol over copper-exchanged zeolites has been developed. Because surface spillover occurs over copper-exchanged zeolites, steady-state methanol production over commercially available zeolites is sustained with a mixture of flowing methane, oxygen, and water. Catalytic activity is highly stable and selective for methanol production. Third, catalytic activity is further improved through the synthetic control of copper speciation in copper-exchanged SSZ-13. The structure directing agent tetraethylenepentamine directs isolated Cu^{2+} species in SSZ-13 zeolites which strongly correlate with catalytic activity, implying some Cu^{2+} site serves as the precursor to the catalytic site. Initial optimization of the amount of isolated Cu^{2+} species in SSZ-13 exhibits 50% improvement over uncontrolled ion-exchanged SSZ-13 and over 100-fold improvement compared to ZSM-5 and MOR zeolites.

The insight of an isolated Cu^{2+} species as the precursor to the catalytic site for methane oxidation will greatly help in directing experiments and calculations of the structure of the catalytic site. Density functional theory has been employed to suggest certain copper-oxo structures anchored inside zeolite channels.^{118, 122, 126, 140, 211, 227} However,

the number of degrees of freedom with respect to the size of copper-oxo complexes, its location within zeolites, and the adsorption of reactants is staggering. Experimental evidence suggesting an isolated copper catalytic active site in SSZ-13 guides computational chemists to a small subset of all possible copper species, greatly speeding their search. As computational power and accuracy grows with time, it is only a matter of time before the catalytic site structure and reaction mechanism is determined.

5.2 Limitations of Current Work

While catalytic methanol production has been greatly improved from conventionally prepared copper-exchanged ZSM-5 or MOR, activity must be increased by at least one order of magnitude before the catalyst and process presented in Chapter 4 will be of industrial interest. At a reforming facility at a shale gas well, methane would be co-fed with air and water vapor into a reactor loaded with Cu-SSZ-13. The methanol and water exiting the reactor would be condensed while the gaseous reactants/products would be either recycled into the reactor or flared. The product methanol would then be purified through distillation. However, under the reaction conditions outlined in Chapter 4, the molar ratio of methanol:water exiting the reactor is less than 0.02. Distillation efficiency is drastically reduced at lower than 10 weight percent methanol.²²⁸ Methane conversion and methanol concentration can be increased by recycling the product stream into the reactor, but the slow kinetics of methane oxidation over Cu-SSZ-13 would require high recycle ratios and could render the entire process uneconomical. Copper-exchanged zeolites must be designed with more active sites or the reaction conditions must be engineered to increase methane conversion and reduce separation costs.

Catalytic activity in copper-exchanged zeolites can be increased by loading more copper, thereby creating more active sites. However, as discussed in Chapter 4, the likelihood of sintering of copper ions into oxide particles increases with copper loading due to shorter distances between ions with concomitant deactivation in catalytic activity. Coking was also observed after long reaction times above 623 K. Calcination of the zeolite did not regenerate catalytic activity. Permanent deactivation of the zeolite could be catastrophic because copper oxide particles catalyze CO₂ production.²²⁶ Thus, the deactivated catalyst must be replaced by fresh catalyst, thereby adding cost and possible down time to the process. Strategies must be developed to mitigate copper sintering by either impeding movement of copper ions within the zeolite or further reducing the surface coverage of copper. The drawback of the latter strategy is the reduction in copper content will reduce methane oxidation activity of the zeolite.

5.3 Future Work and Directions:

About two years ago, we incorporated copper-exchanged zeolites into a process for the low temperature, catalytic oxidation of methane into methanol. While the catalytic activity has been improved two orders of magnitude since this initial discovery, catalyst properties and reaction conditions must be optimized to further improve catalyst activity as discussed above. Concurrently, much is unknown about the chemistry occurring over these copper-exchanged zeolites including, but not limited to, the structure of the active site, the reaction mechanism, and effect of zeolite topology. Lastly, the one-pot synthesis of metal-exchanged SSZ-13 zeolites with tetraethylenepentamine structure directing agents has sufficiently increased methanol production where other reactions with methanol can be observed. An extremely interesting prospect will be coupling methane oxidation with these chemistries such as methanol-to-olefins or methanol dehydration. These respective directions are discussed in more detail below.

Optimization of Methane Oxidation Activity

As discussed above, methane conversion must be increased from 0.1% to at least 1% in order to be of industrial interest. Barring synthetic advances in the preparation of copper-exchanged zeolites with a greater number of active sites, the process variables of interest are copper and aluminum content of the zeolite, reaction temperature, pressure, and space velocity.

We have demonstrated Cu-SSZ-13 zeolites have higher methanol production at higher copper content. However, as discussed earlier, sintering of copper into oxide particles catalyzes CO₂ production, and deactivation of the zeolite becomes more apparent at higher copper loading. This can be rectified by increasing the distance between copper ions by reducing the aluminum content in zeolites, but this strategy also reduces copper loading and methanol production. An optimum value of copper and aluminum content in the zeolite must exist to maximize methanol production while minimizing sintering and CO₂ production.

The same tradeoff for methanol and CO₂ production exists as a function of reaction temperature. In Cu-SSZ-13, methanol production increases according to Arrhenius behavior up to about 573 K. Thereafter methanol over oxidizes into CO₂. However, the maximum temperature in which Cu-SSZ-13 obeys Arrhenius behavior increases as copper loading is reduced. The problem now lies in finding the intermediate copper content in

Cu-SSZ-13 such that the sintering of copper into oxides is minimized at higher temperature while achieving high methanol production rates and selectivity.

The pressure at which the methane oxidation reaction is performed has a straightforward effect on methane oxidation activity. On Cu-ZSM-5, increasing the reaction pressure linearly increased methanol production rates at 483 K, consistent with a first order dependence on methane partial pressure. Thus, increasing the reaction pressure at higher temperature should also increase the methanol production rate. However, the residence time of reactants within the reactor will increase for space velocity at higher reaction pressure, possibly catalyzing side reactions or CO₂ production. Once again, methanol production is intimately related to the reaction pressure and reaction temperature and must be simultaneously optimized with respect to both variables.

Due to the complex relationship between all the process variables highlighted above, a systematic study will be needed across the entire engineering space. It will be prudent to approach these studies according to a design of experiments model to direct which experiments to target first. Additional insight can be gained from building a macrokinetic model to simulate the methane conversion and methanol selectivity as a function of each process variable. This will become especially important in predicting methanol selectivity at > 1% methane conversion because higher methanol partial pressures in the presence of oxygen will favor oxidation into CO₂.

Understanding the Catalytic Site and Reaction Mechanism

The catalytic site and reaction mechanism in copper-exchanged SSZ-13 and other zeolites have not yet been identified. We have made several observations relating copper content, zeolite topology, and counter-cation type to methanol production rates. These three avenues will provide a starting point to characterize the active site and reaction mechanism.

In SSZ-13 and other commercially available zeolite topologies, site-time yield increases at low copper loadings, implying fewer spectator species at low loadings. This is consistent with detailed reaction studies over Cu-SSZ-13 suggesting the catalytic site is an isolated copper ion. Further characterization of the catalytic site should focus on copper-exchanged zeolites at extremely low loadings (Cu/Al < 0.10). Low copper loadings in zeolites afford more homogeneous copper speciation and fewer spectator species. These advantages should make spectroscopic signatures associated with the active site or intermediates more apparent during *in-situ* studies. However, low copper loading will give low signal-to-noise relative to the zeolite support where bulk techniques, such as

powder x-ray diffraction and x-ray absorption spectroscopy, may not give enough signal to be informative. The best chance of characterizing the active site is to use in-situ spectroscopic techniques sensitive to atoms bonded directly to copper atoms, such as Raman, infrared, and UV-visible spectroscopy. Isotopically labelled techniques, such as steady-state isotopic transient kinetic analysis, will indicate the surface coverages of intermediates and the rate determining step.

Methanol production rates are further affected by the size of channels and cages within the zeolite. In zeolite topologies with only channels, ZSM-5 of medium pore sizes was found to have the highest catalytic rate compared to large pore BEA and small pore MOR and FER while the apparent activation energy was higher for smaller pore MOR than ZSM-5. However, methanol production rates further increased for SSZ-13, a zeolite topology with small pores and cages. Based on these results, confinement effects of the zeolite framework drastically affect methane oxidation. Because topologies with cages are the most active, a detailed kinetic, *in-situ* spectroscopic, and computational study of the cage shape and size (CHA, AEI, AFX, RTH) should be performed to understand how the zeolite cages affect the copper speciation, the active sites, and stabilize the transition states of methane oxidation. This information will aid in engineering the ideal support for the copper active sites.

Lastly, the apparent activation energy and catalytic rates were higher when Bronsted acidity was present in the copper-exchanged zeolites as compared to the sodium parent zeolites. Changes in the activation energy suggest the copper active sites interacts with nearby counter cations in the rate-determining step, consistent with recent density functional theory calculations.¹²⁶ The role of the counter-cation can be studied by using different alkali or alkaline earth cations of different size, charge, and Lewis acidity. The interaction of the copper active site with other counter-cations and the zeolite framework can be further modulated by isomorphous substitution of framework aluminum or silicon atoms with other +3 or +4 ions. Zeolites can be made with boron or gallium (+3) in combination with germanium (+4) to modulate the acidity of the zeolite framework. Tuning the acidity of the zeolite framework will allow the precise control of the electron density in the copper ions and ultimately influence the reactivity of the catalytic site.

Methane Oxidation Coupled with Other Reactions

The one-pot synthesis of Cu-SSZ-13 zeolites with tetraethylenepentamine improved the catalytic methanol production rate such that C₂ and C₃ alkanes and olefins were observed, evidence of tandem methane oxidation and methanol-to-olefins reactions. Being

able to directly produce olefins from methane will be of tremendous significance in the energy industry. Olefin selectivity, catalyst stability, and catalytic rates should be optimized under the same strategy outlined for maximizing methane conversion. Several other reactions involving methanol occur between 473-673 K in zeolite systems. First, acid-catalyzed methanol dehydration into dimethyl ether,¹⁸⁹⁻¹⁹⁰ an increasingly important transportation fuel, is already observed at elevated temperatures over Cu-SSZ-13 zeolites. The extent of this reaction can be modulated by the number of Bronsted acid sites and water partial pressure. Second, the methanol-to-gasoline reaction occurs over ZSM-5²⁷⁻²⁸ between 593-673K, potentially allowing C₅ alkanes or higher to be produced directly from methane over Cu-ZSM-5. There is already evidence of C₄ alkane production over copper-exchanged SSZ-13. Third, methanol carbonylation into acetic acid may be possible. MOR and FER zeolites with 8-MR side pockets undergo methanol carbonylation at 423-473 K at 0.1-1.6 MPa under CO atmosphere. Minimizing the reaction temperature and the partial pressure of water, a competitive adsorbant compared to CO, may permit catalytic production of acetic acid from methane over Cu-MOR. Testing and optimization of all these coupled reactions would be an exciting step for methane to become a versatile platform chemical.

Chapter 6 : References

1. Golisz, S.; Brent Gunnoe, T.; Goddard, W., III; Groves, J.; Periana, R., Chemistry in the Center for Catalytic Hydrocarbon Functionalization: An Energy Frontier Research Center. *Catalysis Letters* **2011**, *141* (2), 213-221.
2. Natural Gas Gross Withdrawals and Production. September 30, 2016 ed.; United States Energy Information Administration: online, 2016.
3. Short-Term Energy Outlook. September 7, 2016 ed.; United States Energy Information Administration: online, 2016; Vol. 2016.
4. ExxonMobil *The Outlook for Energy: A View to 2040*; online, 2011.
5. Technically Recoverable Shale Oil and Shale Gas Resources: An Assessment of 137 Shale Formations in 41 Countries Outside the United States. In *Analysis and Projections*, June 13, 2013 ed.; United States Energy Information Administration: online, 2013.
6. Cranmore, R. S., E, *Natural Gas*. John Wiley and Sons Ltd.: 2000; Vol. 1.
7. Thomas, S.; Dawe, R. A., Review of ways to transport natural gas energy from countries which do not need the gas for domestic use. *Energy* **2003**, *28* (14), 1461-1477.
8. Estimated Flared Volumes of Natural Gas from Satellite Data. <http://www.worldbank.org/en/programs/gasflaringreduction> (accessed October 1, 2016).
9. Saha, D.; Grappe, H. A.; Chakraborty, A.; Orkoulas, G., Postextraction Separation, On-Board Storage, and Catalytic Conversion of Methane in Natural Gas: A Review. *Chem. Rev.* **2016**.
10. Methanex Methanol Price Sheet, Sept. 28, 2016. (accessed October 1, 2016).
11. Table: Petroleum and Other Liquid Products. In *Annual Energy Outlook 2016*, 2016 ed.; United States Energy Information Administration: online, 2016.
12. Alvarado, M. The Changing Face of the Global Methanol Industry *IHS Chemical Week* [Online], 2016. <http://www.chemweek.com/lab/The-changing-face-of-the-global-methanol-industry'80172.html>.
13. *World Oil Outlook*; OPEC: 2011; p 286.
14. Xu, J.; Froment, G. F., Methane steam reforming, methanation and water-gas shift: I. Intrinsic kinetics. *AIChE J.* **1989**, *35* (1), 88-96.
15. Bengaard, H. S.; Nørskov, J. K.; Sehested, J.; Clausen, B.; Nielsen, L.; Molenbroek, A.; Rostrup-Nielsen, J., Steam reforming and graphite formation on Ni catalysts. *J. Catal.* **2002**, *209* (2), 365-384.
16. Besenbacher, F.; Chorkendorff, I.; Clausen, B.; Hammer, B.; Molenbroek, A.; Nørskov, J. K.; Stensgaard, I., Design of a surface alloy catalyst for steam reforming. *Science* **1998**, *279* (5358), 1913-1915.
17. Lange, J.-P., Methanol synthesis: a short review of technology improvements. *Catal. Today* **2001**, *64* (1-2), 3-8.
18. Nerlov, J.; Chorkendorff, I., Methanol Synthesis from CO₂, CO, and H₂ over Cu (100) and Ni/Cu (100). *J. Catal.* **1999**, *181* (2), 271-279.
19. Chinchin, G. C.; Denny, P. J.; Parker, D. G.; Spencer, M. S.; Whan, D. A., Mechanism of methanol synthesis from CO₂/CO/H₂ mixtures over copper/zinc oxide/alumina catalysts: use of ¹⁴C-labelled reactants. *Applied Catalysis* **1987**, *30* (2), 333-338.
20. De Klerk, A. In *Gas-to-Liquids Conversion*, Natural Gas Conversion Technologies Workshop, Houston, TX, USA, ARPA-E, United States Department of Energy: Houston, TX, USA, 2012.
21. Iglesia, E., Design, synthesis, and use of cobalt-based Fischer-Tropsch synthesis catalysts. *Appl. Catal., A* **1997**, *161* (1), 59-78.

22. Schulz, H., Short history and present trends of Fischer–Tropsch synthesis. *Appl. Catal., A* **1999**, *186* (1–2), 3–12.
23. Wood, D. A.; Nwaoha, C.; Towler, B. F., Gas-to-liquids (GTL): A review of an industry offering several routes for monetizing natural gas. *Journal of Natural Gas Science and Engineering* **2012**, *9*, 196–208.
24. Dejaifve, P.; Védrine, J. C.; Bolis, V.; Derouane, E. G., Reaction pathways for the conversion of methanol and olefins on H-ZSM-5 zeolite. *J. Catal.* **1980**, *63* (2), 331–345.
25. Chang, C. D.; Chu, C. T.; Socha, R. F., Methanol conversion to olefins over ZSM-5: I. Effect of temperature and zeolite SiO₂Al₂O₃. *J. Catal.* **1984**, *86* (2), 289–296.
26. McCann, D. M.; Lesthaeghe, D.; Kletnieks, P. W.; Guenther, D. R.; Hayman, M. J.; Van Speybroeck, V.; Waroquier, M.; Haw, J. F., A Complete Catalytic Cycle for Supramolecular Methanol-to-Olefins Conversion by Linking Theory with Experiment. *Angew. Chem.* **2008**, *120* (28), 5257–5260.
27. Chang, C. D.; Kuo, J. C.; Lang, W. H.; Jacob, S. M.; Wise, J. J.; Silvestri, A. J., Process studies on the conversion of methanol to gasoline. *Industrial & Engineering Chemistry Process Design and Development* **1978**, *17* (3), 255–260.
28. Mao, C.-H.; Schreiner Jr, M., Methanol-to-gasoline. Google Patents: 1987.
29. Goguen, P. W.; Xu, T.; Barich, D. H.; Skloss, T. W.; Song, W.; Wang, Z.; Nicholas, J. B.; Haw, J. F., Pulse-quench catalytic reactor studies reveal a carbon-pool mechanism in methanol-to-gasoline chemistry on zeolite HZSM-5. *J. Am. Chem. Soc.* **1998**, *120* (11), 2650–2651.
30. Chang, C. D., Hydrocarbons from methanol. *Catalysis Reviews Science and Engineering* **1983**, *25* (1), 1–118.
31. Sunley, G. J.; Watson, D. J., High productivity methanol carbonylation catalysis using iridium: The Cativa™ process for the manufacture of acetic acid. *Catal. Today* **2000**, *58* (4), 293–307.
32. King, S. T., Reaction Mechanism of Oxidative Carbonylation of Methanol to Dimethyl Carbonate in Cu–Y Zeolite. *J. Catal.* **1996**, *161* (2), 530–538.
33. Ellis, B.; Howard, M. J.; Joyner, R. W.; Reddy, K. N.; Padley, M. B.; Smith, W. J., Heterogeneous catalysts for the direct, halide-free carbonylation of methanol. 1996; Vol. 101 B, pp 771–779.
34. Fujimoto, K.; Shikada, T.; Omata, K.; Tominaga, H.-o., VAPOR PHASE CARBONYLATION OF METHANOL WITH SOLID ACID CATALYSTS. *Chem. Lett.* **1984**, *13* (12), 2047–2050.
35. Xu, M.; Lunsford, J. H.; Goodman, D. W.; Bhattacharyya, A., Synthesis of dimethyl ether (DME) from methanol over solid-acid catalysts. *Appl. Catal., A* **1997**, *149* (2), 289–301.
36. Olah, G. A., Beyond oil and gas: the methanol economy. *Angew. Chem. Int. Ed.* **2005**, *44* (18), 2636–2639.
37. Prakash, G. K. S.; Olah, G. A.; Smart, M. C.; Narayanan, S. R.; Wang, Q. J.; Surumpudi, S.; Halpert, G., Polymer electrolyte membranes for use in fuel cells. Google Patents: 2002.
38. Lunsford, J. H., Catalytic conversion of methane to more useful chemicals and fuels: a challenge for the 21st century. *Catal. Today* **2000**, *63* (2–4), 165–174.
39. Holmen, A., Direct conversion of methane to fuels and chemicals. *Catal. Today* **2009**, *142* (1), 2–8.
40. *Petroleum Economist* [Online], 2008, p. 36–38.
41. Patel, B. In *Gas monetisation: a techno-economic comparison of gas-to-liquid and LNG*, 7th World Congress of Chemical Engineering, Glasgow, 2005.
42. Tan, S. H.; Barton, P. I., Optimal dynamic allocation of mobile plants to monetize associated or stranded natural gas, part I: Bakken shale play case study. *Energy* **2015**, *93*, Part 2, 1581–1594.

43. Tan, S. H.; Barton, P. I., Optimal dynamic allocation of mobile plants to monetize associated or stranded natural gas, part II: Dealing with uncertainty. *Energy* **2016**, *96*, 461-467.
44. Wood, D. A. M., S., Monetizing Stranded Gas: Gas Monetization Technologies Remain Tantalizingly on the Brink. *World Oil* 2008, pp 103-108.
45. Fenwick, S. In *Access to GTL Technology is Key*, World XTL Summit, Global Technology Forum: 2012.
46. Palkovits, R.; Antonietti, M.; Kuhn, P.; Thomas, A.; Schüth, F., Solid catalysts for the selective low-temperature oxidation of methane to methanol. *Angew. Chem. Int. Ed.* **2009**, *48* (37), 6909-6912.
47. Tabata, K.; Teng, Y.; Takemoto, T.; Suzuki, E.; Bañares, M. A.; Peña, M. A.; Fierro, J. L. G., Activation of methane by oxygen and nitrogen oxides. *Catalysis Reviews* **2002**, *44* (1), 1-58.
48. Faraldos, M.; Bañares, M. A.; Anderson, J. A.; Hu, H.; Wachs, I. E.; Fierro, J. L. G., Comparison of silica-supported MoO₃ and V₂O₅ catalysts in the selective partial oxidation of methane. *J. Catal.* **1996**, *160* (2), 214-221.
49. Chempath, S.; Bell, A. T., A DFT study of the mechanism and kinetics of methane oxidation to formaldehyde occurring on silica-supported molybdena. *J. Catal.* **2007**, *247* (1), 119-126.
50. Barbero, J. A.; Alvarez, M. C.; Banares, M. A.; Pena, M. A.; Fierro, J. L. G., Breakthrough in the direct conversion of methane into C₁-oxygenates. *Chem. Commun.* **2002**, (11), 1184-1185.
51. Zalc, J. M.; Green, W. H.; Iglesia, E., NO_x-Mediated Homogeneous Pathways for the Synthesis of Formaldehyde from CH₄-O₂ Mixtures. *Ind. Eng. Chem. Res.* **2006**, *45* (8), 2677-2688.
52. Periana, R. A.; Taube, D. J.; Gamble, S.; Taube, H.; Satoh, T.; Fujii, H., Platinum catalysts for the high-yield oxidation of methane to a methanol derivative. *Science* **1998**, *280* (5363), 560-564.
53. Palkovits, R.; Antonietti, M.; Kuhn, P.; Thomas, A.; Schüth, F., Solid Catalysts for the Selective Low-Temperature Oxidation of Methane to Methanol. *Angew. Chem. Int. Ed.* **2009**, *48* (37), 6909-6912.
54. Rosenzweig, A. C.; Frederick, C. A.; Lippard, S. J., Crystal structure of a bacterial non-haem iron hydroxylase that catalyses the biological oxidation of methane. **1993**.
55. Himes, R. A.; Barnese, K.; Karlin, K. D., One is lonely and three is a crowd: two coppers are for methane oxidation. *Angew. Chem. Int. Ed.* **2010**, *49* (38), 6714-6716.
56. Chan, S. I.; Lu, Y. J.; Nagababu, P.; Maji, S.; Hung, M. C.; Lee, M. M.; Hsu, I. J.; Minh, P. D.; Lai, J. C. H.; Ng, K. Y., Efficient Oxidation of Methane to Methanol by Dioxygen Mediated by Tricopper Clusters. *Angew. Chem.* **2013**, *125* (13), 3819-3823.
57. Chan, S. I.; Chen, K. H. C.; Yu, S. S. F.; Chen, C.-L.; Kuo, S. S. J., Toward Delineating the Structure and Function of the Particulate Methane Monooxygenase from Methanotrophic Bacteria. *Biochemistry* **2004**, *43* (15), 4421-4430.
58. Balasubramanian, R.; Smith, S. M.; Rawat, S.; Yatsunyk, L. A.; Stemmler, T. L.; Rosenzweig, A. C., Oxidation of methane by a biological dicopper centre. *Nature* **2010**, *465* (7294), 115-119.
59. Bordeaux, M.; Galarneau, A.; Drone, J., Catalytic, Mild, and Selective Oxyfunctionalization of Linear Alkanes: Current Challenges. *Angew. Chem. Int. Ed.* **2012**, *51* (43), 10712-10723.
60. Nguyen, H.-H. T.; Elliott, S. J.; Yip, J. H.-K.; Chan, S. I., The Particulate Methane Monooxygenase from *Methylococcus capsulatus* (Bath) Is a Novel Copper-containing Three-subunit Enzyme: ISOLATION AND CHARACTERIZATION. *J. Biol. Chem.* **1998**, *273* (14), 7957-7966.

61. Dubkov, K.; Sobolev, V.; Panov, G., Low-temperature oxidation of methane to methanol on FeZSM-5 zeolite. *Kinet. Catal.* **1998**, *39* (1), 72-79.
62. Starokon, E. V.; Parfenov, M. V.; Pirutko, L. V.; Abornev, S. I.; Panov, G. I., Room-temperature oxidation of methane by α -oxygen and extraction of products from the FeZSM-5 surface. *J. Phys. Chem. C* **2011**, *115* (5), 2155-2161.
63. Hammond, C.; Forde, M. M.; Ab Rahim, M. H.; Thetford, A.; He, Q.; Jenkins, R. L.; Dimitratos, N.; Lopez-Sanchez, J. A.; Dummer, N. F.; Murphy, D. M.; Carley, A. F.; Taylor, S. H.; Willock, D. J.; Stangland, E. E.; Kang, J.; Hagen, H.; Kiely, C. J.; Hutchings, G. J., Direct Catalytic Conversion of Methane to Methanol in an Aqueous Medium by using Copper-Promoted Fe-ZSM-5. *Angew. Chem. Int. Ed.* **2012**, *51* (21), 5129-5133.
64. Hammond, C.; Dimitratos, N.; Jenkins, R. L.; Lopez-Sanchez, J. A.; Kondrat, S. A.; Hasbi ab Rahim, M.; Forde, M. M.; Thetford, A.; Taylor, S. H.; Hagen, H., Elucidation and Evolution of the Active Component within Cu/Fe/ZSM-5 for Catalytic Methane Oxidation: From Synthesis to Catalysis. *ACS Catal.* **2013**, *3* (4), 689-699.
65. Hammond, C.; Dimitratos, N.; Lopez-Sanchez, J. A.; Jenkins, R. L.; Whiting, G.; Kondrat, S. A.; ab Rahim, M. H.; Forde, M. M.; Thetford, A.; Hagen, H., Aqueous-phase methane oxidation over Fe-MFI Zeolites; promotion through isomorphous framework substitution. *ACS Catal.* **2013**, *3* (8), 1835-1844.
66. Groothaert, M. H.; Smeets, P. J.; Sels, B. F.; Jacobs, P. A.; Schoonheydt, R. A., Selective oxidation of methane by the bis (μ -oxo) dicopper core stabilized on ZSM-5 and mordenite zeolites. *J. Am. Chem. Soc.* **2005**, *127* (5), 1394-1395.
67. Chen, J.; Li, J.; Wei, Y.; Yuan, C.; Li, B.; Xu, S.; Zhou, Y.; Wang, J.; Zhang, M.; Liu, Z., Spatial confinement effects of cage-type SAPO molecular sieves on product distribution and coke formation in methanol-to-olefin reaction. *Catal. Commun.* **2014**, *46*, 36-40.
68. Baerlocher, C.; McCusker, L. B., Database of Zeolite Structures. 1996.
69. Young, L.; Butter, S.; Kaeding, W., Shape selective reactions with zeolite catalysts: III. Selectivity in xylene isomerization, toluene-methanol alkylation, and toluene disproportionation over ZSM-5 zeolite catalysts. *J. Catal.* **1982**, *76* (2), 418-432.
70. Chen, N. Y.; Lucki, S. J.; Garwood, W. E., Dewaxing of oils by shape selective cracking and hydrocracking over zeolites zsm-5 and zsm-8. Google Patents: 1972.
71. Chen, N.; Garwood, W., Some catalytic properties of ZSM-5, a new shape selective zeolite. *J. Catal.* **1978**, *52* (3), 453-458.
72. Chen, N. Y., *Shape selective catalysis in industrial applications*. CRC press: 1996; Vol. 65.
73. Bhan, A.; Iglesia, E., A Link between Reactivity and Local Structure in Acid Catalysis on Zeolites. *Acc. Chem. Res.* **2008**, *41* (4), 559-567.
74. Narsimhan, K.; Michaelis, V. K.; Mathies, G.; Gunther, W. R.; Griffin, R. G.; Román-Leshkov, Y., Methane to acetic acid over Cu-exchanged zeolites: mechanistic insights from a site-specific carbonylation reaction. *J. Am. Chem. Soc.* **2015**, *137* (5), 1825-1832.
75. Boronat, M.; Martínez, C.; Corma, A., Mechanistic differences between methanol and dimethyl ether carbonylation in side pockets and large channels of mordenite. *PCCP* **2011**, *13* (7), 2603-2612.
76. Boronat, M.; Martínez-Sánchez, C.; Law, D.; Corma, A., Enzyme-like Specificity in Zeolites: A Unique Site Position in Mordenite for Selective Carbonylation of Methanol and Dimethyl Ether with CO. *J. Am. Chem. Soc.* **2008**, *130* (48), 16316-16323.
77. Gounder, R.; Iglesia, E., Catalytic Consequences of Spatial Constraints and Acid Site Location for Monomolecular Alkane Activation on Zeolites. *J. Am. Chem. Soc.* **2009**, *131* (5), 1958-1971.

78. Lee, G.; Maj, J.; Rocke, S.; Garces, J., Shape selective alkylation of polynuclear aromatics with mordenite-type catalysts: A high yield synthesis of 4, 4'-Diisopropylbiphenyl. *Catalysis letters* **1989**, *2* (4), 243-247.
79. Kwak, J. H.; Tonkyn, R. G.; Kim, D. H.; Szanyi, J.; Peden, C. H., Excellent activity and selectivity of Cu-SSZ-13 in the selective catalytic reduction of NO_x with NH₃. *J. Catal.* **2010**, *275* (2), 187-190.
80. Gao, F.; Washton, N. M.; Wang, Y.; Kollár, M.; Szanyi, J.; Peden, C. H. F., Effects of Si/Al ratio on Cu/SSZ-13 NH₃-SCR catalysts: Implications for the active Cu species and the roles of Brønsted acidity. *J. Catal.* **2015**, *331*, 25-38.
81. Gounder, R.; Iglesia, E., Effects of partial confinement on the specificity of monomolecular alkane reactions for acid sites in side pockets of mordenite. *Angew. Chem. Int. Ed.* **2010**, *49* (4), 808-811.
82. Smeets, P. J.; Groothaert, M. H.; Schoonheydt, R. A., Cu based zeolites: A UV-vis study of the active site in the selective methane oxidation at low temperatures. *Catal. Today* **2005**, *110* (3), 303-309.
83. Li, Y.; Hall, W. K., Catalytic decomposition of nitric oxide over Cu-zeolites. *J. Catal.* **1991**, *129* (1), 202-215.
84. Matsumoto, S.; Yokota, K.; Doi, H.; Kimura, M.; Sekizawa, K.; Kasahara, S., Research on new DeNO_x catalysts for automotive engines. *Catal. Today* **1994**, *22* (1), 127-146.
85. Eder, F.; Stockenhuber, M.; Lercher, J., Brønsted acid site and pore controlled siting of alkane sorption in acidic molecular sieves. *J. Phys. Chem. B* **1997**, *101* (27), 5414-5419.
86. Jones, J. H., The Cativa Process for the Manufacture of Acetic Acid. *Platinum Met. Rev.* **2000**, *44* (3), 94.
87. Smith, W. J., Process for preparing carboxylic acids. Google Patents: 1995.
88. Ellis, B.; Howard, M. J.; Joyner, R. W.; Reddy, K. N.; Padley, M. B.; Smith, W. J., Heterogeneous catalysts for the direct, halide-free carbonylation of methanol. *Stud. Surf. Sci. Catal.* **1996**, *101*, 771-779.
89. Bhan, A.; Allian, A. D.; Sunley, G. J.; Law, D. J.; Iglesia, E., Specificity of Sites within Eight-Membered Ring Zeolite Channels for Carbonylation of Methyls to Acetyls. *J. Am. Chem. Soc.* **2007**, *129* (16), 4919-4924.
90. Corma, A., Inorganic solid acids and their use in acid-catalyzed hydrocarbon reactions. *Chem. Rev.* **1995**, *95* (3), 559-614.
91. Dědeček, J.; Kaucký, D.; Wichterlová, B.; Gonsiorová, O., Co²⁺ ions as probes of Al distribution in the framework of zeolites. ZSM-5 study. *PCCP* **2002**, *4* (21), 5406-5413.
92. Dědeček, J.; Sobalík, Z.; Wichterlová, B., Siting and distribution of framework aluminium atoms in silicon-rich zeolites and impact on catalysis. *Catalysis Reviews* **2012**, *54* (2), 135-223.
93. Dědeček, J.; Kaucký, D.; Wichterlova, B., Al distribution in ZSM-5 zeolites: an experimental study. *Chem. Commun.* **2001**, (11), 970-971.
94. Dědeček, J.; Wichterlová, B., Co²⁺ ion siting in pentasil-containing zeolites. I. Co²⁺ ion sites and their occupation in mordenite. A Vis-NIR diffuse reflectance spectroscopy study. *J. Phys. Chem. B* **1999**, *103* (9), 1462-1476.
95. Dědeček, J.; Sobalík, Z.; Tvaruzkova, Z.; Kaucky, D.; Wichterlova, B., Coordination of Cu ions in high-silica zeolite matrixes. Cu⁺ photoluminescence, IR of NO adsorbed on Cu²⁺, and Cu²⁺ ESR study. *The Journal of Physical Chemistry* **1995**, *99* (44), 16327-16337.
96. Itadani, A.; Kuroda, Y.; Nagao, M., Elucidation of a preparation method for copper ion-exchanged ZSM-5 samples exhibiting extremely efficient N₂-adsorption at room temperature: effect of counter ions in the exchange solution. *Microporous Mesoporous Mater.* **2004**, *70* (1), 119-126.

97. Zhang, Y.; Leo, K. M.; Sarofim, A. F.; Hu, Z.; Flytzani-Stephanopoulos, M., Preparation effects on the activity of Cu-ZSM-5 catalysts for NO decomposition. *Catalysis letters* **1995**, *31* (1), 75-89.
98. Lamberti, C.; Bordiga, S.; Salvalaggio, M.; Spoto, G.; Zecchina, A.; Geobaldo, F.; Vlaic, G.; Bellatreccia, M., XAFS, IR, and UV-VIS study of the CuI environment in CuI-ZSM-5. *J. Phys. Chem. B* **1997**, *101* (3), 344-360.
99. Zhang, Y.; Drake, I. J.; Bell, A. T., Characterization of Cu-ZSM-5 prepared by solid-state ion exchange of H-ZSM-5 with CuCl. *Chem. Mater.* **2006**, *18* (9), 2347-2356.
100. Palomino, G. T.; Fiscaro, P.; Bordiga, S.; Zecchina, A.; Giamello, E.; Lamberti, C., Oxidation states of copper ions in ZSM-5 zeolites. A multitechnique investigation. *J. Phys. Chem. B* **2000**, *104* (17), 4064-4073.
101. Gao, F.; Walter, E. D.; Kollar, M.; Wang, Y.; Szanyi, J.; Peden, C. H. F., Understanding ammonia selective catalytic reduction kinetics over Cu/SSZ-13 from motion of the Cu ions. *J. Catal.* **2014**, *319*, 1-14.
102. Attfield, M. P.; Weigel, S. J.; Cheetham, A. K., On the Nature of Nonframework Cations in a Zeolitic deNO_x Catalyst: Cu-Mordenite. *J. Catal.* **1997**, *170* (2), 227-235.
103. Larsen, S. C.; Aylor, A.; Bell, A. T.; Reimer, J. A., Electron paramagnetic resonance studies of copper ion-exchanged ZSM-5. *The Journal of Physical Chemistry* **1994**, *98* (44), 11533-11540.
104. Groothaert, M. H.; Lievens, K.; Leeman, H.; Weckhuysen, B. M.; Schoonheydt, R. A., An operando optical fiber UV-vis spectroscopic study of the catalytic decomposition of NO and N₂O over Cu-ZSM-5. *J. Catal.* **2003**, *220* (2), 500-512.
105. Wichterlova, B.; Sobalik, Z.; Dědeček, J., Cu ion siting in high silica zeolites. Spectroscopy and redox properties. *Catal. Today* **1997**, *38* (2), 199-203.
106. Beutel, T.; Sarkany, J.; Lei, G.-D.; Yan, J.; Sachtler, W., Redox chemistry of Cu/ZSM-5. *The Journal of Physical Chemistry* **1996**, *100* (2), 845-851.
107. Bulanek, R.; Wichterlová, B.; Sobalik, Z.; Tichý, J., Reducibility and oxidation activity of Cu ions in zeolites: Effect of Cu ion coordination and zeolite framework composition. *Appl. Catal., B* **2001**, *31* (1), 13-25.
108. Vanelderden, P.; Hadt, R. G.; Smeets, P. J.; Solomon, E. I.; Schoonheydt, R. A.; Sels, B. F., Cu-ZSM-5: A biomimetic inorganic model for methane oxidation. *J. Catal.* **2011**, *284* (2), 157-164.
109. Llabre i Xamena, F.; Fiscaro, P.; Berlier, G.; Zecchina, A.; Palomino, G. T.; Prestipino, C.; Bordiga, S.; Giamello, E.; Lamberti, C., Thermal Reduction of Cu²⁺-Mordenite and Re-oxidation upon Interaction with H₂O, O₂, and NO. *J. Phys. Chem. B* **2003**, *107* (29), 7036-7044.
110. Davis, M. E.; Lobo, R. F., Zeolite and molecular sieve synthesis. *Chem. Mater.* **1992**, *4* (4), 756-768.
111. Milton, R. M., Molecular sieve adsorbents. Google Patents: 1959.
112. Di Iorio, J. R.; Gounder, R., Controlling the Isolation and Pairing of Aluminum in Chabazite Zeolites Using Mixtures of Organic and Inorganic Structure-Directing Agents. *Chem. Mater.* **2016**, *28* (7), 2236-2247.
113. Ren, L.; Zhu, L.; Yang, C.; Chen, Y.; Sun, Q.; Zhang, H.; Li, C.; Nawaz, F.; Meng, X.; Xiao, F.-S., Designed copper-amine complex as an efficient template for one-pot synthesis of Cu-SSZ-13 zeolite with excellent activity for selective catalytic reduction of NO_x by NH₃. *Chem. Commun.* **2011**, *47* (35), 9789-9791.
114. Martínez-Franco, R.; Moliner, M.; Thogersen, J. R.; Corma, A., Efficient One-Pot Preparation of Cu-SSZ-13 Materials using Cooperative OSDAs for their Catalytic Application in the SCR of NO_x. *ChemCatChem* **2013**, *5* (11), 3316-3323.
115. Zhang, T.; Qiu, F.; Chang, H.; Li, X.; Li, J., Identification of active sites and reaction mechanism on low-temperature SCR activity over Cu-SSZ-13 catalysts prepared by different methods. *Catal. Sci. Technol.* **2016**.

116. Martínez-Franco, R.; Moliner, M.; Franch, C.; Kustov, A.; Corma, A., Rational direct synthesis methodology of very active and hydrothermally stable Cu-SAPO-34 molecular sieves for the SCR of NO_x. *Appl. Catal., B* **2012**, *127*, 273-280.
117. Xie, L.; Liu, F.; Ren, L.; Shi, X.; Xiao, F.-S.; He, H., Excellent Performance of One-Pot Synthesized Cu-SSZ-13 Catalyst for the Selective Catalytic Reduction of NO_x with NH₃. *Environ. Sci. Technol.* **2013**, *48* (1), 566-572.
118. Woertink, J. S.; Smeets, P. J.; Groothaert, M. H.; Vance, M. A.; Sels, B. F.; Schoonheydt, R. A.; Solomon, E. I., A [Cu₂O] 2+ core in Cu-ZSM-5, the active site in the oxidation of methane to methanol. *Proc. Natl. Acad. Sci. U. S. A.* **2009**, *106* (45), 18908-18913.
119. Vanelderen, P.; Vancauwenbergh, J.; Tsai, M. L.; Hadt, R. G.; Solomon, E. I.; Schoonheydt, R. A.; Sels, B. F., Spectroscopy and Redox Chemistry of Copper in Mordenite. *ChemPhysChem* **2014**, *15* (1), 91-99.
120. Alayon, E. M.; Nachtegaal, M.; Ranocchiari, M.; van Bokhoven, J. A., Catalytic conversion of methane to methanol over Cu-mordenite. *Chem. Commun.* **2012**, *48* (3), 404-406.
121. Alayon, E. M. C.; Nachtegaal, M.; Bodi, A.; van Bokhoven, J. A., Reaction Conditions of Methane-to-Methanol Conversion Affect the Structure of Active Copper Sites. *ACS Catal.* **2013**, *4* (1), 16-22.
122. Vanelderen, P.; Snyder, B. E.; Tsai, M.-L.; Hadt, R. G.; Vancauwenbergh, J.; Coussens, O.; Schoonheydt, R. A.; Sels, B. F.; Solomon, E. I., Spectroscopic definition of the copper active sites in Mordenite: selective methane oxidation. *J. Am. Chem. Soc.* **2015**, *137* (19), 6383-6392.
123. Grundner, S.; Markovits, M. A.; Li, G.; Tromp, M.; Pidko, E. A.; Hensen, E. J.; Jentys, A.; Sanchez-Sanchez, M.; Lercher, J. A., Single-site trinuclear copper oxygen clusters in mordenite for selective conversion of methane to methanol. *Nat. Commun.* **2015**, *6*, 7546.
124. Grundner, S.; Luo, W.; Sanchez-Sanchez, M.; Lercher, J. A., Synthesis of single-site copper catalysts for methane partial oxidation. *Chem. Commun.* **2016**, *52* (12), 2553-2556.
125. Wulfers, M. J.; Teketel, S.; Ipek, B.; Lobo, R., Conversion of methane to methanol on copper-containing small-pore zeolites and zeotypes. *Chem. Commun.* **2015**, *51* (21), 4447-4450.
126. Kulkarni, A. R.; Zhao, Z.-J.; Siahrostami, S.; Nørskov, J. K.; Studt, F., Monocopper Active Site for Partial Methane Oxidation in Cu-Exchanged 8MR Zeolites. *ACS Catal.* **2016**, *6*, 6531-6536.
127. Hammond, C.; Conrad, S.; Hermans, I., Oxidative Methane Upgrading. *ChemSusChem* **2012**, *5* (9), 1668-1686.
128. Shu, L.; Nesheim, J. C.; Kauffmann, K.; Münck, E.; Lipscomb, J. D.; Que, L., An Fe₂IVO₂ diamond core structure for the key intermediate Q of methane monooxygenase. *Science* **1997**, *275* (5299), 515-518.
129. Lee, D.; Lippard, S. J., Structural and functional models of the dioxygen-activating centers of non-heme diiron enzymes ribonucleotide reductase and soluble methane monooxygenase. *J. Am. Chem. Soc.* **1998**, *120* (46), 12153-12154.
130. Lee, S. K.; Fox, B. G.; Froland, W. A.; Lipscomb, J. D.; Munck, E., A transient intermediate of the methane monooxygenase catalytic cycle containing an Fe^{IV}Fe^{IV} cluster. *J. Am. Chem. Soc.* **1993**, *115* (14), 6450-6451.
131. Kopp, D. A.; Lippard, S. J., Soluble methane monooxygenase: activation of dioxygen and methane. *Curr. Opin. Chem. Biol.* **2002**, *6* (5), 568-576.
132. Lieberman, R. L.; Rosenzweig, A. C., Crystal structure of a membrane-bound metalloenzyme that catalyses the biological oxidation of methane. *Nature* **2005**, *434* (7030), 177-182.

133. Panov, G.; Sheveleva, G.; Kharitonov, A. e. a.; Romannikov, V.; Vostrikova, L., Oxidation of benzene to phenol by nitrous oxide over Fe-ZSM-5 zeolites. *Appl. Catal., A* **1992**, *82* (1), 31-36.
134. Ovanesyanyan, N.; Shteinman, A.; Dubkov, K.; Sobolev, V.; Panov, G., The state of iron in the Fe-ZSM-5-N₂O system for selective oxidation of methane to methanol from data of Mössbauer spectroscopy. *Kinet. Catal.* **1998**, *39* (6), 792-797.
135. Beznis, N. V.; Weckhuysen, B. M.; Bitter, J. H., Cu-ZSM-5 zeolites for the formation of methanol from methane and oxygen: probing the active sites and spectator species. *Catalysis letters* **2010**, *138* (1-2), 14-22.
136. Zecchina, A.; Rivallan, M.; Berlier, G.; Lamberti, C.; Ricchiardi, G., Structure and nuclearity of active sites in Fe-zeolites: comparison with iron sites in enzymes and homogeneous catalysts. *PCCP* **2007**, *9* (27), 3483-3499.
137. Berlier, G.; Spoto, G.; Fiscaro, P.; Bordiga, S.; Zecchina, A.; Giamello, E.; Lamberti, C., Co-ordination and oxidation changes undergone by iron species in Fe-silicalite upon template removal, activation and interaction with N₂O: an in situ X-ray absorption study. *Microchem. J.* **2002**, *71* (2-3), 101-116.
138. Buda, F.; Ensing, B.; Gribnau, M. C. M.; Baerends, E. J., O₂ Evolution in the Fenton Reaction. *Chemistry – A European Journal* **2003**, *9* (14), 3436-3444.
139. Vanelderen, P.; Vancauwenbergh, J.; Sels, B. F.; Schoonheydt, R. A., Coordination chemistry and reactivity of copper in zeolites. *Coord. Chem. Rev.* **2013**, *257* (2), 483-494.
140. Tsai, M.-L.; Hadt, R. G.; Vanelderen, P.; Sels, B. F.; Schoonheydt, R. A.; Solomon, E. I., [Cu₂O]²⁺ Active Site Formation in Cu-ZSM-5: Geometric and Electronic Structure Requirements for N₂O Activation. *J. Am. Chem. Soc.* **2014**, *136* (9), 3522-3529.
141. Li, B.; Xu, J.; Han, B.; Wang, X.; Qi, G.; Zhang, Z.; Wang, C.; Deng, F., Insight into Dimethyl Ether Carbonylation Reaction over Mordenite Zeolite from in-Situ Solid-State NMR Spectroscopy. *J. Phys. Chem. C* **2013**, *117* (11), 5840-5847.
142. Romañ-Leshkov, Y.; Moliner, M.; Davis, M. E., Impact of Controlling the Site Distribution of Al Atoms on Catalytic Properties in Ferrierite-Type Zeolites†. *J. Phys. Chem. C* **2010**, *115* (4), 1096-1102.
143. Blasco, T.; Boronat, M.; Concepción, P.; Corma, A.; Law, D.; Vidal-Moya, J. A., Carbonylation of Methanol on Metal-Acid Zeolites: Evidence for a Mechanism Involving a Multisite Active Center. *Angew. Chem.* **2007**, *119* (21), 4012-4015.
144. Smeets, P. J.; Hadt, R. G.; Woertink, J. S.; Vanelderen, P.; Schoonheydt, R. A.; Sels, B. F.; Solomon, E. I., Oxygen precursor to the reactive intermediate in methanol synthesis by Cu-ZSM-5. *J. Am. Chem. Soc.* **2010**, *132* (42), 14736-14738.
145. Alayon, E. M. C.; Nachtegaal, M.; Kleymentov, E.; van Bokhoven, J. A., Determination of the electronic and geometric structure of Cu sites during methane conversion over Cu-MOR with X-ray absorption spectroscopy. *Microporous Mesoporous Mater.* **2013**, *166* (0), 131-136.
146. Cheung, P.; Bhan, A.; Sunley, G. J.; Iglesia, E., Selective Carbonylation of Dimethyl Ether to Methyl Acetate Catalyzed by Acidic Zeolites. *Angew. Chem. Int. Ed.* **2006**, *45* (10), 1617-1620.
147. Cheung, P.; Bhan, A.; Sunley, G. J.; Law, D. J.; Iglesia, E., Site requirements and elementary steps in dimethyl ether carbonylation catalyzed by acidic zeolites. *J. Catal.* **2007**, *245* (1), 110-123.
148. Drake, I. J.; Furdala, K. L.; Bell, A. T.; Tilley, T. D., Dimethyl carbonate production via the oxidative carbonylation of methanol over Cu/SiO₂ catalysts prepared via molecular precursor grafting and chemical vapor deposition approaches. *J. Catal.* **2005**, *230* (1), 14-27.
149. Zhang, Y.; Drake, I. J.; Briggs, D. N.; Bell, A. T., Synthesis of dimethyl carbonate and dimethoxy methane over Cu-ZSM-5. *J. Catal.* **2006**, *244* (2), 219-229.

150. Zheng, X.; Bell, A. T., A Theoretical Investigation of Dimethyl Carbonate Synthesis on Cu-Y Zeolite. *J. Phys. Chem. C* **2008**, *112* (13), 5043-5047.
151. Zhang, Y.; Briggs, D. N.; de Smit, E.; Bell, A. T., Effects of zeolite structure and composition on the synthesis of dimethyl carbonate by oxidative carbonylation of methanol on Cu-exchanged Y, ZSM-5, and Mordenite. *J. Catal.* **2007**, *251* (2), 443-452.
152. Zhang, Y.; Bell, A. T., The mechanism of dimethyl carbonate synthesis on Cu-exchanged zeolite Y. *J. Catal.* **2008**, *255* (2), 153-161.
153. Parrillo, D. J.; Adamo, A. T.; Kokotailo, G. T.; Gorte, R. J., Amine adsorption in H-ZSM-5. *Applied Catalysis* **1990**, *67* (1), 107-118.
154. Farneth, W. E.; Gorte, R. J., Methods for Characterizing Zeolite Acidity. *Chem. Rev.* **1995**, *95* (3), 615-635.
155. Parrillo, D. J.; Dolenc, D.; Gorte, R. J.; McCabe, R. W., Adsorption Studies on Cu-ZSM-5: Characterization of the Unique Properties of Ion-Exchanged Cu. *J. Catal.* **1993**, *142* (2), 708-718.
156. Panov, G.; Sobolev, V.; Dubkov, K.; Parmon, V.; Ovanesyan, N.; Shilov, A.; Shteinman, A., Iron complexes in zeolites as a new model of methane monooxygenase. *React. Kinet. Catal. Lett.* **1997**, *61* (2), 251-258.
157. Wang, W.; Seiler, M.; Hunger, M., Role of surface methoxy species in the conversion of methanol to dimethyl ether on acidic zeolites investigated by in situ stopped-flow MAS NMR spectroscopy. *J. Phys. Chem. B* **2001**, *105* (50), 12553-12558.
158. Forester, T.; Howe, R., In situ FTIR studies of methanol and dimethyl ether in ZSM-5. *J. Am. Chem. Soc.* **1987**, *109* (17), 5076-5082.
159. Anderson, M. W.; Klinowski, J., Solid-state NMR studies of the shape-selective catalytic conversion of methanol into gasoline on zeolite ZSM-5. *J. Am. Chem. Soc.* **1990**, *112* (1), 10-16.
160. Blaszkowski, S.; Van Santen, R., Density functional theory calculations of the activation of methanol by a Brønsted zeolitic proton. *The Journal of Physical Chemistry* **1995**, *99* (30), 11728-11738.
161. Delabie, A.; Pierloot, K.; Groothaert, M. H.; Weckhuysen, B. M.; Schoonheydt, R. A., The siting of Cu (II) in mordenite: a theoretical spectroscopic study. *PCCP* **2002**, *4* (1), 134-145.
162. Groothaert, M. H.; Pierloot, K.; Delabie, A.; Schoonheydt, R. A., Identification of Cu (II) coordination structures in Cu-ZSM-5, based on a DFT/ab initio assignment of the EPR spectra. *PCCP* **2003**, *5* (10), 2135-2144.
163. Starokon, E. V.; Parfenov, M. V.; Arzumanov, S. S.; Pirutko, L. V.; Stepanov, A. G.; Panov, G. I., Oxidation of methane to methanol on the surface of FeZSM-5 zeolite. *J. Catal.* **2013**, *300* (0), 47-54.
164. Yoshizawa, K.; Shiota, Y.; Kamachi, T., Mechanistic Proposals for Direct Benzene Hydroxylation over Fe-ZSM-5 Zeolite. *J. Phys. Chem. B* **2003**, *107* (41), 11404-11410.
165. Fella, M. F.; Pidko, E. A.; van Santen, R. A.; Onal, I., A DFT Study of Direct Oxidation of Benzene to Phenol by N₂O over [Fe(μ -O)Fe]²⁺ Complexes in ZSM-5 Zeolite. *J. Phys. Chem. C* **2011**, *115* (19), 9668-9680.
166. Parfenov, M. V.; Starokon, E. V.; Pirutko, L. V.; Panov, G. I., Quasicatalytic and catalytic oxidation of methane to methanol by nitrous oxide over FeZSM-5 zeolite. *J. Catal.* **2014**, *318*, 14-21.
167. Tavernier, S. D.; Schoonheydt, R. A., Coordination of Cu²⁺ in synthetic mordenites. *Zeolites* **1991**, *11* (2), 155-163.
168. Carl, P. J.; Larsen, S. C., EPR Study of Copper-Exchanged Zeolites: Effects of Correlated g- and A-Strain, Si/Al Ratio, and Parent Zeolite. *J. Phys. Chem. B* **2000**, *104* (28), 6568-6575.

169. Nicula, A.; Stamires, D.; Turkevich, J., Paramagnetic Resonance Absorption of Copper Ions in Porous Crystals. *The Journal of Chemical Physics* **1965**, *42* (10), 3684-3692.
170. Kucherov, A.; Slinkin, A.; Kondrat'ev, D.; Bondarenko, T.; Rubinstein, A.; Minachev, K. M., Cu²⁺-cation location and reactivity in mordenite and ZSM-5: esr-study. *Zeolites* **1985**, *5* (5), 320-324.
171. Anderson, M. W.; Kevan, L., Study of copper (2+)-doped zeolite NaH-ZSM-5 by electron spin resonance and electron spin echo modulation spectroscopies. *J. Phys. Chem.* **1987**, *91* (15), 4174-4179.
172. Sass, C. E.; Kevan, L., Electron spin-echo and electron spin-resonance studies of cupric ion-adsorbate interactions in H-, Na-, K-, and Ca-mordenite. *The Journal of Physical Chemistry* **1989**, *93* (11), 4669-4674.
173. Wang, W.; Hunger, M., Reactivity of surface alkoxy species on acidic zeolite catalysts. *Acc. Chem. Res.* **2008**, *41* (8), 895-904.
174. Gottlieb, H. E.; Kotlyar, V.; Nudelman, A., NMR chemical shifts of common laboratory solvents as trace impurities. *J. Org. Chem.* **1997**, *62* (21), 7512-7515.
175. Roy, P. K.; Pirngruber, G. D., The surface chemistry of N₂O decomposition on iron-containing zeolites (II)—The effect of high-temperature pretreatments. *J. Catal.* **2004**, *227* (1), 164-174.
176. Wickramasinghe, N. P.; Shaibat, M.; Ishii, Y., Enhanced Sensitivity and Resolution in 1H Solid-State NMR Spectroscopy of Paramagnetic Complexes under Very Fast Magic Angle Spinning. *J. Am. Chem. Soc.* **2005**, *127* (16), 5796-5797.
177. Aguiar, P. M.; Katz, M. J.; Leznoff, D. B.; Kroeker, S., Natural abundance ¹³C and ¹⁵N solid-state NMR analysis of paramagnetic transition-metal cyanide coordination polymers. *PCCP* **2009**, *11* (32), 6925-6934.
178. Luzgin, M. V.; Kazantsev, M. S.; Wang, W.; Stepanov, A. G., Reactivity of Methoxy Species toward CO on Keggin 12-H₃PW₁₂O₄₀: A Study with Solid State NMR. *J. Phys. Chem. C* **2009**, *113* (45), 19639-19644.
179. Lezcano-González, I.; Vidal-Moya, J. A.; Boronat, M.; Blasco, T.; Corma, A., Identification of Active Surface Species for Friedel-Crafts Acylation and Koch Carbonylation Reactions by in situ Solid-State NMR Spectroscopy. *Angew. Chem. Int. Ed.* **2013**, *52* (19), 5138-5141.
180. Smith, K. T.; Berritt, S.; González-Moreiras, M.; Ahn, S.; Smith, M. R.; Baik, M.-H.; Mindiola, D. J., Catalytic borylation of methane. *Science* **2016**, *351* (6280), 1424-1427.
181. Caballero, A.; Despagnet-Ayoub, E.; Díaz-Requejo, M. M.; Díaz-Rodríguez, A.; González-Núñez, M. E.; Mello, R.; Muñoz, B. K.; Ojo, W.-S.; Asensio, G.; Etienne, M., Silver-Catalyzed CC Bond Formation Between Methane and Ethyl Diazoacetate in Supercritical CO₂. *Science* **2011**, *332* (6031), 835-838.
182. Cavaliere, V. N.; Mindiola, D. J., Methane: a new frontier in organometallic chemistry. *Chem. Sci.* **2012**, *3* (12), 3356-3365.
183. Narsimhan, K.; Iyoki, K.; Dinh, K.; Román-Leshkov, Y., Catalytic Oxidation of Methane into Methanol over Copper-Exchanged Zeolites with Oxygen at Low Temperature. *ACS Central Science* **2016**, *2* (6), 424-429.
184. Tomkins, P.; Mansouri, A.; Bozbag, S. E.; Krumeich, F.; Park, M. B.; Alayon, E. M. C.; Ranocchiari, M.; van Bokhoven, J. A., Isothermal Cyclic Conversion of Methane into Methanol over Copper-Exchanged Zeolite at Low Temperature. *Angew. Chem.* **2016**, *128* (18), 5557-5561.
185. Gao, F.; Kwak, J. H.; Szanyi, J.; Peden, C. H., Current understanding of copper-exchanged Chabazite molecular sieves for use as commercial diesel engine DeNO_x catalysts. *Top. Catal.* **2013**, *56* (15-17), 1441-1459.

186. Sajith, P. K.; Shiota, Y.; Yoshizawa, K., Role of Acidic Proton in the Decomposition of NO over Dimeric Cu(I) Active Sites in Cu-ZSM-5 Catalyst: A QM/MM Study. *ACS Catal.* **2014**, *4* (6), 2075-2085.
187. Cambor, M. A.; Corma, A.; Valencia, S., Spontaneous nucleation and growth of pure silica zeolite- β free of connectivity defects. *Chem. Commun.* **1996**, (20), 2365-2366.
188. Persson, A.; Schoeman, B.; Sterte, J.; Otterstedt, J.-E., The synthesis of discrete colloidal particles of TPA-silicalite-1. *Zeolites* **1994**, *14* (7), 557-567.
189. Yaripour, F.; Baghaei, F.; Schmidt, I.; Perregaard, J., Catalytic dehydration of methanol to dimethyl ether (DME) over solid-acid catalysts. *Catal. Commun.* **2005**, *6* (2), 147-152.
190. Blaszkowski, S. R.; van Santen, R. A., The mechanism of dimethyl ether formation from methanol catalyzed by zeolitic protons. *J. Am. Chem. Soc.* **1996**, *118* (21), 5152-5153.
191. Hassanpour, S.; Yaripour, F.; Taghizadeh, M., Performance of modified H-ZSM-5 zeolite for dehydration of methanol to dimethyl ether. *Fuel Process. Technol.* **2010**, *91* (10), 1212-1221.
192. Vishwanathan, V.; Jun, K.-W.; Kim, J.-W.; Roh, H.-S., Vapour phase dehydration of crude methanol to dimethyl ether over Na-modified H-ZSM-5 catalysts. *Appl. Catal., A* **2004**, *276* (1-2), 251-255.
193. Song, Q.; Liu, W.; Bohn, C. D.; Harper, R. N.; Sivaniah, E.; Scott, S. A.; Dennis, J. S., A high performance oxygen storage material for chemical looping processes with CO₂ capture. *Energy Environ. Sci.* **2013**, *6* (1), 288-298.
194. Hereijgers, B. P.; Bleken, F.; Nilsen, M. H.; Svelle, S.; Lillerud, K.-P.; Bjørgen, M.; Weckhuysen, B. M.; Olsbye, U., Product shape selectivity dominates the Methanol-to-Olefins (MTO) reaction over H-SAPO-34 catalysts. *J. Catal.* **2009**, *264* (1), 77-87.
195. Xue, J.; Wang, X.; Qi, G.; Wang, J.; Shen, M.; Li, W., Characterization of copper species over Cu/SAPO-34 in selective catalytic reduction of NO_x with ammonia: Relationships between active Cu sites and de-NO_x performance at low temperature. *J. Catal.* **2013**, *297*, 56-64.
196. Korhonen, S. T.; Fickel, D. W.; Lobo, R. F.; Weckhuysen, B. M.; Beale, A. M., Isolated Cu²⁺ ions: active sites for selective catalytic reduction of NO. *Chem. Commun.* **2011**, *47* (2), 800-802.
197. Wang, L.; Li, W.; Qi, G.; Weng, D., Location and nature of Cu species in Cu/SAPO-34 for selective catalytic reduction of NO with NH₃. *J. Catal.* **2012**, *289*, 21-29.
198. Bates, S. A.; Verma, A. A.; Paolucci, C.; Parekh, A. A.; Anggara, T.; Yezerets, A.; Schneider, W. F.; Miller, J. T.; Delgass, W. N.; Ribeiro, F. H., Identification of the active Cu site in standard selective catalytic reduction with ammonia on Cu-SSZ-13. *J. Catal.* **2014**, *312*, 87-97.
199. Göttl, F.; Buló, R. E.; Hafner, J.; Sautet, P., What Makes Copper-Exchanged SSZ-13 Zeolite Efficient at Cleaning Car Exhaust Gases? *The Journal of Physical Chemistry Letters* **2013**, *4* (14), 2244-2249.
200. Fickel, D. W.; Lobo, R. F., Copper coordination in Cu-SSZ-13 and Cu-SSZ-16 investigated by variable-temperature XRD. *J. Phys. Chem. C* **2009**, *114* (3), 1633-1640.
201. Verma, A. A.; Bates, S. A.; Anggara, T.; Paolucci, C.; Parekh, A. A.; Kamasamudram, K.; Yezerets, A.; Miller, J. T.; Delgass, W. N.; Schneider, W. F.; Ribeiro, F. H., NO oxidation: A probe reaction on Cu-SSZ-13. *J. Catal.* **2014**, *312*, 179-190.
202. Zones, S., Conversion of faujasites to high-silica chabazite SSZ-13 in the presence of N, N, N-trimethyl-1-adamantammonium iodide. *J. Chem. Soc., Faraday Trans.* **1991**, *87* (22), 3709-3716.

203. Dědeček, J.; Wichterlová, B., Role of Hydrated Cu Ion Complexes and Aluminum Distribution in the Framework on the Cu Ion Siting in ZSM-5. *J. Phys. Chem. B* **1997**, *101* (49), 10233-10240.
204. Giordanino, F.; Vennestrøm, P. N.; Lundegaard, L. F.; Stappen, F. N.; Mossin, S.; Beato, P.; Bordiga, S.; Lamberti, C., Characterization of Cu-exchanged SSZ-13: a comparative FTIR, UV-Vis, and EPR study with Cu-ZSM-5 and Cu- β with similar Si/Al and Cu/Al ratios. *Dalton Trans.* **2013**, *42* (35), 12741-12761.
205. Groothaert, M. H.; van Bokhoven, J. A.; Battiston, A. A.; Weckhuysen, B. M.; Schoonheydt, R. A., Bis(μ -oxo)dicopper in Cu-ZSM-5 and Its Role in the Decomposition of NO: A Combined in Situ XAFS, UV-Vis-Near-IR, and Kinetic Study. *J. Am. Chem. Soc.* **2003**, *125* (25), 7629-7640.
206. Kau, L. S.; Spira-Solomon, D. J.; Penner-Hahn, J. E.; Hodgson, K. O.; Solomon, E. I., X-ray absorption edge determination of the oxidation state and coordination number of copper. Application to the type 3 site in *Rhus vernicifera* laccase and its reaction with oxygen. *J. Am. Chem. Soc.* **1987**, *109* (21), 6433-6442.
207. Kau, L. S.; Hodgson, K. O.; Solomon, E. I., X-ray absorption edge and EXAFS study of the copper sites in zinc oxide methanol synthesis catalysts. *J. Am. Chem. Soc.* **1989**, *111* (18), 7103-7109.
208. Kumashiro, R.; Kuroda, Y.; Nagao, M., New analysis of oxidation state and coordination environment of copper ion-exchanged in ZSM-5 zeolite. *J. Phys. Chem. B* **1999**, *103* (1), 89-96.
209. Kharas, K. C. C.; Liu, D.-J.; Robota, H. J., Structure-function properties in Cu-ZSM-5 no decomposition and NO SCR catalysts. *Catal. Today* **1995**, *26* (2), 129-145.
210. Kuroda, Y.; Kumashiro, R.; Yoshimoto, T.; Nagao, M., Characterization of active sites on copper ion-exchanged ZSM-5-type zeolite for NO decomposition reaction. *PCCP* **1999**, *1* (4), 649-656.
211. Borfecchia, E.; Lomachenko, K.; Giordanino, F.; Falsig, H.; Beato, P.; Soldatov, A.; Bordiga, S.; Lamberti, C., Revisiting the nature of Cu sites in the activated Cu-SSZ-13 catalyst for SCR reaction. *Chem. Sci.* **2015**, *6* (1), 548-563.
212. Kwak, J. H.; Zhu, H.; Lee, J. H.; Peden, C. H.; Szanyi, J., Two different cationic positions in Cu-SSZ-13? *Chem. Commun.* **2012**, *48* (39), 4758-4760.
213. Szanyi, J.; Kwak, J. H.; Zhu, H.; Peden, C. H. F., Characterization of Cu-SSZ-13 NH₃ SCR catalysts: an in situ FTIR study. *PCCP* **2013**, *15* (7), 2368-2380.
214. Paolucci, C.; Parekh, A. A.; Khurana, I.; Di Iorio, J. R.; Li, H.; Albarracin Caballero, J. D.; Shih, A. J.; Anggara, T.; Delgass, W. N.; Miller, J. T., Catalysis in a Cage: Condition-Dependent Speciation and Dynamics of Exchanged Cu Cations in SSZ-13 Zeolites. *J. Am. Chem. Soc.* **2016**, *138* (18), 6028-6048.
215. Kwak, J. H.; Varga, T.; Peden, C. H. F.; Gao, F.; Hanson, J. C.; Szanyi, J., Following the movement of Cu ions in a SSZ-13 zeolite during dehydration, reduction and adsorption: A combined in situ TP-XRD, XANES/DRIFTS study. *J. Catal.* **2014**, *314*, 83-93.
216. Lei, G. D.; Adelman, B. J.; Sárkány, J.; Sachtler, W. M. H., Identification of copper(II) and copper(I) and their interconversion in Cu/ZSM-5 De-NO_x catalysts. *Appl. Catal., B* **1995**, *5* (3), 245-256.
217. Deka, U.; Juhin, A.; Eilertsen, E. A.; Emerich, H.; Green, M. A.; Korhonen, S. T.; Weckhuysen, B. M.; Beale, A. M., Confirmation of Isolated Cu²⁺ Ions in SSZ-13 Zeolite as Active Sites in NH₃-Selective Catalytic Reduction. *J. Phys. Chem. C* **2012**, *116* (7), 4809-4818.
218. Andersen, C. W.; Bremholm, M.; Vennestrom, P. N. R.; Blichfeld, A. B.; Lundegaard, L. F.; Iversen, B. B., Location of Cu²⁺ in CHA zeolite investigated by X-ray diffraction using the Rietveld/maximum entropy method. *IUCrJ* **2014**, *1* (6), 382-386.

219. Valyon, J.; Hall, W. K., Effects of reduction and reoxidation on the infrared spectra from Cu-Y and Cu-ZSM-5 zeolites. *The Journal of Physical Chemistry* **1993**, *97* (27), 7054-7060.
220. Marchese, L.; Chen, J.; Thomas, J. M.; Coluccia, S.; Zecchina, A., Bronsted, Lewis, and redox centers on CoAPO-18 catalysts. 1. vibrational modes of adsorbed water. *The Journal of Physical Chemistry* **1994**, *98* (50), 13350-13356.
221. Iwasaki, M.; Shinjoh, H., NO evolution reaction with NO₂ adsorption over Fe/ZSM-5: In situ FT-IR observation and relationships with Fe sites. *J. Catal.* **2010**, *273* (1), 29-38.
222. Sárkány, J.; Sachtler, W. M. H., Redox chemistry of CuNaZSM-5: Detection of cuprous ions by FTIR. *Zeolites* **1994**, *14* (1), 7-11.
223. Pestryakov, A. N.; Petranovskii, V. P.; Kryazhov, A.; Ozhereliev, O.; Pfänder, N.; Knop-Gericke, A., Study of copper nanoparticles formation on supports of different nature by UV-Vis diffuse reflectance spectroscopy. *Chemical Physics Letters* **2004**, *385* (3-4), 173-176.
224. Praliaud, H.; Mikhailenko, S.; Chajar, Z.; Primet, M., Surface and bulk properties of Cu-ZSM-5 and Cu/Al₂O₃ solids during redox treatments. Correlation with the selective reduction of nitric oxide by hydrocarbons. *Appl. Catal., B* **1998**, *16* (4), 359-374.
225. Bordiga, S.; Regli, L.; Cocina, D.; Lamberti, C.; Bjørgen, M.; Lillerud, K. P., Assessing the Acidity of High Silica Chabazite H-SSZ-13 by FTIR Using CO as Molecular Probe: Comparison with H-SAPO-34. *J. Phys. Chem. B* **2005**, *109* (7), 2779-2784.
226. Sakong, S.; Gross, A., Total Oxidation of Methanol on Cu(110): A Density Functional Theory Study. *J. Phys. Chem. A* **2007**, *111* (36), 8814-8822.
227. Alayon, E. M. C.; Nachtegaal, M.; Bodi, A.; Ranocchiari, M.; van Bokhoven, J. A., Bis (μ -oxo) versus mono (μ -oxo) dicopper cores in a zeolite for converting methane to methanol: an in situ XAS and DFT investigation. *PCCP* **2015**, *17* (12), 7681-7693.
228. Yang, N. S.; Chuang, K. T.; Afacan, A.; Resetarits, M. R.; Binkley, M. J., Improving the Efficiency and Capacity of Methanol-Water Distillation Trays. *Ind. Eng. Chem. Res.* **2003**, *42* (25), 6601-6606.